

Synthesis and characterization of MgAl_2O_4 and $(\text{Mg}_x\text{Zn}_{1-x})\text{Al}_2\text{O}_4$ mixed spinel phosphors

by

**Wael Abed Ibrahim Tabaza
(MSc)**

A thesis submitted in fulfillment of requirement for the degree

PHILOSOPHIAE DOCTOR

in the

Faculty of Natural and Agricultural Sciences

Department of Physics

at the

University of the Free State

Promoter: Dr. R. E. Kroon

Co-Promoter: Prof. H.C. Swart

January 2014

Acknowledgements

بِسْمِ اللَّهِ الرَّحْمَنِ الرَّحِيمِ
"يَوْمَ نَطْوِي السَّمَاءَ كَطَيِّ السِّجِلِّ لِلْكُتُبِ كَمَا بَدَأْنَا أَوَّلَ خَلْقٍ نُعِيدُهُ وَعَدَّا عَلَيْنا إِنَّا كُنَّا فَاعِلِينَ"

[الأنبياء: 104]

The Day when We will fold the heaven like the folding of a [written] sheet for the records. As We began the first creation, We will repeat it. [That is] a promise binding upon Us. Indeed, We will do it.

(Qur'an 21:104)

With great pleasure, I would like to express my gratitude to all who have contributed to this thesis. First and foremost I would like to thank Allah Almighty for His immense blessings and kindness which guided me through all the challenges to face for completed Ph.D.

I am heartily thankful to my supervisor, **Dr R. E. Kroon**, whose encouragement, guidance and support from the beginning to the end, enabled me to develop an understanding of the subject.

I would like to express my thanks and sincere gratitude to my co-supervisor **Prof H.C. Swart**, head of research group in the Physics Department for his strong support, encouragement and guidance throughout my research.

My special thanks are given to my best friend **Dr Samy Khalil Kamel Shaat** for his assistance my, to introducing me to luminescent phosphors, and for his fruitful discussions.

My appreciations go to **Dr Liza Coetzee** for measuring XPS, Auger spectra and SEM images and **Dr Mart-Mari Biggs** for measuring with XPS. I am also grateful to **Mr Shaun Cronje** for

technical assistance and ordering equipment and **Mr Pat van Heerden** for help with computer issues.

I thank all staff members of the Department of Physics (UFS) and post graduate students, specially, to **Prof Koos Terblans**, head of Physics Department, **Prof Petrus Meintjes** and **Prof Ntwaeaborwa** for their support.

I would like to special thank my officemate **Dr Abdelrhman Yousif Mohmmmed Ahmed** for his fruitful discussions.

I would like to thank **Prof Pieter van Wyk** and **Hanlie Grobler** at the University of the Free State Centre for Microscopy for assisting with the TEM and SEM measurements.

I would like to thank my colleague **Mr Abd Ellateef Abbass**, **Mr Mubarak Yagoub**, **Dr Hassan Abdelhalim Abdallah Seed Ahmed**, **Mr Raphael Nyenge** and **Dr Vinod Kumar**.

Special thanks to **Dr Abdalla Shoman** and his family, and **Dr Ayman Elhsnat** and his family **Mr Ahmad Shoman**, **Mr Ashraf Shoman** and **Mr Fayez Shoman** for their social support.

I would like to thank my colleagues in **phosphor group** at University of the Free State for their good discussion.

I would like to express my thanks to **Al-Aqsa Foundation** in South Africa, **Al-Quds foundation** in South Africa, staff in **Palestinian Embassy**.

I would like to thank all my colleagues at the **Islamic University Palestine** for their support and encouragement through this work.

I would like to thank the **National Laser Center**, Pretoria for allowing us to use their PLD system.

The acknowledgement would be incomplete if I do not express my gratitude to the staff of the Department for providing me the help during this study. Namely **Ms Karen Cronje** and **Mrs Yolandie Fick**.

I would like to thank my lovely family in Palestine and friends for the invaluable help and endless encouragement.

Last but not least, a very special thank you to my wife for her unceasing support and to my sweetheart, my lovely kids Lana, Mohammed, Baraa, Yamen and Yazan their love is my worth.

THANK YOU ALL

Wael Tabaza

Dedicated to the memory of my lovely parents, the late

Abed Ibrahim Tabaza and Fatma Mikdad

To my wife, Sheraz Hamdan and my kids,

Lana, Mohammed, Baraa, Yamen and Yazan, for their endless love,

support and encouragement

To my Brothers and Sisters, for their respect and

appreciation

Abstract

Magnesium aluminate (MgAl_2O_4) has received special attention as a technologically important material because of its attractive properties, such as mechanical strength, chemical inertness, a wideband gap, relatively low density, high melting point, high thermal shock resistance, low thermal expansion coefficient, resistance to neutron irradiation and low dielectric loss. It has also been used as a phosphor host activated by a variety of transition metal and lanthanide ions.

Doped and undoped MgAl_2O_4 nanocrystalline powders were successfully prepared by a simple combustion method. The structure of the powders was analyzed with x-ray diffraction (XRD). The XRD data showed that all the samples had the spinel structure and the average particle size of the as-prepared samples was about 25 nm. The morphology of the samples was determined by scanning electron microscopy (SEM) and transmission electron microscopy (TEM). X-ray photoelectron spectroscopy (XPS) was used to obtain more information on the conversion of Ce ions from the non-luminescent Ce^{4+} ion to the luminescent Ce^{3+} oxidation state. The optical properties of the material were measured using photoluminescence (PL) spectroscopy and ultraviolet-visible (UV-Vis) spectroscopy at room temperature.

At a 350 nm excitation wavelength the PL spectra of Ce^{3+} doped MgAl_2O_4 showed a broad green emission band centred at 490 nm. The maximum green emission was obtained for the sample doped with 0.75 mol% Ce. However the Ce^{3+} doped MgAl_2O_4 requires reducing at a high temperature (1400 °C) to convert the non-luminescent Ce^{4+} ions to the luminescent Ce^{3+} ions.

For this reason Bi^{3+} doped MgAl_2O_4 was also investigated. For an excitation wavelength of 335 nm the Bi^{3+} doped MgAl_2O_4 produced a broad blue emission band centred at around 400 nm. The maximum blue emission was obtained for the sample doped with 0.5 mol% Bi. The results indicate that doping MgAl_2O_4 with Bi ions may be more attractive than doping with Ce ions. The blue emission from Bi doped MgAl_2O_4 was found to occur in the wavelength region corresponding to the well known host independent weak f-f excitation peaks of Tb. Therefore the possibility of using Bi^{3+} ions as a sensitizer for Tb^{3+} ions emitting green light was investigated. Although Tb can generally be excited efficiently using its strong f-d transitions, the possibility of exciting it through energy transfer from Bi to the normally weak f-f transitions is important, since the excitation wavelength of Bi (335 nm) is longer and more accessible than the f-d transition wavelength of Tb in MgAl_2O_4 (227 nm). The results show that Bi is a good sensitizer for Tb in the MgAl_2O_4 host and leads to significant enhancement of Tb emissions from the $^5\text{D}_4$ level for excitation wavelengths between 300 nm and 380 nm (with a maximum enhancement of almost 100 times near 328 nm), thereby extending the useable excitation band of Tb to much longer wavelengths compared to Tb single doped samples.

Zinc aluminate (ZnAl_2O_4) also has the spinel structure and has been used as the phosphor host. Therefore it is interesting to consider the mixed spinel magnesium zinc aluminate ($\text{Mg}_x\text{Zn}_{1-x}\text{Al}_2\text{O}_4$) as a host for Tb. The maximum PL intensity of the green emission at 544 nm occurred for $\text{Mg}_{0.75}\text{Zn}_{0.25}\text{Al}_2\text{O}_4$ and the optimum Tb concentration was found to be 0.5 mol%. The blue emission at 416 nm was almost absent for ZnAl_2O_4 , but increased with the Mg content and was a maximum for MgAl_2O_4 . The absence of blue emission peaks is usually attributed to the concentration quenching, but since the same Tb concentration was used for the MgAl_2O_4 :Tb

where blue emissions did occur, it is rather suggested that because of the smaller bandgap of ZnAl_2O_4 , the $^5\text{D}_3$ level lies close to or inside the conduction band and this prevents transitions from this level.

An important application for phosphors is to make thin films for devices such as plasma displays and light emitting diodes. Tb doped $\text{Mg}_{0.75}\text{Zn}_{0.25}\text{Al}_2\text{O}_4$ thin films were fabricated on Si (100) substrates by two different techniques, namely sol-gel spin-coating and pulsed laser deposition (PLD) methods. The atomic force microscopy (AFM) and SEM data showed that the film deposited using a spin-coating method was more uniform and smooth compared to the thin film prepared by PLD. The thin film prepared by PLD has particles on the surface while the spin-coated film was uniform. For the spin-coated samples annealing was necessary, but the morphology of these films was changed after annealing at 1200 °C and the surface formed ridges. The depth profile results obtained by Auger electron spectroscopy (AES) show that there was already some diffusion of the Si substrate into the material of the thin film for the samples annealed at 1000 °C. The emission spectra were similar for both kind of thin films, but there was a variation in the intensity of luminescence of the thin films. The spin coating process is the more simple method for growing the thin films, while PLD is a good technique for synthesizing of the thin films at lower substrate temperatures which might be important for the fabrication of the devices using glass with a melting point around 700 °C.

Table of Contents

Acknowledgements	ii
Abstract	vi
Keyword and acronyms	xv
1. Introduction	
1.1. Overview	1
1.2. Motivation	2
1.3. Research aims	3
1.4. Thesis layout	4
1.5. References	5
2. Background information	
2.1. Introduction	6
2.2. Fundamentals of phosphors	6
2.3. Applications of phosphors	7
2.4. Types of luminescence	9
2.4.1. Photoluminescence	9
2.4.2. Electroluminescence	11
2.4.3. Cathodoluminescence	11
2.4.4. Thermoluminescence	11
2.4.5. Chemiluminescence	12

2.5. Lanthanides	12
2.6. Some luminescent centres	14
2.6.1. Trivalent terbium ion (Tb^{3+})	14
2.6.2. Trivalent europium ion (Eu^{3+})	16
2.6.3. Trivalent cerium ion (Ce^{3+})	17
2.6.4. Trivalent bismuth ion (Bi^{3+})	19
2.7. Energy transfer	20
2.8. Preparation methods of phosphors	22
2.8.1. Combustion synthesis	23
2.8.2. Sol-gel process	27
2.9. Magnesium aluminate and zinc aluminate spinel	29
2.10. References	32
3. Research techniques	
3.1. Introduction	36
3.2. X-ray diffraction	36
3.3. Scanning electron microscopy	40
3.4. Transmission electron microscopy	43
3.5. X-ray photoelectron spectroscopy	44
3.6. Photoluminescence spectroscopy	48
3.7. UV-Vis spectroscopy	50
3.8. Atomic force microscopy	53
3.9. Auger electron spectroscopy	55

3.10. Pulsed laser deposition	57
3.11. Spin coating	61
3.12. References	63
4. Luminescence of Ce doped MgAl ₂ O ₄ prepared by the combustion method	
4.1. Introduction	66
4.2. Materials and methods	68
4.3. Results and discussion	70
4.3.1. Structure and morphology	70
4.3.2. Optical properties	73
4.4. XPS measurements of the charge state of Ce	77
4.5. Conclusion	82
4.6. References	82
5. Blue luminescence from Bi doped MgAl ₂ O ₄ prepared by the combustion method	
5.1. Introduction	85
5.2. Materials and methods	86
5.3. Results and discussion	88
5.3.1. Structure and morphology	88
5.3.2. Optical properties	90
5.4. Conclusion	95
5.5. References	95

6. Optical properties of Bi and energy transfer from Bi to Tb in MgAl_2O_4 phosphor	
6.1. Introduction	97
6.2. Materials and methods	99
6.3. Results and discussion	102
6.3.1. Structure and morphology	102
6.3.2. Optical properties	106
6.3.3. Energy transfer from Bi to Tb	109
6.4. Conclusion	114
6.5. References	114
7. Enhanced luminescence from Tb for the mixed spinel $(\text{Mg}_x\text{Zn}_{1-x})\text{Al}_2\text{O}_4$	
7.1. Introduction	117
7.2. Experimental	118
7.3. Results and discussion	119
7.3.1. Structure	119
7.3.2. Optical properties	122
7.4. Conclusion	126
7.5. References	127
8. Effect of annealing temperature on the optical properties of $\text{Mg}_{0.75}\text{Zn}_{0.25}\text{Al}_2\text{O}_4$ thin films deposited by sol-gel spin-coating	
8.1. Introduction	129

8.2. Materials and methods	130
8.3. Results and discussion	131
8.3.1. Structure and morphology	131
8.3.2. Optical properties	144
8.4. Conclusion	147
8.5. References	147
9. PLD grown $Mg_{0.75}Zn_{0.25}Al_2O_4:Tb$ phosphor thin films	
9.1. Introduction	150
9.2. Experimental	151
9.3. Effects of substrate temperature on the properties of the thin films grown in vacuum	153
9.3.1. Structure	153
9.3.2. Morphology	155
9.3.3. NanoSAM analysis	158
9.3.4. Optical properties	161
9.4. Effects of different gas atmospheres on properties of thin films grown with a substrate temperature of 300 °C.	163
9.4.1. Structure	163
9.4.2. Morphology	164
9.4.3. NanoSAM analysis	167
9.4.4. Optical properties	169
9.5. Conclusion	170

9.6. References	170
10. Conclusion	
10.1. Summary	174
10.2. Suggestions for future work	177

Keywords and acronyms

Keywords

phosphor, magnesium aluminate, spinel, zinc aluminate, combustion method, spin-coating, pulsed laser deposition, cerium, terbium, bismuth, annealing, photoluminescence, energy transfer, thin films.

Acronyms

AES	Auger electron spectroscopy
AFM	Atomic force microscopy
CRT	Cathode ray tube
EDS	Energy dispersive spectroscopy
FED	Field emission display
FWHM	Full width at half maximum
JCPDS	Joint Committee on Powder Diffraction Standards
LCD	Liquid crystal display
PL	Photoluminescence
PLD	Pulsed laser deposition
PMT	Photomultiplier tube
SEM	Scanning electron microscopy
TEM	Transmission electron microscopy
UV	Ultraviolet
UV-Vis	Ultraviolet-visible
XPS	X-ray photoelectron spectroscopy
XRD	X-ray diffraction

1 Introduction

1.1 Overview

Phosphors have a large technological importance in a variety of applications like phosphor lamps, displays devices, lasers, light emitting diodes, optical amplifiers, luminescence sensors and medical diagnostics. The development of applications has created a need for phosphors with enhanced properties [1].

In most cases phosphors are based on luminescent centres, called dopants or activators, located in wide-bandgap hosts. Generally, host materials should exhibit good optical, mechanical and thermal properties [2-4]. There are many types of host materials, such as alkali-earth sulphides, alkali-earth aluminates, rare-earth oxides, nitrides and oxysulfides, lanthanide halides, gallates and silicates, etc. To enhance the luminescent characteristics of phosphors, extensive research has been carried out on rare-earth activated oxide phosphors due to their excellent luminescent characteristics, stability in high vacuum and absence of corrosive gas emission under electron bombardment. Of special interest are the oxides magnesium aluminate (MgAl_2O_4) and zinc aluminate (ZnAl_2O_4), both having the spinel structure, which have shown some promise in the past as phosphor hosts but require further study.

A thin film is a layer of material ranging from fractions of a nanometer (monolayer) to several micrometers in thickness. Thin films play an important role in the high-technology industries. Some of the important applications of thin films are microelectronics,

communications, optical electronics, catalysis and energy generation. Phosphor films have found many important applications such as cathode ray tubes (CRTs), medical imaging, graphics, helmet mounted displays, light emitting diodes, x-ray imaging scintillators, thin film electroluminescence panels, field emission displays (FEDs), gas sensors and thermomechanic devices. Thin film phosphors have several advantages over powders such as higher lateral resolution from smaller grains, better thermal stability and better adhesion to the solid surface [5]. Thin films are usually prepared by several techniques such as evaporation, electron beam deposition, sputtering method, chemical vapour deposition, anodic growth, pulsed laser deposition (PLD) and spin coating [6, 7].

In this study MgAl_2O_4 and ZnAl_2O_4 have been investigated as phosphor host materials, both in powder form and for thin films, for a variety of lanthanide ions as well as for doping with Bi for the first time. The mixed spinel $(\text{Mg}_x\text{Zn}_{1-x})\text{Al}_2\text{O}_4$ was also considered to determine how it compared to the MgAl_2O_4 and ZnAl_2O_4 hosts.

1.2 Motivation

MgAl_2O_4 , corresponding to the mineral spinel, is an optically inert medium and its chemical and thermal stability, transparency, mechanical strength, chemical inertness, wide bandgap, relatively low density and high melting point increases its attractiveness as a host for luminescent ions [8]. It has already been used as a host lattice to produce phosphors emitting a variety of colours, but mainly when doped with transition metal elements such as Ti [9], V [10], Cr [11] and Mn [12]. There has also been some interest in the green emission when doped by Tb^{3+} ions, but more studies are required for MgAl_2O_4 doped with lanthanides. In addition, energy transfer can play an important role to enhance the emission in phosphors [13], but there have been no reports yet of co-doping of

MgAl₂O₄ doped with Tb. We consider adding Ce and Bi as sensitizers to improve the Tb emission in this host.

ZnAl₂O₄ has the same spinel structure as MgAl₂O₄, with almost the same lattice constant but a much smaller bandgap. It is electroconductive and has been considered for thin film electroluminescent and plasma displays, as well as for ultraviolet photo-electronic devices and stress sensors [14-16]. The Mg and Zn ions are similar in size and since the lattice constants of these materials are close to one another and it is interesting to consider the intermediate material (Mg_xZn_{1-x})Al₂O₄ as a possible phosphor host.

Spin coating, which is a simple and a low cost technique, has been used to grow thin films. The surface morphology and thickness can be easily controlled by varying some of the growth parameters such as the spinning speed, the viscosity of the solution and the annealing temperature. PLD is a highly flexible thin-film growth technique which has been successfully applied to a wide range of materials. A lot of research using PLD has been carried out in the department but little has been done using spin coating. While spin coating facilities are available in the department, the NLC labs (in Pretoria) were used for the PLD experiments. The thin films prepared by using the two techniques were compared with each other.

1.3 Research aims

The major aim of the research project was to develop the emission of MgAl₂O₄:Tb phosphor after excitation with both the allowed 4f-5d and forbidden f-f transitions. Parallel to this, a second aim was to prepare (Mg_xZn_{1-x})Al₂O₄:Tb thin films by spin coating and PLD.

The research project consisted of five main experimental points:

- To prepare and characterise MgAl_2O_4 phosphor powders doped with a variety of activators (Ce, Bi, Tb) using the combustion method.
- To study the energy transfer from Ce to Tb in MgAl_2O_4 in order to possibly enhance the emission of Tb^{3+} . Because the results showed that Ce doped MgAl_2O_4 is difficult to prepare and its emission is weak, the energy transfer from Bi to Tb in MgAl_2O_4 was instead investigated as a possible alternative.
- To attempt to enhance the emission of Tb by investigating the mixed spinel phosphor $(\text{Mg}_x\text{Zn}_{1-x})\text{Al}_2\text{O}_4:\text{Tb}$.
- To prepare $(\text{Mg}_x\text{Zn}_{1-x})\text{Al}_2\text{O}_4:\text{Tb}$ thin films by the spin coating technique.
- To prepare $(\text{Mg}_x\text{Zn}_{1-x})\text{Al}_2\text{O}_4:\text{Tb}$ thin films by the PLD technique.

1.4 Thesis layout

This thesis is divided into ten chapters. Chapter 1 includes a general introduction about the work and aims of the study. Chapter 2 provides background information on fundamentals of phosphors and luminescence processes. Chapter 3 gives a brief description of the experimental techniques that were used to synthesize and characterize the phosphors. Luminescent properties of $\text{MgAl}_2\text{O}_4:\text{Ce}$ phosphors prepared by a combustion method are discussed in chapter 4. In chapter 5 the luminescent properties from Bi doped MgAl_2O_4 prepared by the combustion method is reported. Chapter 6 discusses the energy transfer from Bi to Tb in MgAl_2O_4 phosphor. Chapter 7 presents the effects of concentration of Zn in the $(\text{Mg}_x\text{Zn}_{1-x})\text{Al}_2\text{O}_4$ host in terms of luminescent properties. Chapter 8 presents the effect of annealing on the morphology and structure of $\text{Mg}_{0.75}\text{Zn}_{0.25}\text{Al}_2\text{O}_4:\text{Tb}$ thin film grown by sol-gel spin-coating. In chapter 9 photoluminescence properties of the $\text{Mg}_{0.75}\text{Zn}_{0.25}\text{Al}_2\text{O}_4:\text{Tb}$ thin films grown by the PLD technique are presented. Finally, a summary and suggestions for future work are given in chapter 10.

1.5 References

1. D-K. Kim and W. Kang, *J. Bull. Korean Chem. Soc.* **25** (2004) 1859-1862.
2. S. Wu, D. Yang and F. Mazda, *Fundamentals of Liquid Crystal Devices*, John Wiley & Sons (Chichester, 2006).
3. W.M. Yen, S. Shionoya and H. Yamamoto, *Phosphor Handbook*, 2nd Ed., CRC Press (Boca Raton, 2007).
4. S.R. Rotman, *Wide-Gap Luminescent Materials: Theory and Application*, Kluwer Academic (Dordrecht, 1997).
5. J.S. Bae, K.S. Shim, B.K. Moon, B.C. Choi, J.H. Jeong, S. Yi and J.H. Kim, *Thin Solid Films* **479** (2005) 238-244.
6. M.R. Byeon, E.H. Chung, J.P. Kim, T.E. Hong, J.S. Jin, E.D. Jeong, J.S. Bae, Y.D. Kim, S. Park, W.T. Oh, Y.S. Huh, S.J. Chang, S.B. Lee, I.H. Jung and J. Hwang, *Thin Solid Films* **546** (2013) 387-392.
7. J.S. Bae, S.B. Kim, J.H. Jeong, J.C. Park, D.K. Kim, S. Byeon and S. Yi, *Thin Solid Films* **471** (2005) 224-229.
8. O. Shpotyuk, A. Ingram, H. Klym, M. Vakiv, I. Hadzaman and J. Filipecki, *J. Eur. Ceram. Soc.* **25** (2005) 2981-2984.
9. T. Sato, M. Shiraib, K. Tanakab, Y. Kawabea and E. Hanamura, *J. Lumin.* **114** (2005) 155-161.
10. Y. Fujimoto, H. Tanno, K. Izumi, S. Yoshida, S. Miyazaki, M. Shirai, K. Tanaka, Y. Kawabe and E. Hanamura, *J. Lumin.* **128** (2008) 282-286.
11. P. Gluchowski, R. Pazik, D. Hreniak and W. Strek, *Chem. Phys.* **358** (2009) 52-56.
12. J. Lin, Y. Huang, J. Zhang, F. Shi, S. Wei, J. Gao, X. Ding and C. Tang, *Mater. Res. Bull.* **44** (2009) 106-109.
13. H. C. Jung, J. Y. Park, G. S. R. Raju, J. H. Jeong and B. K. Moon, *J. Korean Phys. Soc.* **61** (2011) 439-445.
14. M. García-Hipólito, C.D. Hernández-Pérez, O. Alvarez-Fregoso, E. Martínez, J. Guzmán-Mendoza and C. Falcony, *Opt. Mat.* **22** (2003) 345-351.
15. Z. Lou and J. Hao, *Thin Solid Films* **450** (2004) 334-340.
16. Z. Lou and J. Hao, *Appl. Phys. A* **80** (2005) 151-154.

2 Background information

2.1 Introduction

In this chapter a brief introduction on phosphor materials, the characteristics of phosphors and the phenomenon of luminescence will be given. Then a description of the mechanism of light emission of phosphors based on rare-earth ions (such as Ce, Tb and Eu) as well as their emission and absorption spectra with different types of transitions are reported. The theory of energy transfer that may occur between different activators is discussed briefly. Finally, details of the synthesis of powder and thin films of magnesium aluminate (MgAl_2O_4) spinel, as well as its structure and applications are also given.

2.2 Fundamentals of phosphors

Phosphors are materials that emit light when they are excited with an external energy source. Electrons are first raised to energy levels higher than the ground state and then light may be emitted when these electrons return to the ground state. There are different types of excitation sources such as electrons, x-rays, radiation from radioactive materials, light of a different wavelength, a voltage or electric field [1, 2]. These are discussed further in section 2.4.

The phosphor host or matrix is normally either an insulator or semiconductor, which is usually activated by small amount of dopant (often lanthanide ions, discussed in detail in section 2.5). The phosphor normally is represented by a formula such as $\text{MgAl}_2\text{O}_4:\text{Tb}^{3+}$

(0.5 mol%), where MgAl_2O_4 represents the host, terbium (Tb^{3+}) represents the activator or dopant and the percentage value (0.5 mol%) is the amount of terbium (activator) that was blended per mole of the matrix in the raw material mixture. If the phosphor is co-doped with two rare-earth ions a comma is used to separate them, for example $\text{MgAl}_2\text{O}_4:\text{Ce},\text{Tb}$.

There are many types of host materials such as alkali-earth sulphides, alkali-earth aluminates, rare-earth oxides, nitrides and oxysulfides, lanthanide halides, gallates and silicates etc. Generally, host materials should exhibit good optical, mechanical and thermal properties [3]. The phosphor's properties depend on the grain size of the materials which range from micrometres (bulk) to nanometres (nanophosphors). They can also be grown into thin films for a particular application in light emitting devices. There are many parameters that can affect the emission intensity of the phosphor, i.e. the shape of the phosphor particles, homogenous distribution of activators inside the matrix, the synthesis conditions and the host structure [1, 4]. The effect of the host structure comes from the site symmetry at the cation site and the strength of the crystal field [5].

2.3 Applications of phosphors

Phosphors have been extensively investigated during the last decade due to their potential in various applications such as displays, medical imaging and lighting, cathode-ray-tube (CRT) colour television, x-ray fluorescent screens and fluorescent lamps. Figure 2.1 shows some of these applications. Major advances of CRTs and fluorescent lamps resulted from the improvement of the phosphors. The fluorescent lamp is basically operated with low pressure mercury discharge lamp connected to a layer of phosphor particles inside the surface of the glass tube. Phosphors are used to provide the backlighting for liquid crystal displays (LCDs), which are used in the place of CRTs in products such as mobile phones

and for large flat panel screens. Their main advantages are high resolution, low scattering, very high contrast ratios with wider viewing angles, high quality colours and low power consumption [6].

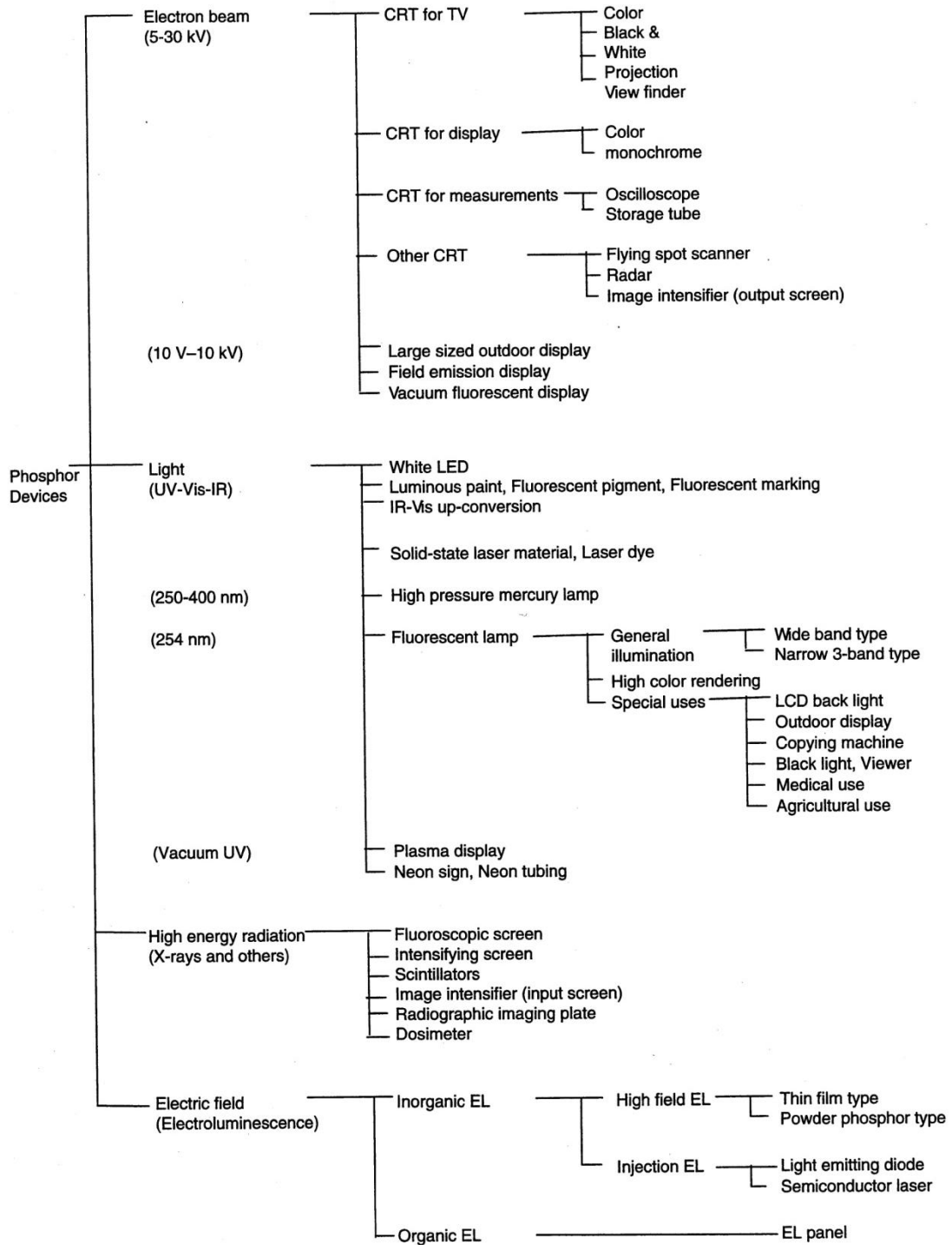


Figure 2.1: Phosphor devices [7].

The phosphors will continue to be used to produce "white" light emitting diode (LED) light sources [8]. LEDs are used in applications such as video displays, computer and advertising panels, general lighting and traffic signals. The advantages of LEDs are longer lifetime, compactness, efficient light output and reduced power consumption (it uses milliwatts of power compared to watts of power for incandescent and fluorescent lamps [9]).

Finally, phosphors have some other simple applications, such as luminous paint with long persistent phosphorescence which can be used for long afterglow phosphor coated signs and light switch locators, etc [7].

2.4 Types of luminescence

The name of the luminescence depends on the type of excitation.

2.4.1 Photoluminescence

When the phosphor material absorbs electromagnetic radiation (i.e. a photon) an electron may be excited to a higher energy quantum state. If the excited electron returns to a lower energy quantum state by emission of a photon, the process is called photoluminescence (PL).

In PL spectra, peaks are observed at a lower energy than the absorption energy. The difference in energy between the PL emission and the absorption is called the Stokes shift [10]. A Jablonski diagram (figure 2.2) shows the processes of absorption, fluorescence and phosphorescence [11].

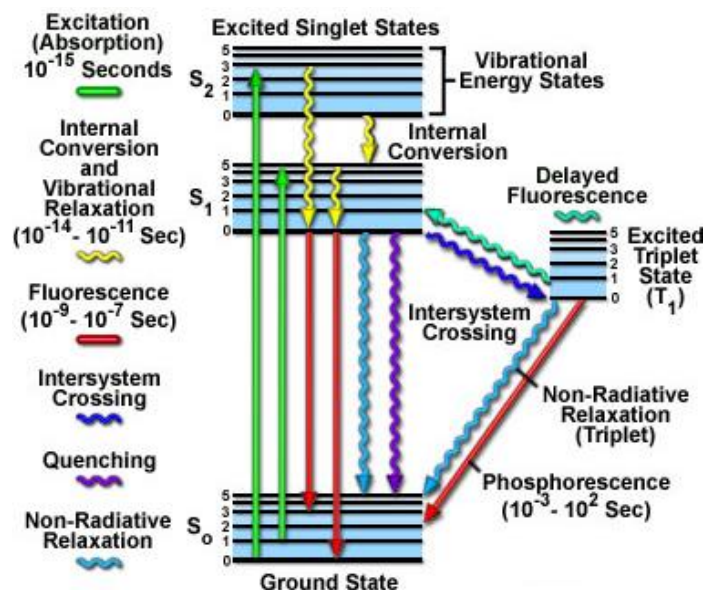


Figure 2.2: Jablonski energy diagram for absorption, fluorescence and phosphorescence [11].

PL is divided into two classes: fluorescence and phosphorescence, depending upon the electronic configuration of the excited state and the emission pathway. Fluorescence is the property of some materials to absorb light at a particular wavelength and emit light of longer wavelength almost immediately, in less than 10^{-7} s and return of the molecule to the ground state. The process of phosphorescence occurs in a manner similar to fluorescence, but the phosphorescence is delayed from 10^{-4} to 10 seconds or more, so these materials appear to glow in the dark. Most phosphorescence processes in phosphorescent materials are emitted relatively fast with lifetimes on the order of milliseconds, nevertheless, some materials have lifetimes up to minutes or even hours. The difference between fluorescence and phosphorescence according to electron spin orientation is that in fluorescence process, an electron does not change its spin orientation (excited singlet state). While in a phosphorescence process, under the appropriate conditions, a spin-flip can occur. When the electron undergoes a spin-flip, a triplet state is created. The transition from triplet state to the ground state is forbidden, which means that the reverse transition from triplet to ground state with the emission of phosphorescence takes more time [12].

2.4.2 Electroluminescence

When a material emits light produced by excitation with an electric field or resulting from a current flow through semiconductors, the process is electroluminescence (EL). The photon emitted results from radiative recombination of electrons and holes created in the phosphor by applying voltage between the two electrodes. One of the electrodes of an electroluminescent device is transparent to the wavelength of the light emitted by the device. The EL of inorganic materials is classified into the two groups: injection EL and high electric field EL. The high field EL is further divided into two types: powder phosphor EL and thin film EL [13].

2.4.3 Cathodoluminescence

Cathodoluminescence (CL) is the process of the emission of light from a material when it is bombarded with an electron beam generated by an electron gun. The exciting primary electrons can be focused into a beam and scanned across the surface (as in a scanning electron microscope), resulting in high spatial resolution CL.

2.4.4 Thermoluminescence

A material may contain defects that can trap electrons and holes. If the temperature is increased, the electrons and holes may obtain enough energy to become free, and then they can recombine. If the recombination is radiative, a photon is emitted and the process is called thermoluminescence. A curve of luminescence intensity versus temperature is called a glow curve [13].

2.4.5 Chemiluminescence

This is emission of light as a result of a chemical reaction, when a molecule has a lower potential energy than its constituent atoms, causing an exothermic reaction that produces light [8].

2.5 Lanthanides

The lanthanides are the elements in the periodic table from La ($Z = 57$) to Lu ($Z = 71$) as given in table 2.1.

Table 2.1: Electron configurations of the lanthanides.

Atomic number	Element	Electron configuration		Valence
		Neutral atom	Trivalent ion	
57	Lanthanum	$4f^0 6s^2 5d$	$4f^0$	3
58	Cerium	$4f^1 6s^2 5d$	$4f^1$	3,4
59	Praseodymium	$4f^3 6s^2$	$4f^2$	3
60	Neodymium	$4f^4 6s^2$	$4f^3$	3
61	Promethium	$4f^5 6s^2$	$4f^4$	3
62	Samarium	$4f^6 6s^2$	$4f^5$	2,3
63	Europium	$4f^7 6s^2$	$4f^6$	2,3
64	Gadolinium	$4f^7 6s^2 5d$	$4f^7$	3
65	Terbium	$4f^9 6s^2$	$4f^8$	3,4
66	Dysprosium	$4f^{10} 6s^2$	$4f^9$	3,4
67	Holmium	$4f^{11} 6s^2$	$4f^{10}$	3
68	Erbium	$4f^{12} 6s^2$	$4f^{11}$	3
69	Thulium	$4f^{13} 6s^2$	$4f^{12}$	3
70	Ytterbium	$4f^{14} 6s^2$	$4f^{13}$	2,3
71	Lutetium	$4f^{14} 6s^2 5d$	$4f^{14}$	3

The ‘rare-earths’ is the traditional name for the lanthanides together with Sc ($Z = 21$) and Y ($Z = 39$). Trivalent lanthanide ions are well known for their characteristic optical properties. Trivalent lanthanides ions have an outer electronic configuration $5s^2 5p^6 4f^n$, where n varies from 1 (Ce^{3+}) to 13 (Yb^{3+}) and indicates the number of electrons in the incomplete $4f$ shell [14, 15]. The $4f^n$ electrons are primarily responsible for the optical

properties of the rare earths. Figure 2.3 presents a substantial part of the energy levels of the trivalent ions of lanthanides that originate from the $4f^n$ configuration as a function of the atomic number.

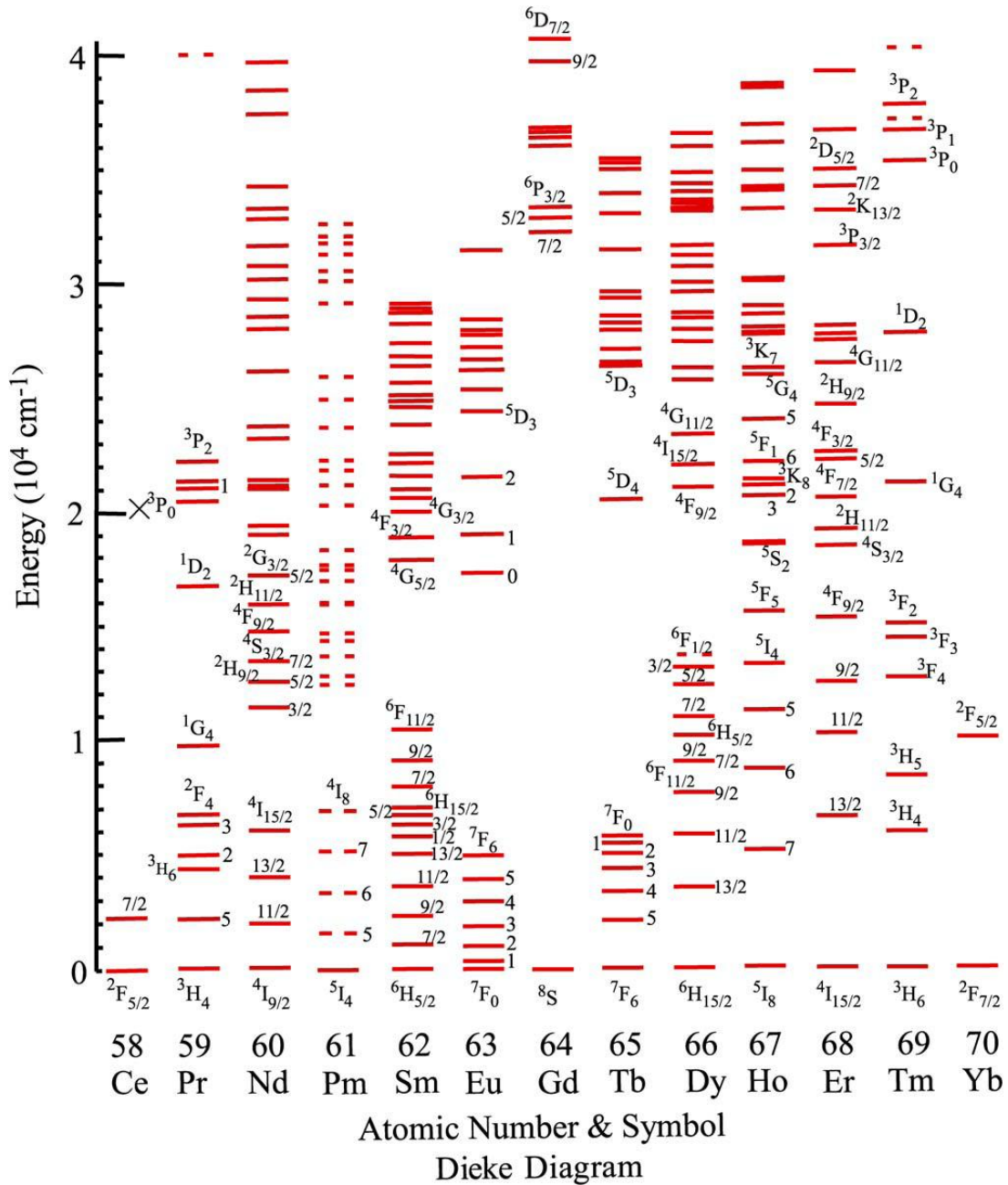


Figure 2.3: Dieke diagram showing the energy levels of the trivalent lanthanides [16].

Most of the rare-earth ions show sharp emission bands, due to optical transitions within the f-manifold, e.g. Tb^{3+} ($4f^8$ configuration) and Eu^{3+} ($4f^6$ configuration). The width and position of the emission bands are almost independent of the chemical environment. For example the transitions of Tb^{3+} and Eu^{3+} are spin and parity forbidden and therefore rather slow (in the ms range). However, for a number of rare-earth ions, also broad emission bands are known, due to 5d-4f transition, e.g. Eu^{2+} ($4f^7$ configuration). These transitions are allowed and consequently very fast (in the μs range or even faster) [17].

Ions such as La^{3+} and Lu^{3+} have a completely empty and filled 4f shell, respectively, and therefore have no optical transitions. Y^{3+} is always treated as a rare-earth ion, because of similar reactivity and coordination behaviour. This ion also has no optical transitions, but luminescent lanthanide ions are often incorporated in host materials with Y^{3+} ions.

2.6 Some luminescent centres

2.6.1 Trivalent terbium ion (Tb^{3+})

The trivalent terbium ion (Tb^{3+}) has been extensively studied due to its bright green emission under ultraviolet (UV) excitation. The Tb 4f energy levels can be seen in figure 2.3. The green emission is attributed to transitions of the type $^5\text{D}_4 \rightarrow ^7\text{F}_j$, consisting of $^5\text{D}_4 \rightarrow ^7\text{F}_6$ (490 nm), $^5\text{D}_4 \rightarrow ^7\text{F}_5$ (544 nm), $^5\text{D}_4 \rightarrow ^7\text{F}_4$ (587 nm) and $^5\text{D}_4 \rightarrow ^7\text{F}_3$ (623 nm). Among these transitions the most intense is the $^5\text{D}_4 \rightarrow ^7\text{F}_5$ which is situated around 544 nm.

Also, there can be considerable blue emission from the $^5\text{D}_3$ level. The emission transitions from $^5\text{D}_3 \rightarrow ^7\text{F}_j$ are dominated by $^5\text{D}_3 \rightarrow ^7\text{F}_6$ (376 nm), $^5\text{D}_3 \rightarrow ^7\text{F}_5$ (418 nm), $^5\text{D}_3 \rightarrow ^7\text{F}_4$ (440 nm), $^5\text{D}_3 \rightarrow ^7\text{F}_3$ (360 nm) and $^5\text{D}_3 \rightarrow ^7\text{F}_2$ (478 nm) bands. The intensity ratio of the green

emission from 5D_4 to the blue emission from 5D_3 depends mainly on the Tb^{3+} concentration. For high concentration the electrons from 5D_3 level are nonradiatively dissipated through cross relaxation to the lower energy level of 5D_4 decreasing the blue emission.

The 4f-4f transitions are forbidden by the parity selection rule [18, 13], which states that electronic transitions between energy levels with the same parity cannot occur. In reality, this transition can occur because the parity rule is relaxed due to perturbation such as electron vibration coupling and uneven crystal field term from host lattice. However, the lifetime is long and emissions occur as sharp lines in the spectra.

The 4f electrons are well shielded from the surrounding external fields by the 5s and 5p electrons. The influence of the crystal field on the optical transitions within the $4f^n$ configuration is very small. Therefore the emission is independent on the host.

The excitation of Tb is divided into two regions, the first from f-d excitation and the other from f-f excitation. The range for the f-d excitation is below 300 nm while the f-f excitation band is between 300 and 500 nm. The f-f excitation is weak because it is not allowed. The 4f-5d transitions are dipole allowed unlike the f-f transitions, and the 5d states are diffuse and overlap with ligand orbitals. For this reason the 4f-5d excitation strongly depends on the crystal field of the host and therefore varies over the spectral range of the deep UV region.

The typical excitation and emission of Tb^{3+} doped in SiO_2 is shown in figure 2.4. In this figure the emission is green because of the relatively high concentration of Tb (1.0%) [19].

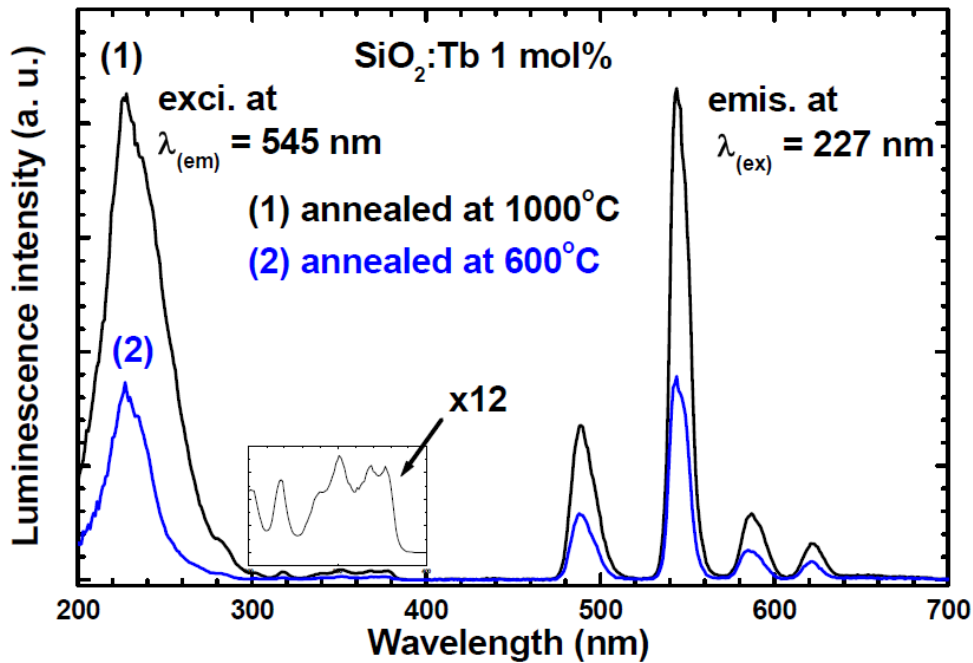


Figure 2.4: Emission and excitation of Tb^{3+} doped SiO_2 [20].

2.6.2 Trivalent europium ion (Eu^{3+})

Eu^{3+} doped compounds emitting bright red light have been extensively used as phosphors in many fields, such as display applications, and the material shows typical f-f transitions of Eu^{3+} ions [21]. The transitions are $^5\text{D}_0 \rightarrow ^7\text{F}_J$, the most common of which have $J=0, 1, 2, 3$ and 4. The $^5\text{D}_0 \rightarrow ^7\text{F}_2$ peak (615 nm) is highly sensitive to the structure and environment effects. The intensity of electric dipole transitions strongly depends on the site symmetry whereas the magnetic dipole transitions do not depend on the site symmetry as they are parity allowed. If Eu^{3+} occupies an inversion symmetry site in the crystal site, the orange red emission, magnetic dipole transition $^5\text{D}_0 \rightarrow ^7\text{F}_1$ which is about 590 nm is dominant. If the Eu^{3+} does not occupy an inversion symmetry site, the red emission, electric dipole transition $^5\text{D}_0 \rightarrow ^7\text{F}_2$ (around 615 nm) is the dominant peak.

In addition to 5D_0 , the emission from 5D_1 and 5D_2 can also be observed in the green and blue region for some hosts [22]. The excitation and emission of Eu^{3+} doped in Y_2O_3 are illustrated in figure 2.5.

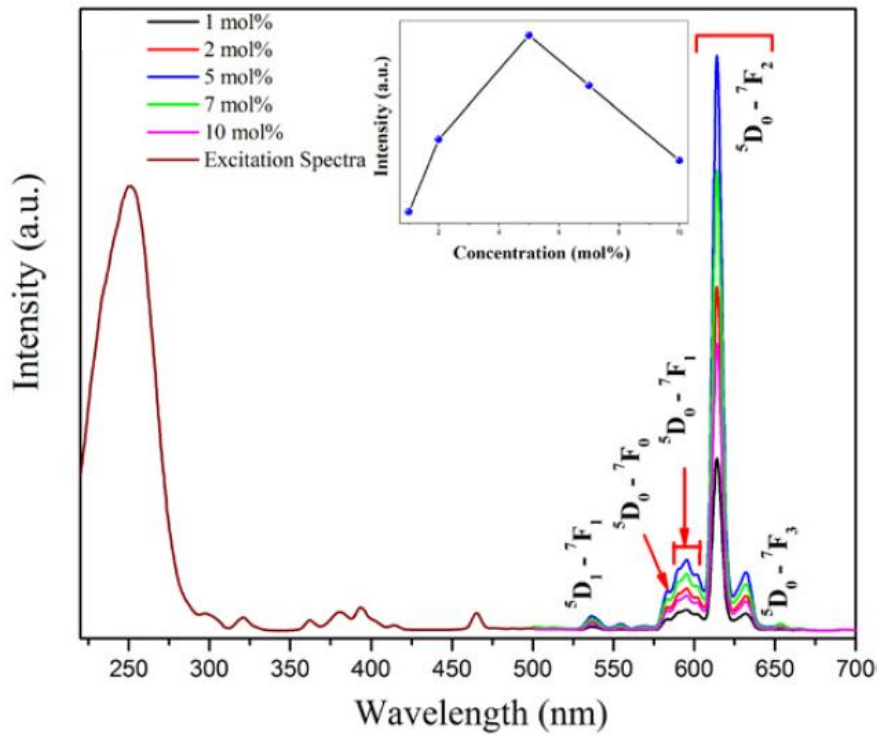


Figure 2.5: The excitation and emission of Eu^{3+} doped Y_2O_3 [23].

2.6.3 Trivalent cerium ion (Ce^{3+})

There has been a wide investigation of the optical properties of Ce doped compounds. There is great interest in Ce^{3+} doped compounds or crystals for applications as phosphors, white LEDs, scintillators and tuneable lasers [7, 24]. Most Ce^{3+} activated phosphors show broad band emission range in the UV to visible due to the $4f^05d^1-4f^1$ transition of Ce^{3+} [25], which are characterized by broad-band fluorescence with lifetime in the order of few tens of ns, thus providing high light output and fast response time [5].

Usually, the trivalent cerium ion Ce^{3+} with the electronic configuration $4f^1$ yields two levels ${}^2F_{7/2}$ and ${}^2F_{5/2}$ as the ground states separated by $\sim 2000 \text{ cm}^{-1}$ due to spin-orbit coupling [26]. The lower manifold ${}^2F_{5/2}$ is populated and the manifold ${}^2F_{7/2}$ is almost empty at room temperature. The excited $5d^1$ configuration is split by the crystal field in 2 to 5 components. The total splitting amounts to some 15000 cm^{-1} . As the positions of the energy levels of $5d$ excited states of Ce^{3+} are not only affected by the crystal field but also by the degree of covalent bonding, it causes variations in the absorption and emission from UV to long wavelength by varying the host lattice [5].

In some hosts there is problem that the Ce^{3+} is converted to Ce^{4+} which is non-luminescent because the $4f$ levels are unoccupied. To convert non-luminescent Ce^{4+} ions to the luminescent Ce^{3+} charge state requires annealing in a reducing atmosphere e.g. H_2 [27, 28].

The excitation and emission of Ce^{3+} doped SiO_2 are illustrated in figure 2.6.

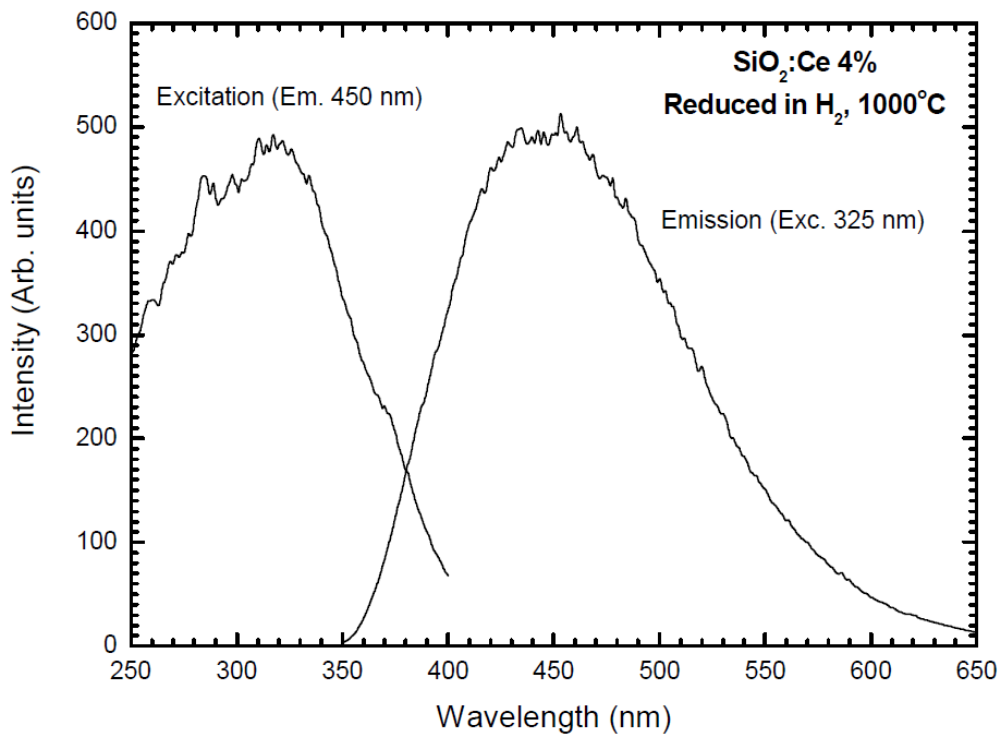


Figure 2.6: Emission and excitation of Ce^{3+} doped SiO_2 [20].

2.6.4 Trivalent bismuth ion (Bi^{3+})

Metallic impurities with an outer ns^2 configuration ground state such as Ti^+ , Pb^{2+} , Bi^{3+} and Sb^{3+} ions may also be excellent luminescence activators [7]. Bi atoms are the heaviest member of the group 15 (pnictogen) with an electronic configuration $[\text{Xe}]4f^{14}5d^{10}6s^2p^3$ and Bi^{3+} ions, with outermost $6s^2$ electrons, have been widely used as activators for various host materials including oxides, phosphates, aluminates and borates [29]. The $6s^2$ ground state has a single energy level $^1\text{S}_0$ while the $6s^16p^1$ excited configuration has energy levels $^3\text{P}_0$, $^3\text{P}_1$, $^3\text{P}_2$ and $^1\text{P}_1$ in order of increasing energy. Electron transitions between the $^1\text{S}_0$ ground state and the $^3\text{P}_j$ levels are spin forbidden, but optical absorption can occur to the high energy $^1\text{P}_1$ level [5]. However, spin-orbit coupling between the $^1\text{P}_1$ and $^3\text{P}_1$ levels makes the lower energy transitions $^1\text{S}_0 \leftrightarrow ^3\text{P}_1$ possible and the luminescence from Bi^{3+} activated phosphors is usually attributed to this transition. In some materials the $^1\text{P}_1 \rightarrow ^1\text{S}_0$ emission is also observed [30]. The outer electron orbitals of Bi^{3+} are not shielded (as in the case of the 4f energy levels of trivalent lanthanide ions) so the broad luminescence band shows a strong dependence on the composition and crystal structure of the host lattice and the emission wavelength is tuneable from the UV, through blue to green [31]. The excitation and emission of Bi^{3+} doped in different hosts are illustrated in figure 2.7.

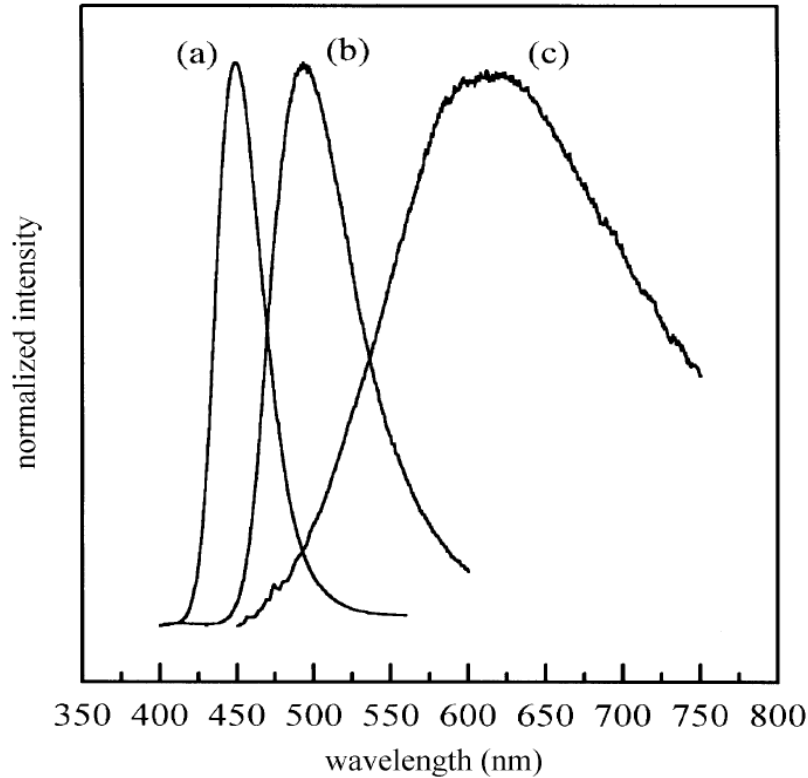


Figure 2.7: Emission and excitation of Bi^{3+} doped phosphors. (a) CaS:Bi , (b) SrS:Bi and (c) BaS:Bi [32].

2.7 Energy transfer

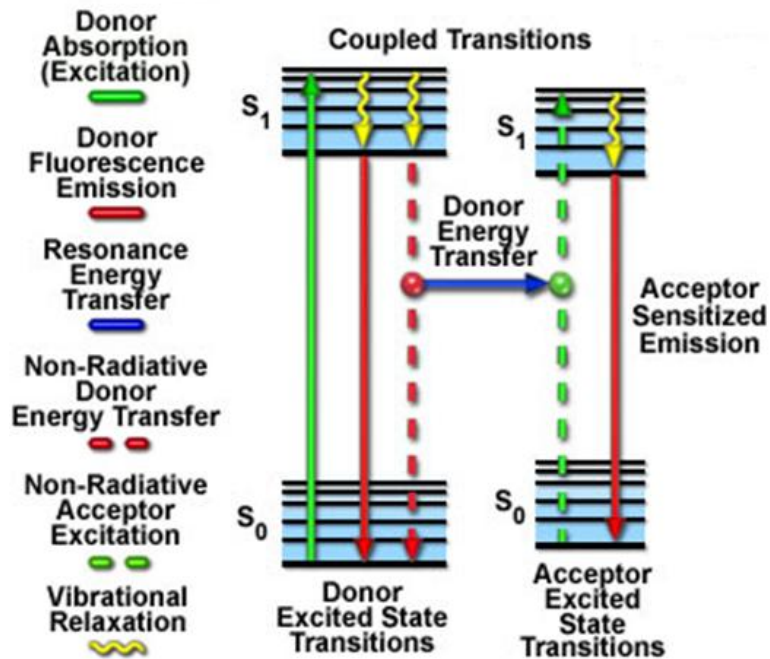


Figure 2.8: Jablonski diagram illustrating coupled transitions between donor emission and acceptor absorbance in fluorescence resonance energy transfer [33].

Energy transfer has become widely used in all applications of fluorescence, including medical diagnostics, application in LEDs and optical imaging [34]. Energy transfer occurs between a donor molecule and another centre called an acceptor. The energy donor, which is called the sensitizer, is denoted by (D) whereas the energy acceptor, which is called the activator, is denoted by (A). Energy transfer between a donor ion and an acceptor ion can be written similar to a chemical reaction:



where D and A represent the ground states of donor and acceptor respectively, while D* and A* represents their excited states.

The donor ion can transfer its energy to other acceptor ions at different sites or different lattice environments (see figure 2.8). In order for energy transfer to occur it is necessary that one of the energy levels of A lies at the same levels as D* [21]. The excited donor molecules can typically emit at UV and visible wavelengths that overlap with the absorption spectrum of the acceptor (see figure 2.9). The rate of energy transfer depends upon the extent of spectral overlap of the emission spectrum of the donor with the absorption spectrum of the acceptor [8, 35]. However, the energy transfer occurs without the emission of photons by the donor and is called nonradiative energy transfer.

The emission of the activator ions can be sensitized directly or indirectly. Direct sensitization is when the excitation energy is absorbed by one of the activator ions and transfer to the neighbouring ion, i.e. Ce³⁺ - Ce³⁺ energy transfer (energy transfer between two identical centres). Indirect sensitization occurs when the excitation energy is absorbed by the host lattice or a co-activator and transferred to the activator ion, i.e. energy transfer between two non-identical centres such as energy transfer from Ce³⁺ to Tb³⁺ [36].

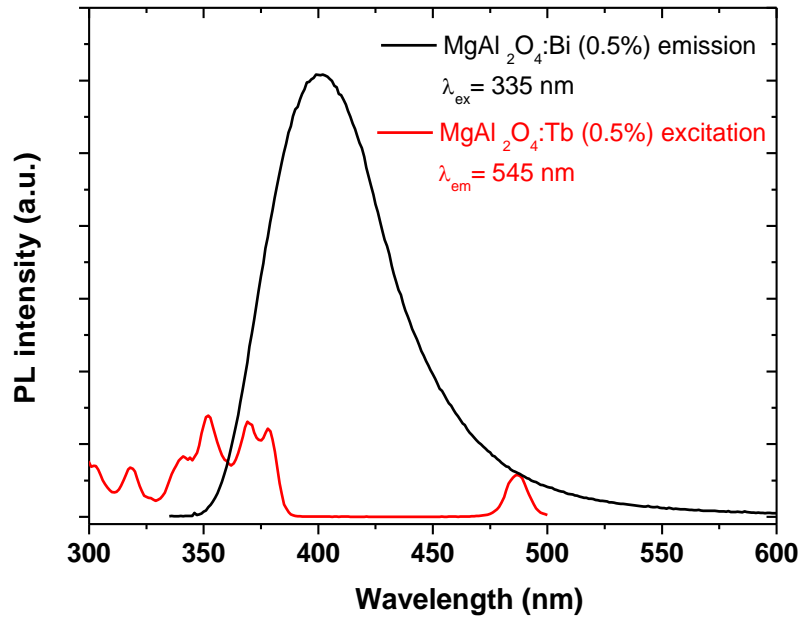


Figure 2.9: The spectral overlap between the donor (D) emission spectrum of Bi and the acceptor (A) excitation spectrum of Tb in MgAl₂O₄.

The energy transfer process can be explained by two phenomena, namely Dexter exchange and Förster resonance. In both phenomena, the energy transfer occurs by the nonradiative energy transfer mechanism. In the Dexter exchange mechanism, the donor and acceptor orbitals must overlap with each other. In the Förster resonance process, on the other hand, energy from the donor is transferred to the acceptor through a long range coulombic interaction, typically a dipole-dipole interaction or more generally multipole interaction. In this phenomenon, there is no need of short contact between the donor and acceptor.

2.8 Preparation methods of phosphors

Recently, there have been improvements in ways of synthesising phosphor materials, which can control the particle size and shape. The commonly used synthesis methods are: combustion synthesis [37, 38], sol-gel processing [39], the microwave process [40], spray

pyrolysis [41], precipitation [42], solid-state reactions [40, 43] and hydrothermal synthesis [44].

The solid-state reaction method requires high reaction temperature for a long time period. Therefore it is difficult to prepare phosphor particles with controlled shape and fine size by this method. Another major problem with solid-state reaction method is very high cost, particularly to obtain nano-sized particles due to multiple steps and long processing time [45].

Combustion synthesis is a self-propagating high temperature synthetic method and an effective, low cost method for the production of homogeneous, very fine agglomerated multicomponent oxide ceramic powders without intermediate decomposition and/or calcination steps.

Sol-gel processing offers many advantages which include low processing temperature, high purity, molecular level homogeneity and more flexibility in the components of the glass.

Due to their advantages, the sol-gel processing and combustion synthesis were used in this study, and are discussed in further detail.

2.8.1 Combustion Synthesis

Combustion synthesis has been investigated as a method to produce homogeneous, crystalline nanoparticles without extensive high temperature (>1500 °C) annealing and mechanical separation such as grinding or milling steps [46]. The method produces rapid,

exothermic, self-sustaining reactions resulting from the appropriate combination of salts such as nitrates or acetates (oxidizers) and a suitable organic fuel like urea, carbohydrazide, glycine, etc. (reductant). A composition of metal nitrates and fuel in which the fuel reacts completely with all of the metal nitrates in the mixture so that no residues remain in the product material is known as a stoichiometric ratio. Equation 2 is an example of a stoichiometric combustion reaction of magnesium nitrate $\text{Mg}(\text{NO}_3)_2 \cdot 6\text{H}_2\text{O}$, aluminium nitrate $\text{Al}(\text{NO}_3)_3 \cdot 9\text{H}_2\text{O}$ and urea ($\text{CH}_4\text{N}_2\text{O}$) to form MgAl_2O_4 :



When the complete reaction occurs, only the gaseous products N_2 , CO_2 and H_2O are released and no residuals are left in the synthesized MgAl_2O_4 material.

Figure 2.10 is a schematic diagram for the preparation of nanocrystalline MgAl_2O_4 powders by the combustion process. Combustion reactions are initiated in a muffle furnace or on a hot plate at temperatures of preheated at 400-550 °C. These temperatures are clearly much lower than the temperature at which crystallization of the desired phase takes place during conventional processing.

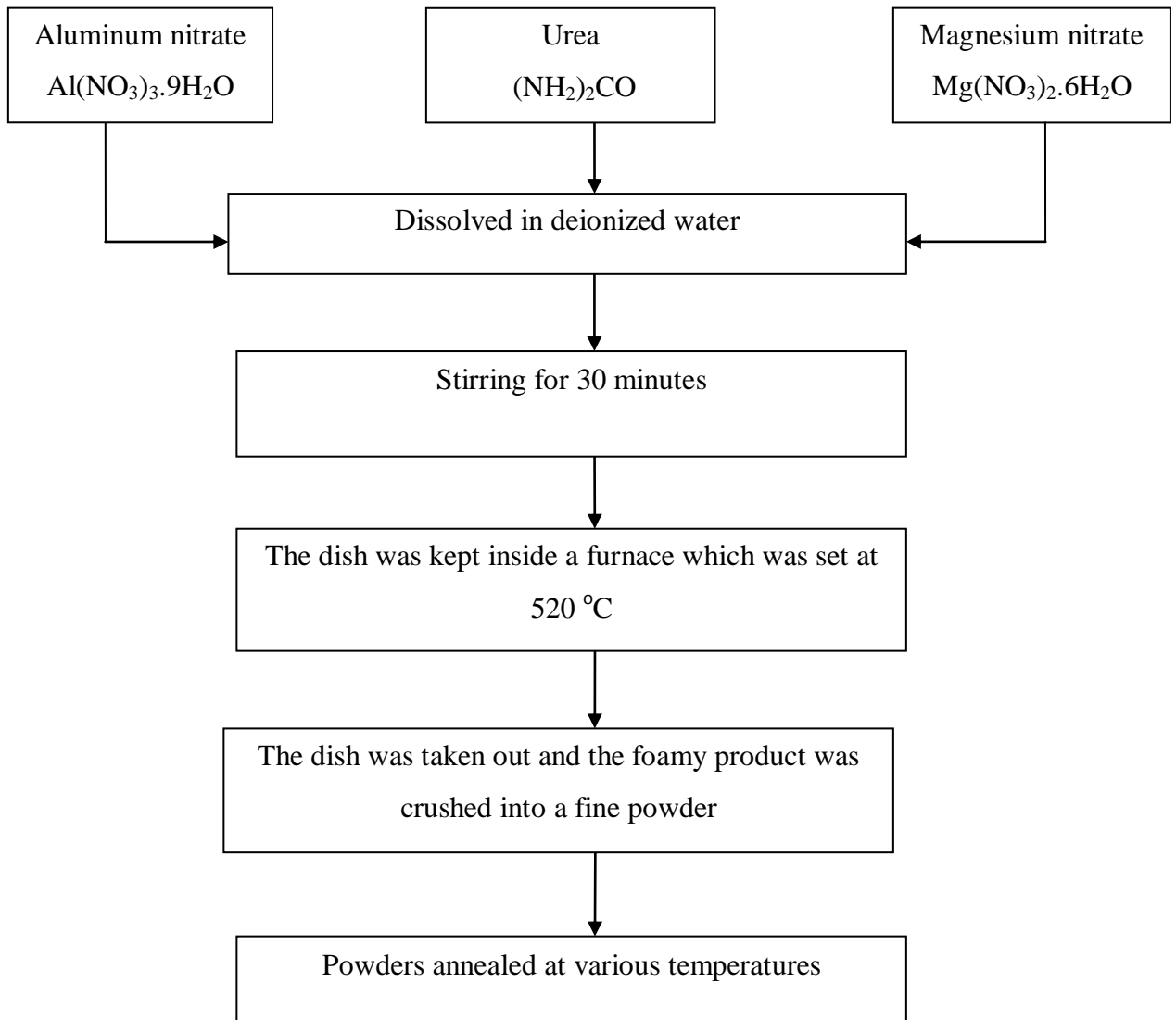


Figure 2.10: Schematic diagram for preparation of nanocrystalline MgAl_2O_4 powder by combustion process.

In a typical reaction the precursor mixture of deionized water, metal nitrates and fuel boils, dehydrates, decomposes and flames after about 5 minutes. The resultant product appears as a porous foam (see figure 2.11). The chemical energy released during the exothermic reaction between the metal nitrates and fuel can rapidly heat the system to a high temperature ($>1500\text{ }^\circ\text{C}$) and sustain that high temperature in the absence of an external heat source. Thus, the target phase(s) can be achieved with significantly reduced external energy input [47].

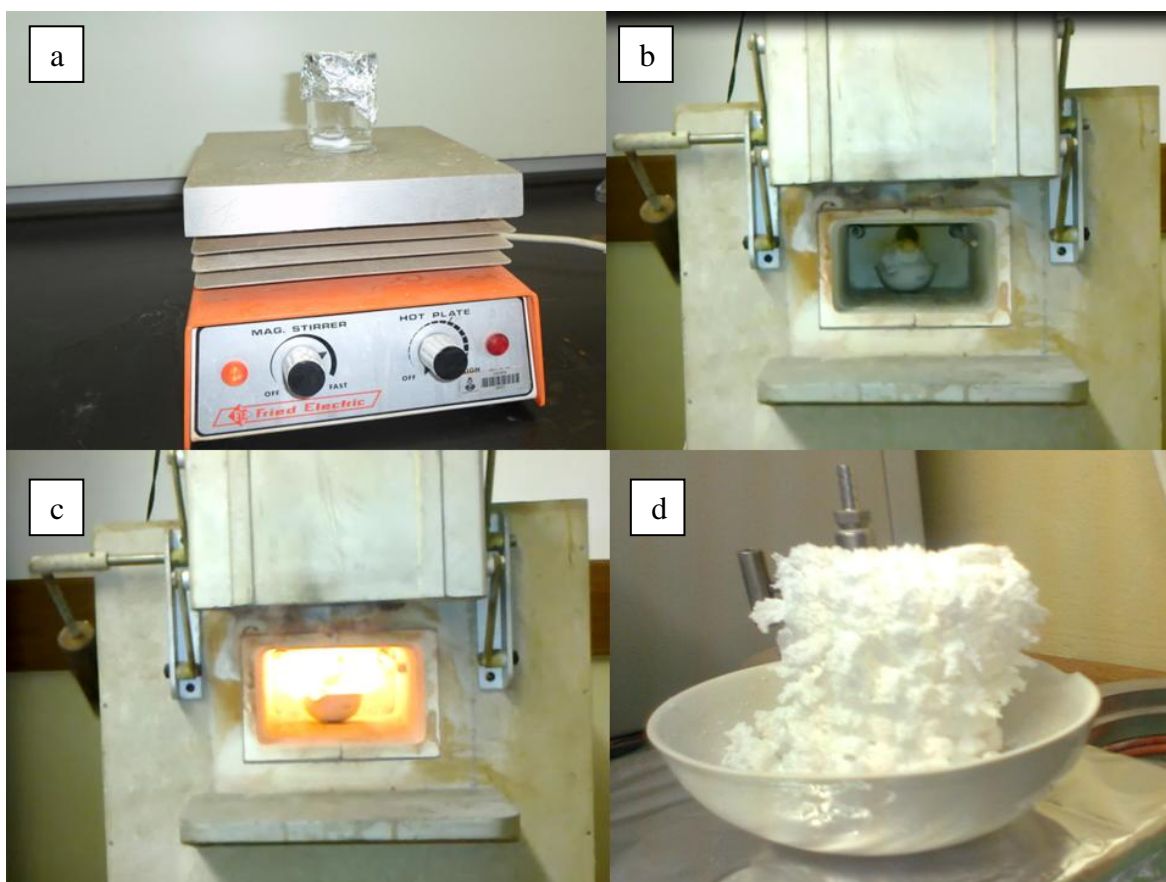


Figure 2.11: The equipment used for the combustion method: (a) stirring, (b) preheated to 520 °C, (c) flaming and (d) porous foam.

There are some advantages to this method, i.e. the generation of high reaction temperature which can volatilize low boiling point impurities and therefore results in higher purity products, the simple exothermic nature of the self-propagating high temperature reaction and its short time result in low operating and processing costs and the large amount of gas evolved during combustion results in a porous product in which the agglomerates formed are so weak that they can be easily crushed and ground into a fine powder [8].

2.8.2 Sol-gel process

The process of controlling a nanomaterial's particle size and shape as well as the crystallinity is the fundamental object of modern materials chemistry. Sol-gel synthesis has been developed in recent years as a potential alternative to the conventional hydrolytic route to inorganic oxides. The sol-gel process is an attractive alternative to other methods for synthesis of ceramics, fibres, membranes and glasses [48]. There are some advantages to this method, i.e. low temperature synthesis, simple equipment to be used, control of the particle size and shape, low cost, homogeneous compositions, high purity and low heat-treatment temperatures [49]. The sol-gel process is very useful for thin film deposition because of the capability to coat materials of various shapes and different surfaces, to control the composition easily for obtaining solutions with homogeneity and controlled concentration without using expensive equipment [50]. The sol-gel process consists of two steps. First one forms a sol. Then conversion of the sol to a gel occurs by hydrolysis and condensation reactions. The steps of sol-gel method are shown in figure 2.12.

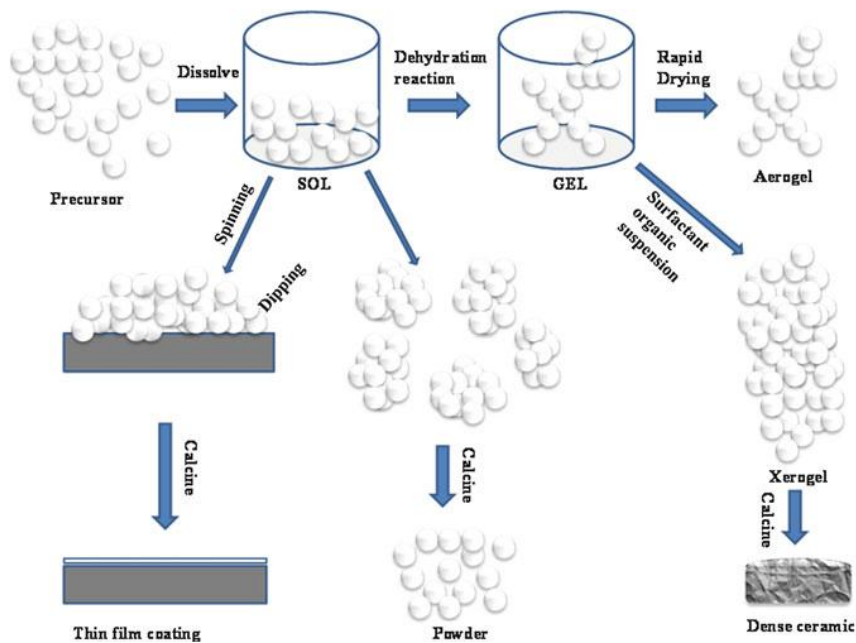


Figure 2.12: Steps involve in sol-gel method [8].

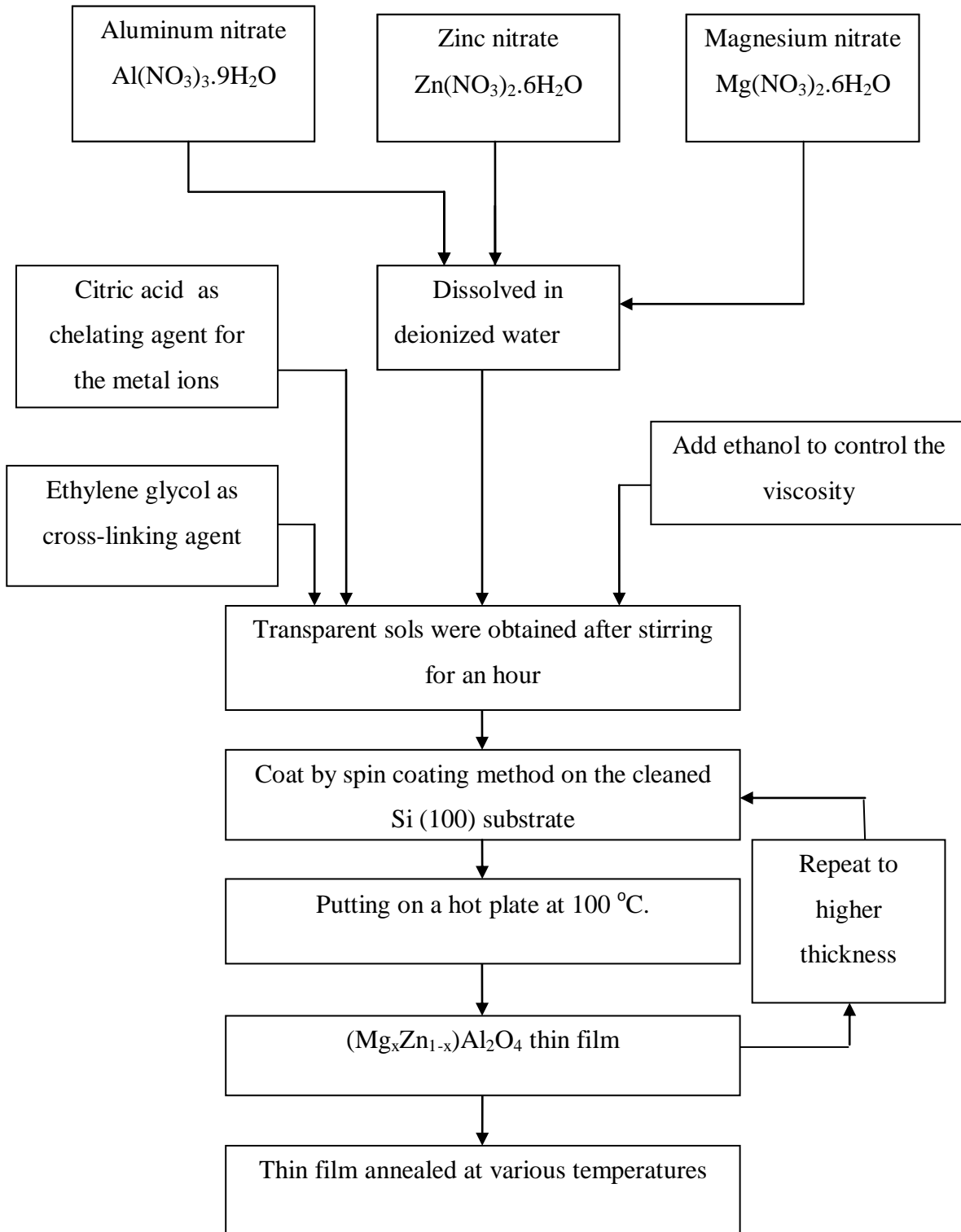


Figure 2.13: Schematic diagrams to synthesize $(\text{Mg}_x\text{Zn}_{1-x})\text{Al}_2\text{O}_4$ phosphor by using the sol-gel method and to prepare thin films by spin-coating.

The starting materials employed in sol–gel process are often in the form of metal alkoxides, which readily undergo hydrolysis and condensation to form hydroxides and oxide. However, metal salts such as chlorides, acetates, nitrates are cheaper and easier to handle than metal alkoxides, and hence are good alternatives if they are readily converted to oxides by thermal decomposition. The metal salts have high solubility in water or organic solvents.

Pechini's method is a simple method used to prepare metal oxide powders where polymeric precursors are made from metal salts, ethylene glycol and citric acid. The precursors are dissolved in the deionized water or ethanol at low temperature from 70 – 130 °C. This method allows the metal cations to be mixed at a molecular level and the stoichiometric compositions to be achieved by chelating the metal ions in solution by citric acid, on which many studies have been reported [51, 52]. The schematic diagram to synthesize $(\text{Mg}_x\text{Zn}_{1-x})\text{Al}_2\text{O}_4$ phosphor by using the sol-gel method and prepare thin films is shown in figure 2.13.

2.9 Magnesium aluminate and zinc aluminate spinel

Phosphors based on oxide matrices are attractive host materials for the development of advanced phosphors due to their ease of synthesis and stability. Aluminate phosphors, having excellent chemical and thermal stability and high emission efficiency, are important luminescent materials for fluorescent lamps and plasma display panels [13]. Aluminate phosphors are usually activated by rare-earth ions, such as Eu^{2+} , Ce^{3+} , and Tb^{3+} , and emit blue to green colours upon UV or near ultraviolet light excitation.

MgAl_2O_4 and ZnAl_2O_4 have the spinel structure as shown in figure 2.14, belonging to the cubic space group $Fd\bar{3}m$ [53, 54]. Although the general formula of spinel is AB_2O_4 , the unit cell formula of spinel is expressed as $\text{A}_8\text{B}_{16}\text{O}_{32}$. The 32 oxygen ions form a face-centred cubic lattice, providing 64 tetrahedral sites and 32 octahedral sites. In normal spinel the divalent A cations are located in one-eighth of the tetrahedral sites and the trivalent B cations occupy one-half of the octahedral sites [55].

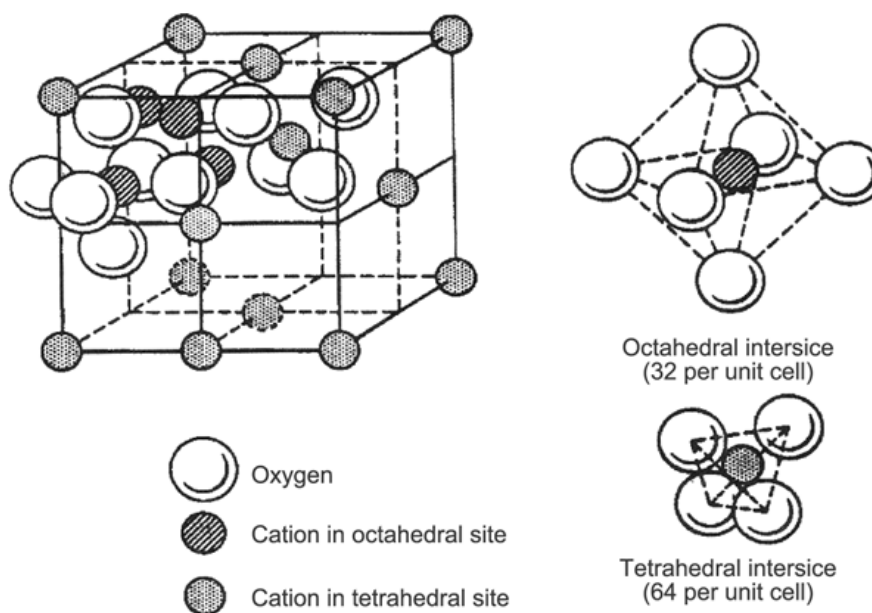


Figure 2.14: Structure of spinel lattice [56].

For MgAl_2O_4 spinel the Mg^{2+} cations fill tetrahedral sites and the Al^{3+} cations reside in octahedral positions [57]. The lattice parameter of natural MgAl_2O_4 is given by $a = 0.808$ nm [58]. MgAl_2O_4 has received a great deal of attention as a technologically important material because of its mechanical strength, chemical inertness, wide bandgap (6.8 eV), relatively low density, high melting point (2105 °C), high thermal shock resistance, low thermal expansion coefficient, resistance to neutron irradiation and low dielectric loss [39,

59]. It has been employed in several applications, such as humidity sensors [60], tuneable solid-state lasers [61] and interesting thermal and optical properties.

MgAl₂O₄ can be easily doped by transition metal ions such as Ti, Mn, Cr or V. In the particular case of Ti doped MgAl₂O₄ spinel, a strong visible blue emission around 455-490 nm under excitation at 280 nm was observed [62]. The luminescence properties of Cr³⁺ doped natural MgAl₂O₄ mineral were investigated by Głuchowski *et al.* [63]. MgAl₂O₄:Mn has used as green phosphor for television tubes [64] while V doped MgAl₂O₄ crystals act as a white light source [65]. In addition, MgAl₂O₄ has also been considered as a phosphor host activated by various rare-earth ions, especially in the trivalent charge state. Several previous studies have described the luminescence of Tb doped MgAl₂O₄ [51, 66]. High luminous efficiency of bright red colour was displayed with Eu doping [67, 68]. Long afterglow emission from defects in MgAl₂O₄ was reported to be enhanced by doping with Ce [69].

ZnAl₂O₄ is widely used as a catalyst and has also been patented for UV reflective optical coatings. It is electroconductive and has been considered for thin film electroluminescent and plasma displays, as well as for UV photo-electronic devices and stress sensors [70, 71]. ZnAl₂O₄ is a wide band gap semiconductor with an optical band gap of 3.8 eV [72]. ZnAl₂O₄ has been used as phosphor hosts for a variety of luminescent ions. Pitale *et al.* studied ZnAl₂O₄:Mn green light emitting powder phosphors that were prepared by the combustion method [73]. The luminescent properties of ZnAl₂O₄:Ce³⁺, Tb³⁺ phosphor were studied by Tshabalala *et al.* [74]. ZnAl₂O₄:Eu has been used as a red phosphor [75], while ZnAl₂O₄:Tb has been used as a green phosphor [76].

2.10 References

1. W.M. Yen, S. Shionoya and H. Yamamoto, *Measurements of Phosphor Properties*, Taylor & Francis Group (New York, 2007).
2. M.C. Goldberg, *Luminescence Applications in Biological, Chemical, Environmental, and Hydrological Sciences*, American Chemical Society (Washington, 1989).
3. S.R. Rotman, *Wide-Gap Luminescent Materials: Theory and Application*, Kluwer Academic (Dordrecht, 1997).
4. H. Jung, D. Park and Y.C. Park, *J. Bull. Korean Chem. Soc.* **19** (1998) 1320-1325.
5. G. Blasse and B.C. Grabmaier, *Luminescent materials*, Springer-Verlag (Berlin, 1994).
6. S. Wu, D. Yang and F. Mazda, *Fundamentals of Liquid Crystal Devices*, John Wiley & Sons (Chichester, 2006).
7. W.M. Yen, S. Shionoya and H. Yamamoto, *Phosphor Handbook*, 2nd Ed., CRC Press (Boca Raton, 2007).
8. A. Kitai, *Luminescent Materials and Applications*, John Wiley & Sons (Chichester, 2008).
9. K.N. Shinde, S.J. Dhoble, H.C. Swart and K. Park, *Phosphate Phosphors for Solid-State Lighting*, Springer-Verlag (Berlin, 2012).
10. L. Ozawa, *Cathodoluminescence and Photoluminescence - Theories and Practical Applications*, Taylor & Francis Group (New York, 2007).
11. Fluorescence Microscopy [online]
<http://micro.magnet.fsu.edu/primer/techniques/fluorescence/fluorescenceintro.html>
12. S.M. Khopkar, *Basic Concepts of Analytical Chemistry*, New Age International (New Delhi, 2004).
13. R. Xie, Y.Q. Li, N. Hirosaki and H. Yamamoto, *Nitride Phosphors and Solid-State Lighting*, Taylor and Francis (New York, 2011)
14. J.G. Solé, L.E. Bausá and D. Jaque, *An Introduction to the Optical Spectroscopy of Inorganic Solids*, John Wiley & Sons (Chichester, 2005).
15. S. Cotton, *Lanthanides and Actinides Chemistry*, John Wiley & Sons (Chichester, 2006).
16. K.A. Gschneidner Jr., J.G. Bünzli and V.K. Pecharsky, *Handbook on the Physics and Chemistry of Rare Earths* **37** (2007) 8.
17. C. Ronda, *Luminescence From Theory to Applications*, Wiley (Weinheim, 2008).

18. E.G. Yukihara and S.W.S. Mckeever, *Optically Stimulated Luminescence Fundamentals and Applications*, John Wiley & Sons (Chichester, 2011)
19. H.A.A. Seed Ahmed, O.M. Ntwaeaborwa, M.A. Gusowski, J.R. Botha and R.E. Kroon, *Phys. B* **407** (2012) 1653-1655.
20. H.A.A. Seed Ahmed, *Luminescence from lanthanide ions and the effect of co-doping in silica and other hosts*, PhD thesis, University of the Free State, Bloemfontein, South Africa, 2012.
21. B.D. Bartolo, V. Goldberg and D. Pacheco, *Luminescence of inorganic solids*, Plenum Press (New York, 1978).
22. Y. Zhang and J. Hao, *J. Mater. Chem. C* **1** (2013) 5607-5618.
23. S. Som and S.K. Sharma, *J. Phys. D: Appl. Phys.* **45** (2012) 415102 (11 pages).
24. Z. Xia and W. Wu, *Dalton Trans.* **42** (2013) 12989-12997.
25. K.W. Krämer, P. Dorenbos, H.U. Güdel and C.W.E. van Eijk, *J. Mater. Chem.* **16** (2006) 2773-2780.
26. H. Long, X. Xue-Wen, L. Zun-Ming, F. Ying, L. Yang-Xian and T. Cheng-Chun, *Chin. Phys. B* **19** (2010) 127807 (5 pages).
27. W. Chen, Y. Wang, X. Xu, W. Zeng and Y. Gong, *ECS Solid State Lett.* **1** (2012) 17-19.
28. X. Fu, L. Fang, S. Niu and H. Zhang, *J. Lumin.* **142** (2013) 163-166.
29. L.G. Jacobsohn, M.W. Blair, S.C. Tornga, L.O. Brown, B.L. Bennett and R.E. Muenchausen, *J. Appl. Phys.* **104** (2008) 124303 (7 pages).
30. Y. Porter-Chapman, E. Bourret-Courchesne and S.E. Derenzo, *J. Lumin.* **128** (2008) 87-91.
31. H. Fukada, M. Konagai, K. Ueda, T. Miyata and T. Minami, *Thin Solid Films* **517** (2009) 6054-6057.
32. C. Kim, C. Pyun, H. Choi and S. Kim, *J. Bull. Korean Chem. Soc.* **20** (1999) 337-340.
33. S. Saini, H. Singh and B. Bagchi, *J. Chem. Sci.* **118** (2006) 23-35.
34. J.R. Lakowicz, *Principles of Fluorescence Spectroscopy*, 3rd Ed, Springer Science and Business Media (New York, 2006).
35. A.H. Kitai, *Solid State Luminescence Theory, materials and devices*, Chapman & Hall (London, 1993).

36. H.A.A. Seed Ahmed, O.M. Ntwaeaborwa and R.E. Kroon, *J. Lumin.* **135** (2013) 15-19.
37. R. Ianoş and R. Lazău, *Mater. Chem. Phys.* **115** (2009) 645-648.
38. S.T. Aruna and A.S. Mukasyan, *Curr. Opinion Solid State and Mater. Sci.* **12** (2008) 44-50.
39. Z. Xiaolin, Z. Haijun, Y. Yongjie and L. Zhanjie, *Mater. Sci. Eng. A* **379** (2004) 112-118.
40. I. Gómez, M. Hernández, J. Aguilar and M. Hinojosa, *Ceram. Int.* **30** (2004) 893-900.
41. S. Choi, K. Kim, Y. Moon, B. Park and H. Jung, *Mater. Res. Bull.* **45** (2010) 979-981.
42. H. Yang, L. Yuan, G. Zhu, A. Yu and H. Xu, *Mater. Lett.* **63** (2009) 2271-2273.
43. J. Lee, H. Park, K. Yoo, B. Kim, J.C. Lee and S. Park, *J. Eur. Ceram. Soc.* **27** (2007) 965-968.
44. M. Zawadzki and J. Wrzyszczyk, *Mater. Res. Bull.* **35** (2000) 109-114.
45. Z. Fang, *Rapid Production of Micro- and Nano-particles Using Supercritical Water*, Springer-Verlag (Berlin, 2010).
46. M. Nazarov and D. Noh, *New Generation of Europium- and Terbium-Activated Phosphors: From Synthesis to applications*, Taylor & Francis (New York, 2012).
47. W. M. Yen and M. J. Weber, *Inorganic Phosphors Compositions, Preparation and Optical Properties*, CRC Press (New York, 2004).
48. H. Kozuka and S. Sakka, *Handbook of Sol-Gel Science and Technology Processing Characterization and Applications*, Kluwer Academic (New York, 2005).
49. C.J. Brinker and G.W. Scherer, *Sol-gel Science: The Physics and Chemistry of Sol-gel Processing*, Academic Press (New York, 1990).
50. C.B. Carter and M.G. Norton, *Ceramic Materials Science and Engineering*, Springer Media (New York, 2007).
51. R.J. Wiglusz and T. Grzy, *Opt. Mater.* **33** (2011) 1506-1513.
52. X. Duan, M. Pan, F. Yu and D. Yuan, *J. Alloys Compd.* **509** (2011) 1079-1083.
53. D. Levy, A. Pavese and M. Hanfland, *Am. Mineral.* **88** (2003) 93-98.
54. W. Li, G. Zhou and T.C. Mak, *Advanced Structural Inorganic Chemistry*, Oxford University Press (New York, 2008).
55. M.D. Graef and M.E. McHenry, *Structure of Materials: An Introduction to Crystallography, Diffraction and Symmetry*, 2nd Ed, Cambridge University Press (New York, 2012).

56. A. Kalendová, D. Veselý and J. Brodinová, *Anti-Corrosion Meth. Mater.* **51** (2004) 6-17.
57. A.F. Wells, *Structural Inorganic Chemistry, 4th Ed*, Oxford University Press (London, 1975).
58. K.E. Sickafus and J.M. Wills, *J. Am. Ceram. Soc.* **82** (1999) 3279-3292.
59. S. Roy, N. Vegten and A. Baiker, *J. Catalysis* **271** (2010) 125-131.
60. O. Shpotyuk, A. Ingram, H. Klym, M. Vakiv, I. Hadzaman and J. Filipecki, *J. Eur. Ceram. Soc.* **25** (2005) 2981-2984.
61. A. Jouini, A. Yoshikawa, Y. Guyot, A. Brenier, T. Fukuda and G. Boulon, *Opt. Mater. (Amsterdam, Neth.)* **30** (2007) 47-49.
62. T. Sato, M. Shiraib, K. Tanakab, Y. Kawabea, E. Hanamur, *J. Lumin.* **114** (2005) 155-161.
63. P. Głuchowski, R. Pązik, D. Hreniak and W. Stręk, *Chem. Phys.* **358** (2009) 52-56.
64. T.H. Maiman, R.H. Hoskins, B.H. Soffer, R.C. Pastor and M. A. Pearson. 1968 US Patent No. 3396119.
65. Y. Fujimoto, H. Tanno, K. Izumi, S. Yoshida, S. Miyazaki, M. Shirai, K. Tanaka, Y. Kawabe and E. Hanamura, *J. Lumin.* **128** (2008) 282-286.
66. I. Omkaram, G. Seeta Rama Raju and S. Buddhudu, *J. Phys. Chem. Solids* **69** (2008) 2066-2069.
67. X. Chen, C. Ma and S. Bao, *Solid State Sci.* **12** (2010) 857-863.
68. V. Singh, M.M. Haque and D. Kim, *J. Bull. Korean Chem. Soc.* **28** (2007) 2477-2480.
69. D. Jia and W.M. Yen, *J. Lumin.* **101** (2003) 115-121.
70. M. García-Hipólito, C. D. Hernández-Pérez, O. Alvarez-Fregoso, E. Martínez, J. Guzmán-Mendoza and C. Falcony, *Opt. Mat.* **22** (2003) 345-351.
71. Z. Lou and J. Hao, *Thin Solid Films* **450** (2004) 334-340.
72. X.Y. Chen, C. Ma, *Opt. Mat.* **32** (2010) 415-421.
73. S.S. Pitale, V. Kumar, I.M. Nagpure, O.M. Ntwaeaborwa and H.C. Swart, *Appl. Surf. Sci.* **257** (2011) 3298-3306.
74. K.G. Tshabalala, S-H. Cho, J-K. Park, S.S. Pitale, I.M. Nagpure, R.E. Kroon, H.C. Swart and O.M. Ntwaeaborwa, *J. Alloys Compd.* **509** (2011) 10115-10120.
75. I. Miron, C. Enache and I. Grozescu, *J. Nanomat. Biostr.* **7** (2012) 967-972.
76. M. García-Hipólito, A. Corona-Ocampo, O. Alvarez-Fregoso, E. Martínez, J. Guzmán-Mendoza and C. Falcony, *Phys. stat. sol. (a)* **201** (2004) 72-79.

3

Research techniques

3.1 Introduction

In this chapter, a brief description of the experimental techniques used to synthesize and characterize the powder and thin film phosphors is presented. The techniques include x-ray diffraction (XRD), scanning electron microscopy (SEM), atomic force microscopy (AFM), energy dispersive spectroscopy (EDS), ultraviolet–visible (UV-Vis) spectroscopy, x-ray photoelectron spectroscopy (XPS), photoluminescence (PL) spectroscopy and Auger electron spectroscopy (AES). The pulsed laser deposition (PLD) technique and the spin coating method were used to grow thin luminescent films on Si (100) substrates. SEM was used to study the morphology of the powders whereas AFM and SEM were used for the thin films. XRD was used to identify the crystalline phases and obtain the crystallite size of the nanoparticles. XPS was used to explore the atoms in the sample surface and identify the oxidation state of Ce ions. AES was used to monitor changes in the surface chemical composition and measure depth profiles of the thin films. Each of the techniques is discussed in the following sections.

3.2 X-ray diffraction

XRD was used for studying the structural properties of the powders and thin films. The technique can inform researchers on the degree of crystallinity, phase identification, lattice parameters, preferred orientation of the crystal (especially in the thin film) and grain size [1]. With the XRD pattern the identification of an unknown crystalline material becomes

possible. Files of d-spacings for hundreds of thousands of inorganic compounds for comparison are available in the Powder Diffraction Files (PDF) of the International Centre for Diffraction Data (ICDD).

Bragg's law is the basis of determination of lattice constants by XRD analysis. This law relates the wavelength of electromagnetic radiation to the diffraction angle and the lattice spacing in a crystalline sample. When a monochromatic x-ray beam with wavelength λ is incident onto a crystal sample, the constructive diffraction (or interference) from parallel planes of atoms with inter-planar spacing d occur if Bragg's law (figure 3.1) is satisfied:

$$2d \sin \theta = n\lambda \quad (1)$$

where n is an integer that indicates the order of the reflection, θ is Bragg angle and d is the interplanar distance. By measuring the Bragg angle, the interplanar distance can be obtained if the wavelength of the x-ray beam is known [2].

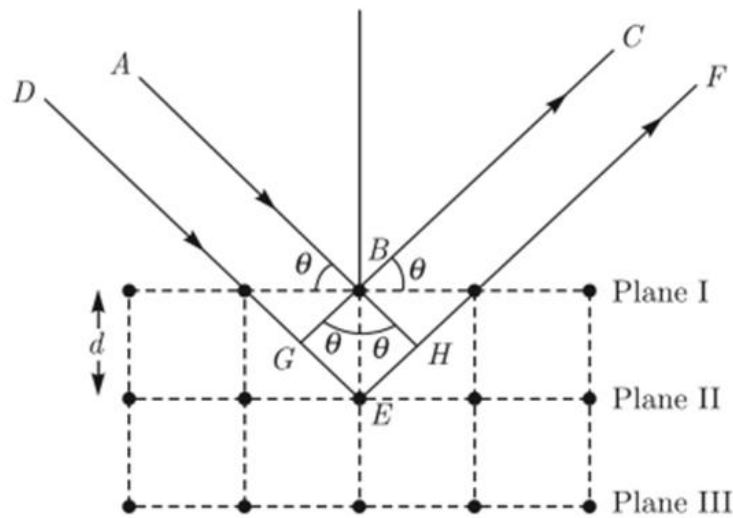


Figure 3.1: Schematic diagram of Bragg's diffraction from a set of parallel planes [2].

The lattice parameters are related with Miller indexes (hkl) of each reflection plane and interplanar distance (d_{hkl}). For example for cubic structures with lattice parameter a one has [3]

$$a = d_{hkl} \sqrt{h^2 + k^2 + l^2} \quad (2)$$

In 1918, Scherrer first observed that a small crystallite size could induce peak broadening of XRD spectra. Scherrer's equation [1] is

$$D = \frac{k\lambda}{\beta \cos \theta} \quad (3)$$

where D is the particle diameter, θ is the diffraction angle and β is the full width at half maximum (FWHM) of an XRD peak. In this work k is taken as 0.9 [4]. From the width of the diffraction peak using the Scherrer's equation, one can calculate the average crystallite size.

The strain induced in powders due to crystal imperfection and distortion was calculated using the formula:

$$\varepsilon = \frac{\beta}{4 \tan \theta} \quad (4)$$

Williamson-Hall analysis is employed for estimating crystallite size and lattice strain.

Williamson-Hall equation [5] is

$$\beta \cos \theta = \frac{k\lambda}{D} + 4\varepsilon \sin \theta \quad (5)$$

From the linear relation between $4\sin\theta$ along the x-axis and $\beta\cos\theta$ along the y-axis, the crystalline size was estimated from the y-intercept and the strain ε from the slope of the line.

An x-ray diffractometer consist of three basic elements: an x-ray tube, a sample holder and an x-ray detector. The x-rays are produced in a cathode ray tube by heating a filament to produce electrons. When a voltage is applied, the electrons are accelerated towards a target material (usually Cu, Fe, Mo or Cr) and when electrons have sufficient energy to dislodge

the inner shell electrons of the target material, characteristic x-rays will be produced in addition to a continuous x-ray background (bremsstrahlung). The characteristic x-ray spectrum consists of several components, the most important being K_α and K_β . Each component has a specific characteristic wavelength [6]. Copper is the most commonly used target material for single crystal diffraction, with the wavelength of Cu K_α radiation being 1.5406 \AA . The monochromatization process selects a single wavelength from a x-ray spectrum using a β -filter. Nickel strongly absorbs x-rays below 1.5 \AA and can be used to filter the K_β x-rays from copper, as shown in figure 3.2.

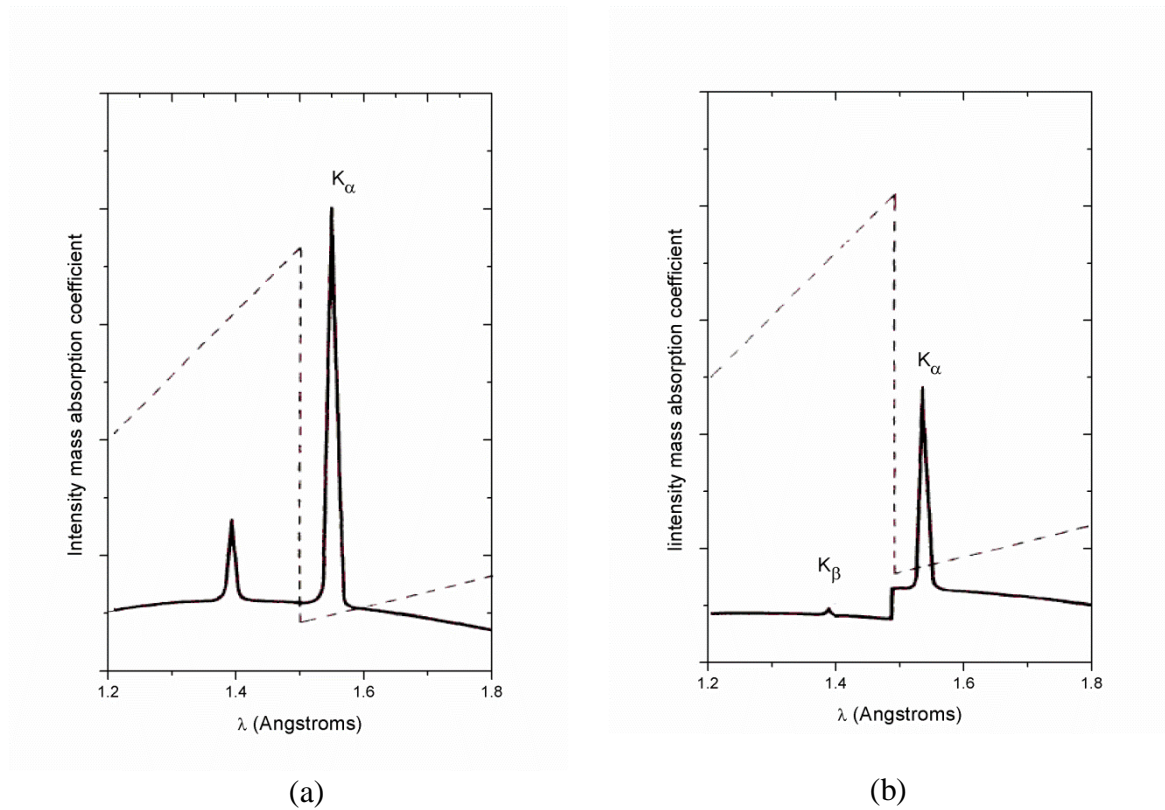


Figure 3.2: Comparison of the spectra of copper radiation (a) before and (b) after passage through a nickel filter (schematic). The dashed line represents the absorption of nickel [1].

As the sample and detector are rotated, the intensity of the reflected x-rays is recorded. When the geometry of the incident x-rays impinging on the sample satisfies the Bragg

equation (1) constructive interference occurs and diffraction peaks of the sample will be observed. The XRD data for this study were obtained using a Bruker D8 Advance x-ray diffractometer equipped with a copper anode x-ray tube (figure 3.3).



Figure 3.3: Bruker D8 Advance x-ray diffractometer.

3.3 Scanning Electron Microscopy

SEM can provide information about the topography and morphology of a material by producing images of a sample surface. During SEM measurements a focused electron beam is scanned across the sample and an image is built up by detecting secondary electron intensity as a function of the primary beam position [7]. Figure 3.4 shows a simple diagram of SEM. The electron beam is emitted from electron gun and accelerated towards

to the surface of the sample. The electron beam generally has energies that range from a few keV to 50 keV and it is focused by condenser lenses into a beam with a very fine spot size. This beam then passes through the objective lens, where pairs of coils deflect the beam either linearly or in a raster fashion over a rectangular area of the sample surface. A metal sample is conductive and requires no preparation before being studied. Non-metallic samples such as ceramics need to be prepared with a thin conductive coating such as Au [8] to prevent charging. The coating process is done by using a sputter coater.

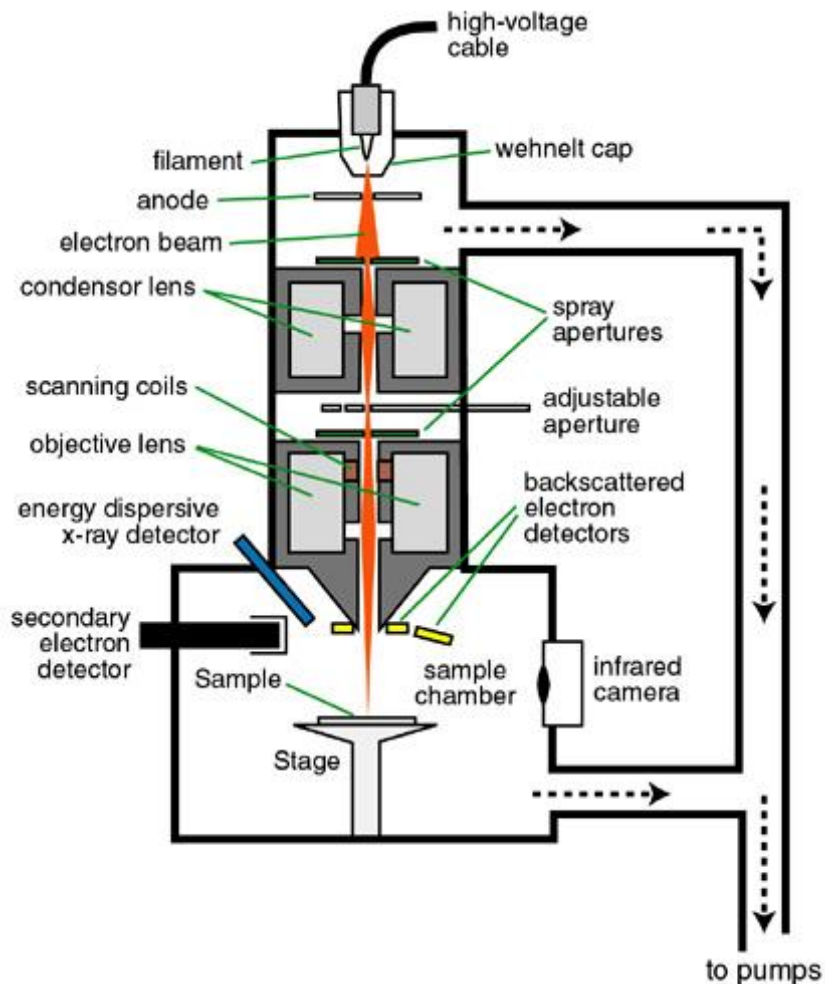


Figure 3.4: Schematic diagram of a typical SEM [9].

When the electron beam hits the specimen on the stage, it also causes backscattered electrons and characteristic x-rays to be emitted from the sample (see figure 3.5). Detectors can then monitor these signals and convert them into other images. EDS is based on the collection and energy analysis of characteristic x-rays coming from the specimen. The EDS spectrum displays peaks corresponding to the energy levels for which the most x-rays have been received. Each of these peaks is unique to an atom, and therefore characteristic of a specific element. The higher a peak in a spectrum, the more concentrated the element in the specimen will be.

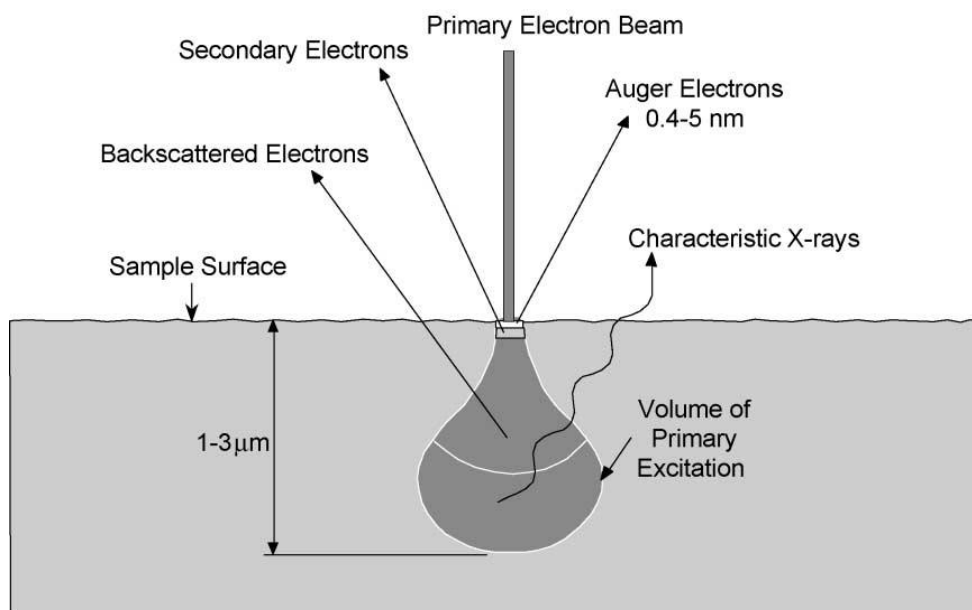


Figure 3.5: The energies produced from electron beam interaction with solid matter [10].

The Shimadzu Superscan SSX-550 was the SEM used in the present study and its photograph is shown in figure 3.6.



Figure 3.6: The Shimadzu Superscan SSX-550 SEM at the Centre for Microscopy at the University of the Free State.

3.4 Transmission electron microscopy

During TEM a beam of electrons is transmitted through a very thin sample and interacts with the sample as it passes through. The focused electron beam in TEM can be used to produce images and to determine the crystallographic and morphological information of the material, including the particle shape and size distribution in the sample. TEM requires an ultra high vacuum and the accelerating voltage is considerably higher than in an SEM, typically 100-400 kV. Powder samples to be measured by TEM are often ground and then dispersed in ethanol. A drop is then placed onto an amorphous support film on a circular metal grid (generally copper). The specimen must be no more than a few hundred nanometres in thickness (less than 200 nm).

In this study the images of phosphor particles were obtained using a Philips CM100 Model transmission electron microscope shown in figure 3.7.



Figure 3.7: The Philips CM100 TEM at the Centre for Microscopy at University of the Free State.

3.5 X-ray photoelectron spectroscopy

XPS, also known as electron spectroscopy for chemical analysis, is a powerful technique used for characterizing the chemical composition of the surface of the phosphor material [11, 12].

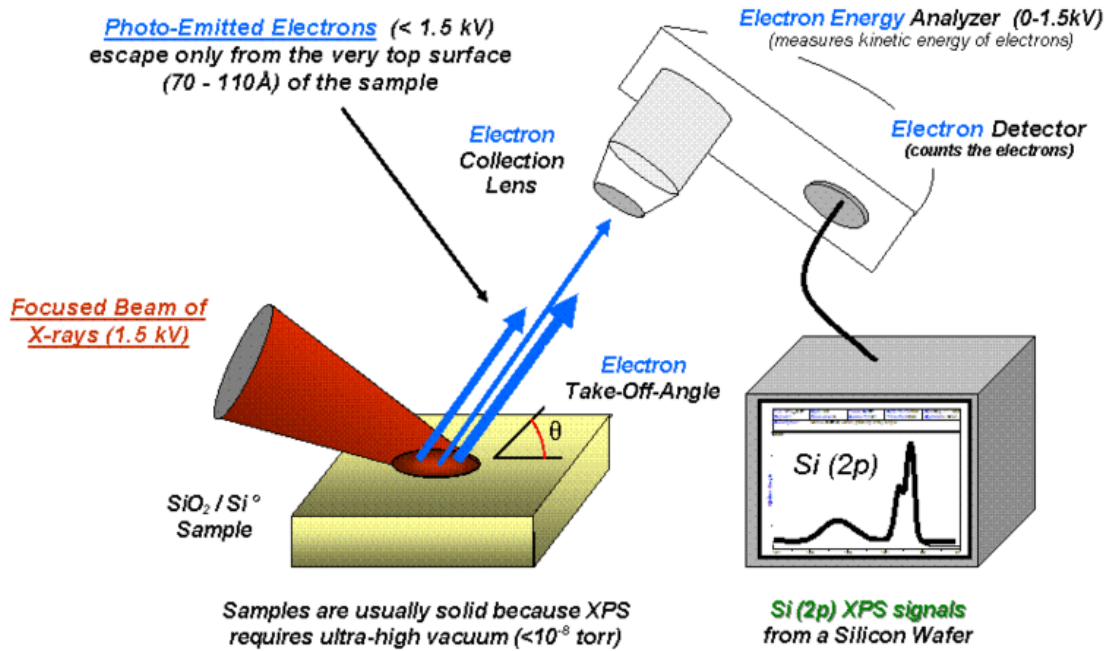


Figure 3.8: The schematic diagram of XPS with a high resolution scan of Si peaks [13].

In XPS (figure 3.8), when an x-ray beam is directed to the sample surface the energy of the x-ray photon is absorbed completely by a core electron of an atom. Monochromatic x-ray sources often used are Mg K α (1253.6 eV) or Al K α (1486.6 eV) [11]. If the photon energy $h\nu$ is large enough, the core electron with binding energy E_B will then escape from the atom and be emitted out of the surface. This process is called photoemission and the emitted electron is referred to as a photoelectron. Only photoelectrons from atoms near the surface can escape, making XPS a surface sensitive technique. By conservation of energy, a photoelectron will have kinetic energy E_k satisfying [12, 14]

$$h\nu = E_B + E_k + \phi_{sp} \quad (6)$$

where ϕ_{sp} is the spectrometer work function. Because the Fermi levels of the sample and spectrometer are aligned, only the spectrometer work function is needed. If the spectrometer and the sample are grounded, then the zero energy level of E_B will be aligned as illustrated in Figure 3.9.

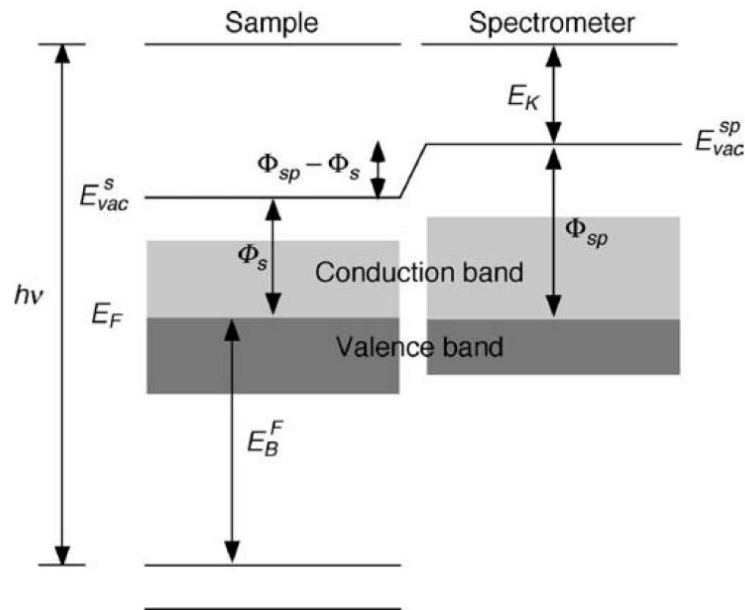


Figure 3.9: Zero level of E_B and E_k for grounded sample and the spectrometer [15].

Since E_k can be measured by the energy analyzer, the binding energy E_B can be obtained and a plot made of the number of photoelectrons with different binding energies. The binding energy of a photoelectron is characteristic of the atomic orbital from which the electron originated and so the emitting atom can be identified. The peak areas indicate the relative concentration of different atoms on the material surface. The shape of each peak and the binding energy can be slightly altered by the neighbouring atoms and oxidation state of the emitting atom, hence XPS can provide chemical bonding information as well.

Note that in addition to photoelectrons, Auger electrons may also be emitted by the sample atoms. The Auger process is explained in more detail in section 3.9, but it should be noted that some extra peaks occur in XPS spectra as a result of these Auger electrons. Since these are not true binding energy peaks, their position will change when the x-ray energy is changed whereas the binding energy peaks associated with photoelectrons will stay at the same position.

As photoelectrons are emitted from insulating materials after x-ray bombardment, the surface becomes positively charged. The charge on the insulating surface must be controlled by charge neutralization. The goal of charge neutralization is to provide uniform and stable surface potential. Traditionally, flood guns are used to provide a source of low energy electrons to take the place of the ejected photoelectrons in XPS. Other techniques to reduce differential charging may include placing the sample on a conductive platform and mixing the sample with another substance, such as carbon black powder in a 50/50 ratio.

XPS data was collected by a PHI 5400 Versaprobe using Al x-rays and analysed using the software MultiPak. Figure 3.10 shows the PHI 5400 XPS spectrometer.

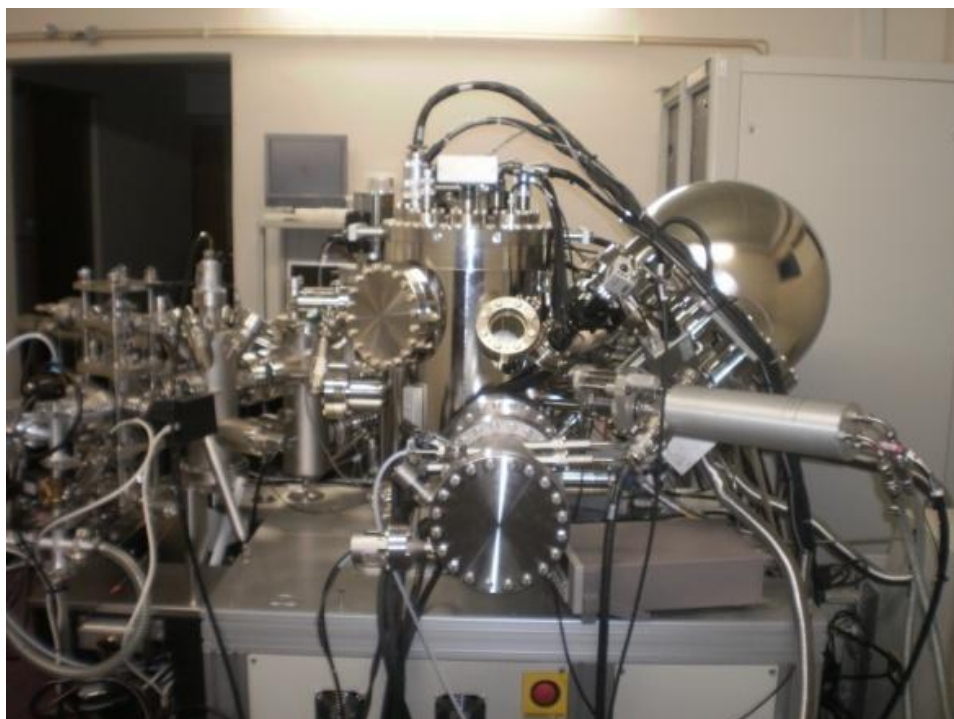


Figure 3.10: PHI 5400 Versaprobe XPS.

3.6 Photoluminescence spectroscopy

PL spectroscopy has emerged as an important tool for studying the optical and electronic properties of solid state materials suited for optoelectronic applications. PL spectroscopy can be used as a powerful tool to understand the excitation and emission processes. By this technique, a sample is excited by photons (generally in the UV range) and the excess energy released by the sample through the emission of light is detected and recorded for different modes, i.e. excitation and emission.

The emission spectrum is obtained by plotting the relationship between the wavelength and the intensity of the emitted light from a sample excited by an appropriate excitation source of constant energy. In the case of an excitation spectrum, on the other hand, the relationship is obtained by observing changes in the emitted light intensity at a set wavelength while the excitation wavelength is changed.

The schematic diagram of general basic equipment for PL is shown in figure 3.11. This instrument has a source (exciting light) of white light from a xenon lamp which is collected by an elliptical mirror and directed to the entrance slit of a monochromator. Xenon lamps are useful because of their high intensity at all wavelengths ranging upward from 250 nm [16]. The slits of the monochromator determine the amount of monochromatic light that is used to illuminate the sample. The emitted light is analysed with a spectrometer and detected with a photomultiplier tube (PMT). The output of the PMT signal is amplified and recorded.

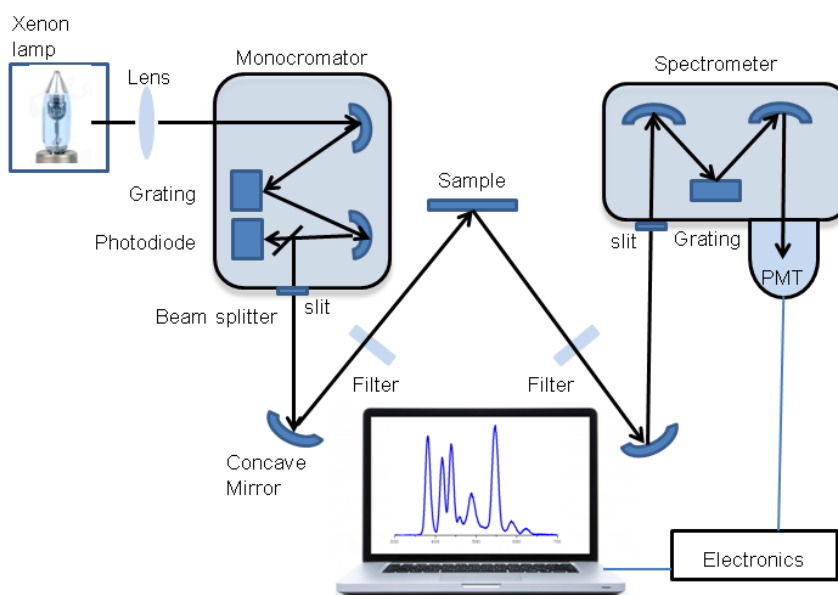


Figure 3.11: Schematic diagram of PL spectrometer, modified from [17].

The emission and excitation spectra for the powder and thin film samples were measured using a Cary Eclipse fluorescence spectrophotometer as presented in figure 3.12. The measurements were made using both the fluorescence mode and the phosphorescence mode. The fluorescence emission was collected and measured when the lamp flashes, and in the phosphorescence mode is measured after the lamp has stopped flashing. All measurements were made at room temperature.



Figure 3.12: Cary Eclipse fluorescence spectrophotometer.

3.7 UV-Vis spectroscopy

UV-Vis spectroscopy is used for the measurement of the intensity of absorption of ultraviolet and visible light after it passes through a sample or after reflection from a sample surface. The basic parts of the spectrophotometer are a light source, a monochromator with diffraction grating to separate the different wavelengths of light, a sample holder and a detector as shown in figure 3.13.

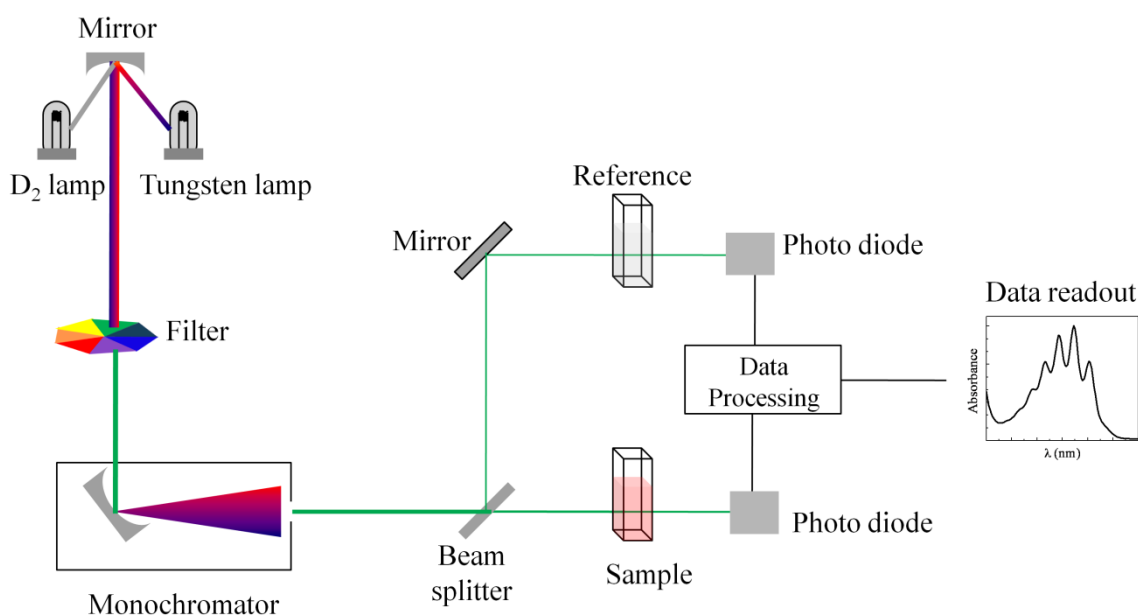


Figure 3.13: Schematic of UV- visible spectrophotometer [18].

The UV-Vis spectral range is approximately 190 to 900 nm, as defined by the working range of typical commercial UV-Vis spectrophotometers [19]. The light source is usually a deuterium discharge lamp for UV measurements and a tungsten-halogen lamp for visible measurements. The detector converts a light signal into an electrical signal and is typically a photodiode or photomultiplier tube (PMT). First a background scan is recorded without the sample present, and then the light passing through the sample (I) is compared to a

reference beam (I_0) to obtain the ratio I / I_0 which does not depend on changes of the incident light intensity and is called the transmittance

$$T = I / I_0. \quad (7)$$

The absorption coefficient α for a uniform medium can be defined in terms of the intensity change of a monochromatic light beam in a unit distance that the beam travelled in the medium by [20]

$$\frac{dI}{dx} = -\alpha I. \quad (8)$$

Therefore, the beam intensity as a function of the distance x can be written as:

$$I = I_0 e^{-\alpha x} \quad (9)$$

and so $T = I / I_0 = e^{-\alpha x}$. The absorbance (A) is defined as follows:

$$A = -\log T \quad (10)$$

and so $A = -\log e^{-\alpha x} = 0.4343 \alpha x$. It is therefore clear that the absorbance and absorption coefficient are proportional to one another.

The optical band gap (E_g) of a material is calculated using the value of α in the following equation for semiconductors [21]

$$\alpha h\nu = B(h\nu - E_g)^n \quad (11)$$

where B is a constant which depends on the effective mass of the holes and electrons and the refractive index of the material, but is independent of the frequency; h is Planck constant, ν is the frequency of the incident photons, and n depends on the type of transition. The value of n for allowed direct, allowed indirect, forbidden direct and forbidden indirect transitions are 1/2, 2, 3/2, and 3 respectively [21, 22].

For phosphor powders the absorption coefficient and band gap values can be estimated using diffuse reflectance spectroscopy measurements. For diffuse reflectance measurements the UV/Vis instrument must be equipped with an integrating sphere coated with a white standard, intended to collect the light reflected by the standard and the sample. The reflectivity R can be transformed into a value proportional to the absorption coefficient using the Kubelka-Munk function [23]:

$$k = \frac{1-R^2}{2R} \quad (12)$$

Our diffuse reflectance spectra were recorded by a Lambda 950 UV-Vis spectrophotometer with an integrating sphere. The standard used was spectralon. The UV-Vis spectrophotometer used in this study is shown in figure 3.14.



Figure 3.14: Lambda 950 UV-Vis spectrophotometer.

3.8 Atomic Force Microscopy

AFM is a powerful tool in the suite of nanoscale characterization techniques that provides a variety of information including topography and mechanical properties. AFM has significantly impacted the fields of materials science, chemistry, biology, physics and semiconductors. AFM operates by measuring the force between a probe and the sample. AFM images of a sample surface enabling the presentation of three-dimensional topography. With good samples, meaning they are clean with no excessively large surface features, resolution in the horizontal plane ranges from 0.1 to 1.0 nm and in the z-direction is 0.1 nm.

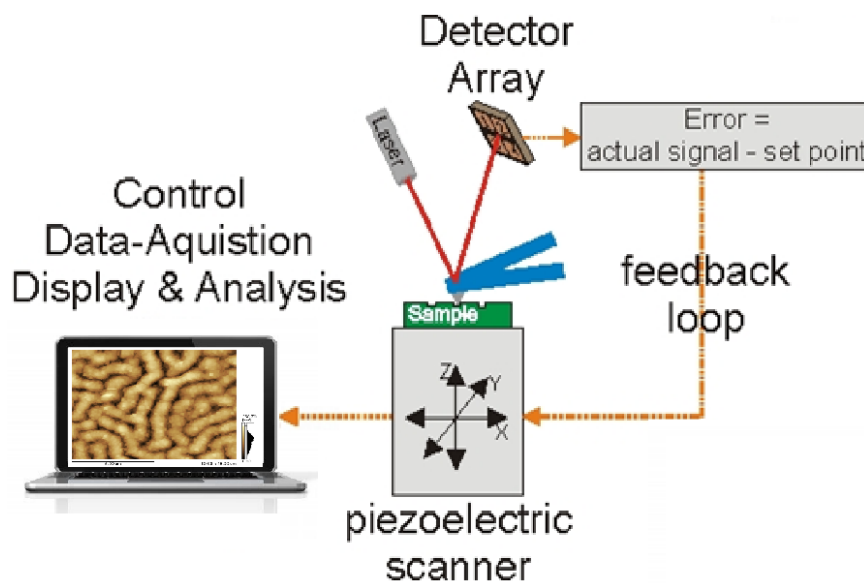


Figure 3.15: Schematic setup of an AFM, modified from [24].

The schematic diagram of general basic equipment of AFM is shown in figure 3.15. The AFM consists of a cantilever with a sharp tip (probe) at its end that is used to scan the specimen surface. The cantilever is typically silicon or silicon nitride with a tip radius of

curvature in the order of nanometres. The forces between the tip and the sample surface lead to a deflection of the cantilever. A detector is used to measure the cantilever deflection. The deflection of the cantilever is most commonly detected optically using a focused laser beam reflected from the top surface of the cantilever into an array of photodiode.

In this work, the surface topography and roughness were examined from images captured in contact mode using a Shimadzu SPM-9600 AFM as is shown in figure 3.16. The surface root-mean-square (RMS) roughness values were estimated from the analysis of AFM images of the films surfaces.



Figure 3.16: Shimadzu SPM-9600 AFM.

3.9 Auger Electron Spectroscopy

AES is a surface sensitive analytical technique used mainly to determine elemental compositions of materials and in certain cases to identify the chemical states of surface atoms. Auger electrons are produced when an electron with sufficient primary energy (3-5 keV) interacts with an atom. The process is shown in figure 3.17.

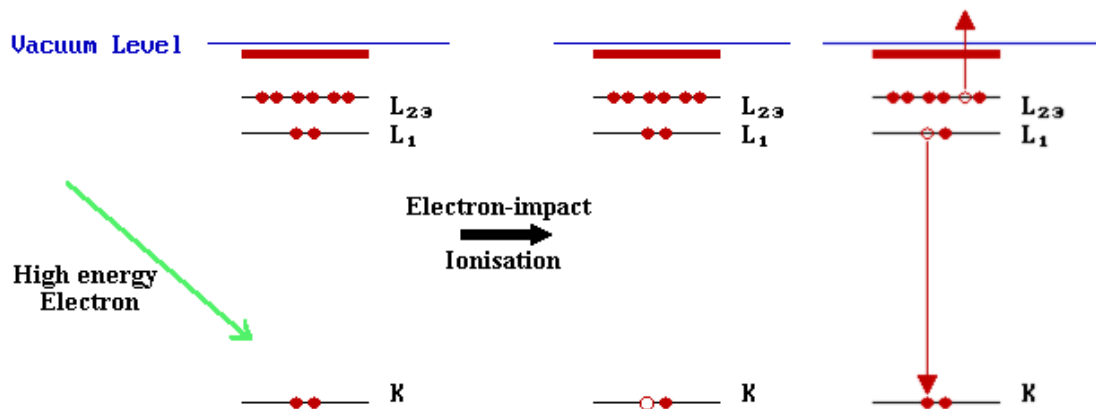


Figure 3.17: Relaxation of the ionized atom by the emission of a KL_1L_{23} Auger electron.

First a secondary electron will be emitted from the core level, such as a K level [7]. Then another electron falls from a higher level (L_1 in this case) to fill the vacancy in the K -shell. Thirdly the energy liberated in this process ($E_K - E_{L1}$) is simultaneously transferred to a second electron, for example in the L_{23} shell. A fraction of this energy is required to overcome the binding energy of this second electron, and the remainder is retained by this emitted Auger electron as kinetic energy. In the Auger process illustrated in figure 3.16,

the final state is a doubly-ionized atom with core holes in the L_1 and L_{23} shells. The Auger electron will have energy given by

$$E = (E_K - E_{L1}) - E_{L23}. \quad (13)$$

This excitation process is labelled as a KL_1L_{23} Auger transition, or simply as KLL. In the KLL transition, the L shell ends up with two vacancies. If one just considers these three electronic levels there are clearly several possible Auger transitions: specifically KL_1L_1 , KL_1L_{23} and $KL_{23}L_{23}$. AES surface analysis can detect all elements except hydrogen and helium [20]. Since the Auger process is a three-electron process, it is obvious why hydrogen and helium cannot be detected; both have less than three electrons. AES surface analysis is performed under ultra-high vacuum conditions, using an electron beam typically in the 3 to 25 keV range. With AES a primary electron beam is used to excite Auger electrons (figure 3.5), although secondary electrons, backscattered electrons and x-rays are also produced. For this reason, SEM images can be obtained by detecting low energy secondary electrons emitted from the surface. Auger maps, obtained by measuring the emitted Auger electron intensity while scanning the electron beam, reveal the lateral distribution of elements across the sample surface. AES is a surface sensitive technique because the Auger electrons are emitted from only about the first 5 nm from the surface.

One of the most important applications of AES is depth profiling because it provides a convenient way of analyzing the composition of thin surface layers. In this technique the sample is eroded by ion sputtering such as argon ions [25]. The sample is bombarded with ions accelerated in an ion gun to energy in the range 1 to 4 keV. As these energetic ions strike the sample a small amount of energy is transferred to the surface atoms, which causes them to leave the sample. The ion beam is rastered on the surface for a known time

to remove a uniform layer of the sample. A sputter depth profile, which plots the Auger signal as a function of sputter time, shows elemental concentration as a function of depth into the material. The system used in this work was a PHI 700 Scanning Auger Nanoprobe (figure 3.18).



Figure 3.18: The PHI 700 Scanning Auger Nanoprobe.

3.10 Pulsed laser deposition

PLD is a physical vapour deposition process carried out in a vacuum system, which shares some process characteristics common with molecular beam epitaxy and some with sputter deposition [26, 27]. It is one of the most versatile methods for oxide film growth. Thin films are obtained by vaporizing (ablating) a target material using laser pulses of high-energy, ultraviolet laser wavelength and nanosecond pulse width that is strongly absorbed

by a small volume of the target. The ablated material travels to and deposits on the substrate, placed opposite to the target, resulting in thin film growth. It is generally easier to obtain the desired stoichiometry in the deposited films than with other deposition technologies.

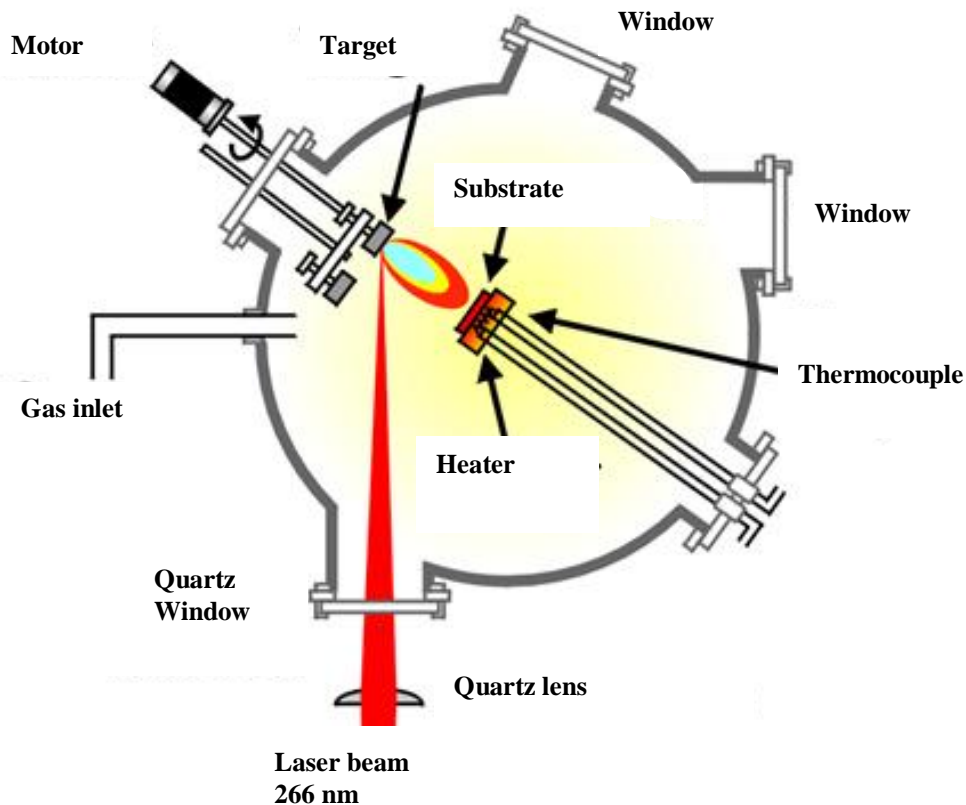


Figure 3.19: Schematic diagram of PLD system, modified from [28].

A schematic diagram of a typical PLD setup is shown in figure 3.19. Contained in a vacuum chamber connected to a turbo pump is a carousel capable of carrying up to six targets (25 mm in diameter) and a pulsed laser beam is focused onto a target of the material to be deposited. For sufficiently high laser energy density, each laser pulse vaporizes or ablates a small amount of the material creating a plasma plume. High-energy ultraviolet laser pulses can be readily provided via excimer lasers or frequency-tripled or

quadrupled Nd:YAG solid-state lasers. In some cases, a more efficient source is an infrared laser whose energy corresponds to a vibrational mode of the ablation target material. The ablated material is ejected from the target in a highly forward-directed plume and adheres on the substrate. Parameters which control the instantaneous deposition rate are the laser energy density at the target, pulse energy, distance between target and substrate, the type of substrate, the substrate temperature and the ambient gas properties, i.e. pressure and mass which determine the interaction with the ablated particles and, subsequently, the kinetic energy of the particles arriving at the substrate. As a consequence, this kinetic energy can be varied from high initial energy in vacuum to low energies resulting from thermalization at sufficient large ambient pressure. In PLD, a background gas is one of the important parameters during fabrication of oxide thin films, because the formation of multi-cation thin film materials often requires a reactive species (e.g. molecular oxygen). Interaction of ablated species with the background gas often produces molecular species in the ablation plume.

Substrate heaters are an important component of any PLD system. When using a heater the samples must be bonded to the heater block with thermally conductive metal paste. For our work used a silver paste up to 300 °C or nickel paste up to 700 °C to achieve good thermal conductivity between the block and substrate.

Advantages of PLD are numerous. Complex oxide compositions with high melting points can be deposited easily, provided the target materials absorb the laser energy. PLD allows the growth of films under a highly reactive gas ambient over a wide range of pressure and relatively high deposition rates. The target composition is transferred instantaneously leading to a stoichiometric deposition from the target to substrate. There is excellent

control of the thickness of the film by changing the amount of material arriving on the substrate, which is dependent on to the number of the pulses and the distance between the target and the substrate. The films can be deposited at low and high temperature, which is a major advantage whenever there is a need for experimenting with different target compositions. Disadvantages of PLD include that this technique is very popular for small size samples but is problematic as the sample size gets progressively larger. When bonding substrates of larger diameter with silver paste, it becomes very difficult to achieve a uniform bond thickness and thus uniform substrate temperature. Differential thermal expansion between the substrate and block also becomes an issue as the substrate size increases [29-31].

Figure 3.20 shows the PLD system at the National Laser Centre (NLC, CSIR), Pretoria, which was used in this study.

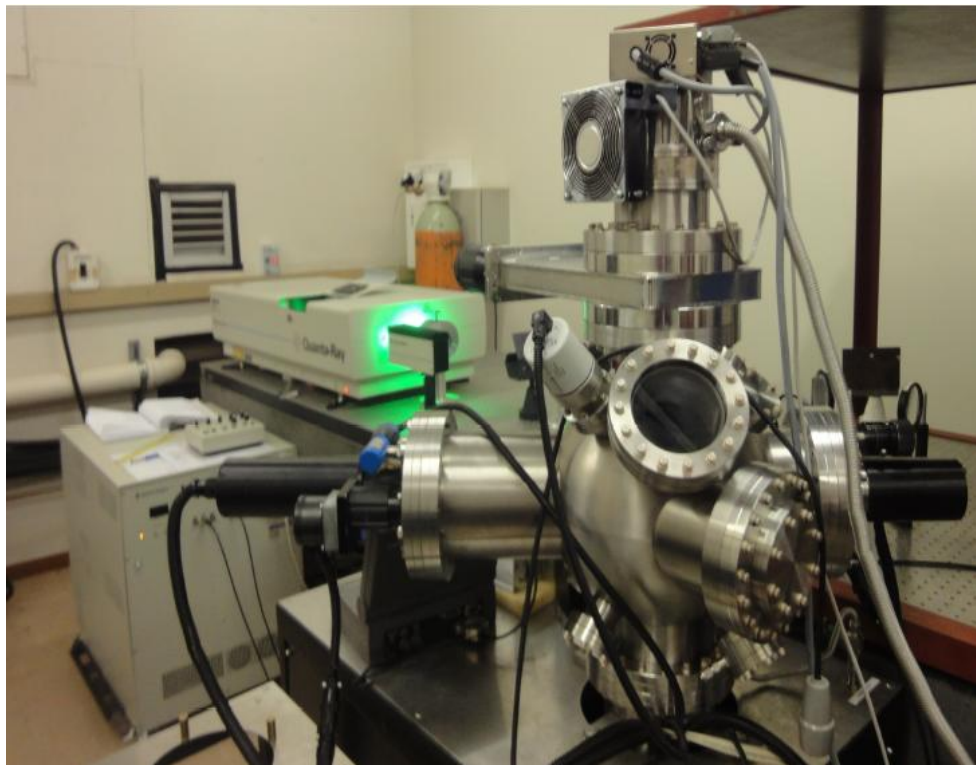


Figure 3.20: PLD system at the National Laser Centre (NLC, CSIR), Pretoria.

3.11 Spin coating

Spin coating, also known as spin casting, uses a liquid precursor deposited onto a smooth substrate such as Si, glass or fused silica. This process has been widely used in the manufacture of integrated circuits, flat screen display coatings, solar cells, detectors, sensors, optical mirrors, colour television screens and magnetic disks for data storage [32]. It is currently the predominant technique employed to produce uniform thin films with thickness of the order of micrometres and nanometres [33]. Spin coating involves depositing a small quantity of fluid solution onto the centre of a substrate and then spinning the substrate at high speed (1000 to 5000 rpm). At high velocity the centripetal acceleration causes the solution to spread on the surface of the substrate. The film thickness and other properties depend on the nature of the solution and the spin process. The nature of the solution parameters are viscosity, drying rate, percentage of solids, surface tension, etc. The parameters for the spin process are velocity, centripetal acceleration, spinning time, etc. [34]. Repeated depositions are carried out to increase the thickness of films as desired. Thermal treatment is often carried out in order to crystallize the amorphous spin coated film. Figure 3.21 illustrates the stage of the spin coating process.

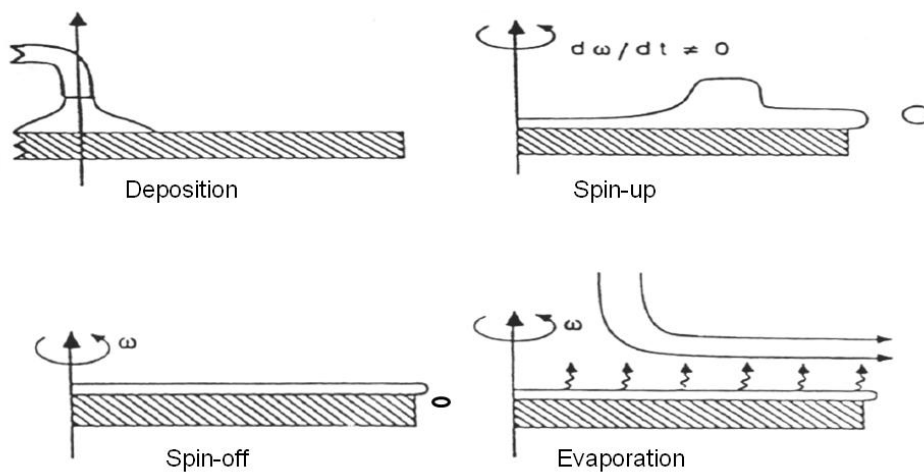


Figure 3.21: Stages of the spin coating process [35].

There are some advantages to fabrication film by this method. The film thickness is easily controlled by changing spin speed, repeated depositions and a different viscosity of the solution. Another advantage of spin coating is the ability of the film to be uniform and homogeneous. It is a low cost and fast operating system. The disadvantages of spin coating are few. Large substrates cannot be spun at a sufficiently high rate in order to allow the film to thin. The biggest disadvantage of spin coating is its lack of material efficiency. Typical spin coating processes utilize only 2–5% of the material dispensed onto the substrate [32, 36].

For this work the model spin coater used was a SPEN 150 from Semiconductor Production System shown in figure 3.22.



Figure 3.22: SPEN 150 from Semiconductor Production System.

3.12 References

1. B.D. Cullity, *Elements of x-ray diffraction*, Addison-Wesley Publishing Company (Reading, 1956).
2. A. Kumar, *Introduction to Solid State Physics*, PHI Learning Private Limited (New Delhi, 2010).
3. V.K. Pecharsky and P.Y. Zavalij, *Fundamentals of Powder Diffraction and Structural Characterization of Materials*, 2nd Ed., Springer (New York, 2009).
4. M.N. Rahaman, *Ceramic Processing and Sintering*, 2nd Ed., Marcel Dekker (New York, 2005).
5. V.D. Mote, Y. Purushotham and B.N. Dole, *J. Theor. Appl. Phys.* **6** (2012) 1-8.
6. P. Luger, *Modern X-Ray Analysis on Single Crystals*, Walter de Gruyter and Co. (Berlin, 1980).
7. D.K. Schroder, *Semiconductor Material and Device Characterization*, 3rd Ed., John Wiley & Sons (Hoboken, 2006).
8. R.F. Egerton, *Physical Principles of Electron Microscopy: An Introduction to TEM, SEM, and AEM*, Springer Media (New York, 2005).
9. Planetary Materials Microanalysis Facility [online]
<http://www4.nau.edu/microanalysis/Microprobe-SEM/Instrumentation.html>
10. K. Janssens and R.V. Grieken, *Non-destructive microanalysis of cultural heritage materials*, Elsevier (New York, 2004).
11. Z. Li and H. Meng, *Organic Light-Emitting Materials and Devices*, Taylor & Francis (New York, 2007).
12. C.R. Brundle, C.A. Evans, Jr. and S. Wihon, *Encyclopedia of Materials Characterization Surfaces, Interfaces, Thin Films*, Reed Publishing (London, 1992).
13. X-ray photoelectron spectroscopy [online]
http://chemwiki.ucdavis.edu/Physical_Chemistry/Spectroscopy/Photoelectron_Spectroscopy
14. C.D. Wagner, W.M. Riggs, L.E. Davis and J.F. Moulder, in: G.E. Muilenberg, *Handbook of X Ray Photoelectron Spectroscopy*, Perkin-Elmer Corporation (Minnesota, 1979).
15. K.W. Kolasinski, *Surface Science: Foundations of Catalysis and Nanoscience*, 2nd Ed., John Wiley & Sons (Chichester, 2008).

16. W.T. Mason, *Fluorescent and Luminescent Probes for Biological Activity, A Practical Guide to Technology for Quantitative Real-Time Analysis*, 2nd Ed., Academic Press (London, 1999).
17. D.V. Rosse, *Focus on Materials Science Research*, Nova Science Publishers (New York, 2007)
18. Ultraviolet–visible spectroscopy [online]
http://en.wikipedia.org/wiki/Ultraviolet%E2%80%93visible_spectroscopy
19. F. Rouessac, A. Rouessac, *Chemical analysis: modern instrumentation methods and techniques*, John Wiley & Sons (Chichester, 2004)
20. J.R. Meyer-Arendt, *Introduction to Classical and Modern Optics*, 4th Ed., Prentice Hall (Englewood Cliffs, 1995).
21. N. Kavcar, *Solar Energy Materials and Solar Cells* **52** (1998) 183-195.
22. B. Bhattacharjee, D. Ganguli, K. Iakoubovskii, A. Stesmans and S. Chaudhuri, *Bull. Mater. Sci.* **25** (2002) 175-180.
23. W.M. Yen, S. Shionoya and H. Yamamoto, *Measurements of Phosphor Properties*, Taylor & Francis Group (New York, 2007).
24. Scanning probe microscopy [online]
http://www.brucherseifer.com/html/scanning_probe_microscopy.html
25. S. Hofmann, G. Ertl, H. Lüth and D. L. Mills, *Auger- and X-Ray Photoelectron Spectroscopy in Materials Science*, Springer (Heidelberg, 2012).
26. D.R. Vij, *Handbook of Applied Solid State Spectroscopy*, Springer Media (New York, 2006).
27. R. Eason, *Pulsed Laser Deposition of Thin Films*, John Wiley & Sons (Hoboken, 2007).
28. ECE Pulsed Laser Deposition [online]
<https://www.egr.msu.edu/eceshop/testingfacility/laser/>
29. H. Morkoç and Ü. Özgür, *Zinc Oxide Fundamentals, Materials and Device Technology*, Wiley (Weinheim, 2009).
30. G. Korotcenkov, *Chemical Sensors Fundamentals of sensing materials, volume 1: General approaches*, Momentum Press (New York, 2010).
31. M.A. Herman, W. Richter and H. Sitter, *Epitaxy, Physical Principles and Technical Implementation*, Springer (Berlin, 2004).
32. N. Sahu, B Parija and S. Panigrahi, *Indian J. Phys.* **83** (2009) 493-502.

33. S. Franssila, *Introduction to Microfabrication*, 2nd Ed., John Wiley & Sons (Chichester, 2010).
34. The Key Stages in Spin Coating [online]
<http://www.smartcoater.com/1/category/spin%20coating%20models/1.html>
35. A.M. Taleb, W.A.A. Twej, B.T. Chia and A.J.H. Al-wattar, *African Physical Review* **3** (2009) 117-124.
36. L.C. Klein, *Sol-Gel Optics: Processing and Applications*, Springer (Murray Hill, 1994).

4 Luminescence of Ce doped MgAl_2O_4 prepared by the combustion method

4.1 Introduction

Spinel oxides find many applications as magnetic, electric, ceramic, catalysis and optical materials. They have the formula AB_2O_4 , where A and B represent divalent and trivalent cations respectively [1] and belong to the cubic space group $Fd\bar{3}m$ [2]. The arrangement of Mg, Al and O atoms in the magnesium aluminate (MgAl_2O_4) is shown in figures 4.1 and 4.2, as drawn with the Diamond crystal software [3]. Figure 4.1 shows the unit cell and figure 4.2 shows the cations coordination. The cations occupy twice the number of octahedral sites as tetrahedral sites and in the normal spinel arrangement these are occupied by Al^{3+} and Mg^{2+} ions respectively.

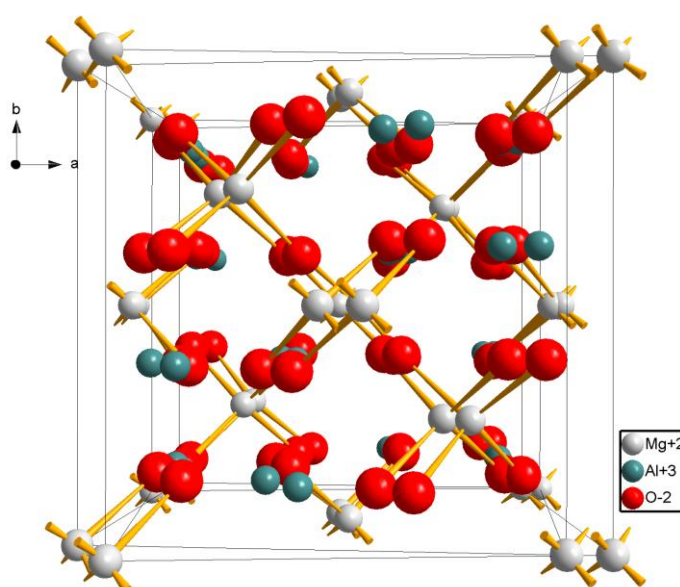


Figure 4.1: Spinel structure of MgAl_2O_4 . Oxygen anions are represented as red spheres, Al^{3+} cations as blue spheres and Mg^{2+} cations as grey spheres.

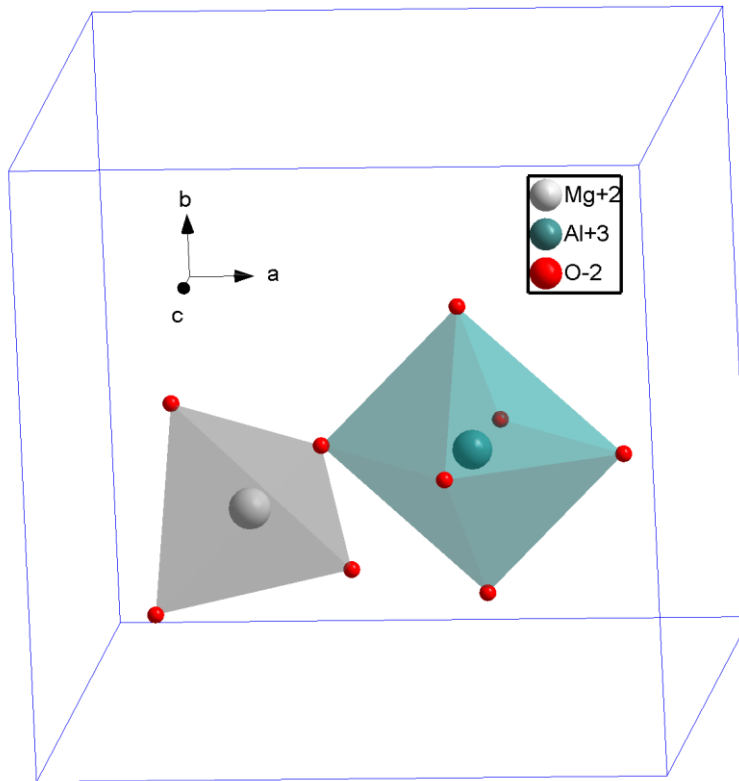


Figure 4.2: Octahedral sites of Al³⁺ cations and tetrahedral sites of Mg²⁺ cations in the normal spinel structure.

MgAl₂O₄ has received a great deal of attention as a technologically important material because of its mechanical strength, chemical inertness, wide bandgap (6.8 eV), relatively low density, high melting point (2105 °C), high thermal shock resistance, low thermal expansion coefficient, resistance to neutron irradiation and low dielectric loss [4,5]. It has been employed in several applications, such as humidity sensors [6] and tuneable solid-state lasers [7]. MgAl₂O₄ has also been assessed as a phosphor host doped with Tb [8, 9], Eu [10,11], Ti [12], V [13], Cr [14] and Mn [15] ions. Long afterglow emission from defects in MgAl₂O₄ was reported to be enhanced by doping with Ce [16]. Ce is an important activator for phosphors e.g. YAG:Ce [17], SiO₂:Ce [18], ZnAl₂O₄:Ce,Tb [19] and Dorenbos [20] has collected the emission properties in many hosts since knowledge

about the Ce luminescence can be extrapolated to other lanthanide ions. There are many methods to prepare spinel powders, such as solid-state reaction [21], precipitation [22], hydrothermal synthesis [23], sol-gel methods [24], co-precipitation [25], and the combustion or microwave combustion methods [26]. Combustion synthesis occurs via a highly exothermic redox reaction between metal nitrates and an organic fuel. This technique can produce a homogenous product in a short amount of time without using expensive high temperature furnaces and has been used to prepare new nanocrystalline phosphor powders $\text{MgAl}_2\text{O}_4:\text{Ce}^{3+}$ with different concentrations of Ce from 0.25 to 2 mol%.

4.2 Materials and methods

MgAl_2O_4 was prepared from analytical grade magnesium nitrate $\text{Mg}(\text{NO}_3)_2 \cdot 6\text{H}_2\text{O}$, aluminium nitrate $\text{Al}(\text{NO}_3)_3 \cdot 9\text{H}_2\text{O}$ and urea ($\text{CH}_4\text{N}_2\text{O}$). Approximately 10 mmol of aluminium nitrate was added to stoichiometric amounts of the other reactants in about 6 ml of distilled water, which was stirred vigorously for 30 min to obtain a homogeneous transparent solution. The transparent solution of reagents was transferred into a porcelain crucible which was placed in a muffle furnace maintained at 520 °C. Within a few minutes the water boiled off and the sample ignited as the exothermic combustion reaction occurred, giving off copious quantities of gas and heating the material to well above the furnace temperature. After the reaction the foamy white product was removed from the furnace and, after cooling to room temperature, it was crushed into powder using a pestle and mortar. Doping of samples with Ce ions was achieved by replacing an appropriate amount of aluminium nitrate with the same amount of cerium nitrate $\text{Ce}(\text{NO}_3)_3 \cdot 6\text{H}_2\text{O}$. The size (inter-ion distance) of the tetrahedral and octahedral sites in MgAl_2O_4 , shown in figure

4.2, are given by $\sqrt{3}(u - 0.125)a$ and $(3u^2 - 2u + 0.375)^{1/2}a$ respectively, where u is called the oxygen parameter [27]. When $u = 0.25$ the oxygen anions form a perfect cubic close packed array and the octahedral size is 15.5% larger, but for increasing u the oxygen atoms shift along the [111] direction in the unit cell so as to increase the size of the tetrahedral sites at the expense of the octahedral sites, until at $u = 0.2625$ these are equal. This is almost identical to the oxygen parameter for MgAl_2O_4 ($u = 0.2624$) showing that the size of the two sites in this material are very similar. In spinels, Mg^{2+} in a tetrahedral site has a radius of 58.5 pm, while Al^{3+} in an octahedral site has a radius of 53 pm [28], both of which are small compared to the ionic radii of lanthanide ions, like Ce^{3+} (103.4 pm). It is therefore unclear where dopant ions will be incorporated in the lattice, but from an analysis of Eu^{3+} emission in MgAl_2O_4 , Singh *et al.* [11] concluded that the Eu^{3+} ions probably occupied the octahedral Al^{3+} sites and we assume the same for Ce^{3+} ions. Further annealing of the as-prepared samples was carried out in air at 1400 °C or a reducing atmosphere of 4% H_2 in Ar at 1300 °C or 1400 °C for 5 h.

X-ray diffraction (XRD) measurements were made at room temperature using a Bruker D8 Advance diffractometer (40 kV, 40 mA) with Cu $K\alpha$ x-rays (154.06 pm). Scanning electron microscope (SEM) images of the particle morphology were obtained using a Shimadzu SSX-550 and a PHI 700 NanoSAM. Luminescence properties were measured using a Cary Eclipse fluorescence spectrophotometer and diffuse reflection spectra were measured using a Lambda 950 UV-Vis spectrophotometer, using spectralon as a reference material. X-ray photoelectron spectroscopy (XPS) was used to characterize the valance state of Ce ions in the phosphor before and after reducing in H_2 . The XPS analysis was carried out with a PHI 5000 Versaprobe using monochromatic Al $K\alpha$ radiation ($h\nu = 1486.6$ eV) and analysed with Multipack v8.2c software. The binding energies were

calibrated by taking the C1s peak (284.6 eV) of adventitious carbon as reference and charging was minimized by using a low energy electron flood gun. Some spectra were taken after sputtering the surface with an Ar ion gun (2 kV, 2 μ A, 1 mm x 1 mm raster) to reduce the amount of adventitious carbon.

4.3 Results and Discussion

4.3.1 Structure and morphology

The XRD spectra of the powders, as-prepared by the combustion method or after further heat treatment at 1400 °C for 5 h, are shown in figure 4.3(a). They match the expected data for MgAl₂O₄ (JCPDS 74-1132), with the main peak of the cubic structure corresponding to the crystal plane with Miller indices {311} at $2\theta = 36.86^\circ$ for the undoped samples. The average crystallite size D was estimated from the full-width at half-maximum β of the diffraction peaks at angle θ by using the Scherrer equation $D = 0.9\lambda/(\beta\cos\theta)$, where λ is the x-ray wavelength and found to be ~25 nm for the as-prepared powder, but this increased to ~65 nm after further heat-treatment. When the MgAl₂O₄ is doped with Ce, figure 4.3(b) shows that the {311} XRD peaks shift slightly to lower 2θ values. This corresponds to an increase in the lattice parameter from 0.808 nm in the undoped samples to 0.814 nm in the 1 mol% Ce doped samples, which is understandable since the ionic size of Ce is much larger than that of Al, and indicates that Ce is successfully incorporated in the lattice.

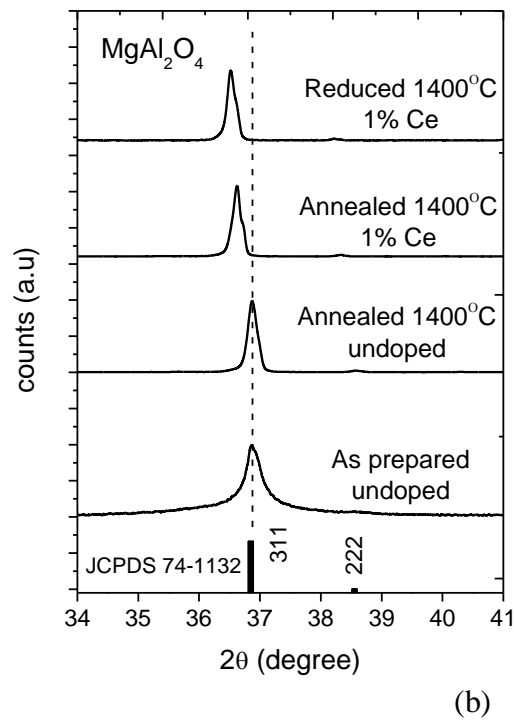
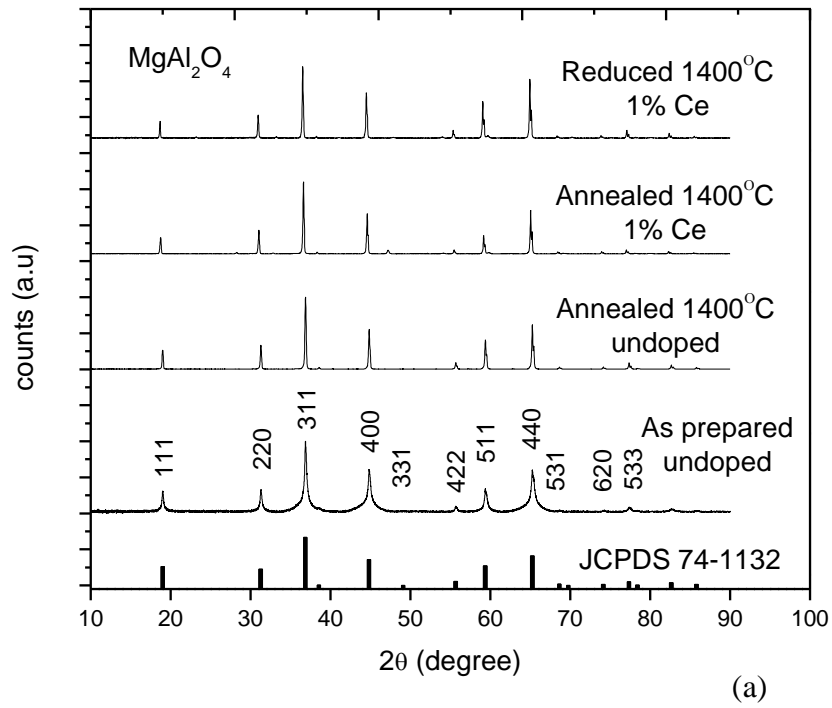


Figure 4.3: (a) XRD spectra of MgAl₂O₄ phosphor powders. (b) Detail of the 311 peak.

The SEM image in figure 4.4(a) shows the as-prepared (undoped) MgAl_2O_4 produced with the combustion process after grinding with a mortar and pestle. This results in irregular shaped particles ranging in size from less than a micron to several tens of microns. Figure 4.4(b) shows a higher magnification image of a fractured particle surface from a different region in which several pores occur. Such pores can also be seen in the large particle in the bottom right of figure 4.4(a) and are found in materials produced using combustion synthesis because of the evolution of a great quantity of gas during the process. Figure 4.4(c) shows the as-prepared sample doped with 0.75 mol% Ce, which has a similar morphology as the undoped sample (figure 4.4(a)).

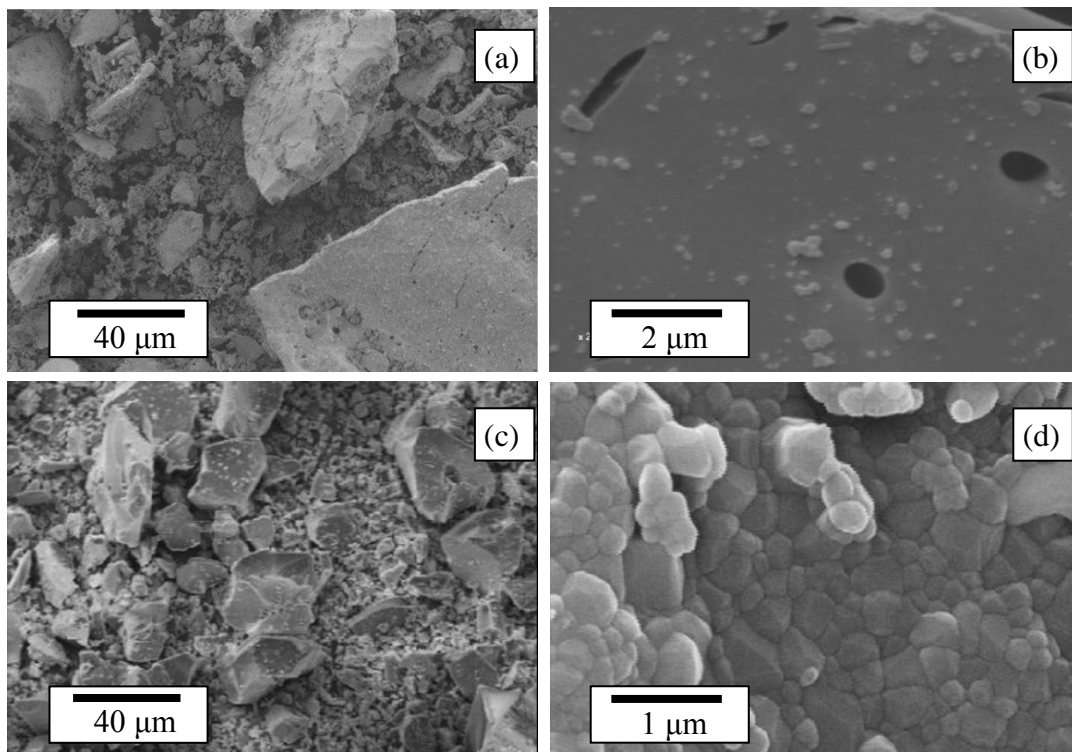


Figure 4.4: SEM images MgAl_2O_4 powders obtained by the combustion method: (a, b) As prepared, undoped. (c) As prepared, doped 0.75 mol% Ce. (d) Reduced at 1400 $^{\circ}\text{C}$ for 5 h, doped 0.75 mol% Ce.

The image in figure 4.4(d) shows a sample that has been reduced at 1400 °C for 5 h. The surface is faceted and it appears that grain growth has occurred. These grains are less than a micron in size, but nevertheless much larger than the ~65 nm crystallite size estimated from the XRD results, indicating that the grains consist of smaller crystallites.

4.3.2 Optical properties

As prepared MgAl_2O_4 samples doped with Ce, as well as those subsequently annealed in air up to a temperature of 1400 °C did not show any luminescence. Since it is possible for Ce to take on the tetravalent charge state (Ce^{4+}) which is non-luminescent, instead of the luminescent trivalent (Ce^{3+}) state, this prompted us to anneal the samples in a reducing atmosphere of 4% H_2 in Ar. From these reduced samples green fluorescence in a broad band centred at 490 nm was obtained as shown in figure 4.5. The excitation and emission of Ce^{3+} ions occur through allowed f-d transitions, the energy (and therefore wavelength) of which are host dependent. For example, Ce emission in YAlO_3 occurs at 345 nm while in $\text{Y}_3\text{Al}_5\text{O}_{12}$ it occurs at 535 nm [20]. In this work the luminescence at 490 nm is attributed to the transition of electrons excited to the 5d level returning to the $^2\text{F}_{7/2}$ and $^2\text{F}_{5/2}$ states of the 4f level, although the peaks corresponding to the two final states are not resolved. The excitation spectra show a number of peaks in the range 300-400 nm. The 5d-level of Ce generally splits into five states, so one can expect a corresponding number of possible f-d excitation bands. The inset of figure 4.5 shows the emission intensity as a function of Ce doping concentration, with the maximum occurring for 0.75 mol%.

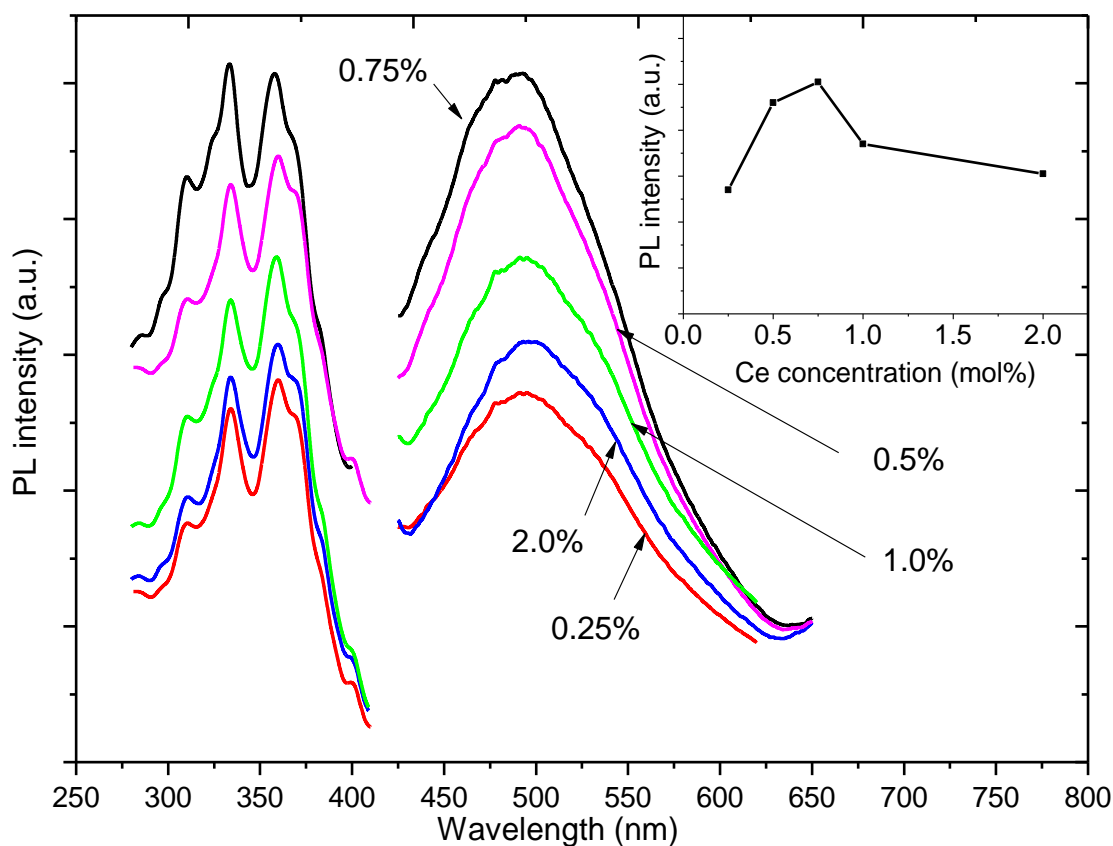


Figure 4.5: Room temperature luminescence spectra of $\text{MgAl}_2\text{O}_4:\text{Ce}^{3+}$ reduced for 5 h at 1400 °C, measured with the Cary Eclipse fluorescence spectrophotometer. The inset shows the luminescence peak intensity as a function of Ce doping concentration.

UV-vis diffuse reflection spectroscopy was used to study the absorption characteristics of MgAl_2O_4 and the effects of Ce doping as well as the annealing process. Figure 4.6(a) compares the diffuse reflectance spectra of the different samples. For the undoped host (as-prepared) the reflectance remains high even for very short wavelengths, and the host only begins to absorb below 300 nm.

The reflectivity R can be transformed into a value proportional to the absorption using the Kubelka-Munk function $K = (1 - R)^2 / (2R)$, and the Tauc plot of $(Kh\nu)^n$ against $h\nu$ (with $n = 2$, applicable for a direct bandgap material) is given in figure 4.6(b), from which the optical bandgap is estimated to be 5.85 eV. When 2 mol% Ce is incorporated in the as-prepared material the reflectance spectrum changes dramatically, with absorption occurring at much longer wavelengths. The change in reflectivity can be attributed to the Ce dopant, but not to Ce^{3+} ions since this sample is not luminescent. Ce^{4+} ions in the sample are expected to have a broad absorption band due to charge transfer between Ce^{4+} and O^{2-} ions which can account for the decreased reflectivity [29]. Samples annealed in air at 1400 °C as well as those reduced at 1300 °C show similar reflectivity curves, indicating that Ce remains in the form of tetravalent ions in these samples. However, by reducing the material at 1400 °C one obtains a change in the reflectivity and absorption peaks appear in the range 250-380 nm.

From the present data, there is not an obvious correlation between the PL excitation peaks (figure 4.5) and the troughs of reflectivity (figure 4.6(a)), but the change in reflectivity spectrum indicates that part of the Ce^{4+} ions have been converted to Ce^{3+} ions. This was further investigated and confirmed with XPS measurements.

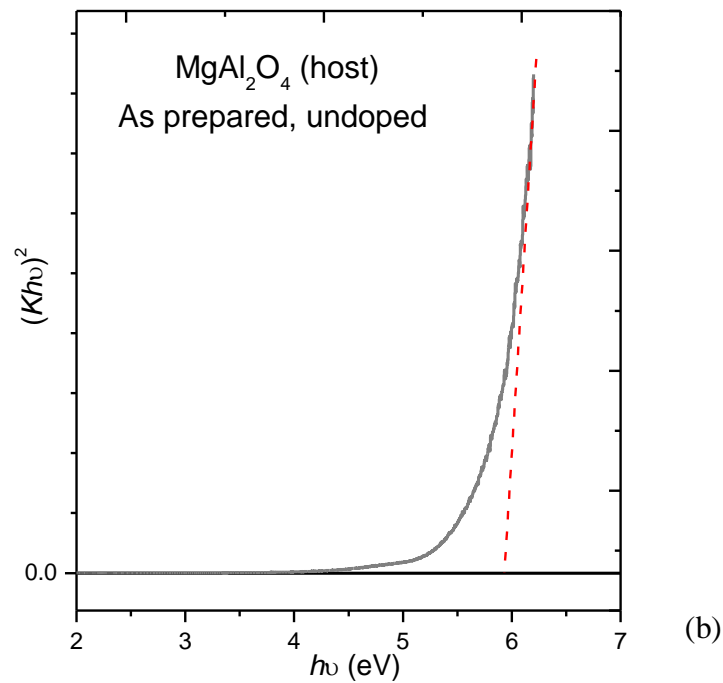
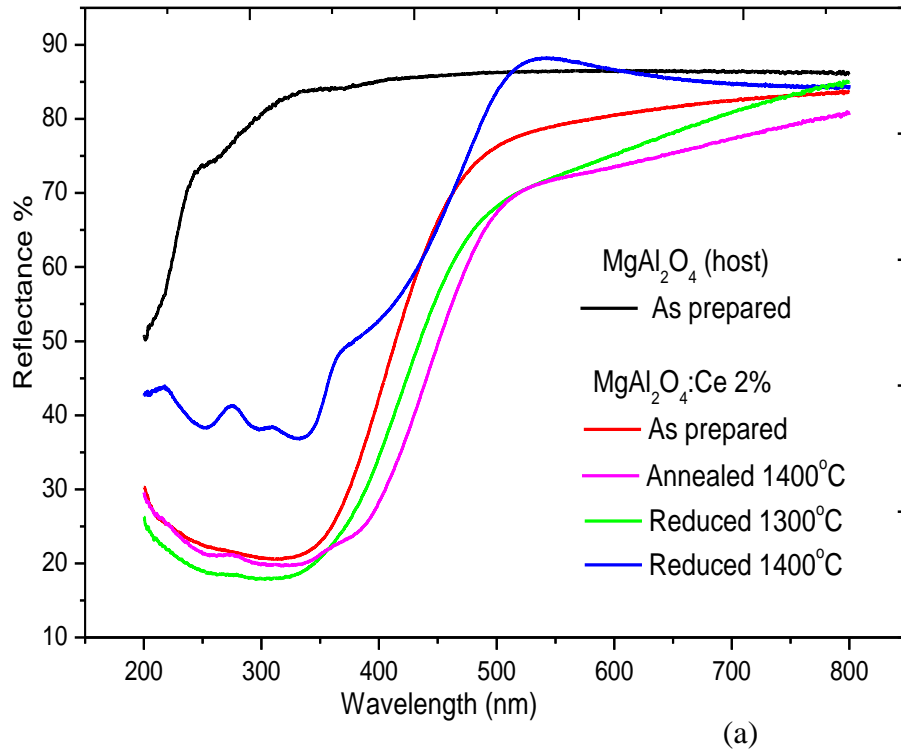


Figure 4.6: (a) Diffuse reflectance spectra of MgAl_2O_4 samples. (b) Estimate of the direct optical bandgap of undoped MgAl_2O_4 host using Kubelka-Munk function.

4.4 XPS measurements of the charge state of Ce

Although optimum luminescence was obtained by doping MgAl_2O_4 with 0.75 mol% Ce, measuring such a low concentration of Ce with XPS is difficult and so samples for XPS analysis were doped with 2 mol% Ce. Figure 4.7 shows an XPS survey scan for binding energy up to 1400 eV of such a sample after reducing at 1400 °C for 5 h, with the peaks corresponding to Mg, Al, O and Ce labelled, as well as the C1s peak due to adventitious carbon.

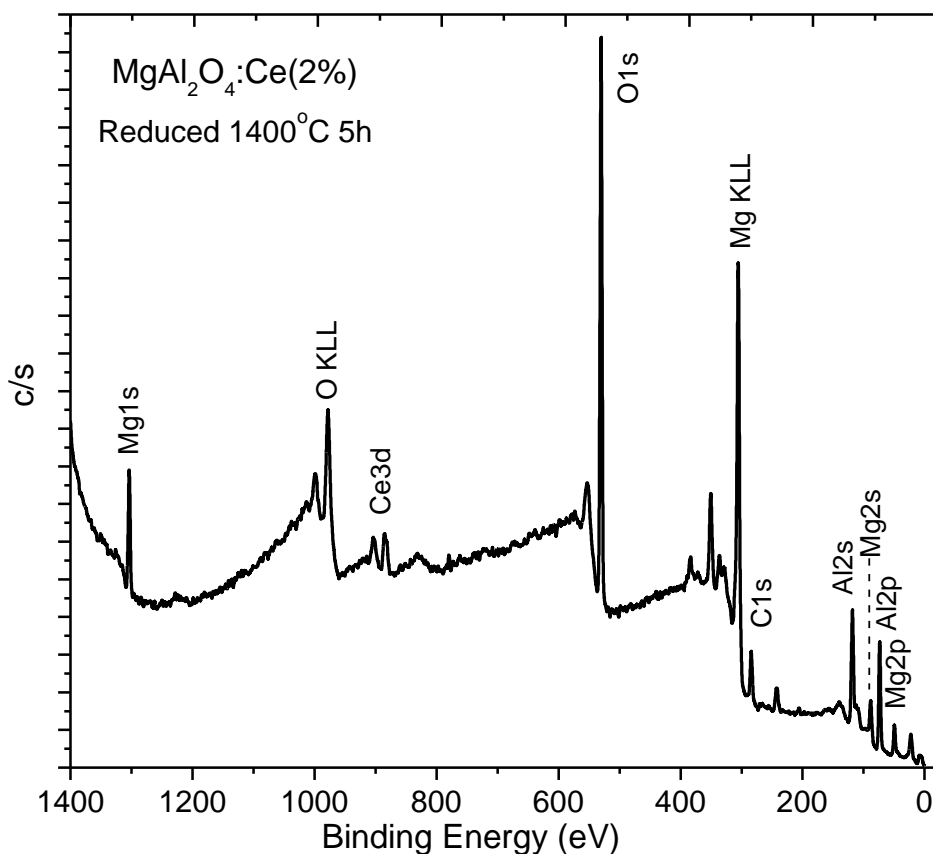


Figure 4.7: XPS survey scan of Ce doped MgAl_2O_4 reduced at 1400 °C for 5 h.

Figure 4.8 shows high resolution XPS scans of the Ce 3d peaks under various conditions. In general, the peaks associated with electrons emitted from orbitals having non-zero

orbital angular momentum (with $\ell > 0$, i.e. p, d and f levels) occur as doublets due to spin-orbit splitting, with the area under the peaks having the ratio $\ell : \ell + 1$. Specifically for d orbitals ($\ell = 2$), the $d_{3/2}$ peak occurs at a higher binding energy than the $d_{5/2}$ peak and its area is $2/3$ the size. This is the case for pure metallic Ce (not shown) where the binding energy of the $d_{3/2}$ peak is 901.9 eV while the binding energy of the $d_{5/2}$ peak is 883.8 eV, giving a split of 18.1 eV [30].

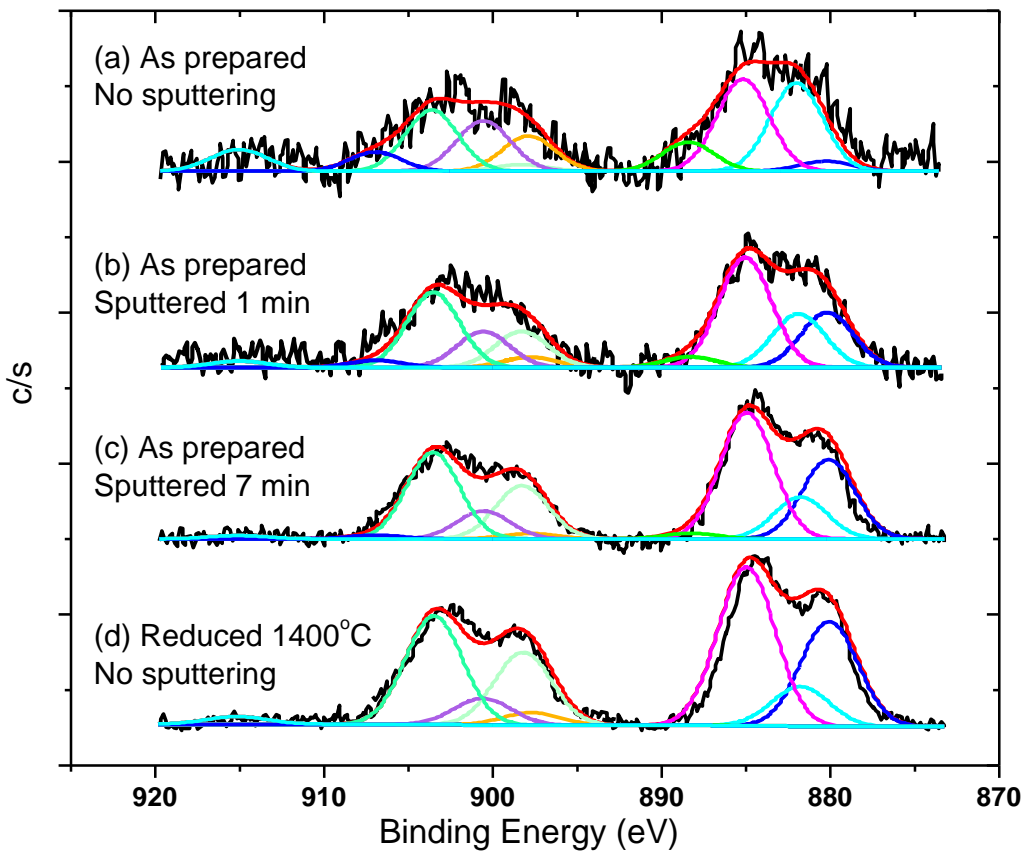


Figure 4.8: XPS high resolution scans of the Ce peaks in as-prepared $\text{MgAl}_2\text{O}_4:\text{Ce}$ samples for different sputtering times, and after reducing.

However, the Ce 3d XPS spectrum in Ce compounds is considerably more complicated and is composed of up to five spin-orbit doublets, three of which are associated with Ce⁴⁺ ions and two of which are associated with Ce³⁺ ions [31]. The reason for multiple doublets in both cases is hybridization of the 4f orbitals (with conduction electrons in the case of metals, or ligand ion orbitals in the case of insulators) resulting in multiple 4f configurations which affect the 3d electron binding energies. For Ce⁴⁺ ions there are doublets for the Ce(IV) 4f⁰, 4f¹ and 4f² configurations, while for Ce³⁺ ions (having an additional electron) there are doublets for the Ce(III) 4f¹ and 4f² configurations. In MgAl₂O₄:Ce, the five Ce 3d XPS doublets are due to hybridization of the Ce 4f orbitals with the O 2p orbitals of the MgAl₂O₄ host, and are listed in Table 4.1. Although the Ce 3d XPS spectra therefore provide information on the Ce charge state, quantification of the ratio of Ce³⁺ to Ce⁴⁺ ions is not an easy task. Different approaches have been summarized by Skála *et al.* [32] and recently Papparazzo [33] has pointed out the importance of physically meaningful and consistent curve-fitting in addition to obtaining good fits to experimental data. Considering these difficulties, which are significant when working with Ce compounds such as CeO₂, it is a challenge to apply the theory to dopant levels of Ce in MgAl₂O₄. After background subtraction with the Shirley method, spectra were fitted simply with Gaussian peaks, keeping the peak positions and FWHMs fixed, as well as maintaining the 2:3 ratio of the area of the spin-orbit split peaks. Although numerical results are given, these should rather be interpreted qualitatively than quantitatively. Figure 4.8(a) shows the Ce 3d peaks of the as-prepared sample. The corresponding data for the fit in Table 4.1 shows that the sample contains 62% Ce⁴⁺ and 38% Ce³⁺ ions.

Figure 4.8(b) and (c) show the spectra of the same sample after 1 and 7 min of Ar ion sputtering respectively, which was done to reduce the adventitious carbon on the sample.

Although sputtering improves the quality (signal-to-noise ratio) of the XPS spectra, there is also a change in the form of the peaks and the fitting data in table 4.1 reveals that as sputtering continues there is a very significant increase in the proportion of Ce^{3+} ions, from 38% in the unsputtered sample to 62% after 1 min of sputtering and 79% after 7 min of sputtering. Although this may suggest the possibility that Ce^{4+} dominates near the surface and that Ce^{3+} occurs below the surface, the photoluminescence and diffuse reflectivity results which are not surface sensitive indicate that Ce is not in the trivalent charge state. Instead, the increasing proportion of Ce^{3+} with sputtering is consistent with previous results that Ce^{4+} can be reduced to Ce^{3+} by means of Ar ion sputtering as well as x-ray irradiation and heating in a vacuum [34]. For this reason, samples used for evaluating the relative proportion of trivalent and tetravalent Ce ions should not be sputter cleaned and, even then, the percentage of Ce^{4+} might be lowered by the XPS x-ray source and should be considered as a lower bound rather than an actual value. This could explain why, although the as-prepared sample shows only 68% Ce^{4+} , no luminescence is obtained from the sample implying almost all the Ce is in the tetravalent charge state. Figure 4.8(d) shows the Ce peaks of the unsputtered sample which has undergone reducing for 5 h at 1400 °C. The peak near 916 eV associated with Ce^{4+} ions does not occur in this sample, and the fitting results in Table 4.1 show that the proportion of Ce^{3+} ions is 84% after the reducing process, compared to 38% for the unsputtered as-prepared sample. The photoluminescence, diffuse reflectance and XPS data therefore all indicate that Ce^{4+} ions are converted to Ce^{3+} ions only after the high temperature reducing treatment, which then results in luminescence from Ce^{3+} for those samples.

Table 4.1: Fitting data for XPS Ce 3d peaks. The area ratio for each spin-orbit doublet is fixed as 2:3 and the FWHM as 3.7 eV. The percentages are for the doublet area compared to the total area under all the peaks.

	Ce⁴⁺			Ce³⁺	
	Ce ⁴⁺ (3d ⁹ 4f ⁰)O(2p ⁶)	Ce ⁴⁺ (3d ⁹ 4f ¹)O(2p ⁵)	Ce ⁴⁺ (3d ⁹ 4f ²)O(2p ⁴)	Ce ³⁺ (3d ⁹ 4f ¹)O(2p ⁶)	Ce ³⁺ (3d ⁹ 4f ²)O(2p ⁵)
BE d _{3/2} (eV)	898.3	888.7	882.2	880.4	885.4
BE d _{5/2} (eV)	915.7	907.5	901.0	898.7	903.8
Spin-orbit splitting (eV)	17.4	18.8	18.8	18.3	18.4
As-prepared: no sputtering	14%	12%	36%	4%	34%
	Ce ⁴⁺ total: 62%			Ce ³⁺ total: 38%	
As-prepared: 1 min sputter	7%	6%	25%	20%	42%
	Ce ⁴⁺ total: 38%			Ce ³⁺ total: 62%	
As-prepared: 7 min sputter	2%	2%	17%	30%	49%
	Ce ⁴⁺ total: 21%			Ce ³⁺ total: 79%	
Reduced: no sputtering	4%	0%	12%	33%	51%
	Ce ⁴⁺ total: 16%			Ce ³⁺ total: 84%	

It is also valuable to consider the contributions that the different hybridization states make to the total Ce³⁺ and Ce⁴⁺ total peak area percentages. In all cases the 4f² configurations have the largest percentage (i.e. they correspond to the biggest XPS peaks), showing that both the trivalent and tetravalent ions are being strongly influenced by their bonding to oxygen. This is understandable considering the large relative size of the Ce ions compared to the octahedral and tetrahedral sites in the lattice. Although for the as-prepared unsputtered sample the total Ce³⁺ proportion was 38%, only 4% is attributed to the Ce³⁺(3d⁹4f¹)O(2p⁶) configuration while the rest is associated with the Ce³⁺(3d⁹4f²)O(2p⁵) configuration. In the latter configuration the Ce³⁺ ion's 4f electron orbitals are strongly influenced by the oxygen 2p orbitals, which may influence the Ce 4f-4d transitions and render this configuration non-luminescent. The photoluminescence results should then be compared only to the percentages for the Ce³⁺(3d⁹4f¹)O(2p⁶) configuration, for which

there is a good correlation. For the reduced samples only 16% of the Ce is in the tetravalent state, but the large proportion of Ce in the $Ce^{3+}(3d^94f^2)O(2p^5)$ configuration (51%), which is strongly influenced by the oxygen 2p orbitals and appears to be non-luminescent, limits the potential optical applications for Ce luminescence in this host.

4.5 Conclusion

Ce doped $MgAl_2O_4$ has been successfully synthesized by the combustion method. XRD showed that the Ce is successfully incorporated in the lattice. However, the samples only show luminescence after further high temperature heat treatment in a reducing atmosphere. The green emission intensity was measured as a function of Ce doping concentration, with the maximum occurring for 0.75 mol%. UV-vis diffuse reflectance spectroscopy and XPS results provide evidence that the reducing heat treatment is required to convert Ce from the non-luminescent Ce^{4+} oxidation state to the luminescent Ce^{3+} oxidation state. There are two XPS doublets associated with the Ce^{3+} ions but the results indicate a correlation of the Ce luminescence intensity with only the $Ce^{3+}(3d^94f^1)O(2p^6)$ configuration, suggesting that the $Ce^{3+}(3d^94f^2)O(2p^5)$ configuration for which the Ce^{3+} ion's 4f electron orbitals are strongly influenced by the oxygen 2p orbitals may be non-luminescent.

4.6 References

1. R.C. Ropp, *Luminescence and the Solid State*, 2nd Ed, Elsevier (Amsterdam, 2004).
2. D. Levy, A. Pavese and M. Hanfland, *Am. Mineral.* **88** (2003) 93-98.
3. Diamond - Crystal and Molecular Structure Visualization. [online]
<http://www.crystalimpact.com/diamond>
4. J. Xiaolin, Z. Haijun, Y. Yongjie and L. Zhanjie, *Mater. Sci. Eng, A* **379** (2004) 112-118.

5. S. Roy, N. Vegten and A. Baiker, *J. Catalysis* **271** (2010) 125-131.
6. O. Shpotyuk, A. Ingram, H. Klym, M. Vakiv, I. Hadzaman and J. Filipecki, *J. Eur. Ceram. Soc.* **25** (2005) 2981-2984.
7. A. Jouini, A. Yoshikawa, Y. Guyot, A. Brenier, T. Fukuda and G. Boulon, *Opt. Mater. (Amsterdam, Neth.)* **30** (2007) 47-49.
8. I. Omkaram, G. Seeta Rama Raju and S. Buddhudu, *J. Phys. Chem. Solids* **69** (2008) 2066-2069.
9. R.J. Wiglusz and T. Grzyb, *Opt. Mater. (Amsterdam, Neth.)* **33** (2011) 1506-1513.
10. X. Chen, C. Ma and S. Bao, *Solid State Sci.* **12** (2010) 857-863.
11. V. Singh, M.M. Haque and D. Kim, *J. Bull. Korean Chem. Soc.* **28**(12) (2007) 2477.
12. T. Sato, M. Shiraib, K. Tanakab, Y. Kawabea and E. Hanamur, *J. Lumin.* **114** (2005) 155-161.
13. Y. Fujimoto, H. Tanno, K. Izumi, S. Yoshida, S. Miyazaki, M. Shirai, K. Tanaka, Y. Kawabe and E. Hanamura, *J. Lumin.* **128** (2008) 282-286.
14. P. Gluchowski, R. Pazik, D. Hreniak and W. Strek, *Chem. Phys.* **358** (2009) 52-56.
15. J. Lin, Y. Huang, J. Zhang, F. Shi, S. Wei, J. Gao, X. Ding and C. Tang, *Mater. Res. Bull.* **44** (2009) 106-109.
16. D. Jia and W.M. Yen, *J. Lumin.* **101** (2003) 115-121.
17. H. Lee, C. Cheng and C. Huang, *Mater. Res. Bull.* **44** (2009) 1081-1085.
18. R.E. Kroon, H.A.A. Seed Ahmed, O.M. Ntwaeaborwa, L.F.Koao, I.M.Nagpure, M.A. Gusowski, J.R. Botha and H.C. Swart, *Phys. B (Amsterdam, Neth.)* **407** (2012) 1595-1598.
19. K.G. Tshabalala, S-H. Cho, J-K. Park, S.S. Pitale, I.M. Nagpure, R.E. Kroon, H.C. Swart and O.M. Ntwaeaborwa, *J. Alloys Compd.* **509** (2011) 10115.
20. P. Dorenbos, *J. Lumin.* **91** (2000) 155-176.

21. N. Kashii, H. Maekawa and Y. Hinatsu, *J. Am. Ceram. Soc.* **82** (1999) 1844-1848.
22. E.N. Alvar, M. Rezaei and H.N. Alvar, *Powder Technol.* **198** (2010) 275-278.
23. M.M. Amini, M. Mirzaee and N. Sepanj, *Mat. Res. Bull.* **42** (2007) 563-570.
24. S. Rezgui and B.C. Gates, *J. Non-Cryst. Solids* **210** (1997) 287-297.
25. M.M. Rashad, Z.I. Zaki and H. El-Shall, *J. Mater. Sci.* **44** (2009) 2992-2998.
26. R. Ianos and R. Lazau, *Mater. Chem. Phys.* **115** (2009) 645-648.
27. R.J. Hill, J.R. Craig and G.V. Gibbs, *Phys. Chem. Miner.* **4** (1979) 317-339.
28. H.St.C. O'Neal and A. Navrotsky. *Am. Mineral.* **68** (1983) 181-194.
29. C. Weiping, Z. Ye and Z. Lide, *J. Phys.: Condens. Matter* **10** (1998) L473-L477.
30. J.F. Moulder, W.F. Stickle, P.E. Sobol and K.D. Bomben, *Handbook of X-ray Photoelectron Spectroscopy*, ULVAC-PHI (Chigasaki, 1995).
31. S. Bera, V.K. Mittal, R. Krishnan, T. Saravanan, S. Velmurugan, K. Nagarajan and S.V. Narasimhan, *J. Nucl. Mater.* **393** (2009) 120-125.
32. T. Skála, F. Sutara, K. Prince and V. Matolin, *J. Electron Spectrosc. Relat. Phenom.* **169** (2009) 20-25.
33. E. Paparazzo, *Mater. Res. Bull.* **46** (2011) 323-326.
34. J.L.M. Rupp, T. Drobek, A. Rossi and L.J. Gauckler, *Chem. Mater.* **19** (2007) 1134-1142.

5

Blue luminescence from Bi doped MgAl₂O₄ prepared by the combustion method

5.1 Introduction

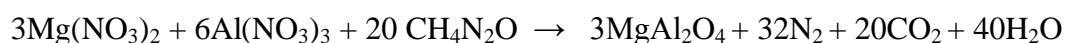
Phosphor materials are widely applied in lighting, displays, lasers and scintillators and it is necessary that the phosphor host exhibits good optical, mechanical and thermal properties. Magnesium aluminate (MgAl₂O₄), corresponding to the mineral spinel, is considered to be an optically inert medium and its chemical and thermal stability increases its attractiveness as a host for luminescent ions [1]. Rare-earth ions are often used as activators for phosphor materials, especially in the trivalent charge state where luminescence is generally due to f-f electron transitions [2,3]. However, metallic impurities with an outer ns² configuration ground state such as Tl⁺, Pb²⁺, Bi³⁺ and Sb³⁺ ions may also be excellent luminescence activators [4]. Bi atoms have an electronic configuration [Xe]4f¹⁴5d¹⁰6s²p³ and Bi³⁺ ions, with outermost 6s² electrons, have been widely used as activators for various host materials including oxides, phosphates, aluminates and borates [5]. The 6s² ground state has a single energy level ¹S₀ while the 6s¹6p¹ excited configuration has energy levels ³P₀, ³P₁, ³P₂ and ¹P₁ in order of increasing energy. Electron transitions between the ¹S₀ ground state and the ³P_J levels are spin forbidden, but optical absorption can occur to the high energy ¹P₁ level. However, spin-orbit coupling between the ¹P₁ and ³P₁ levels makes the lower energy transitions ¹S₀↔³P₁ possible and the luminescence from Bi³⁺ activated phosphors is usually attributed to this transition. In some materials the ¹P₁→¹S₀ emission is also observed [6]. The outer electron orbitals of Bi³⁺ are not shielded (as in the case of the 4f energy levels of trivalent lanthanide ions) so the broad luminescence band shows a

strong dependence on the composition and crystal structure of the host lattice and the emission wavelength is tuneable from the ultraviolet, through blue to green [7].

Spinel powders have been prepared by solid-state reaction [2], precipitation [8], hydrothermal synthesis [3] and sol-gel synthesis [9]. Alternatively, synthesis via the combustion method [10] occurs via a highly exothermic redox reaction between metal nitrates and an organic fuel and this technique can produce a homogenous product in a short amount of time without using expensive high temperature furnaces. This method has been used to prepare novel $\text{MgAl}_2\text{O}_4\text{:Bi}$ nanocrystalline phosphor powders in order to study their optical properties.

5.2 Materials and methods

MgAl_2O_4 was prepared by combustion synthesis using magnesium nitrate $\text{Mg}(\text{NO}_3)_2 \cdot 6\text{H}_2\text{O}$ and aluminium nitrate $\text{Al}(\text{NO}_3)_3 \cdot 9\text{H}_2\text{O}$ as precursors and urea $\text{CH}_4\text{N}_2\text{O}$ as the fuel according to the reaction



where the waters of crystallization of the nitrates have been omitted for simplicity. Either 5 or 10 mmol of aluminium nitrate was added to stoichiometric amounts of the other reactants in about 3 or 6 ml of distilled water, which was stirred vigorously for 30 min to obtain a homogeneous transparent solution. The transparent solution of reagents was transferred into a porcelain crucible which was placed in a muffle furnace maintained at

520 °C. Within a few minutes the water boiled off and the sample ignited as the exothermic combustion reaction occurred, giving off copious quantities of gas and heating the material to well above the furnace temperature. After the reaction the foamy white product was removed from the furnace and, after cooling to room temperature, it was crushed into powder using a pestle and mortar. Doping of samples with Bi ions was achieved by replacing an appropriate amount of aluminium nitrate with the same amount of bismuth nitrate $\text{Bi}(\text{NO}_3)_3 \cdot 5\text{H}_2\text{O}$. In spinel the Al^{3+} ions occupying octahedral sites and the Mg^{2+} ions in tetrahedral sites are both small (effective ionic radii of 53 and 58.5 pm respectively [11]) compared to 6-coordinated Bi^{3+} ions (103 pm [12]). Although the Mg^{2+} ion is the larger of the two, the Al^{3+} ion has the same valence as Bi^{3+} and occupies the octahedral site with higher coordination number (6). From these considerations it appears that Bi^{3+} ions would not easily substitute the host cations, nor if it did which site it would prefer. However, lanthanide ions are also large and since it has been suggested that Eu^{3+} ions occupy the Al^{3+} ions sites in spinel [13], that is the assumption made here. However, it has also been reported that Eu^{3+} ions may occupy the Mg^{2+} sites in spinel [14].

X-ray diffraction (XRD) measurements were made using a Bruker D8 Advance diffractometer (40 kV, 40 mA) with Cu $K\alpha$ x-rays (154.06 pm). Scanning electron microscope (SEM) images of the particle morphology were obtained using a Shimadzu SSX-550 instrument. Diffuse reflection spectra were measured using a Lambda 950 UV–Vis spectrophotometer (with spectralon as a reference material) and photoluminescence (PL) properties were measured using a Cary Eclipse fluorescence spectrophotometer and a 325 nm He-Cd laser.

5.3 Results and discussion

5.3.1 Structure and morphology

The XRD pattern of pure MgAl_2O_4 shown in figure 5.1 matches the standard JCPDS card no. 74-1132 well. The main peak of the cubic structure, corresponding to the crystal plane with Miller indices $\{311\}$, is centred at $2\theta = 36.86^\circ$.

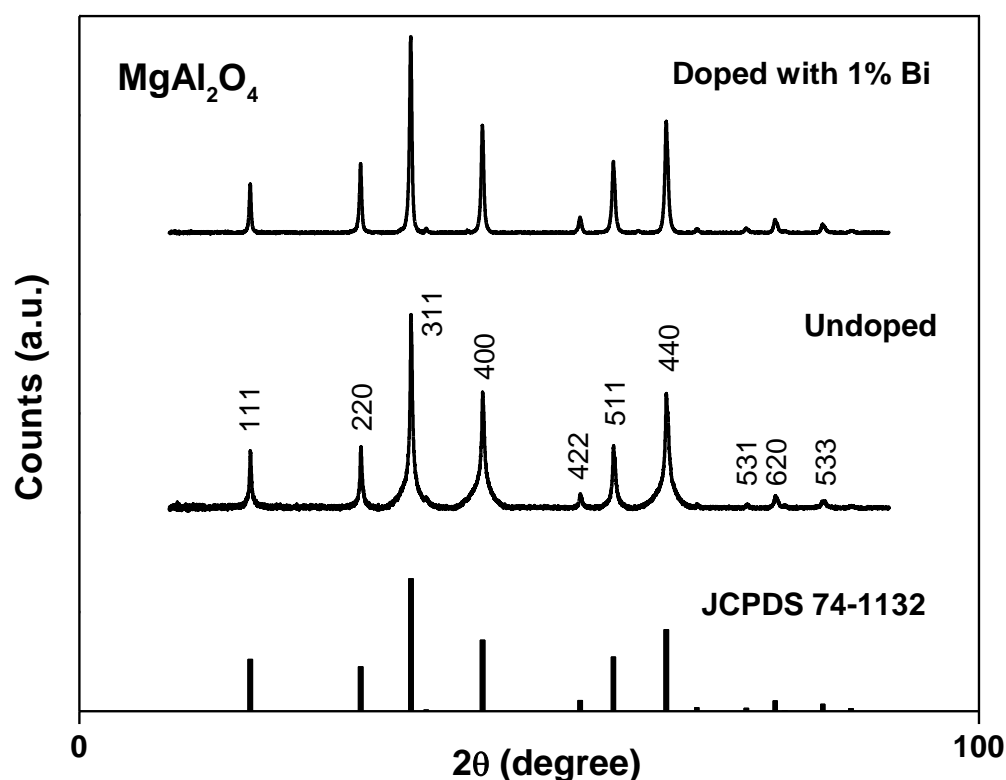


Figure 5.1: X-ray diffraction patterns of MgAl_2O_4 prepared by the combustion method, pure and doped with Bi.

The peaks are not Gaussian in shape, but are superimposed on a broad base (amorphous halo), indicating that the material between the crystallites is in a disordered state. For the sample doped with 1 mol% Bi no extra peaks are observed, nor was a shift of the peak positions detected. However, the peaks are now sharper, so the addition of a small amount

of Bi has produced samples with better crystallinity. Bismuth oxide has a much lower melting point (817 °C) compared to Mg and Al oxides (> 2000 °C). Since the temperature during synthesis is estimated to be near 1500 °C [15], the addition of Bi may act like a flux, thereby improving the crystallinity. The average crystallite size D was estimated from the full-width at half-maximum β of the diffraction peaks at angle θ by using the Scherrer equation $D = \frac{0.9\lambda}{\beta \cos \theta}$ where λ is the x-ray wavelength and was about 25 nm for both the pure and doped samples. This value is approximate only, considering the non-Gaussian peak shape for the undoped sample and possible impurity or strain broadening of the peaks in the doped sample.

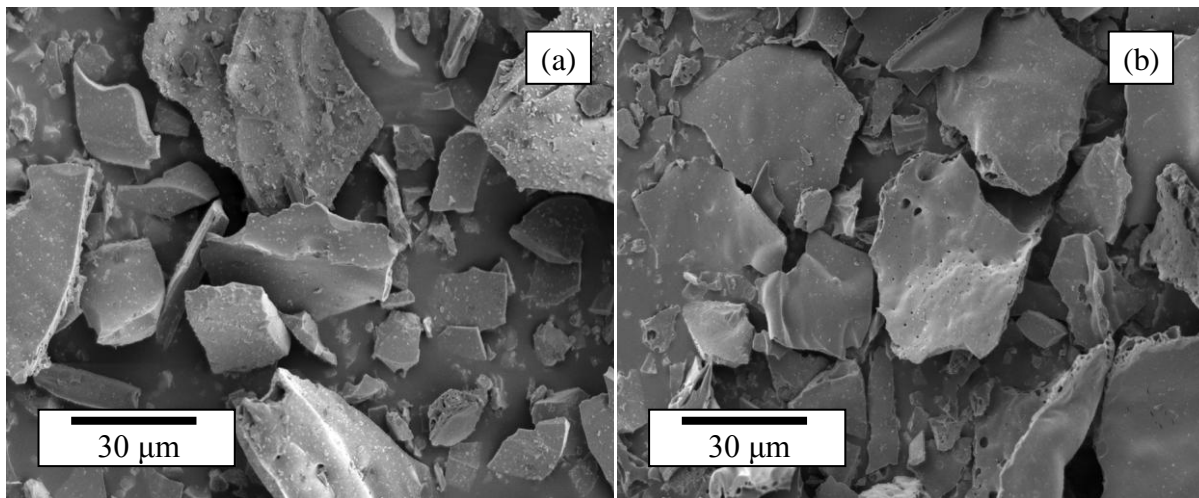


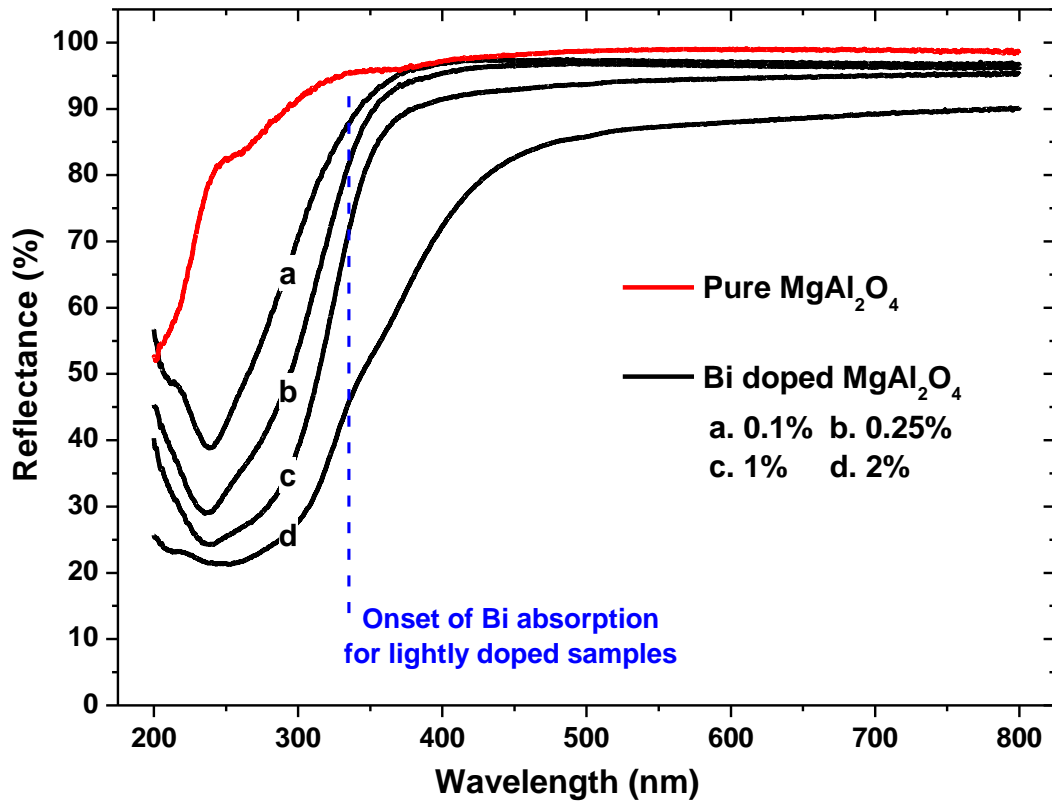
Figure 5.2: SEM images of MgAl_2O_4 powders obtained by the combustion method. (a) Undoped and (b) doped with 0.5 mol% Bi.

The SEM image in figure 5.2(a) shows the morphology of the undoped MgAl_2O_4 particles produced with the combustion process after grinding the foamy product with a mortar and pestle. The particle size varies up to several tens of microns and depends on the amount of grinding, but it is evident that large flat, plate-like particles occur. This is characteristic of material made by combustion synthesis due to the large amount of gas that evolves during

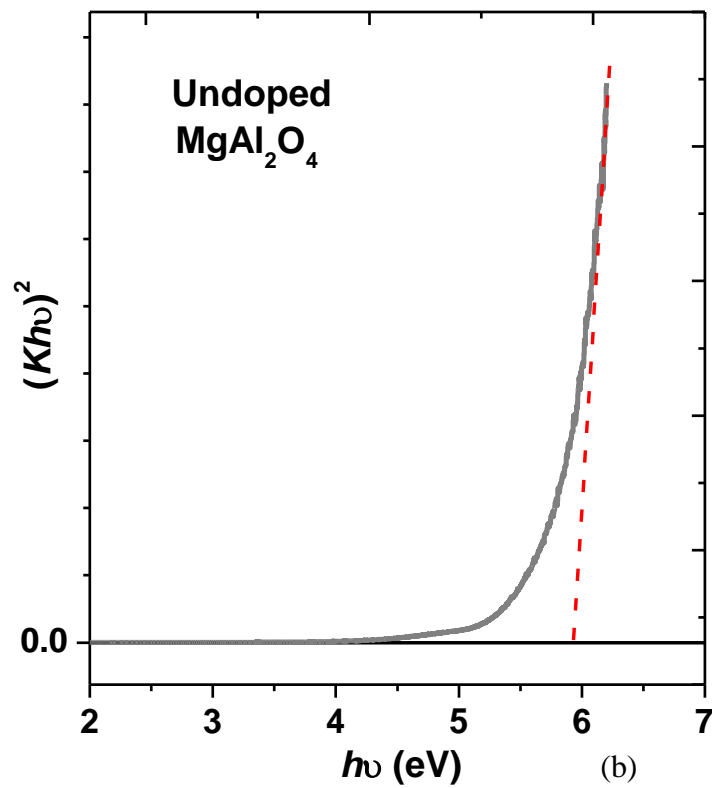
the reaction. The variation in thickness of the plates is due to the non-uniform distribution of temperature and mass flow in the combustion flame. Figure 5.2(b) shows that the sample doped with 0.5 mol% Bi, which has a similar morphology as the undoped sample. These SEM images show several pores in the particles which are formed by the escaping gases during the combustion reaction. These particles are much larger than the crystallite size estimated from the XRD results, indicating that the particles consist of smaller crystallites.

5.3.2 Optical properties

UV-Vis diffuse reflection spectroscopy was used to study the absorption characteristics of MgAl_2O_4 and the effects of Bi dopant measured with the Lambda 950 UV-Vis spectrophotometer at room temperature. Figure 5.3(a) compares the diffuse reflectance spectra of the different samples. For the undoped host (as-prepared) the reflectance remains high even for very short wavelengths, and the host only begins to absorb below 300 nm. The reflectivity R can be transformed into a value proportional to the absorption using the Kubelka-Munk function $K = (1 - R)^2/(2R)$, and the Tauc plot of $(Kh\nu)^n$ against $h\nu$ (with $n = 2$, applicable for a direct bandgap material) is given in Figure 5.3(b), from which the optical bandgap is estimated to be about 5.85 eV. When 1 mol% Bi is incorporated in the as-prepared material the reflectance spectrum changes dramatically, with absorption occurring at much longer wavelengths.



(a)



(b)

Figure 5.3: (a) Diffuse reflectance spectra of MgAl₂O₄ samples. (b) Estimate of the direct optical bandgap of undoped MgAl₂O₄ host using Kubelka-Munk function.

Figure 5.4(a) shows the PL excitation and emission spectra (for excitation with the xenon lamp at 335 nm) for the $\text{MgAl}_2\text{O}_4:\text{Bi}$ (0.5 mol%) measured with the Cary-Eclipse fluorescence spectrophotometer, as well as the emission spectrum obtained when the sample is excited at 325 nm by a He-Cd laser. A single broad band of blue fluorescence emission was observed centred near 400 nm, which has an optimal excitation wavelength of 335 nm. This excitation wavelength corresponds to the onset of absorption in Bi doped MgAl_2O_4 samples as seen in Figure 5.3(a). The excitation and emission are attributed to $^1\text{S}_0 \leftrightarrow ^3\text{P}_1$ transitions of Bi^{3+} ions, with a Stokes shift of 0.60 eV. For comparison, in Bi doped Y_2O_3 two emission bands occur at 410 and 520 nm with Stokes shifts of 0.31 eV and 1.24 eV respectively, which are attributed to Bi^{3+} ions in two different host lattice sites [5]. The single emission band in our results (figure 5.4(a)) indicates that only one site occurs for Bi^{3+} ions in spinel. Shoulders on both the low and high wavelength sides of the emission peak observed using the Cary-Eclipse (but not the laser PL system) require further study. Figure 5.4(b) shows that the luminescence intensity is a maximum for a Bi^{3+} doping concentration of 0.5 mol%. Above that concentration the luminescence intensity decreases. While such an effect is often attributed to concentration quenching, the optimal concentration is rather low. Instead, it is suggested that the large size of the Bi^{3+} ions limits the amount of Bi that can be successfully incorporated into the host and that excess amounts of dopant leads to defects or quenching centres which then limit the luminescence intensity.

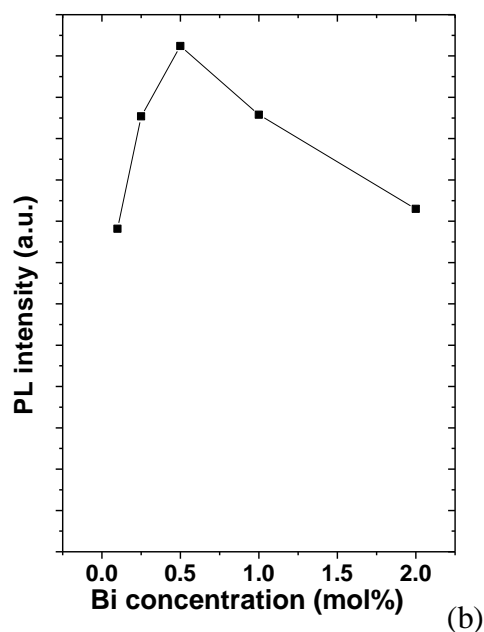
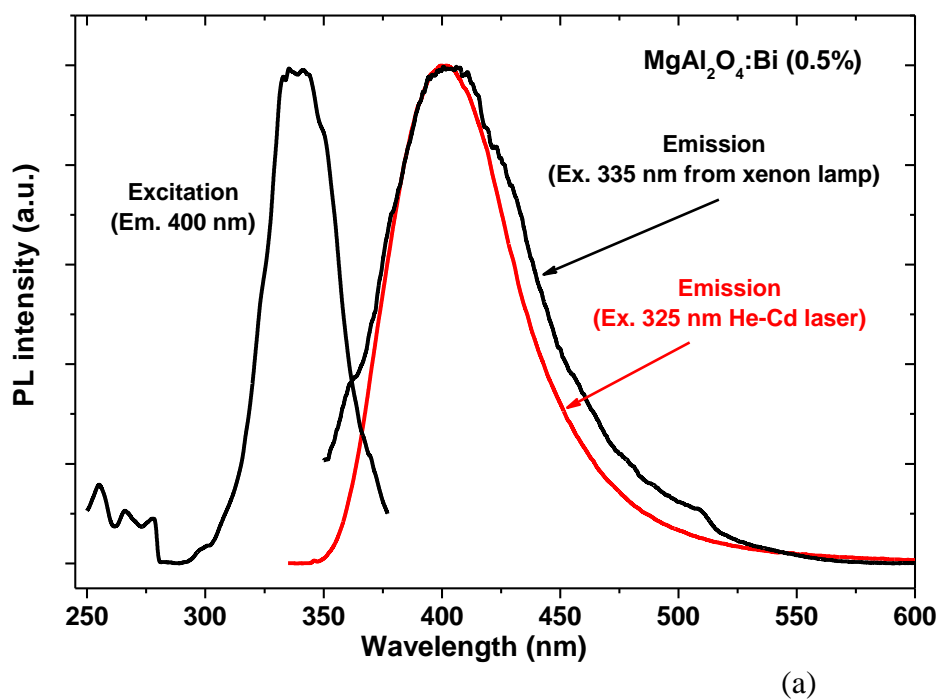


Figure 5.4: (a) Room temperature luminescence spectra of $\text{MgAl}_2\text{O}_4:\text{Bi}^{3+}$ (0.5 mol%) measured with the Cary Eclipse fluorescence spectrophotometer (using a xenon lamp) as well emission when excited by a He-Cd laser. (b) Luminescence peak intensity as a function of Bi doping concentration measured with the Cary Eclipse fluorescence spectrophotometer for excitation wavelength of 335 nm.

Figure 5.5 compares the PL emission spectra of Bi (0.5 mol%) and Ce (0.75 mol%) doped MgAl_2O_4 , both excited by a He-Cd laser at 325 nm. The fluorescence of the Ce doped sample is a broad band centred near 470 nm and is attributed to the transition of electrons that have been excited to the 5d level returning to the $^2\text{F}_{7/2}$ and $^2\text{F}_{5/2}$ states of the 4f level, although the peaks corresponding to the two final states are not resolved. Ce is often used as a sensitizer for Tb ions in many phosphor hosts because it can be excited efficiently and also transfer energy to Tb as a result of an overlap of its emission spectrum with the f-f excitation bands of Tb. The Tb f-f excitation bands occur in almost the same position independent of the host, beginning near 380 nm and extending to shorter wavelengths.

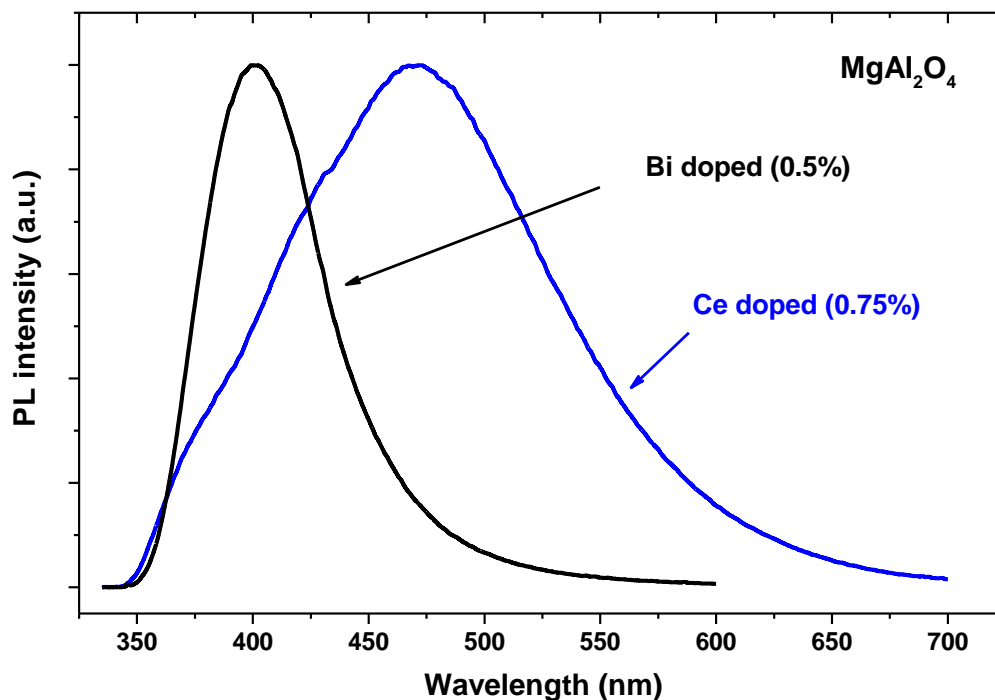


Figure 5.5: Comparison of the normalized emission spectra for Bi and Ce doped MgAl_2O_4 , both excited with a He-Cd laser at 325 nm.

This region is better overlapped by the Bi emission spectrum, suggesting that Bi may act as a good sensitizer for Tb. In addition, the Bi doped sample is more easily prepared, since it does not require annealing. The Ce doped sample had to be annealed in a reducing atmosphere of 4% H₂ in Ar at 1400 °C for 2 h in order to convert non-luminescent Ce⁴⁺ ions to trivalent Ce³⁺ ions before emission was obtained. Bi therefore seems a strong candidate to replace Ce in Ce,Tb co-doped samples, and co-doping spinel with Bi and Tb will therefore be the focus of future work.

5.4 Conclusion

Nanocrystalline Bi doped MgAl₂O₄ has been successfully synthesized by the combustion method. A broad band blue fluorescence emission centred at 400 nm was observed for excitation at 335 nm, which is attributed to the ³P₁ → ¹S₀ transition of Bi³⁺ ions. The emission intensity was measured as a function of Bi doping concentration, with the maximum occurring for 0.5 mol% of Bi doping. The results indicate that doping MgAl₂O₄ with Bi ions may be an attractive alternative to doping it with Ce ions, which give broad blue-green luminescence in this host but requires reducing at a high temperature (1400 °C) to convert non-luminescent Ce⁴⁺ ions to the luminescent Ce³⁺ charge state. The emission of Bi also suggests that it may be act as a good sensitizer for Tb ions in MgAl₂O₄.

5.5 References

1. J.H. Lim, B.N. Kim, Y. Kim, S. Kang, R.J. Xie, I.S. Chong, K. Morita, H. Yoshida and K. Hiraga, *Appl. Phys. Lett.* **102** (2013) 031104 (4 pages).
2. I. Omkaram, G. Seeta and S. Buddhudu, *J. Phys. Chem. Solids* **69** (2008) 2066-2069.
3. X. Chen, C. Ma and S. Bao, *Solid State Sci.* **12** (2010) 857-863.

4. W.M. Yen, S. Shionoya and H. Yamamoto, *Phosphor Handbook*, 2nd Ed, CRC Press (Boca Raton, 2007).
5. L.G. Jacobsohn, M.W. Blair, S.C. Tornga, L.O. Brown, B.L. Bennett and R.E. Muenchausen, *J. Appl. Phys.* **104** (2008) 124303 (7 pages).
6. Y. Porter-Chapman, E. Bourret-Courchesne and S.E. Derenzo, *J. Lumin.* **128** (2008) 87-91.
7. H. Fukada, M. Konagai, K. Ueda, T. Miyata and T. Minami, *Thin Solid Films* **517** (2009) 6054-6057.
8. E.N. Alvar, M. Rezaei and H. Alvar, *Powder Technol.* **198** (2010) 275-278.
9. Z. Xiaolin, Z. Haijun, Y. Yongjie and L. Zhanjie, *Mater. Sci. Eng. A* **379** (2004) 112-118.
10. R. Ianoş and R. Lazău, *Mater. Chem. Phys.* **115** (2009) 645-648.
11. H. O'Neal C. St and A. Navrotsky, *Am. Mineral.* **68** (1983) 181-194.
12. X.Y. Huang, X.H. Ji and Q.Y. Zhang, *J. Am. Ceram. Soc.* **94** (2011) 833-837.
13. V. Singh, M.M. Haque and D. Kim, *J. Bull. Korean Chem. Soc.* **28(12)** (2007) 2477-2480.
14. R.J. Wiglusz, T. Grzyb, S. Lis and W. Strek, *J. Lumin.* **130** (2010) 434-441.
15. K.C. Patil, M.S. Hegde, T. Ratan and S.T. Aruna, *Chemistry of Combustion Synthesis, Properties and Applications Nanocrystalline Oxide Materials*, World Scientific (New Jersey, 2008).

6 Optical properties of Bi and energy transfer from Bi to Tb in MgAl_2O_4 phosphor

6.1 Introduction

Magnesium aluminate (MgAl_2O_4), corresponding to the mineral spinel, has been prepared by various methods such as solid-state reaction [1], precipitation [2], hydrothermal synthesis [3] and the sol-gel method [4]. Alternatively, synthesis using the combustion method [5] occurs via a highly exothermic redox reaction between metal nitrates and an organic fuel and this technique can yield a homogenous product in a short amount of time without using expensive high temperature furnaces. MgAl_2O_4 is of interest because of its mechanical strength, chemical inertness, wide bandgap, relatively low density, high melting point, high thermal shock resistance, low thermal expansion coefficient, resistance to neutron irradiation and low dielectric loss [4,6]. In addition, it has also been considered as a phosphor host activated by various transition metal and lanthanide ions [7]. As an alternative to such ions, the trivalent bismuth ion (Bi^{3+}) is an interesting luminescence activator for phosphors due to electron transitions between the $6s^2$ ground state and the $6s6p$ excited states. The $6s^2$ ground state has a single energy level 1S_0 while the $6s^16p^1$ excited configuration has energy levels 3P_0 , 3P_1 , 3P_2 and 1P_1 in order of increasing energy. Electron transitions between the 1S_0 ground state and the 3P_J levels are spin forbidden, but optical absorption can occur to the high energy 1P_1 level. However, spin-orbit coupling between the 1P_1 and 3P_1 levels makes the lower energy transitions $^1S_0 \leftrightarrow ^3P_1$ possible and the luminescence from Bi^{3+} activated phosphors is usually attributed to this transition. In some materials the $^1P_1 \rightarrow ^1S_0$ emission is also observed [8]. The outer electron orbitals of

Bi^{3+} are not shielded (as in the case of the 4f energy levels of trivalent lanthanide ions) so the broad luminescence band shows a strong dependence on the composition and crystal structure of the host lattice and the emission wavelength is tuneable from the ultraviolet, through blue to green [9]. Although we are not aware of any previous reports about Bi doped MgAl_2O_4 , the material Bi doped ZnGa_2O_4 (also having the spinel structure) has been evaluated for its luminescence properties. Bi doping is reported to enhance the blue host-defect emission of ZnGa_2O_4 [10] and Bi doped ZnGa_2O_4 ceramics have been identified as potential white-colour persistent phosphors [11]. In this study Bi doped MgAl_2O_4 has been prepared using the combustion method and characterized by x-ray diffraction, UV-visible spectroscopy, scanning and transmission electron microscopy and photoluminescence spectroscopy.

Several previous studies have described the luminescence of Tb doped MgAl_2O_4 [1,12-15]. All of these studies report luminescence due to transitions from the $^5\text{D}_4$ excited level to the $^7\text{F}_j$ levels, of which green light near 543 nm corresponding to the $^5\text{D}_4 \rightarrow ^7\text{F}_5$ transition is the strongest. Some of them also report blue luminescence bands below 450 nm from the excited $^5\text{D}_3$ level to the $^7\text{F}_j$ levels [1,13], which in the case of a sample doped with 0.6 mol% Tb and measured at low temperature (9 K) actually dominated the spectrum [12]. The studies differ greatly concerning the optimal Tb doping level for maximum luminescence, giving values of 0.01 mol% [1], 0.5 mol% [13] or even reporting no concentration quenching for Tb doping up to 5 mol% [14]. Although all three of these studies report f-f excitation bands between 300 and 400 nm, there is some variation regarding the position of the f-d excitation band with reported values of 286 and 260 nm [1], 245 nm [13] and 236 nm [14]. The last of these corresponds well to f-d absorption reported at 5.3 eV (234 nm) [12]. The assignment of the f-d excitation wavelengths in ref.

[1] is questionable because these peaks are less intense than the f-f peaks, whereas the allowed f-d transitions are expected to be significantly more intense than the forbidden f-f transitions, as observed in refs. [13] and [14]. Tb doped phosphors generally cannot be excited efficiently via the weak f-f transitions and either require excitation at shorter wavelengths through the allowed f-d transition or, alternatively, sensitization through energy transfer from a co-dopant. The latter option is often preferable because shorter wavelength excitation sources can be less accessible and more costly, while longer excitation wavelengths can also pass through ordinary glass and some plastics, avoiding the need for quartz. Often Ce is used as a sensitizer for Tb [16,17], but this has proved difficult in MgAl_2O_4 because it requires annealing at a high temperature (1400 °C) in a reducing atmosphere in order to convert non-luminescent Ce^{4+} ions to the luminescent Ce^{3+} charge state [7]. Bi has been employed as a sensitizer to transfer energy to various lanthanide ions, e.g. Er [18], Yb [19], Dy and Pr [20], and especially Eu [21-24]. Bi may also act as a sensitizer for Tb ions [25], but this combination has not been studied much. Therefore MgAl_2O_4 co-doped with Bi and Tb was investigated to ascertain whether Bi could be used as an alternative to Ce to sensitize Tb emission in MgAl_2O_4 .

6.2 Materials and methods

Nanocrystalline MgAl_2O_4 host material was synthesized using the combustion method from the nitrate precursors $\text{Mg}(\text{NO}_3)_2 \cdot 6\text{H}_2\text{O}$ and $\text{Al}(\text{NO}_3)_3 \cdot 9\text{H}_2\text{O}$, with urea ($\text{CH}_4\text{N}_2\text{O}$) acting as the fuel. Generally about 10 mmol of $\text{Al}(\text{NO}_3)_3 \cdot 9\text{H}_2\text{O}$ was added with the other reactants in approximately 6 ml of distilled water, which was then stirred vigorously for 30 min to obtain a homogeneous transparent solution. This was transferred to a porcelain crucible and which was placed into a muffle furnace maintained at 520 °C. Within a few minutes the water boiled off and the sample ignited as the exothermic combustion reaction

occurred, giving off copious quantities of gas and heating the material to well above the furnace temperature. After the reaction the foamy white product was removed from the furnace and, after cooling to room temperature, it was crushed into powder using a pestle and mortar.

The nitrates $\text{Bi}(\text{NO}_3)_3 \cdot 5\text{H}_2\text{O}$ and $\text{Tb}(\text{NO}_3)_3 \cdot 5\text{H}_2\text{O}$ were used to dope the samples. In the normal spinel structure Mg^{2+} ions occupy tetrahedral sites while Al^{3+} ions occupy octahedral sites. The anion to cation distances for these sites are $R_{\text{tet}} = \sqrt{3}(u - 1/8)a$ and $R_{\text{oct}} = (3u^2 - 2u + 3/8)^{1/2}a$ respectively, where $u = 0.2624$ is the so-called oxygen parameter for MgAl_2O_4 which has lattice constant $a = 808.32$ pm [26,27]. This gives almost identical bond lengths for the cations in the tetrahedral sites (192.4 pm) and octahedral sites (192.6 pm). The O^{2-} anions in spinel have distorted tetrahedral (fourfold) coordination, so subtracting their ionic radius (138 pm [28]) leaves space for cations of radius ~ 54.5 pm. This matches reasonably well with the ionic radii of Mg^{2+} (57 pm with fourfold coordination [28]) and Al^{3+} (53.5 pm with sixfold coordination [28]). The ions Bi^{3+} and Tb^{3+} do not have ionic radii listed for fourfold coordination, but for sixfold coordination their ionic radii are given as 103 pm and 92.3 pm respectively [28]. These ions are therefore much larger than the host cations, which could make substitution difficult. In previous reports for MgAl_2O_4 concentrations of Tb up to 1.5% [1] and 5% [14] are reported to have been successfully incorporated, but the issue of the relative sizes of the ions was not discussed. MgAl_2O_4 has also been doped with other large lanthanide ions, e.g. Eu^{3+} (ionic radius 94.7 pm for sixfold coordination [28]), and Singh *et al.* [29] prepared samples based on the formula $\text{Mg}_{0.99}\text{Eu}_{0.01}\text{Al}_2\text{O}_4$ but concluded from the emission spectra that the Eu^{3+} ions probably occupied octahedral Al^{3+} sites and not the Mg^{2+} sites as suggested by the formula. Chen *et al.* [30] produced nanocrystalline MgAl_2O_4 with 2%

Eu^{3+} and found from the emission spectra that the Eu^{3+} ions were in a low symmetry environment, and based on the large difference between host and dopant ions they suggested that the most feasible location of Eu^{3+} was on surfaces of the nanocrystals. However, for Bi doped in the spinel ZnGa_2O_4 , Zhuang *et al.* [11] give the formula $\text{ZnGa}_{1.98}\text{O}_4:\text{Bi}_{0.02}$ which suggests that Bi substitutes Ga in the lattice despite the fact that the ionic radius Bi^{3+} is much larger than octahedrally coordinated Ga^{3+} (62 pm [28]). It is relevant to note that although the sizes of the tetrahedral and octahedral sites in the spinel structure are equal when the oxygen parameter is $u = 0.2625$ (almost the value for MgAl_2O_4), as u decreases the size of the octahedral sites grows at the expense of the tetrahedral site. Compounds having the spinel structure with u as low as ~ 0.24 occur [26], which if applied with the lattice constant of MgAl_2O_4 predicts space for a cation in the octahedral site of ~ 72.5 pm. Although this is still rather smaller than the dopant ions considered, deformation of the ions or lattice or the introduction of associated defects may make the incorporation of these large ions possible. Although it is therefore unclear whether the dopants will substitute the host cations or whether they will instead occur on the surfaces of the nanocrystals, we have prepared our doped MgAl_2O_4 samples on the assumption that the dopant ions substitute Al^{3+} ions occupying octahedral sites.

The structure of the prepared samples was characterized by x-ray diffraction (XRD) measurements using a Bruker D8 Advance diffractometer (40 kV, 40 mA) with $\text{Cu K}\alpha$ x-rays (154.06 pm). Scanning electron microscope (SEM) images of the particle morphology were obtained using a Shimadzu SSX-550 instrument, transmission electron microscopy (TEM) was performed using a Philips CM100 microscope and diffuse reflection spectra were measured using a Lambda 950 UV-vis spectrophotometer with spectralon as the reference material. Luminescence properties were measured using a Cary Eclipse

fluorescence spectrophotometer, using the fluorescence mode for measuring the Bi emission and the phosphorescence mode for measuring the Tb emission. All measurements were performed at room temperature.

6.3 Results and discussion

6.3.1 Structure and morphology

Figure 6.1(a) shows the XRD patterns of undoped and doped MgAl_2O_4 , together with the standard data for MgAl_2O_4 from JCPDS card 74-1132. The main peak of the cubic structure corresponding to the crystal plane with Miller indices $\{311\}$ occurs at $2\theta = 36.86^\circ$ for the undoped sample. The patterns for samples doped with Bi or co-doped with Bi and Tb are similar to those from the pure host, although it can be seen that the base of the peaks for the undoped sample are broader. These peaks are not Gaussian in shape, but are superimposed on a broad base, which could be explained by the presence of very small crystallites existing together with larger nanocrystals. To confirm this, the sample was examined using TEM and a typical image is shown in figure 6.2. Large particles consisting of many crystallite grains occur in the dark thicker regions, but near the edges individual crystallites can be distinguished and they range in size from a few nanometres up to about 20 nm. For the samples containing Bi the diffraction peaks lack the broad base, so the addition of a small amount of Bi produces samples lacking the very small crystallites. Bismuth oxide has a much lower melting point (817°C) compared to Mg and Al oxides ($>2000^\circ\text{C}$) and since the temperature during synthesis is estimated to be near 1500°C [31] the addition of Bi may act like a flux, improving crystal growth and thereby reducing the occurrence of very small crystallites. Figure 6.1(b) shows Williamson-Hall plots for the doped samples, according to which the peak broadening is attributed to both crystallite size

as well as microstrain according to $\beta \cos \theta = \frac{K\lambda}{D} + 4\varepsilon \sin \theta$, where β is the 2θ -FWHM (in radians) of the diffraction peaks at angle θ , λ is the x-ray wavelength, K is a shape factor taken as 0.9, D is the crystallite size and ε is the microstrain [32].

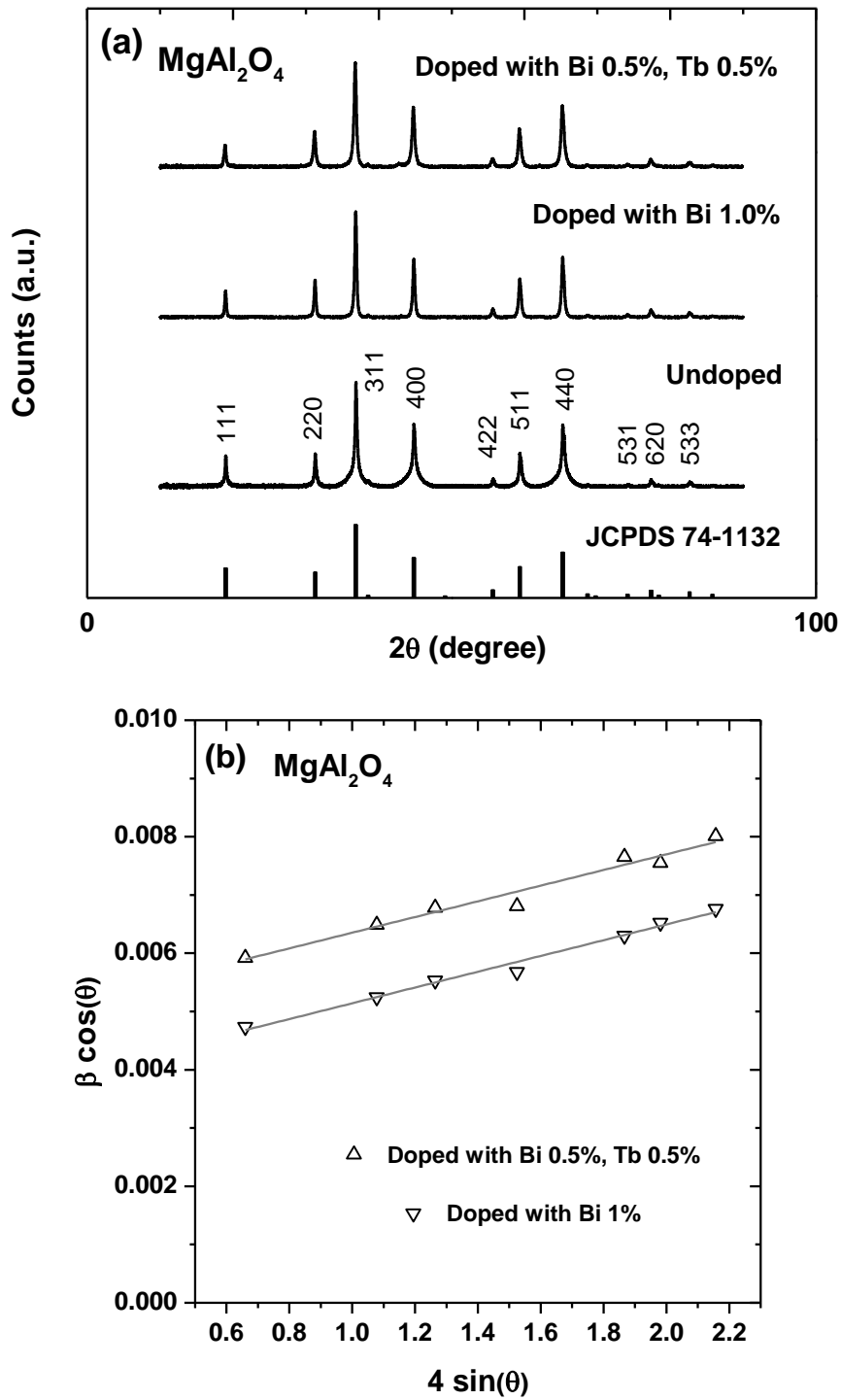


Figure 6.1: (a) XRD patterns of pure and doped MgAl₂O₄ samples. (b) Williamson-Hall plots for doped MgAl₂O₄ samples.

The plots of $\beta \cos \theta$ versus $4 \sin \theta$ have slope equal to the microstrain and an intercept of $\frac{K\lambda}{D}$ from which the crystallite size can be determined. For both the Bi doped and Bi,Tb co-doped samples the slope is the same and has a value of 0.0014 (or 0.14%), indicating only a small amount of microstrain in this material produced with the combustion method. This low level of microstrain may suggest that the dopants could be located on the surfaces of the nanocrystals rather than substituting the host cations, or that stress-relieving defects are associated with substitutional sites. The crystallite size of the co-doped sample containing 0.5 mol% Bi and 0.5 mol% Tb is 28 nm, while for the singly doped sample containing 1 mol% Bi the crystallite size is 37 nm, which is consistent with the suggestion that the addition of Bi improves crystal growth.

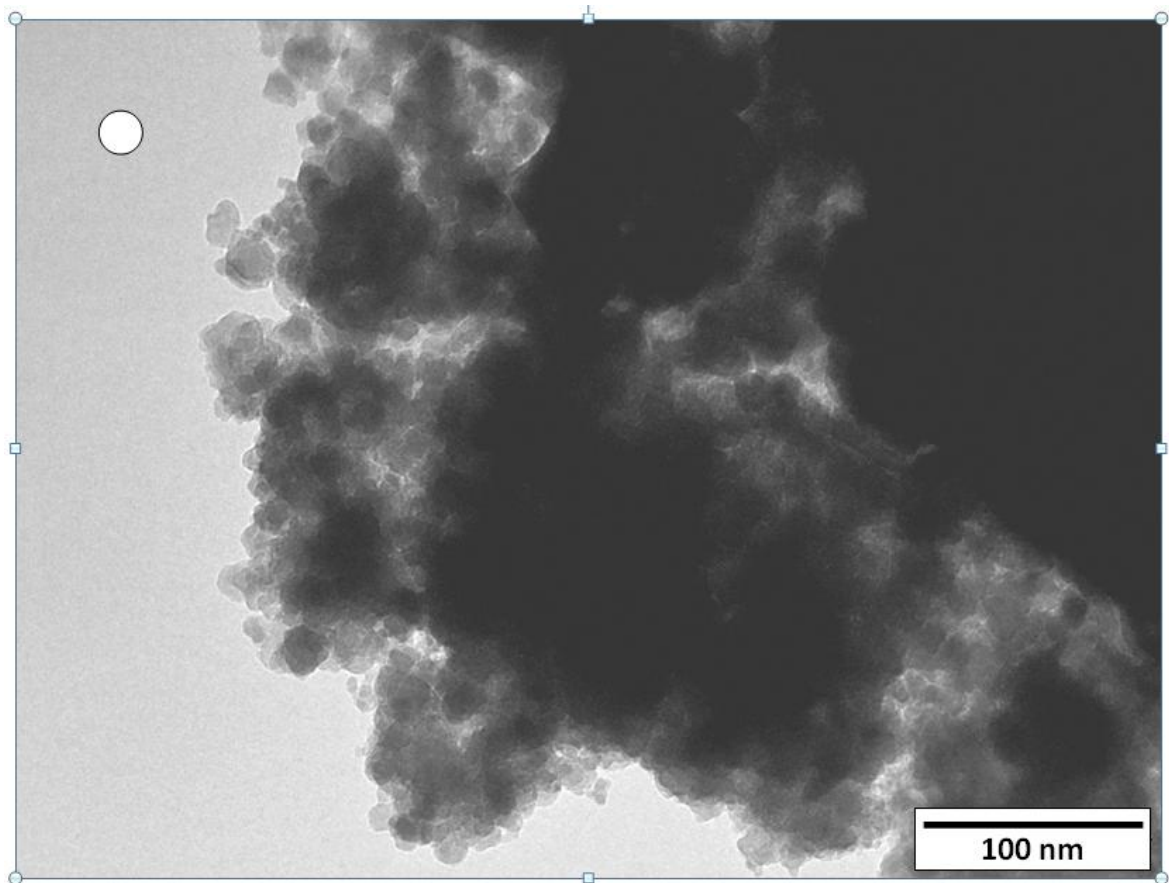


Figure 6.2: TEM image of undoped MgAl_2O_4 obtained by the combustion method. The circle added to the image has a diameter of 20 nm for comparison with the size of the crystallites.

The SEM image in figure 6.3(a) shows the morphology of the undoped MgAl_2O_4 particles produced with the combustion process after grinding the foamy product with a mortar and pestle. The particle size varies up to several tens of microns and depends on the amount of grinding, but it is evident that large flat, plate-like particles occur. This is characteristic of material made by combustion synthesis due to the large amount of gas that evolves during the reaction. The variation in thickness of the plates is due to the non-uniform distribution of temperature and mass flow in the combustion flame. Figure 6.3(b) shows that the sample doped with 0.5 mol% Bi and 0.5 mol% Tb has a similar morphology to that of the undoped sample. These SEM images show several pores in the particles which are formed by the escaping gases during the combustion reaction. These particles are much larger than the crystallite size calculated from the XRD data, indicating that the particles consist of much smaller crystallites.

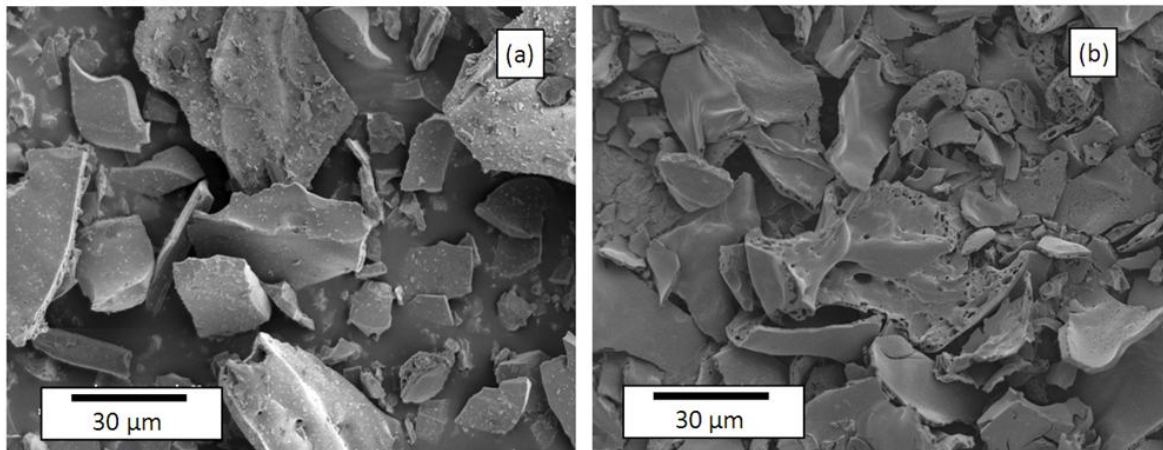


Figure 6.3: SEM images of MgAl_2O_4 powders obtained by the combustion method (a) undoped and (b) doped with 0.5% Bi, 0.5% Tb.

6.3.2 Optical properties

Diffuse reflection spectroscopy was used to study the absorption characteristics of MgAl_2O_4 and the effects of the Bi dopant. Figure 6.4 shows that for the undoped host material the reflectance remains high even for very short wavelengths and the host only begins to absorb below 300 nm, which is due to the wide bandgap of MgAl_2O_4 . When Bi is incorporated in the material the reflectance spectrum changes significantly as a result of strong absorption of the Bi below approximately 350 nm.

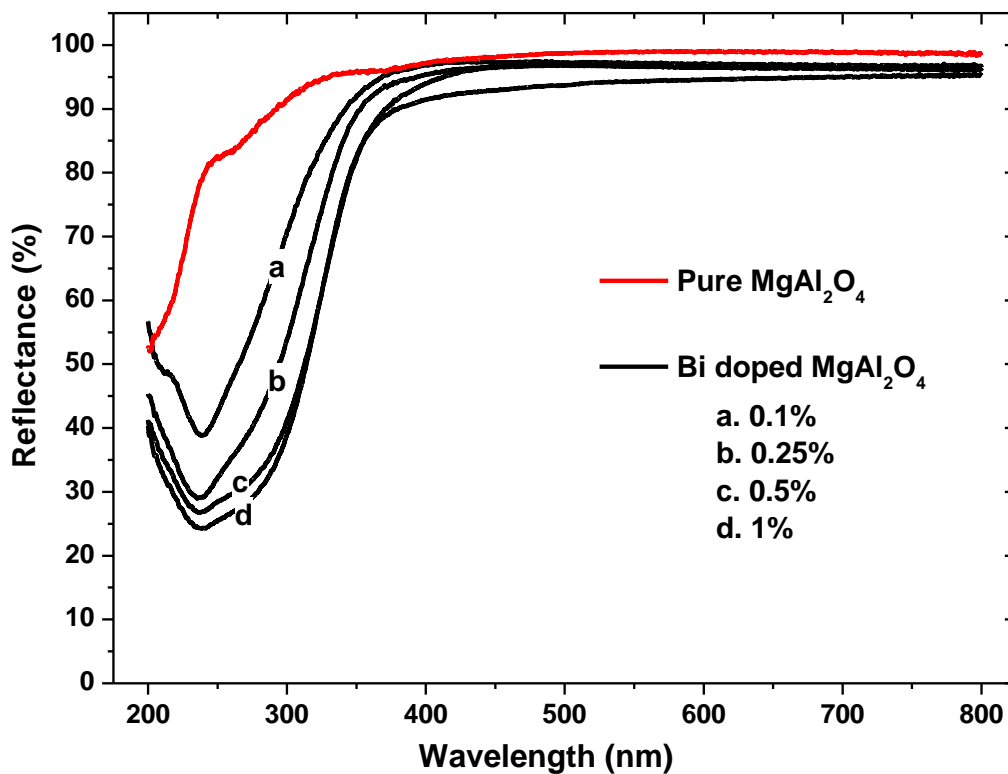


Figure 6.4: Diffuse reflectance spectra of undoped and Bi doped MgAl_2O_4 samples.

The emission and excitation spectra of $\text{MgAl}_2\text{O}_4:\text{Bi}$ 0.5 mol% phosphor are presented in figure 6.5. The Bi^{3+} singly doped sample exhibits a broad band of blue fluorescence emission which extends from 350 to 500 nm when excited by 335 nm. Except for a decrease in intensity, the emission spectrum does not change when the excitation wavelength is varied. The excitation and emission are attributed to $^1\text{S}_0 \leftrightarrow ^3\text{P}_1$ transitions of Bi^{3+} ions with a Stokes shift of $\sim 4850 \text{ cm}^{-1}$ (0.60 eV). For comparison, in Bi doped Y_2O_3

two emission bands occur at 410 nm and 520 nm with Stokes shifts of 0.31 eV and 1.24 eV respectively, which are attributed to Bi^{3+} ions in two different host lattice sites [33]. The single emission band in our results (figure 6.5) indicates that only one site occurs for Bi^{3+} ions in the material. With varying the Bi doping concentration, the inset of figure 6.5 shows that the maximum luminescence occurred from samples doped with 0.5 mol% and that a further increase resulted in concentration quenching.

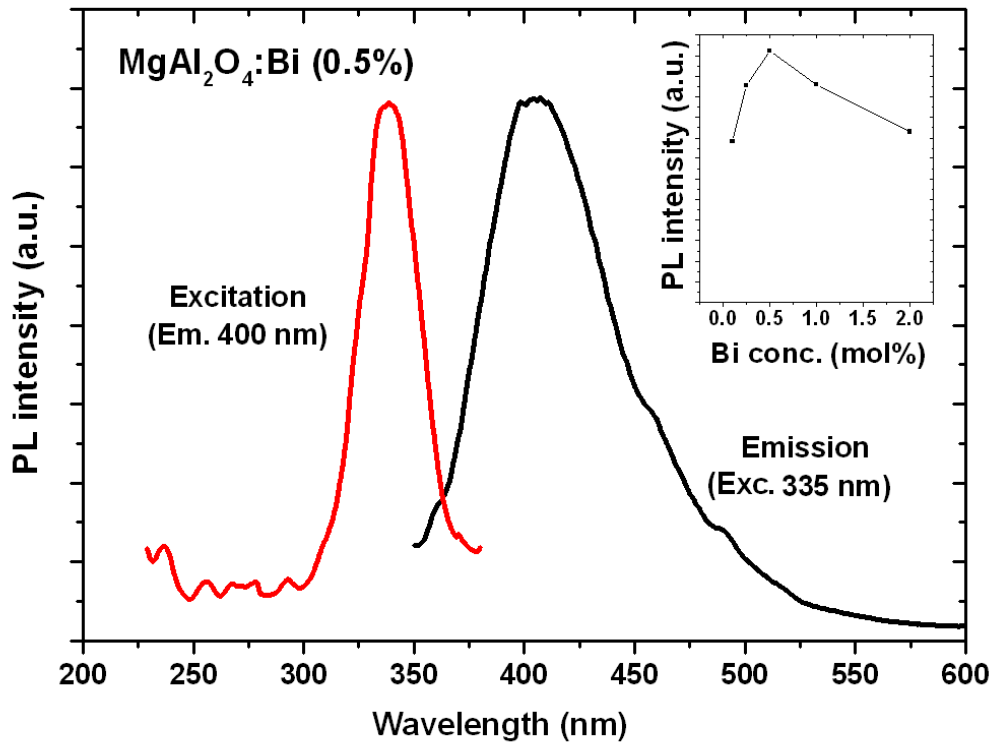


Figure 6.5: Excitation and emission spectra of the $\text{MgAl}_2\text{O}_4:\text{Bi}$ 0.5 mol% phosphor. The inset shows the peak emission intensity as a function of Bi concentration.

Figure 6.6 shows the excitation and emission spectra of $\text{MgAl}_2\text{O}_4:\text{Tb}$ 0.5 mol%. The excitation spectrum of Tb^{3+} consists of two parts, one in the range from 200 to 300 nm corresponding to the 4f-5d transitions and a second consisting of several excitation peaks between 300 and 500 nm corresponding to various f-f transitions. The peak of the strong f-d excitation band is at 227 nm which is similar to the value of 236 nm given in ref. [14], while the f-f excitation transitions are very much weaker and can only be clearly seen in the inset of figure 6.6. The emission spectra showed the characteristic emission bands of

Tb^{3+} attributed to the ${}^5\text{D}_4 \rightarrow {}^7\text{F}_J$ transitions ($J = 6,5,4,3$), with the dominant green band of the ${}^5\text{D}_4 \rightarrow {}^7\text{F}_5$ transition at 544 nm, together with weaker blue emission lines below 480 nm corresponding to ${}^5\text{D}_3 \rightarrow {}^7\text{F}_J$ ($J = 6,5,4$) transitions. A comparison of the broad emission band of Bi in figure 6.5 to the weak f-f excitation band in figure 6.6 shows an overlap of the short wavelength part of the Bi emission with the f-f excitation band of Tb below 380 nm as well as an overlap of the long wavelength part of the Bi emission with the ${}^7\text{F}_6 \rightarrow {}^5\text{D}_4$ excitation peak of Tb near 480 nm, suggesting that efficient energy transfer from the Bi^{3+} to Tb^{3+} ions may occur.

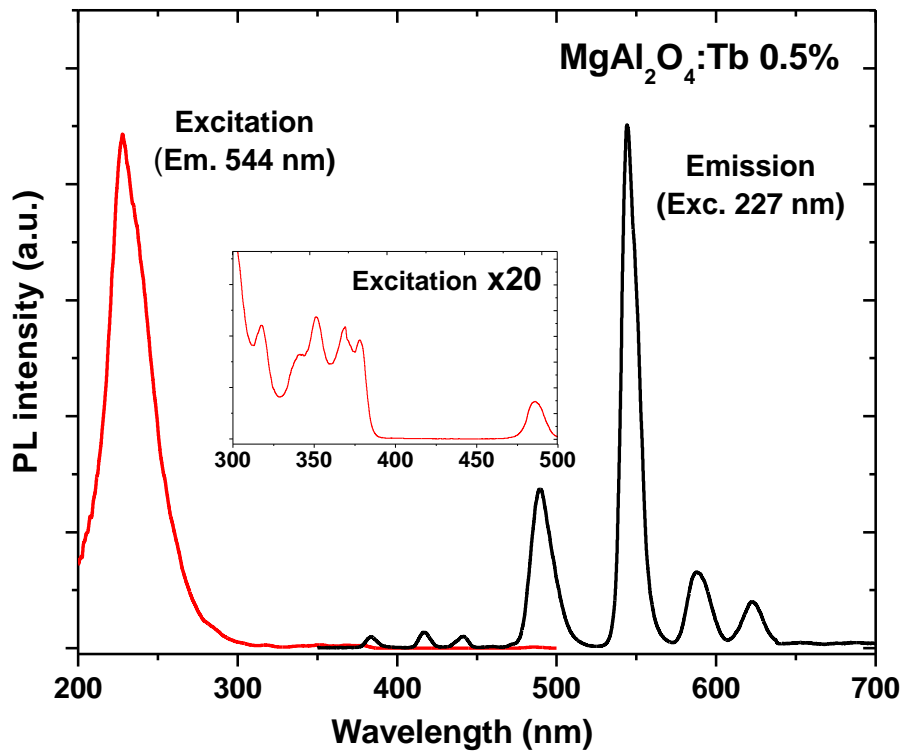


Figure 6.6: Excitation and emission spectra of $\text{MgAl}_2\text{O}_4:\text{Tb}$ 0.5 mol% phosphor. The inset shows the weak f-f excitation bands of Tb.

6.3.3 Energy transfer from Bi to Tb

Figure 6.7(a) compares the excitation spectra of the single doped Tb 0.5 mol% sample with the co-doped Bi 0.5 mol%, Tb 0.5 mol% MgAl₂O₄ sample while monitoring the ⁵D₄→⁷F₅ transition of Tb at 544 nm. There is only a small difference in the emission intensity between the samples for excitation using the Tb f-d band near 227 nm, but a dramatic increase for the longer wavelengths to about 380 nm, which coincides with the onset of the Tb f-f excitation band (as seen in the inset of figure 6.6). The enhancement factor for the Tb emission as a result of co-doping with Bi can be obtained by dividing the excitation spectrum for the co-doped sample with that for the single doped sample. The result is given in figure 6.7(b) and a maximum enhancement of almost 100 times occurs for an excitation wavelength near 328 nm. The position of this peak is influenced by a minimum in the Tb f-f excitation spectrum at this wavelength (as seen in the inset of figure 6.6). Nevertheless, the general correspondence of the enhancement factor in figure 6.7(b) and the Bi excitation spectrum in figure 6.5 provides evidence that energy transfer occurs from the Bi³⁺ ions to the f-f levels of Tb³⁺ ions, resulting in emission corresponding to the Tb³⁺ ⁵D₄ → ⁷F₅ transition.

The experimental results did not show a significant enhancement of the blue Tb³⁺ emission peaks originating from the ⁵D₃ level after co-doping with Bi, suggesting that energy is transferred to the Tb³⁺ ⁵D₄ level. This is supported by the fact that the Bi emission has a wavelength of about 400 nm, while the excitation wavelength for the Tb³⁺ ⁵D₃ level is 380 nm, suggesting that there is insufficient energy available for energy transfer from the Bi³⁺ ³P₁ level to the Tb³⁺ ⁵D₃ level. Figure 6.8 presents the proposed energy diagram showing the energy transfer process. The levels of Bi are shown as parabolas in order to account for the Stokes shift between excitation and emission, while this is unnecessary for Tb because

the 4f levels are shielded. For Bi the levels with forbidden transitions from the ground state are shown as dashed curves and only the position of the 3P_1 level is known from our experimental results, while the other Bi levels are uncertain.

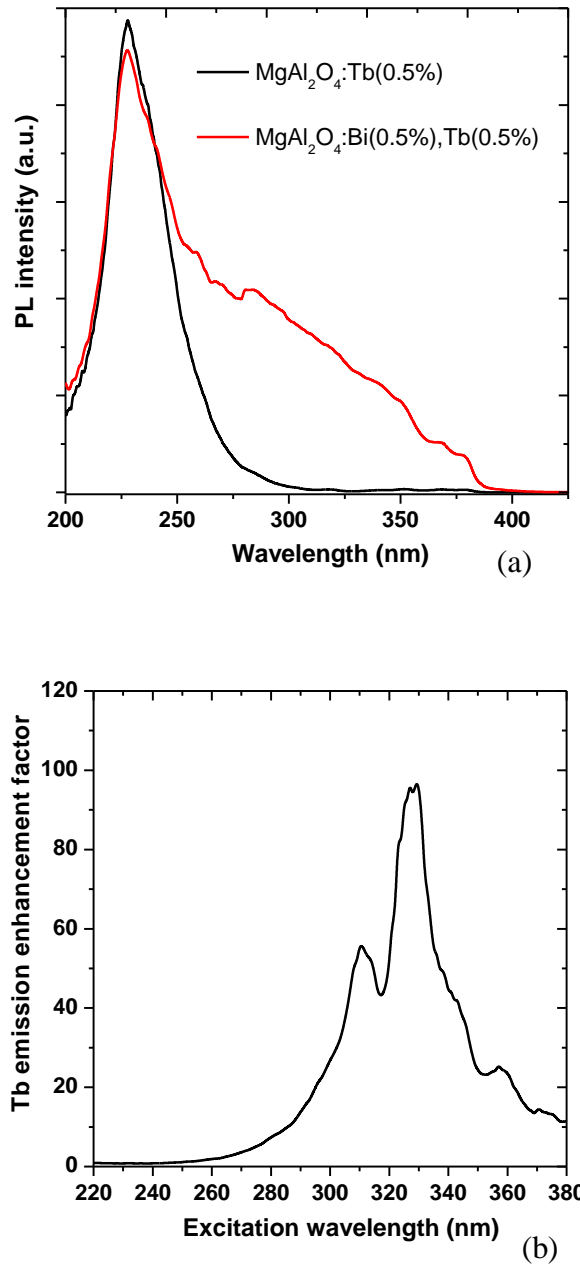


Figure 6.7: (a) Excitation spectra of the MgAl₂O₄:Tb 0.5 mol% and MgAl₂O₄:Bi 0.5mol%, Tb 0.5 mol%. (b) Enhancement factor calculated for the Tb emission as a result of co-doping with Bi.

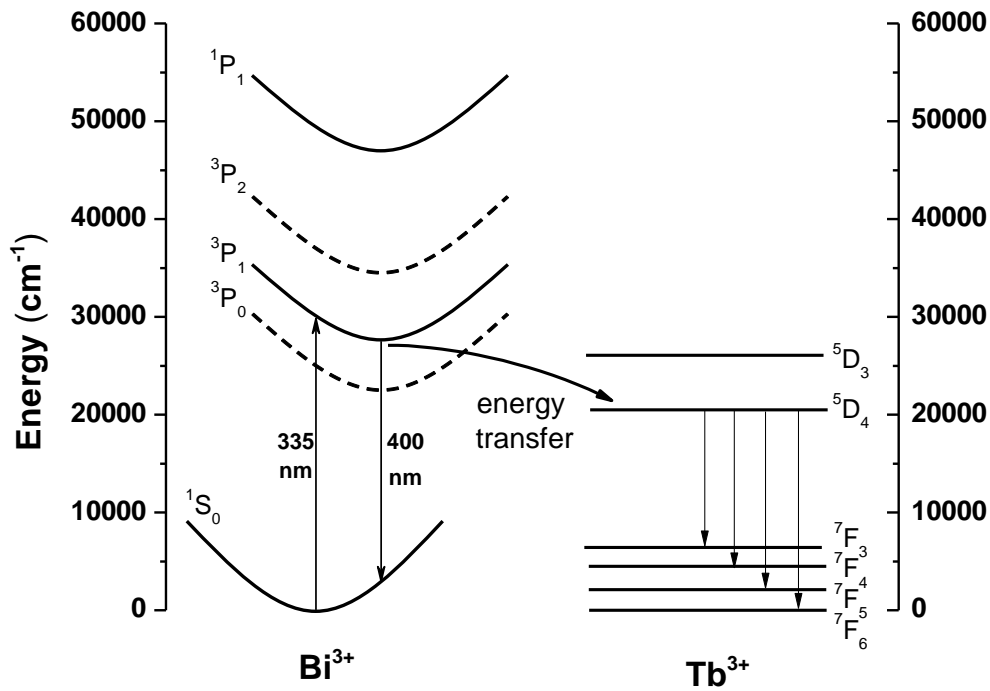


Figure 6.8: Energy level diagrams of Bi³⁺ and Tb³⁺ showing the energy transfer process from Bi to Tb in co-doped MgAl₂O₄.

To determine the optimum concentration of Bi which can give a high emission from Tb using 328 nm excitation, the concentration of Tb ions was kept constant at 0.5 mol% and the concentration of Bi ions was varied from 0 up to 2 mol%. Figure 6.9 shows the relative intensity of Tb emission associated with the ⁵D₄→⁷F₅ transition at 544 nm as a function of Bi concentration, with respect to the single doped sample. The results show that the Tb emission increases as the Bi concentration increased up to 0.5 mol% and then decreases at higher concentrations. This concentration for maximum enhancement of the Tb emission is the same as the concentration for maximum Bi emission intensity for single doped samples.

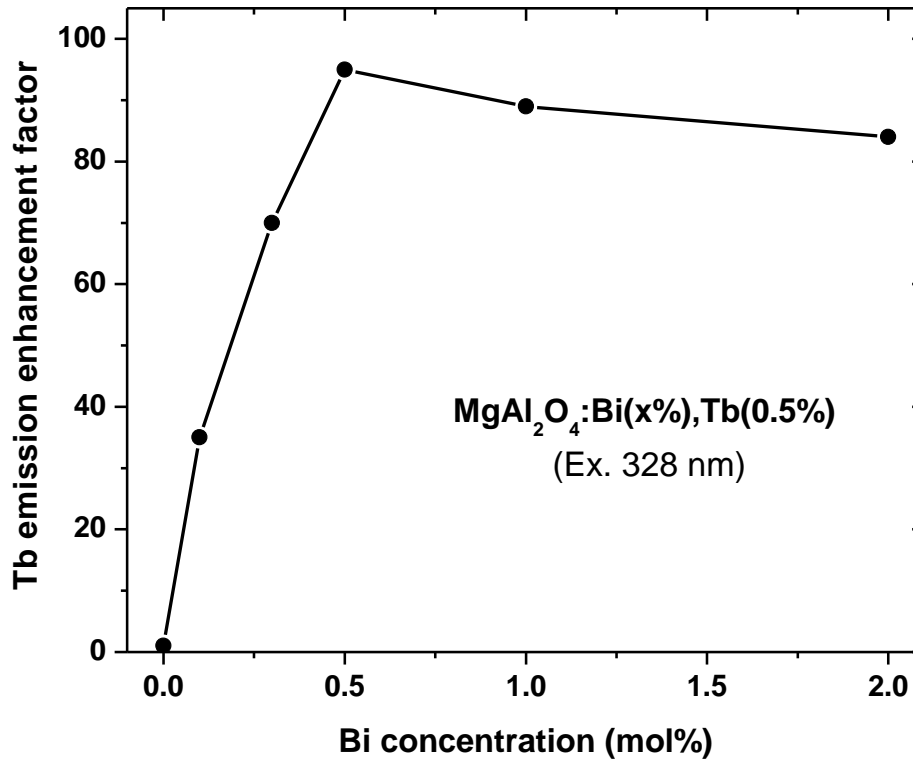


Figure 6.9: The enhancement factor for the emission intensity of Tb at 544 nm as a function of Bi concentration, i.e. the emission intensity for a sample co-doped with Bi and Tb relative to the emission intensity of the single Tb doped sample.

For energy transfer from Bi to Tb, if the Bi concentration is fixed and the Tb concentration is increased, the emission intensity from the Bi should be reduced. The efficiency of energy transfer from Bi to Tb is defined by $\eta_{ET} = 1 - I/I_0$, where I_0 is the Bi (sensitizer) emission intensity in a single doped sample and I is the reduced Bi emission intensity in the sample co-doped with Tb [34]. The decreasing Bi emission with increasing Tb concentration is shown in figure 6.10(a) and the corresponding energy transfer efficiencies are plotted in figure 6.10(b). The energy transfer efficiency is 75% for the sample doped with 0.5 mol% Bi and 2 mol% Tb, showing that the energy transfer process from Bi^{3+} to Tb^{3+} ions is very efficient.

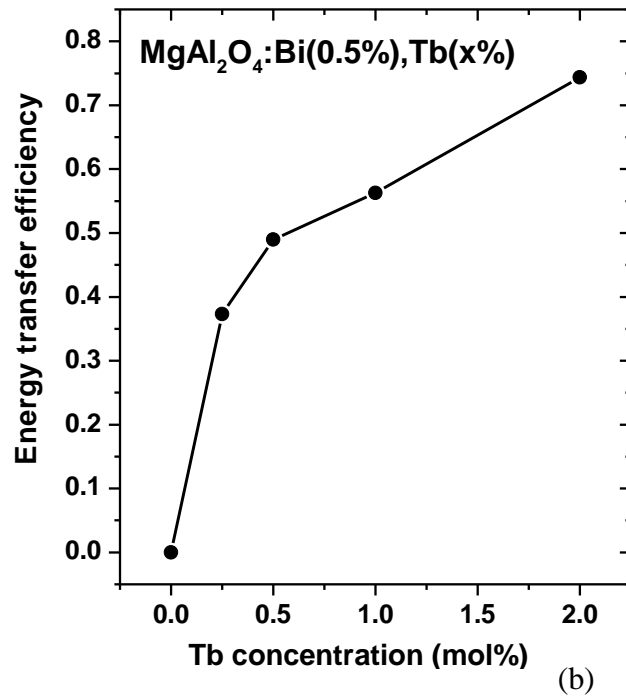
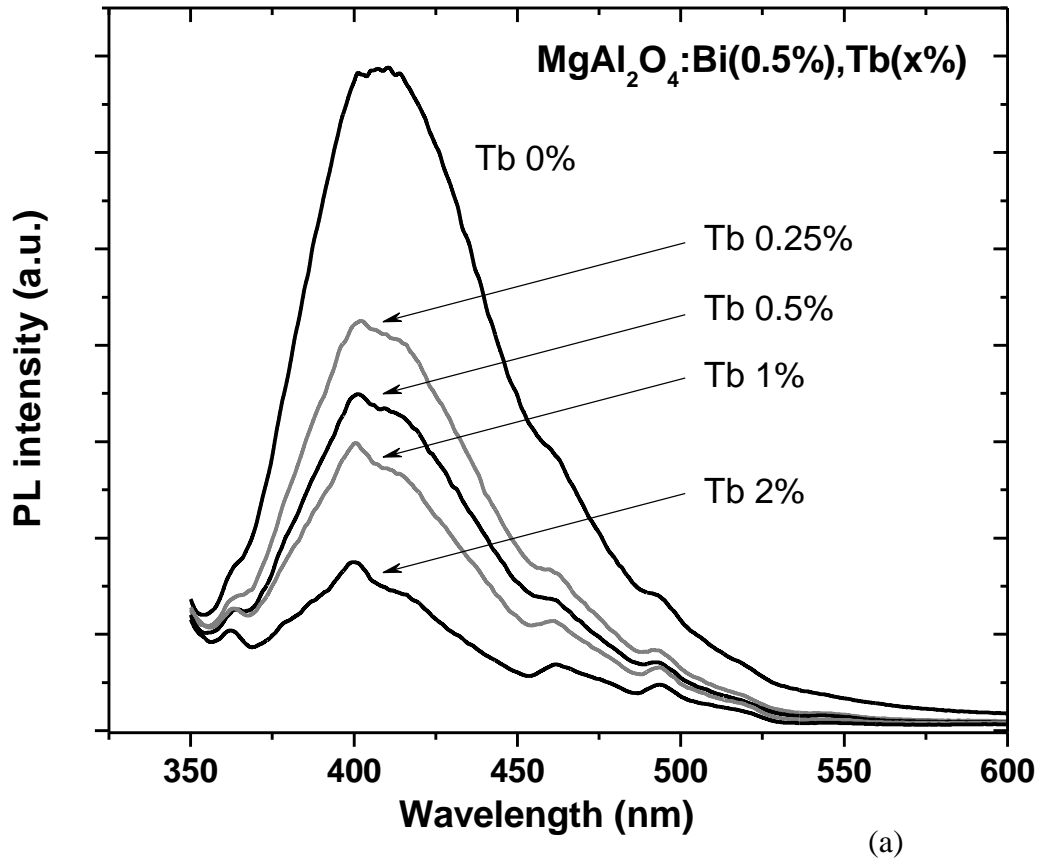


Figure 6.10: (a) The intensity of Bi emission with different Tb doping concentrations. (b) Energy transfer efficiency from Bi to Tb as a function of Tb concentration.

6.4 Conclusion

Bi has been shown to be an effective dopant in MgAl_2O_4 produced by the combustion method. XRD results indicate that the addition of small amounts of Bi increases the crystal growth of the host material. The phosphor emits light near 400 nm when excited at 335 nm, which is attributed to $^1\text{S}_0 \leftrightarrow ^3\text{P}_1$ transitions of Bi^{3+} ions with a Stokes shift of $\sim 4850 \text{ cm}^{-1}$ (0.60 eV). Concentration quenching occurs if the Bi concentration is increased above 0.5 mol%. The Bi emission band overlaps Tb^{3+} f-f excitation peaks and this leads to efficient energy transfer from Bi to Tb in co-doped samples. This leads to significant enhancement of Tb emissions from the $^5\text{D}_4$ level for excitation wavelengths between 300 nm and 380 nm (with a maximum enhancement of almost 100 times near 328 nm), thereby extending the useable excitation band of Tb to much longer wavelengths compared to Tb single doped samples. The results suggest that Bi offers an attractive alternative to Ce which is often used to sensitize Tb in many other hosts.

6.5 References

1. I. Omkaram, G. Seeta Rama Raju and S. Buddhudu, *J. Phys. Chem. Solids* **69** (2008) 2066-2069.
2. E. N. Alvar, M. Rezaei and H. Alvar, *Powder Technol.* **198** (2010) 275-278.
3. X. Chen, C. Ma and S. Bao, *Solid State Sci.* **12** (2010) 857-863.
4. Z. Xiaolin, Z. Haijun, Y. Yongjie and L. Zhanjie, *Mater. Sci. Eng. A* **379** (2004) 112-118.
5. R. Ianoş and R. Lazău, *Mater. Chem. Phys.* **115** (2009) 645-648.
6. S. Roy, N. Vegten and A. Baiker, *J. Catalysis* **271** (2010) 125-131.
7. W.A.I. Tabaza, H.C. Swart and R.E. Kroon, *Phys. B* (2013). In press:
<http://www.sciencedirect.com/science/article/pii/S0921452613006881>

8. Y. Porter-Chapman, E. Bourret-Courchesne and S.E. Derenzo, *J. Lumin.* **128** (2008) 87-91.
9. H. Fukada, M. Konagai, K. Ueda, T. Miyata and T. Minami, *Thin Solid Films* **517** (2009) 6054-6057.
10. W.N. Kim, H.L. Park and G.C. Kim, *Mater. Lett.* **59** (2005) 2433-2436.
11. Y. Zhuang, J. Ueda and S. Tanabe, *Opt. Mater. Express* **2** (2012) 1378-1383.
12. H. Nakagawa, K. Ebisu, M. Zhang and M. Kitaura, *J. Lumin.* **102-103** (2003) 590-596.
13. E. Alagu Raja, S. Menon, B. Dhabekar, N.S. Rawat and T.K. Gundu Rao, *J. Lumin.* **129** (2009) 829-835.
14. R.J. Wiglusz and T. Grzyb, *Opt. Mater.* **33** (2011) 1506-1513.
15. S.A. Hassanzehah-Tabrizi, *Opt. Mater.* **33** (2011) 1607-1609.
16. H.A.A. Seed Ahmed, O.M. Ntwaeaborwa and R.E. Kroon, *J. Lumin.* **135** (2013) 15-19.
17. H.A.A. Seed Ahmed, O.M. Ntwaeaborwa and R.E. Kroon, *Curr. Appl. Phys.* **13** (2013) 1264-1268.
18. Q. Xu, B. Lin and Y. Mao, *J. Lumin.* **128** (2008) 1965-1968.
19. X.Y. Huang, X.H. Ji and Q.Y. Zhang, *J. Am. Ceram. Soc.* **94** (2011) 833-837.
20. L. Tian, *J. Rare Earths* **28** (2010) 37-39.
21. Y.N. Xue, F. Xiao and Q.Y. Zhang, *Spectrochim. Acta, Part A* **78** (2011) 607-611.
22. G. Ju, Y. Hu, L. Chen, X. Wang, Z. Mu, H. Wu and F. Kang, *J Electrochem. Soc* **158** (2011) J294-J299.
23. G. Ju, Y. Hu, L. Chen, X. Wang, Z. Mu, H. Wu and F. Kang, *J. Lumin.* **132** (2012) 717-721.
24. L. Han, Y. Wang, J. Zhang and Y. Wang, *Mater. Chem. Phys.* **139** (2013) 87-91.

25. J.Y. Park, H.C. Jung, G.S.R. Raju, B.K. Moon, J.H. Jeong, S. Son and J.H. Kim, *Mater. Res. Bull.* **45** (2010) 572-575.
26. H.St.C. O'Neill and A. Navrotsky. *Am. Mineral.* **68** (1983) 181-194.
27. R.J. Hill, J.R. Craig and G.V. Gibbs, *Phys. Chem. Miner.* **4** (1979) 317-339.
28. R.D. Shannon, *Acta Cryst. A* **32** (1976) 751-767.
29. V. Singh, M.D. Masuqul Haque and D.-K. Kim, *J. Bull. Korean Chem. Soc.* **28** (2007) 2477-2480.
30. X.Y. Chen, C. Maa, Z.J. Zhang and X.X. Li, *Microporous Mesoporous Mater.* **123** (2009) 202-208.
31. K.C. Patil, M.S. Hegde, T Ratan and S.T. Aruna, *Chemistry of Combustion Synthesis, Properties and Applications Nanocrystalline Oxide Materials*, World Scientific (New Jersey, 2008).
32. V.D. Mote, Y. Purushotham and B.N. Dole, *J. Theor. Appl. Phys.* **6** (2012) 6 (8 pages).
33. L.G. Jacobsohn, M.W. Blair, S.C. Tornga, L.O. Brown, B.L. Bennett and R.E. Muenchausen, *J. Appl. Phys.* **104** (2008) 124303 (7 pages).
34. R.E. Kroon, H.C. Swart, O.M. Ntwaeaborwa and H.A.A. Seed Ahmed, *Phys. B* (2013). In press:
<http://www.sciencedirect.com/science/article/pii/S0921452613006820>

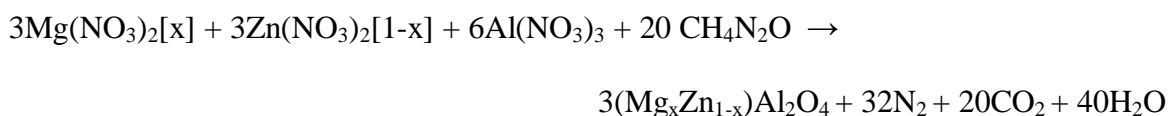
7 Enhanced luminescence from Tb for the mixed spinel $(\text{Mg}_x\text{Zn}_{1-x})\text{Al}_2\text{O}_4$

7.1 Introduction

Spinel, which have the general formula AB_2O_4 , often occur naturally as minerals but are also synthesized and studied for their interesting electrical, magnetic and optical properties. MgAl_2O_4 finds diverse applications due to its mechanical strength, chemical inertness, relatively low density, high melting point, high thermal shock resistance, low thermal expansion coefficient, resistance to neutron irradiation and low dielectric loss, and has been used for humidity sensors [1] and tuneable solid-state lasers [2]. ZnAl_2O_4 is widely used as a catalyst and has also been patented for UV reflective optical coatings [3]. It is electroconductive and has been considered for thin film electroluminescent and plasma displays, as well as for ultraviolet (UV) photo-electronic devices and stress sensors [4-6]. Both materials have been used as phosphor hosts for a variety of luminescent ions [7,8] and $\text{MgAl}_2\text{O}_4:\text{Mn}$ has used as green phosphor for television tubes [9] while $\text{MgAl}_2\text{O}_4:\text{Ce}$ has been investigated as a long afterglow phosphor [10]. An important difference between the materials is that the bandgap of MgAl_2O_4 (7.8 eV [11]) is much larger than that of ZnAl_2O_4 (3.8-4.1 eV [12]). However, since Mg and Zn ions are similar in size, the lattice constants of these materials are close to one another and it is interesting to consider the intermediate material $(\text{Mg}_x\text{Zn}_{1-x})\text{Al}_2\text{O}_4$ as a possible phosphor host. In this paper, the combustion method is used to prepare undoped as well as Tb^{3+} -doped $(\text{Mg}_x\text{Zn}_{1-x})\text{Al}_2\text{O}_4$ with different proportions of Mg ($0 \leq x \leq 1$), and the structural and optical properties are reported.

7.2 Experimental

$(\text{Mg}_x\text{Zn}_{1-x})\text{Al}_2\text{O}_4$ was prepared using the combustion method according to the reaction



where the waters of crystallization of the nitrates have been omitted for simplicity.

Analytical grade $\text{Al}(\text{NO}_3)_3 \cdot 9\text{H}_2\text{O}$, $\text{Zn}(\text{NO}_3)_2 \cdot 4\text{H}_2\text{O}$ and $\text{Mg}(\text{NO}_3)_2 \cdot 6\text{H}_2\text{O}$ were used as oxidizers and urea ($\text{CH}_4\text{N}_2\text{O}$) was used as a fuel. Generally about 10 mmol of $\text{Al}(\text{NO}_3)_3 \cdot 9\text{H}_2\text{O}$ was added to stoichiometric amounts of the other reactants in about 6 ml of distilled water, which was stirred vigorously for 30 min to obtain a homogeneous transparent solution. In some cases MgO dissolved in concentrated nitric acid was used as the source of magnesium nitrate. The solution was transferred to a porcelain crucible and placed into a muffle furnace at 520 °C. Within a few minutes the water boiled off and the sample ignited as the exothermic combustion reaction occurred, giving off copious quantities of gas and heating the material to well above the furnace temperature. After the reaction the foamy white product was removed from the furnace and crushed into powder using a pestle and mortar, after which it was annealed in air at 700 °C for 4 hours. Doping of samples with Tb^{3+} ions was achieved by replacing an appropriate amount of $\text{Al}(\text{NO}_3)_3 \cdot 9\text{H}_2\text{O}$ with the same amount of $\text{Tb}(\text{NO}_3)_3 \cdot 5\text{H}_2\text{O}$.

X-ray diffraction (XRD) measurements were made at room temperature using a Bruker D8 Advance diffractometer operating at 40 kV and 40 mA with Cu $\text{K}\alpha$ x-rays of wavelength 154.178 pm. A Shimadzu SSX-550 scanning electron microscope (SEM) was used to obtain images of the samples. Luminescence properties were measured at room temperature using a Cary Eclipse fluorescence spectrophotometer and excitation spectra

were measured at 10 K using synchrotron radiation at the SUPERLUMI station at DESY [13] and corrected for the response of the system using sodium salicylate.

7.3 Results and discussion

7.3.1 Structure

Figure 7.1 shows a SEM image of one of the samples ($\text{Mg}_{0.75}\text{Zn}_{0.25}\text{Al}_2\text{O}_4:\text{Tb}$ 0.5 mol%) after the combustion process. It reveals the formation of different sized agglomerates displaying an irregular morphology in the form of plates. The pores are consistent with the fact that a large amount of gas evolves during the combustion synthesis.

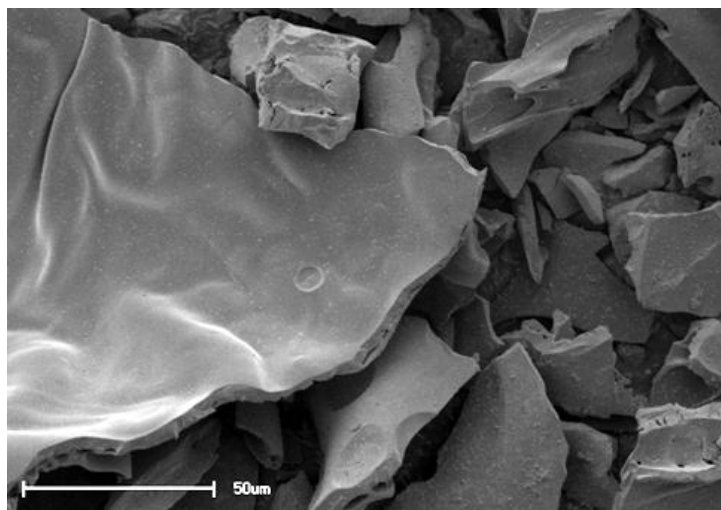


Figure 7.1: SEM image of $\text{Mg}_{0.75}\text{Zn}_{0.25}\text{Al}_2\text{O}_4:\text{Tb}$ 0.5 mol% produced with the combustion method.

The XRD spectra of undoped $(\text{Mg}_x\text{Zn}_{1-x})\text{Al}_2\text{O}_4$ before and after annealing revealed no significant differences and the results from the annealed samples are shown in figure 7.2, together with the expected patterns for MgAl_2O_4 (JCPDS 75-0710) and ZnAl_2O_4 (JCPDS 82-1043) spinels. These correspond very well to the experimental results, confirming the successful preparation of the host materials. From the positions of the peaks it is clear that the lattice parameter changes very little between the two materials and that

$(\text{Mg}_x\text{Zn}_{1-x})\text{Al}_2\text{O}_4$ has the same spinel structure irrespective of the magnesium content (x). This is due to the similar ionic radii of Mg^{2+} (58.5 pm) and Zn^{2+} (58 pm) [14]. However, the x-ray scattering factor of Zn is greater than that of Mg due to its higher atomic number (more electrons) and so the relative size of the x-ray diffraction peaks vary significantly with composition, as can be seen by comparing the heights of the (220) and (400) reflections relative to the (311) reflection between them.

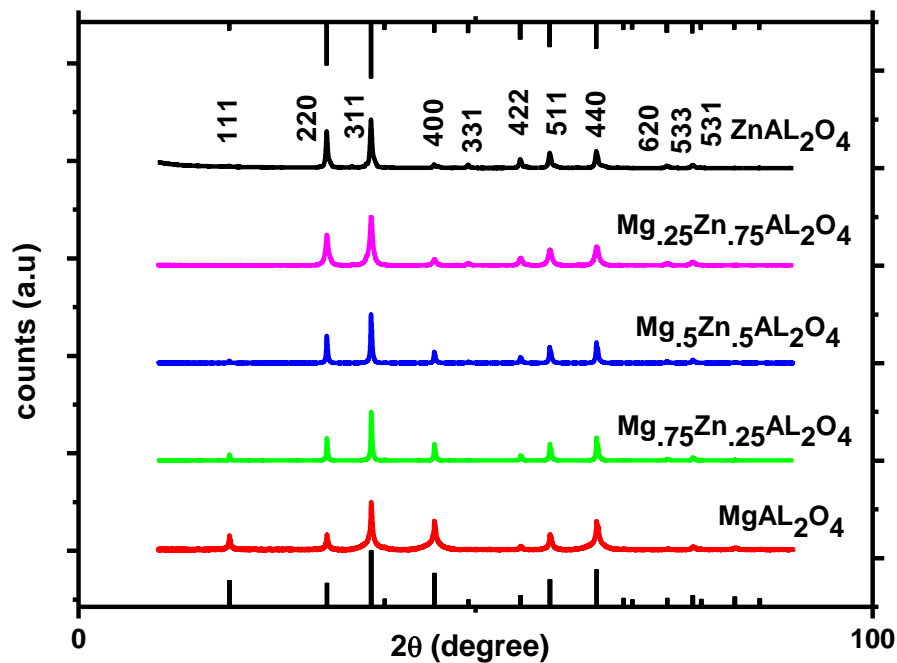
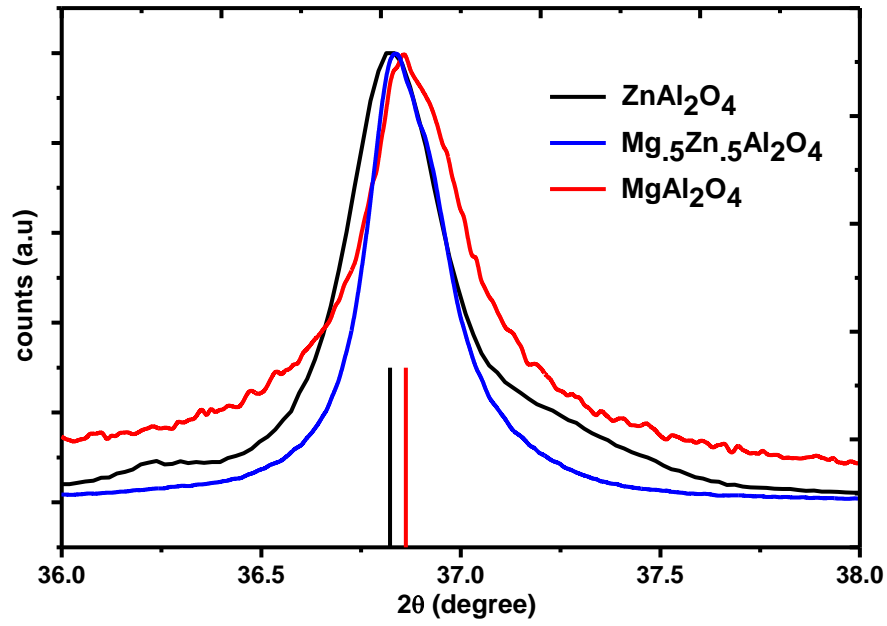
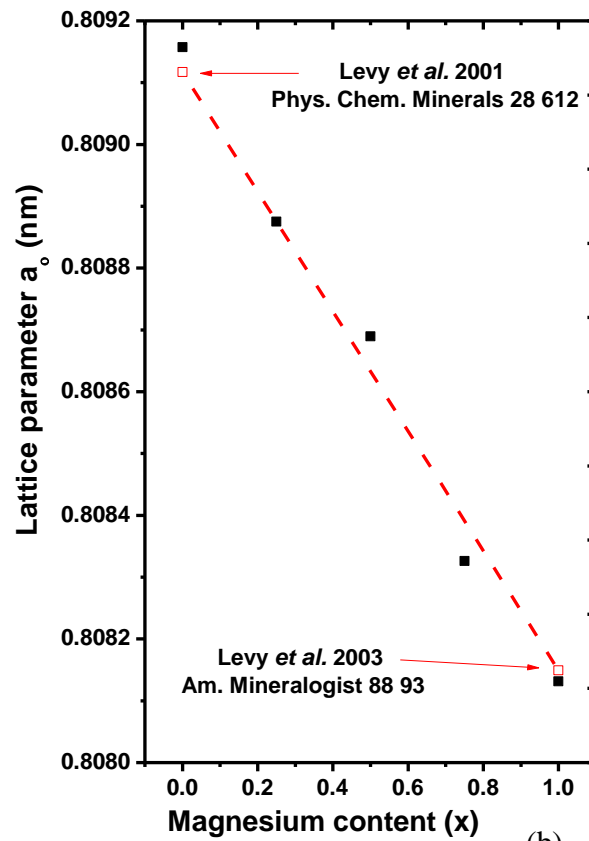


Figure 7.2: X-ray diffraction spectra of $(\text{Mg}_x\text{Zn}_{1-x})\text{Al}_2\text{O}_4$.

Figure 7.3(a) shows the (311) XRD reflection in more detail, together with the expected 2θ position in MgAl_2O_4 and ZnAl_2O_4 . Figure 7.3(b) shows the lattice parameter as a function of composition and it varies linearly between the values for the boundary compounds. The width of this peak does not vary substantially with composition and its full-width-at-half-maximum was used to determine the crystallite size of about 25 nm using the Scherrer equation $D = 0.9\lambda/(\beta \cos\theta)$, where λ is the x-ray wavelength and θ the diffraction angle.



(a)



(b)

Figure 7.3: (a) Detail of (311) XRD peak of $(\text{Mg}_x\text{Zn}_{1-x})\text{Al}_2\text{O}_4$. (b) Lattice parameter of $(\text{Mg}_x\text{Zn}_{1-x})\text{Al}_2\text{O}_4$ as a function of Mg content (x). The dashed line joins the lattice parameters for MgAl_2O_4 [15] and ZnAl_2O_4 [16].

In figure 7.3(a) small peak on the low angle side can be seen for ZnAl_2O_4 (at 36.2°) which is absent for MgAl_2O_4 . This peak is due to a small amount of ZnO impurity formed during the reaction, and could not easily be removed by varying the quantities of reactants during the combustion process. No extra peaks were observed in the samples doped with Tb^{3+} , indicating that it was successfully incorporated in the lattice, where it is assumed that it substitutes the Al^{3+} ions which have the same valency [17].

7.3.2 Optical properties

Figure 7.4 shows the photoluminescence excitation and emission spectra for the $(\text{Mg}_x\text{Zn}_{1-x})\text{Al}_2\text{O}_4:\text{Tb}(0.5 \text{ mol}\%)$ samples measured with the Cary-Eclipse. Together with usual green emission from Tb^{3+} ions in the wavelength region longer than 480 nm, corresponding to ${}^5\text{D}_4 \rightarrow {}^7\text{F}_J$ ($J=3,4,5,6$) transitions, there is also blue emission below 480 nm corresponding to ${}^5\text{D}_3 \rightarrow {}^7\text{F}_J$ ($J=4,5,6$) transitions for some samples. As is common for hosts doped with Tb, the green ${}^5\text{D}_4 \rightarrow {}^7\text{F}_5$ emission line at 544 nm is the strongest.

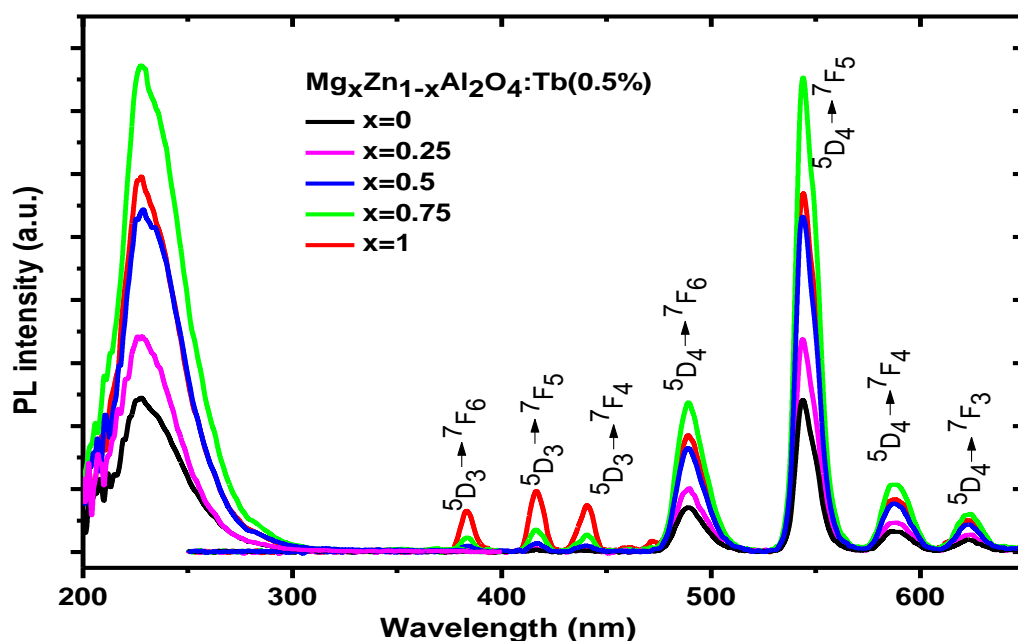


Figure 7.4: Room temperature excitation spectra of $(\text{Mg}_x\text{Zn}_{1-x})\text{Al}_2\text{O}_4$ measured with the Cary Eclipse.

Figure 7.5(a) shows the intensity of the green (544 nm) and blue (416 nm) luminescence as a function of composition. The intensity of the blue emission from the 5D_3 level increases with increasing Mg concentration. The relative intensity of the blue and green emissions from Tb are often discussed in terms of cross-relaxation effects [18], where for low concentrations of Tb^{3+} ions which are then isolated from one another blue emission from the 5D_3 level can be observed, whereas when the Tb concentration is increased, electrons excited to the 5D_3 level may transfer some of their energy to neighbouring Tb^{3+} ions and thereby drop to the 5D_4 level, from which they emit radiatively instead of from the 5D_3 level. However, since all the samples in figure 7.5(a) are doped to the same Tb concentration of 0.5 mol%, this cross-relaxation effect cannot simply explain the observed change in the blue emission. If clustering of Tb ions occurs more predominantly in the samples containing small amounts of Mg then cross-relaxation may indeed play a role, but a more likely explanation of the effect is the changing size of the bandgap as a function of composition. $ZnAl_2O_4$ has the smallest bandgap and therefore the Tb 5D_3 level will lie closest (or possibly inside) the conduction band for this material. Electrons excited to the 5D_3 level could therefore be transferred to the conduction band, which would account for the lack of blue emissions from this level. With increasing Mg content the bandgap increases and blue emission from the 5D_3 level becomes possible, and increases in intensity as the level moves further from the conduction band. The maximum green emission occurs for the intermediate composition $Mg_{0.75}Zn_{0.25}Al_2O_4$ and is superior to that of both $ZnAl_2O_4$ and $MgAl_2O_4$. Figure 7.5(b) shows the Tb emission intensity as a function of doping concentration for this composition. The maximum intensity occurs for the Tb^{3+} concentration of 0.5 mol%, in agreement with the value reported previously for $MgAl_2O_4:Tb$ [19].

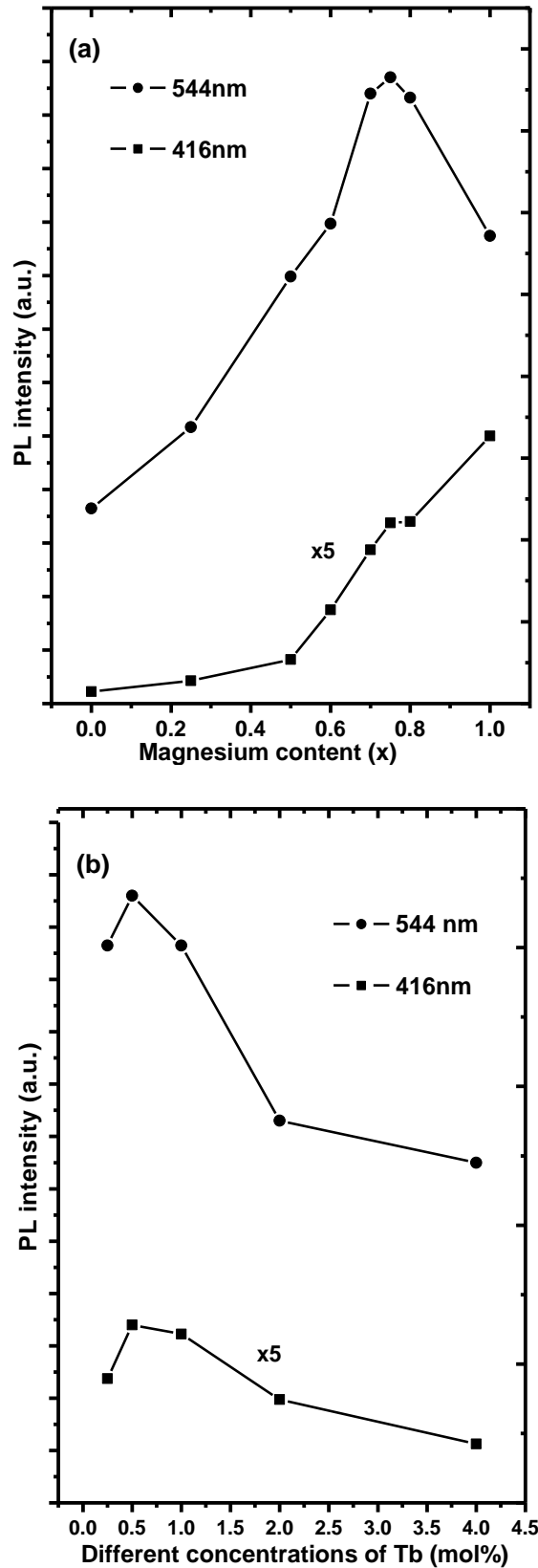


Figure 7.5: Intensity of the green (544 nm) and blue (416 nm) luminescence from: (a) $(\text{Mg}_x\text{Zn}_{1-x})\text{Al}_2\text{O}_4:\text{Tb}(0.5 \text{ mol}\%)$ as a function composition. (b) $\text{Mg}_{0.75}\text{Zn}_{0.25}\text{Al}_2\text{O}_4:\text{Tb}$ for different Tb doping concentrations.

The Tb³⁺ excitation spectra in figure 7.4 (measured with the Cary-Eclipse using the green $^5D_4 \rightarrow ^7F_5$ emission line at 544 nm) consist of broad bands in the region from 220 to 300 nm originating from the f-d transition. A small shift in the peak with changing composition is apparent. Although the relative intensity of these peaks is reliable, the spectra are not corrected for the response of the system, which can only measure down to 200 nm since this is the range of the xenon lamp. Low temperature (10 K) excitation spectra extending down to 100 nm and corrected for the system response were measured for the same transition using synchrotron radiation at SUPERLUMI (DESY) and are shown in figure 7.6. Here the relative intensities are not reliable due to the increased challenge of positioning samples reproducibly, but the excitation curve is accurate.

From figure 7.6 it is clear that the excitation bands measured with the Cary-Eclipse (figure 7.4) are truncated at shorter wavelengths and that more than one excitation band occurs. Generally there are five allowed f-d transitions for Tb [20], which have been modelled in several hosts [21]. In $Y_3(Al_{1-x}Ga_x)_5O_{12}$ the peak positions have been found to shift apart as the Ga content decreases and the bandgap increases [22]. Although five distinct bands cannot be identified in our spectra, the range of the f-d excitation region is not dissimilar to that reported for Tb in other hosts and a widening of the region with increasing Mg content and therefore bandgap is apparent. On the short wavelength side there is a shift to shorter wavelengths as the Mg content increases, but on the longer wavelength side the extreme excitation spectrum corresponds to $x = 0.75$, which also corresponds to the maximum green emission intensity. The wavelength corresponding to the host bandgap energy varies from about 130 nm for $MgAl_2O_4$ to 260 nm for $ZnAl_2O_4$, and although the f-d excitation overlaps most of this region, it does not appear that there is an excitation peak corresponding to band-to-band transitions i.e. the Tb is not excited through the host.

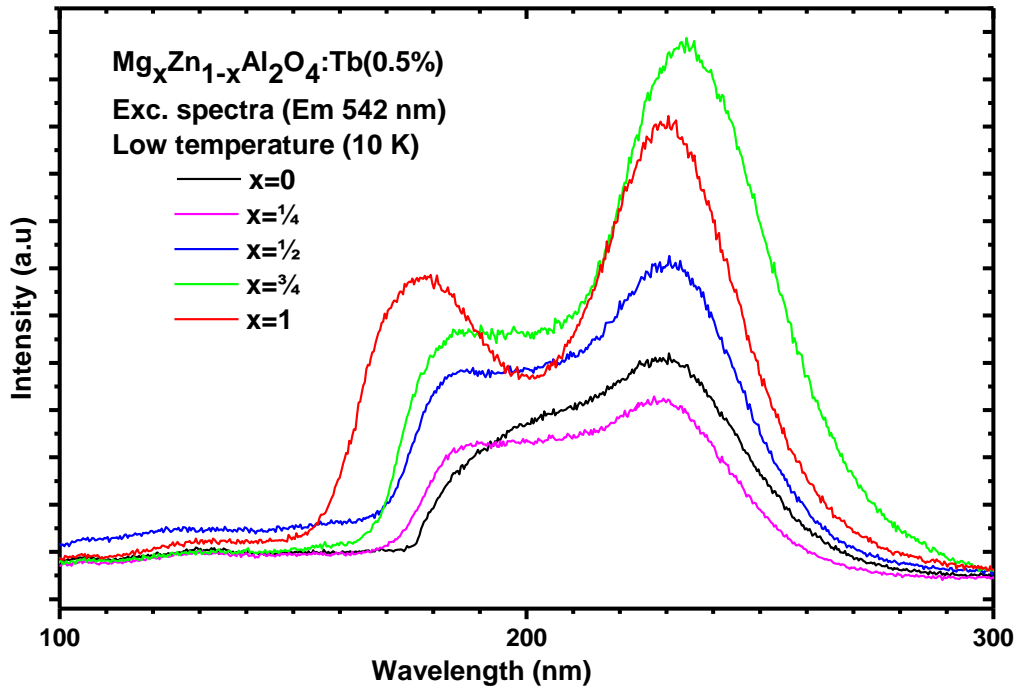


Figure 7.6: Low temperature excitation spectra of $(\text{Mg}_x\text{Zn}_{1-x})\text{Al}_2\text{O}_4$ measured at SUPERLUMI.

7.4 Conclusion

The mixed spinel $(\text{Mg}_x\text{Zn}_{1-x})\text{Al}_2\text{O}_4$ has been successfully synthesized using the combustion method and doped with Tb. The maximum PL intensity of the green emission at 544 nm occurred for $\text{Mg}_{0.75}\text{Zn}_{0.25}\text{Al}_2\text{O}_4$ and the optimum Tb concentration was found to be 0.5 mol%. The blue emission at 416 nm was almost absent for ZnAl_2O_4 , but increased with the Mg content and was a maximum for MgAl_2O_4 . This is attributed to the increasing bandgap with Mg content.

7.5 References

1. O. Shpotyuk, A. Ingram, H. Klym, M. Vakiv, I. Hadzaman and J. Filipecki, *J. Eur. Ceram. Soc.* **25** (2005) 2981-2984.
2. A. Jouini, A. Yoshikawa, Y. Guyot, A. Brenier, T. Fukuda and G. Boulon, *Opt. Mat.* **30** (2007) 47-49.
3. J.F. Cordaro (1998) US Patent No. 5820669.
4. M. García-Hipólito, C.D. Hernández-Pérez, O. Alvarez-Fregoso, E. Martínez, J. Guzmán-Mendoza and C. Falcony, *Opt. Mat.* **22** (2003) 345-351.
5. Z. Lou and J. Hao *Thin Solid Films* **450** (2004) 334-340.
6. Z. Lou and J. Hao, *Appl. Phys. A* **80** (2005) 151-154.
7. K.G. Tshabalala, S-H. Cho, J-K. Park, S.S. Pitale, I.M. Nagpure, R.E. Kroon, H.C. Swart and O.M. Ntwaeaborwa *J. Alloys Compd.* **509** (2011) 10115-10120.
8. R. J. Wiglusz and T. Grzyb, *Opt. Mat.* **33** (2011) 1506-1513.
9. T.H. Maiman, R.H. Hoskins, B.H. Soffer, R.C. Pastor and M.A. Pearson (1968) US Patent No. 3396119.
10. D. Jia and W.M. Yen, *J. Lumin.* **101** (2003) 115-121.
11. S.K. Sampath, D.G. Kanhere and R. Pandey, *J. Phys.: Condens. Matter* **11** (1999) 3635-3644.
12. H. Dixit, N. Tandon, S. Cottenier, R. Saniz, D. Lamoen, B. Partoens, V. van Speybroeck and M. Waroquier, *New J. Phys.* **13** (2011) 063002 (10 pages).
13. G. Zimmerer, *Rad. Meas.* **42** (2007) 859-864.
14. H.St.C. O'Neill and A. Navrotsky. *Am. Mineral.* **68** (1983) 181-194.
15. D. Levy, A. Pavese and M. Hanfland, *Am. Mineral.* **88**(2003) 93-98.
16. D. Levy, A. Pavese, A. Sani and V. Pischedda, *Phy. Chem. Minerals* **28** (2001) 612-618.

17. D. Silva, A. Abreu, M R. Davolos and M. Rosaly, *Opt. Mat.* **33** (2011) 1226-1233.
18. J.Y. Park, H.C. Jung, G.S.R. Raju, B.K. Moon, J.H. Jeong and J.H. Kim, *J. Lumin.* **130** (2010) 478-482.
19. E. Aluga Raja, B. Dhabekar, S. Menon, S.P. More, T.K. Gundu Rao and R.K. Kher, *Indian J. Pure & Applied Phys.* **47** (2009) 420.
20. P. Dorenbos, *J. Phys.: Condens. Matter* **15** (2003) 6249-6268.
21. L. van Pieterse, M.F. Reid, G.W. Burdick and A. Meijerink, *Phys Rev B* **65** (2002) 045114.
22. A. Mayolet, W. Zhang, E. Simoni, J. C. Krupa and P. Martin, *Opt. Mat.* **4** (1995) 757.

8

Effect of annealing temperature on the optical properties of $\text{Mg}_{0.75}\text{Zn}_{0.25}\text{Al}_2\text{O}_4$ thin films deposited by sol-gel spin-coating

8.1 Introduction

Phosphor films find many uses for light emitting devices and display applications such as cathode ray tubes and light emitting diodes. Thin film phosphors have several advantages compared with powders, such as higher lateral resolution from smaller grains, better thermal stability and better adhesion to the solid surface [1]. Thin films are usually prepared by several techniques such as evaporation, electron-beam deposition, sputtering method, pulse laser deposition, chemical vapour deposition and sol-gel spin-coating [2-4]. Among these techniques sol-gel spin-coating is attractive due to its low cost, low temperature operation and environmental friendliness [5-7]. Moreover sol-gel spin-coating has been widely used in the development of optical materials for optoelectronic devices because it is easily controlled by varying some the growth parameters such as the spin speed, the viscosity of the solution and the annealing temperature.

Spinel oxides find many applications as magnetic, electric, ceramic, catalysis and optical materials. They have the formula AB_2O_4 , where A and B represent divalent and trivalent cations respectively [8] and belong to the cubic space group $Fd\bar{3}m$ [9]. The cations occupy twice the number of octahedral sites as tetrahedral sites and in the normal spinel arrangement these are occupied by Al^{3+} and Mg^{2+} ions respectively. The most promising spinel oxides are magnesium aluminate (MgAl_2O_4) and zinc aluminate (ZnAl_2O_4) which

have received special attention as technologically important materials because of their attractive physical properties [10, 11]. Both these materials are used as phosphor hosts for a variety of luminescent ions [12, 13] and have been considered for thin film electroluminescence [14, 15]. Since Mg and Zn ions are similar in size, the lattice constants of these materials are close to one another and it is interesting to consider the intermediate material $(\text{Mg}_x\text{Zn}_{1-x})\text{Al}_2\text{O}_4$ as a possible phosphor host. Some works on sol-gel thin films have been published using MgAl_2O_4 and ZnAl_2O_4 separately [16, 17], while $(\text{Mg}_x\text{Zn}_{1-x})\text{Al}_2\text{O}_4$ thin film fabrication has not been reported yet.

For $(\text{Mg}_x\text{Zn}_{1-x})\text{Al}_2\text{O}_4$ powders doped with Tb prepared by the combustion method, the optimum green luminescence was found to correspond to $x = 0.75$ with a Tb concentration of 0.5 mol%. In the present study, $\text{Mg}_{0.75}\text{Zn}_{0.25}\text{Al}_2\text{O}_4:\text{Tb}$ thin films were fabricated using the sol-gel spin-coating method. The structure and morphology of the films as well as their optical properties were investigated.

8.2 Materials and methods

The Si(100) substrates were cleaned ultrasonically using acetone, ethanol and distilled water. The starting materials for synthesis of 0.5 mol% Tb doped $\text{Mg}_{0.75}\text{Zn}_{0.25}\text{Al}_2\text{O}_4$ were magnesium nitrate ($\text{Mg}(\text{NO}_3)_2 \cdot 6\text{H}_2\text{O}$, 0.00375 mol), aluminium nitrate ($\text{Al}(\text{NO}_3)_3 \cdot 9\text{H}_2\text{O}$, 0.01 mol) and zinc nitrate ($\text{Zn}(\text{NO}_3)_2 \cdot 4\text{H}_2\text{O}$, 0.00125 mol). The Tb^{3+} ions were obtained by replacing an appropriate amount of $\text{Al}(\text{NO}_3)_3 \cdot 9\text{H}_2\text{O}$ with the same amount of $(\text{Tb}(\text{NO}_3)_3 \cdot 5\text{H}_2\text{O})$, 0.00025 mol). All chemicals were mixed together with 100 ml of ethanol at 70 °C by magnetic stirring for 30 min to obtain a homogeneous transparent solution. The ethanol is used to improve the wetting property between the solution and the substrate and control the viscosity of the solution. Then 10 ml of ethylene glycol was added to the

solution as a complexing agent and stirring continued for a further 2 h. The transparent solution was then spin-coated using an SPS SPIN 150 from Semiconductor Production Systems on 2 cm x 2 cm substrates at 3000 rpm for 30 s, followed by drying at 110 °C on a hot plate for 10 min and then annealing in a furnace at 500 °C for 10 min. The process was repeated several times to obtain films with the desired thickness. The sample was cleaved to four pieces for annealing at 600 °C, 800 °C, 1000 °C and 1200 °C for 1 h in the atmospheric air.

The structure of the thin films was characterized by x-ray diffraction (XRD) using a Bruker D8 Advance diffractometer operating at 40 kV and 40 mA with Cu K α x-rays of wavelength 1.5406 Å. The surface morphology and roughness were examined by atomic force microscopy (AFM) with a Shimadzu SPM-9600 set in contact mode. Chemical composition analyses and depth profiles were carried out using a PHI 700 nano scanning Auger electron microprobe (NanoSAM). Surveys were done with a 25 kV 10 nA electron beam and a 2 kV Ar ion gun was used for sputtering. The optical properties of the thin films were measured using a Cary Eclipse spectrophotometer at room temperature using a monochromatized xenon flash lamp as an excitation source.

8.3 Results and discussion

8.3.1 Structure and morphology

Figure 8.1 shows the XRD patterns of $\text{Mg}_{0.75}\text{Zn}_{0.25}\text{Al}_2\text{O}_4:\text{Tb}^{3+}$ powder [18] and the thin films produced in this study by spin-coating. All peaks of the XRD patterns of the thin films annealed between 600 °C and 1000 °C were consistent with the structure of magnesium aluminate (JCPDS 75-0710) and zinc aluminate (JCPDS 82-1043) spinels. The (311) diffraction peak is strongest for the powder sample, however in thin films the

dominant peak observed was the (111) reflection. This shows that the films have preferential growth in the (111) orientation on the Si(100) substrate. Bae *et al.* reported that the orientation of ZnGa_2O_4 spinel thin film phosphors deposited by a pulsed laser ablation changed with the substrate temperature, oxygen pressure and a type of substrates that was used, and that the (111) reflection was dominant when using a $\text{Al}_2\text{O}_3(0001)$ substrate at a temperature of 550°C and an O_2 pressure of 100 mTorr [19].

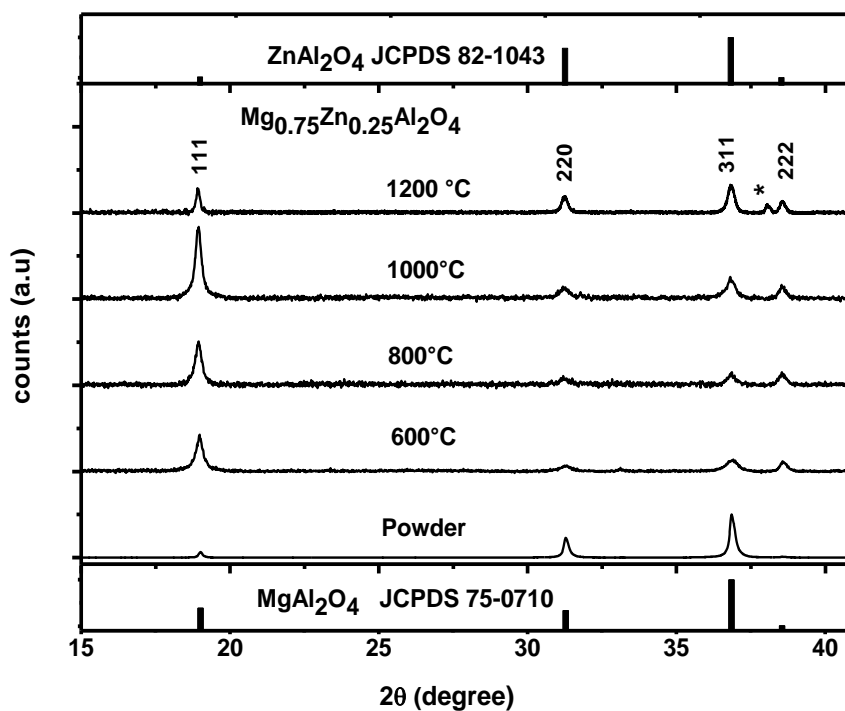


Figure 8.1: XRD spectra of $\text{Mg}_{0.75}\text{Zn}_{0.25}\text{Al}_2\text{O}_4:\text{Tb}^{3+}$ powder and thin films annealed at different temperature

In order to quantify the effect of the annealing temperature on the film texture, we analyzed the evolution of the texture coefficient $T_C(hkl)$, which gives the measure of orientation of each reflection compared with a completely randomly oriented sample.

$T_C(hkl)$ for all the planes was calculated using the expression [20]

$$T_c(hkl) = \frac{I(hkl)/I_0(hkl)}{N^{-1} \sum I(hkl)/I_0(hkl)} \quad (1)$$

where I is the measured intensity of the reflection, I_0 is the corresponding intensity from the JCPDS standard intensity for a powder sample and N is the number of diffraction peaks observed in the XRD pattern. Because there is no JCPDS file for the mixed composition $\text{Mg}_{0.75}\text{Zn}_{0.25}\text{Al}_2\text{O}_4$ used here, we used the intensities from our powder sample instead. Texture coefficients close to unity suggest that the sample consists of randomly oriented crystallites, while values larger than unity indicate that a preferred orientation exists in the sample. The intensity of the XRD peaks for the film and the powder were measured and are given in Table 1, and were used to calculate the texture coefficients shown in figure 8.2. The texture coefficient of the (111) planes is about 2.7, much larger than unity and showing this is the preferential orientation. Meanwhile, the texture coefficient of the (220) and (311) planes are only about 0.1 showing that very few grains have this orientation parallel to the surface. This preferred orientation is independent of the annealing temperature up to 1000 °C.

Table 1: The XRD peak intensity for the (111), (220) and (311) planes of $\text{Mg}_{0.75}\text{Zn}_{0.25}\text{Al}_2\text{O}_4:\text{Tb}^{3+}$ powder and thin films annealed at different temperature (arbitrary units).

	$I(111)$	$I(220)$	$I(311)$
Powder	262	932	2003
Film annealed at 600 °C	1708	291	562
Film annealed at 800 °C	2053	440	625
Film annealed at 1000 °C	3397	603	1054

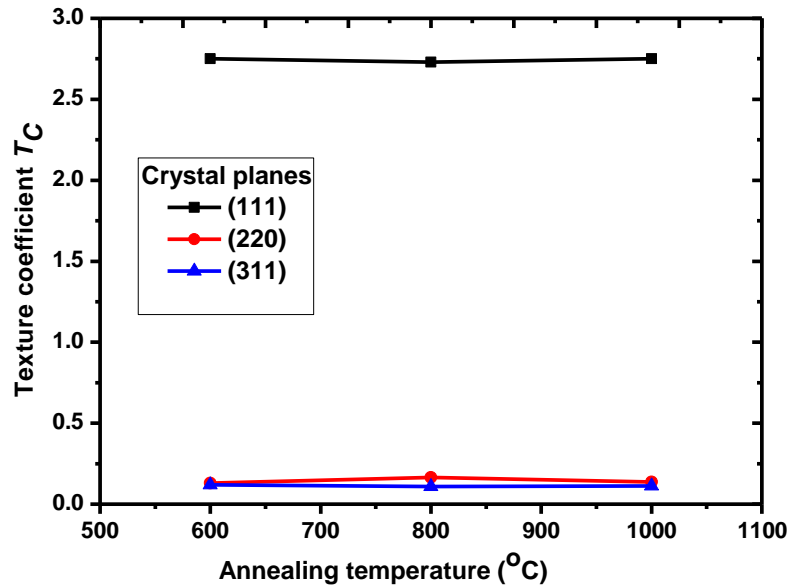


Figure 8.2: Texture coefficient of thin film with different annealing temperature calculated from XRD pattern.

The XRD patterns in figure 8.1 of the thin films were sharpened up to 1000 °C, which indicates that the crystalline size has increased with an increase in the annealing temperature. The crystallite size was estimated by the Scherrer formula

$$D = \frac{k\lambda}{\beta \cos \theta} \quad (2)$$

where D is the characteristic crystal size, β is the angular width of the peak at half maximum height (radians), λ is the x-ray wavelength and θ the diffraction angle. The results are shown in figure 8.3 and as expected the crystallite size was found to increase with an increase of the annealing temperature. In figure 8.3 the crystallite sizes calculated from the (111) reflections are larger than those of the other planes. This shows that the crystallites are not equiaxed but elongated along the (111) preferred orientation direction.

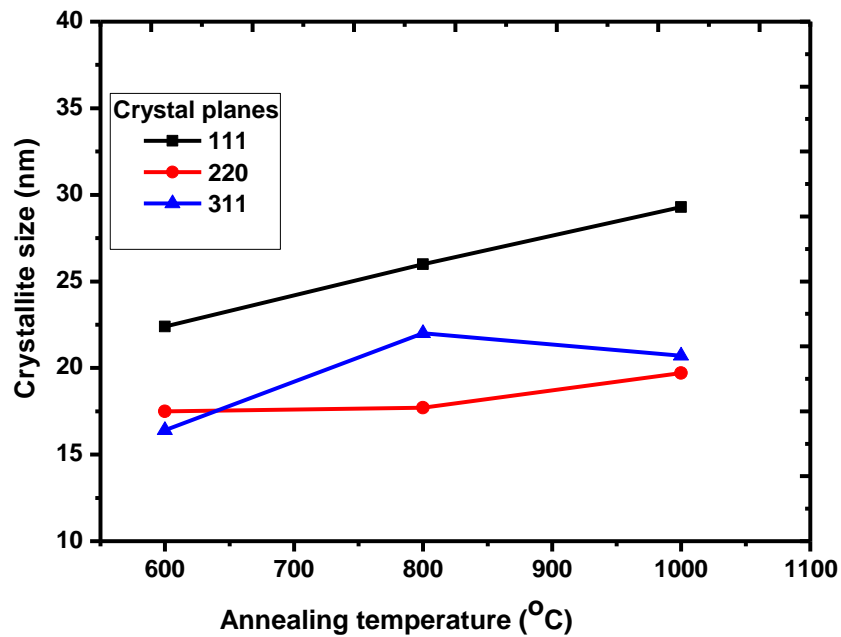


Figure 8.3: Crystallite size of thin film with different annealing temperature calculated from XRD powder pattern.

As can be seen in figure 8.1 the annealing of the sample at 1200 °C resulted in a change in the relative size in the peaks, compared to the sample at lower temperature. The relative intensity of the peak (311) increased and (111) decreased and the pattern is similar to the powder. This means there is a change of the orientation of the $Mg_{0.75}Zn_{0.25}Al_2O_4$ thin film. For this sample there is a random orientation of crystallites. In addition, the sample annealed at 1200 °C shows an extra new peak labelled with an asterisk (*) in the pattern centred at 38°, showing the existence of a new phase. The change in orientation and the new peak indicate that a new compound was formed as a result of atomic interdiffusion between the substrate and the film. The new compound may be formed by reaction of Mg, Zn or Al with Si to produce new material, probably a silicate. A recent publication showed similar behaviour reported by Yousif *et al.* [21] where the conversion of an

$Y_3(Al;Ga)_5O_{12}$ thin film to α - Y_2SiO_7 was observed when the films were annealed at temperatures of 1200 °C.

Figure 8.4(a) shows the AFM image of the surface of a film which has been annealed at 600 °C for 1 h. This produces a thin film that is smooth (rms roughness is approximately 1.0 nm) with no cracks and that has homogeneously distributed grains. To check the uniformity of the film structure, the AFM images were obtained by scanning at about 10 different regions and all showed similar morphologies.

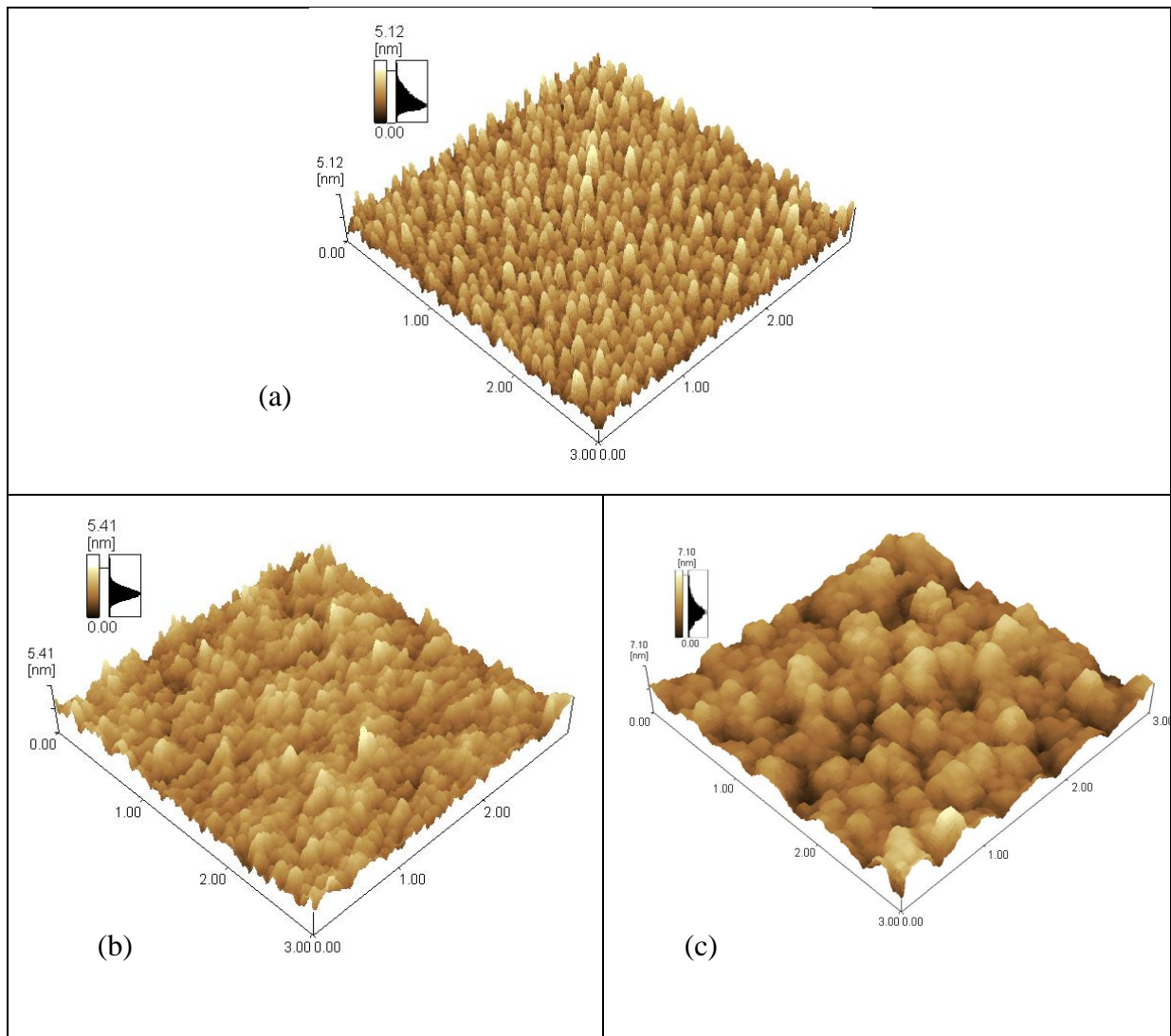


Figure 8.4: AFM images of the surface of $Mg_{0.75}Zn_{0.25}Al_2O_4:Tb^{3+}$ thin films having 10 layers on Si substrate annealed for 1 h at (a) 600 °C, (b) 800 °C and (c) 1000 °C respectively.

When the annealing temperature is increased to 800 °C (figure 8.4 (b)), the film is still smooth, but the roughness increases to 1.2 nm because the particle size has increased. The roughness has increased to 1.8 nm for the thin film annealed at 1000 °C.

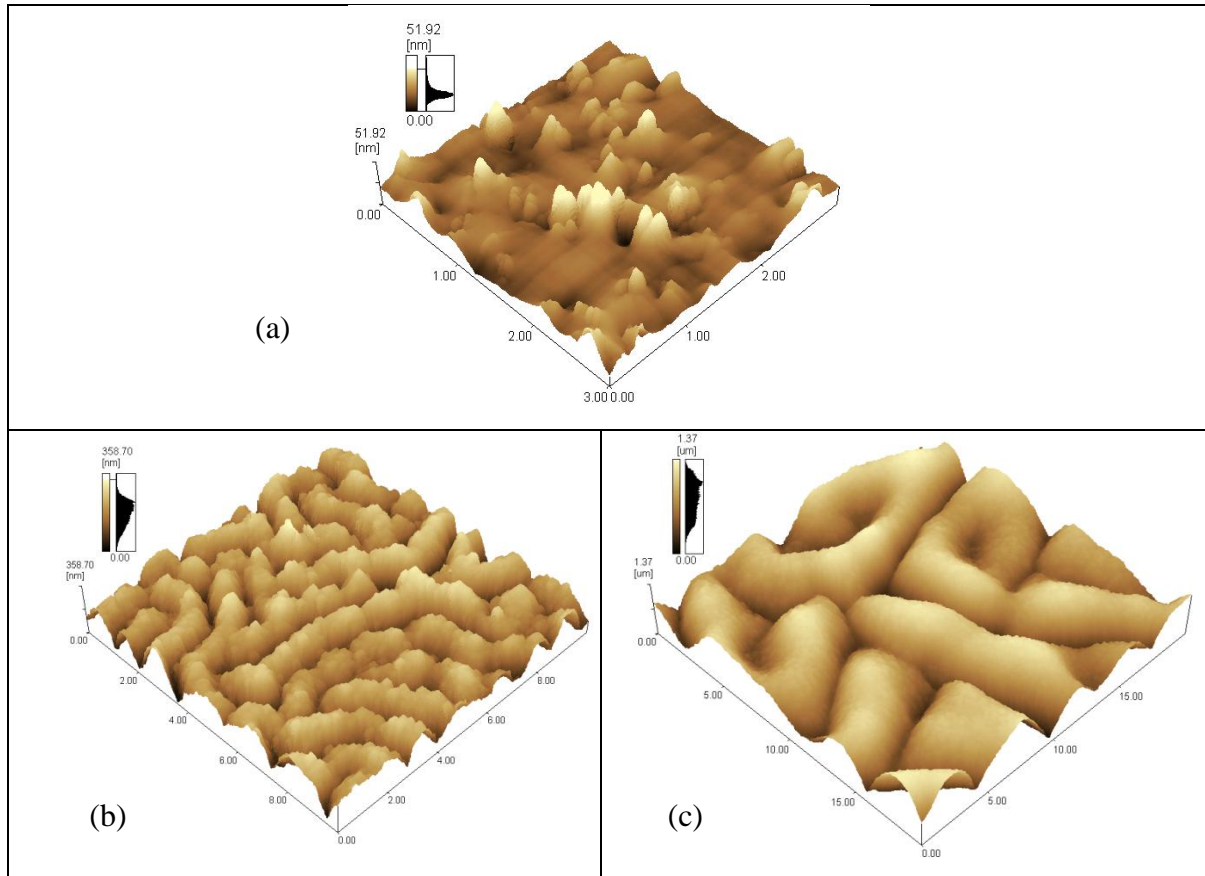


Figure 8.5: AFM images of the surface of $\text{Mg}_{0.75}\text{Zn}_{0.25}\text{Al}_2\text{O}_4:\text{Tb}^{3+}$ thin films on Si substrate annealed at 1200 °C for 1 h having (a) 5 layers, (b) 10 layers and (c) 20 layers respectively.

Figure 8.5 shows the AFM images of the surface of films of different thicknesses (number of layers) which have been annealed at 1200 °C for 1 h. The morphology of these films is significantly different from those annealed at lower temperatures (figure 8.4). After annealing at 1200 °C the surface of the films is not smooth and the surface has regions consisting out of features of similar hills and valleys. The roughness of the films increases

with the number of layers, from 40 nm for 5 layers to 65 nm for 10 layers and above 200 nm for 20 layers.

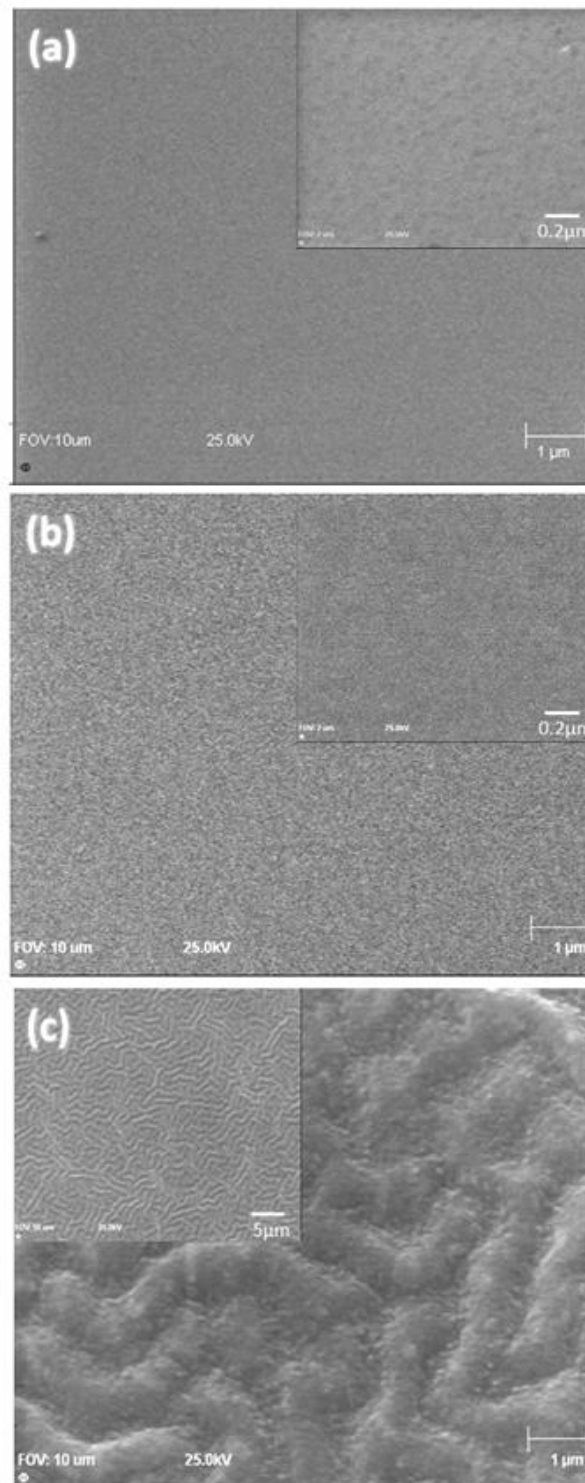


Figure 8.6: SEM images for the thin film surfaces for 10 layers after annealing for 1 h at (a) 600 $^{\circ}\text{C}$, (b) 1000 $^{\circ}\text{C}$ and (c) 1200 $^{\circ}\text{C}$. The insets show the same samples at different magnifications.

In order to compare the film surfaces after annealing at different temperatures, SEM micrographs of the thin films are shown in figure 8.6. As it can be seen in figure 8.6 (a), taken with different magnifications, the surface of the film annealed at 600 °C is smooth and no cracks can be observed. When increasing the annealing temperature to 1000 °C (figure 8.6 (b)) the film surface remains smooth. In figure 8.6 (c) showing the SEM images of the film annealed at 1200 °C, the surface of the film has changed completely. The surface consists of a hill and valley structure consistent with the AFM results. Clearly the change in surface morphology is related to the change in texture, the interdiffusion between the thin film layer and the Si substrate and possibly the formation of a new phase, and this was investigated further using AES.

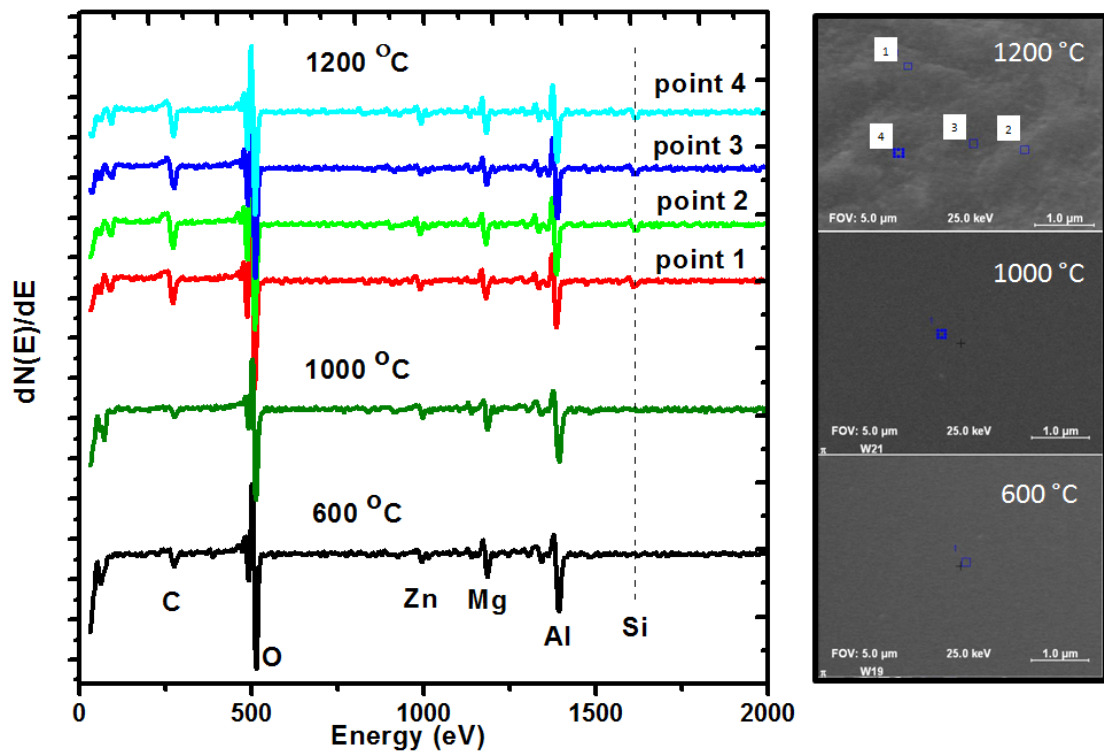


Figure 8.7: AES spectra of $Mg_{0.75}Zn_{0.25}Al_2O_4:Tb$ thin films of 10 layers after annealing at 600 °C, 1000 °C and 1200 °C.

Figure 8.7 compares the AES spectra of the samples after annealing at 600 °C, 1000 °C and 1200 °C. The results for the films annealed at 600 °C and 1000 °C are similar and

confirm the presence of all the major elements, namely Mg, Al, Zn and O in the $\text{Mg}_{0.75}\text{Zn}_{0.25}\text{Al}_2\text{O}_4:\text{Tb}$ thin films. The doping concentration of Tb (0.5 mol%) was too small for it to be easily detected, while all the films showed the presence of some adventitious C.

In the film annealed at 1200 °C the AES measurements were made at several points because the surface is not uniform. All measured points on the film showed the presence of an additional small Si peak together with the major elements found in the film. Except for this, the only significant difference between the samples annealed at low temperature and 1200 °C is in the low energy region (< 200 eV) and therefore this was investigated further.

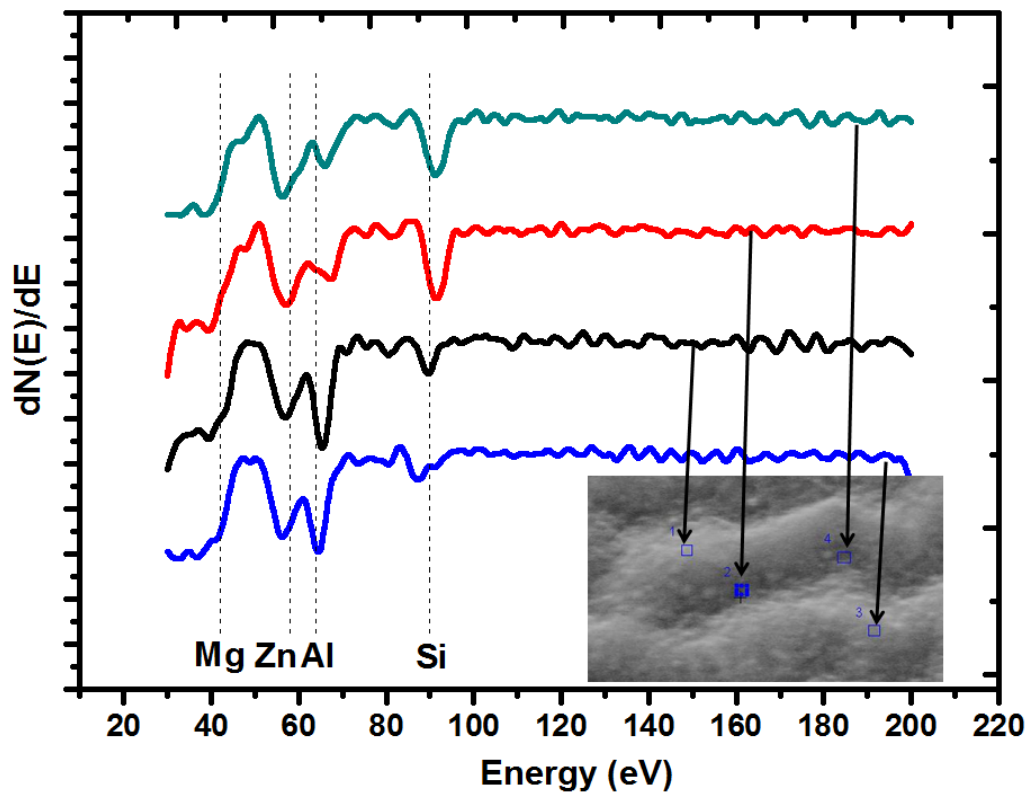


Figure 8.8: High resolution AES spectra of the low energy region of $\text{Mg}_{0.75}\text{Zn}_{0.25}\text{Al}_2\text{O}_4:\text{Tb}$ thin films of 10 layers after annealing at 1200 °C.

Further study for the change in the $\text{Mg}_{0.75}\text{Zn}_{0.25}\text{Al}_2\text{O}_4:\text{Tb}$ film's morphology after annealing at 1200 °C is represented in figure 8.8 by considering the Auger spectra for the low energy range. As can be seen clearly from the SEM micrograph (inset), there are two

regions (the valleys and hills) that can be distinguished. Two measurements were done in each of these regions, namely spots 1 and 3 on the top of the hills and spots 2 and 4 at the bottom of valleys. The Auger electron spectra in figure 8.8 compare the Si, Al, Zn and Mg peaks. According to the Auger Handbook [22], the peak positions are expected at 96, 70, 64 and 48 eV respectively. However, it was necessary to shift these values 6 eV lower to get a match with the experimental data, possibly due to charging. The concentration of the Si for the top region is smaller than for the bottom region, whereas the concentration of Al is larger on the top region than the lower region. From the spectra it appears that the concentration of Mg and Zn in the two regions does not differ significantly. This means the Si can diffuse to the bottom region from the substrate before the top region and that the Si takes the place of the Al.

To further study the changes of the sol-gel spin-coated thin films with annealing temperature, Auger depth profiles were made by sputtering the surface with an Ar ion gun. Figure 8.9 shows the measured AES depth profiles of the films after annealing at 600 °C and 1000 °C. Assuming a 27 nm/min sputtering rate (as measured for Si), we estimate the thickness of the $\text{Mg}_{0.75}\text{Zn}_{0.25}\text{Al}_2\text{O}_4:\text{Tb}$ film (10 layers) to be approximately 220 nm after annealing at 600 °C and 265 nm after annealing at 1000 °C for 1 h. The thickness was estimated by using the point (depth) where the Si concentration in the AES profiles is 50% of the maximum concentration as an estimation of the film thickness. Moreover, the films are homogeneous in composition except very near the surface and the interface region. However, considering the Si distribution it is clear that for the sample annealed at 1000 °C the Si has diffused significantly into the $\text{Mg}_{0.75}\text{Zn}_{0.25}\text{Al}_2\text{O}_4:\text{Tb}$ film.

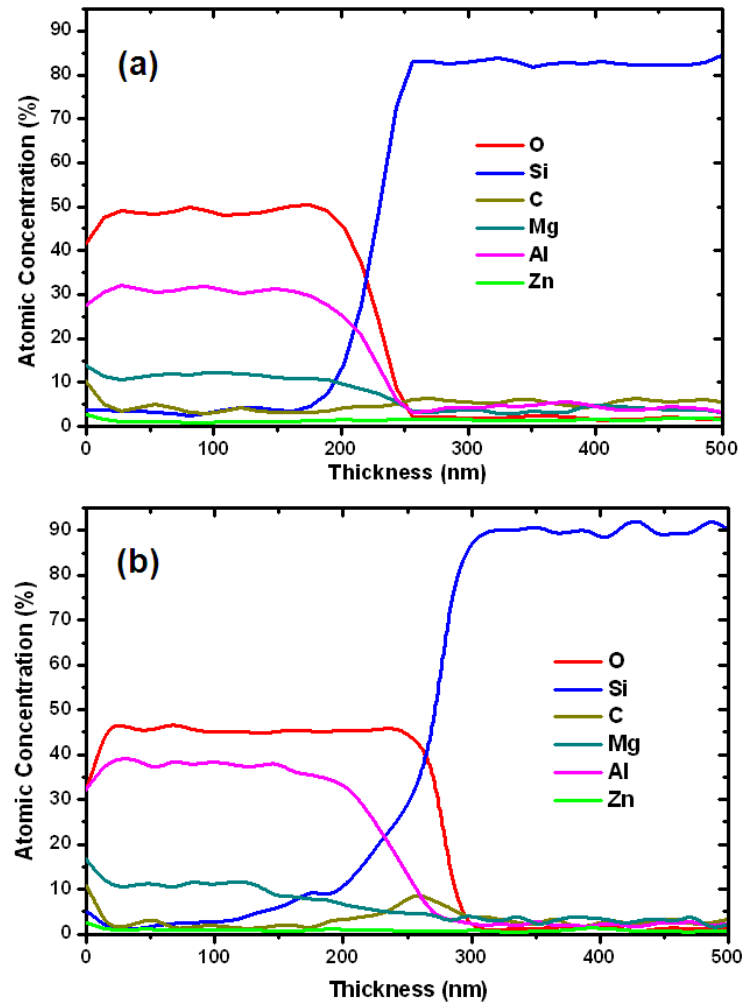


Figure 8.9: The depth profiles for the $\text{Mg}_{0.75}\text{Zn}_{0.25}\text{Al}_2\text{O}_4:\text{Tb}$ thin films of 10 layers after annealing at (a) 600 °C and (b) 1000 °C for 1 h.

Figure 8.10 shows the measured Auger depth profiles of the film after annealing at 1200 °C. The depth profiles of this film were measured at two positions, namely point (1) at the lower region (valley) and point (2) at the higher region (hill). In both the depth profiles the main elements i.e. Mg, Zn, Al, and O were found, but the film also contains a large amount of Si from the substrate showing that at this annealing temperature Si diffuses readily from the substrate through the thin film. We estimate the thickness of the film to be approximately 500 nm at point (1) and 700 nm at point (2). After annealing at 1200 °C the thin film is inhomogeneous, i.e. the concentration of the main elements changes significantly with depth.

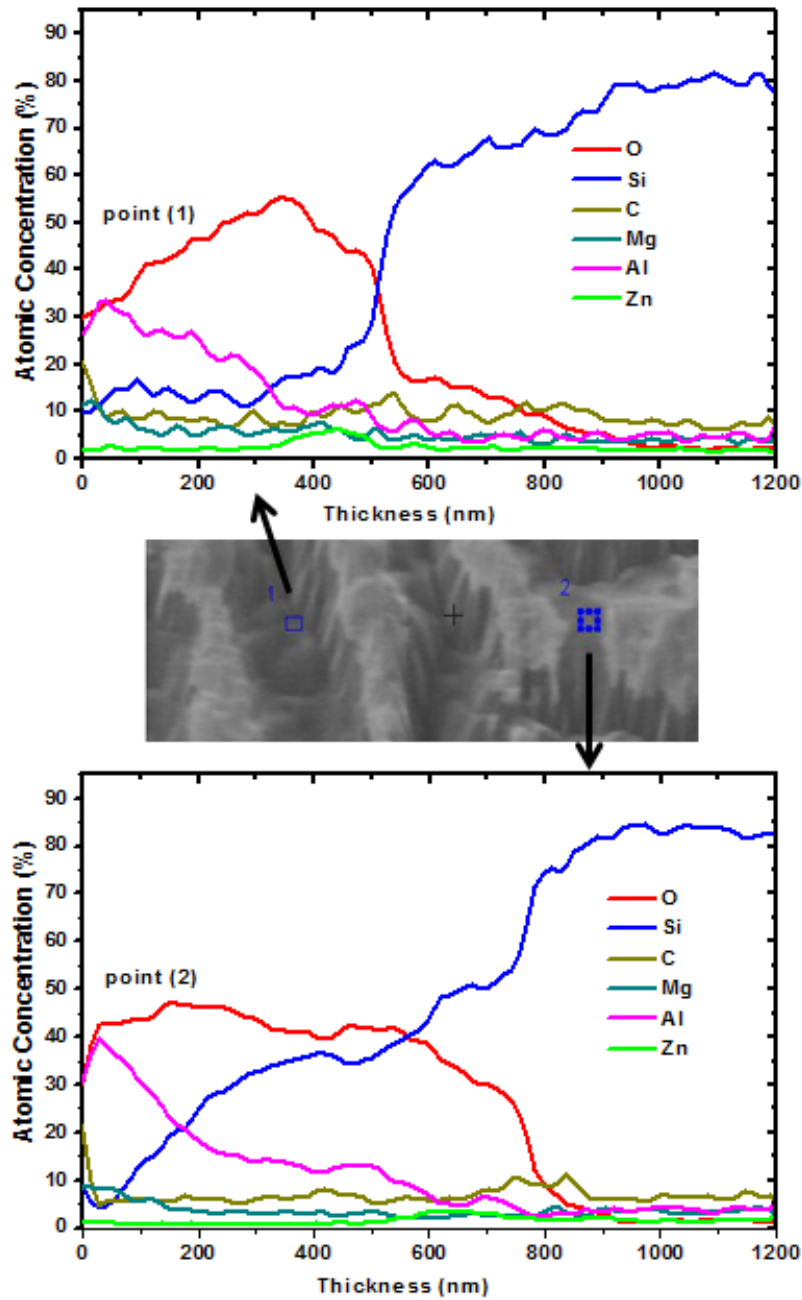


Figure 8.10: The depth profile for the $Mg_{0.75}Zn_{0.25}Al_2O_4:Tb$ thin film of 10 layers after annealing at $1200\text{ }^\circ\text{C}$ for 1 h.

At both points the Al concentration decreases from a maximum value of about 30 – 40% near the surface (which is similar to the Al concentration in the layers shown in figure 8.9 annealed at lower temperature) to near zero close to the interface, while the concentration of Mg is low except in the top 100 – 200 nm of the layer. Although Si occurs throughout the layer at both points, its concentration inside the layer is much higher at point (2),

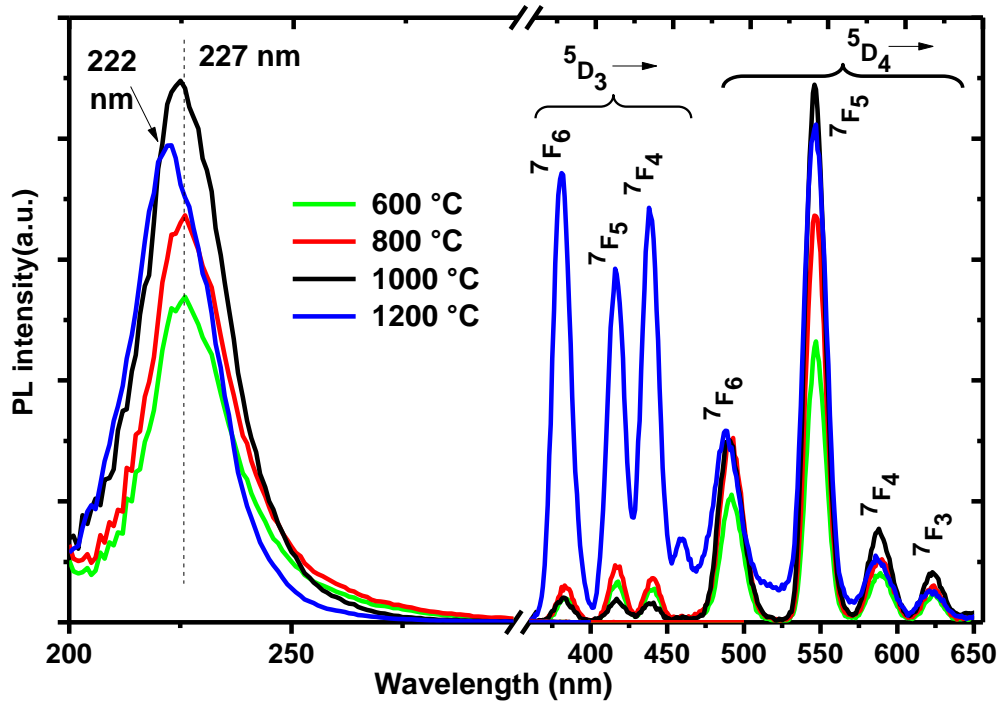
suggesting that the hill features are formed by greater diffusion of Si from the substrate into the layer in these regions. The original thin film before annealing was only about 200 nm thick (see figure 8.9(a)) and after annealing at 1200 °C the profile for the top-most part of the layer (up to about 100 nm) still retains some similarity to the original layer. Below this the Mg concentration is low and the Al concentration is decreasing with depth, while the Si concentration is uniform and fairly low (~15%) at point (1) or high and increasing with depth at point (2). This material in this region probably consists of a mixture of alumina (Al₂O₃) and Al-containing silicates. Near the interface where the Al concentration becomes low there is a layer of SiO_x with varying x, leading up to the Si substrate.

For the thin film annealed at 1200 °C the XRD pattern contained a new peak at ~38°, indicating the formation of a new phase, but this single peak was insufficient to identify the material. Unlike the thin films annealed at lower temperatures which have a definite texture, the crystallites of the thin film annealed at 1200 °C have random orientation (since the relative intensities of the peaks are similar to that of the powder sample). The thin film annealed at 1200 °C has a morphology with ridges (regions corresponding to hills and valleys) and the Auger depth profile indicates that the Si diffuses from the substrate through the thin film. The thermal expansion for MgAl₂O₄ and ZnAl₂O₄ are $\sim 7.6 \times 10^{-6} \text{ }^\circ\text{C}^{-1}$ while that of Si is $\sim 2.6 \times 10^{-6} \text{ }^\circ\text{C}^{-1}$ [23, 24]. The thermal expansion for thin film is larger than the substrate, so the area of the film tends to increase relative to the substrate with heating and the area mismatch will lead to stress which may be responsible for the difference in Si diffusion rate in different areas and hence the increase in the roughness.

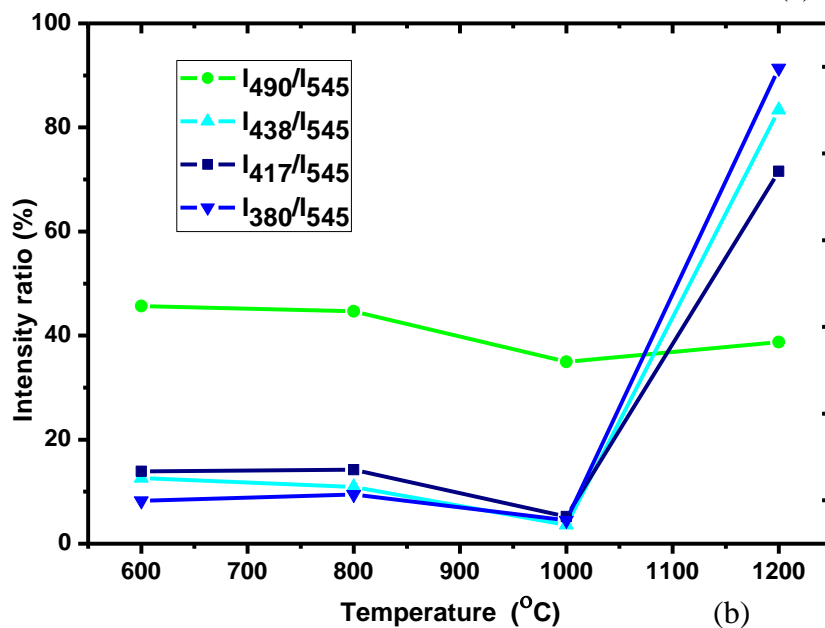
8.3.2 Optical properties

Figure 8.11(a) shows the photoluminescence excitation and emission spectra of Tb^{3+} for the $Mg_{0.75}Zn_{0.25}Al_2O_4$ films annealed at different temperatures. The Tb^{3+} excitation spectra (using the green $^5D_4 \rightarrow ^7F_5$ emission line at 545 nm) consists of broad bands in the region from 200 to 300 nm originating from the spin-allowed f-d transition. The excitation peak shifts from 227 nm for the thin films annealed up to 1000 °C to 222 nm for the sample annealed at 1200 °C. Together with usual green emissions from Tb^{3+} ions in the wavelength region longer than 480 nm (corresponding to $^5D_4 \rightarrow ^7F_J$ (J=3,4,5,6) transitions) there are also blue emissions below 480 nm (corresponding to $^5D_3 \rightarrow ^7F_J$ (J=4,5,6) transitions). As is common for most hosts doped with Tb the green $^5D_4 \rightarrow ^7F_5$ emission line at 545 nm is the strongest. The intensity of the 545 nm peak increased with increasing annealing temperature up to 1000 °C, but was a little weaker for the thin film annealed at 1200 °C. Although the blue emission increased after annealing at 800 °C compared to 600 °C, it then decreased for the sample annealed at 1000 °C. After annealing at 1200 °C the intensity of the blue lines increased dramatically.

Figure 8.11 (b) shows the ratio of the intensity of the peaks at 490 nm, 438 nm, 417 nm, and 380 nm compared to the strongest green emission peak at 545 nm for different annealing temperatures. The ratio I_{490}/I_{545} for emission from the 5D_4 level remained almost the same (~45%) for the annealing temperatures 600 °C and 800 °C, whilst for annealing temperatures of 1000 °C and 1200 °C the intensity ratio I_{490}/I_{545} decreased (~35%). The ratios I_{438}/I_{545} , I_{417}/I_{545} and I_{380}/I_{545} for luminescence peaks originating from the 5D_3 level follow same behaviour up to 1000 °C, but then dramatically increases for the sample annealed at 1200 °C.



(a)



(b)

Figure 8.11: (a) Room temperature luminescence spectra of $\text{Mg}_{0.75}\text{Zn}_{0.25}\text{Al}_2\text{O}_4:\text{Tb}$ film for 10 layers after different annealing temperatures and (b) Relative emission intensity ratios as a function of the different annealing temperatures of the films.

Annealing at 800 °C improves the crystallinity and the emission is increased for all lines of the green and blue emission, but the ratio does not change. After annealing at 1000 °C a small amount of Si diffuses inside the film. The diffusing Si atoms may produce defects

that reduce the 5D_3 level lifetime of the Tb ions, resulting in a decrease of the blue emission intensity but an increase in the green emission from the 5D_4 level to which the electrons decay. This would explain the reduction in the intensity ratio for the blue peaks, although the intensity ratio of the green peak would not be expected to change. The strong increase in the blue emission lines after annealing at 1200 °C is interesting. It is well known that the blue emission lines of Tb are stronger in samples that weakly doped and that the blue emission decreases with increasing Tb concentration due to cross-relaxation of the Tb ions [25]. For annealing at 1200 °C there is a large increase in the film thickness from 220 nm (figure 8.9) to about 600 nm (figure 8.10), meaning that the effective Tb concentration is decreased, resulting in the stronger blue emission. However, we suggested earlier that the diffusing Si produced defects that decreased the 5D_3 level lifetime of the Tb from which the blue emission originates. Alternatively, after annealing at 1200 °C it is known from the XRD data that a new phase is formed, and from the Auger data it seems likely this is a Si rich material such as a silicate. The Tb concentration in this new host may be low and it could be responsible for the increased blue emission.

8.4 Conclusion

$Mg_{0.75}Zn_{0.25}Al_2O_4:Tb$ thin phosphor films of about 200 nm thickness were prepared on Si(100) substrates by using sol-gel spin-coating technique. After annealing between 600 °C and 1000 °C the XRD patterns showed that the thin films had a spinel structure with strong (111) texture and that the crystallite size increased with increasing annealing temperature. The emission increased after annealing at 800 °C compared to 600 °C. The intensity of the 545 nm peak increased with increasing annealing temperature up to 1000 °C. After annealing the thin film at 1200 °C, the intensity of the blue lines increased and the surface morphologies changed from smooth and flat to a rough structure similar to hills

and valleys. The results show that diffusion of Si from the substrate occurs through the thin film which increases in thickness. An additional XRD peak shows that a new material, probably a silicate, is formed.

8.5 References

1. J.S. Bae, K.S. Shim, B.K. Moon, B.C. Choi, J. H. Jeong, S. Yi and J.H. Kim, *Thin Solid Films* **479** (2005) 238- 244.
2. J.S. Bae, S.B. Kim, J.H. Jeong, J.C. Park, D.K. Kim, S. Byeon and S. Yi, *Thin Solid Films* **471** (2005) 224- 229.
3. Z. Lou and J. Hao, *Thin Solid Films* **450** (2004) 334-340.
4. K.T. Hillie and H.C. Swart, *Appl. Surf. Sci.* **253** (2007) 8513-8516.
5. S. Sakka, *Handbook of Sol-gel Science and Technology Processing, Characterization and Applications*, Kluwer Academic Publishers (New York, 2005).
6. Y. Hu, F.W. Wang and H. Lin, *Mater. Chem. Phys.* **107** (2008) 82-84.
7. R. F. Martins and O. A. Serra, *J. Braz. Chem. Soc.* **21** (2010) 1395-1398.
8. R.C. Ropp, *Luminescence and the Solid State, 2nd Ed*, Elsevier (Amsterdam, 2004).
9. D. Levy, A. Pavese and M. Hanfland, *Am. Mineral.* **88** (2003) 93-98.
10. J. Xiaolin, Z. Haijun, Y. Yongjie and L. Zhanjie, *Mater. Sci. Eng. A* **379** (2004) 112-118.
11. R. Chandramohan, V. Dhanasekaran, R. Arumugam, K. Sundaram, J. Thirumalai and T. Mahalingam, *J. Nanomat. Biostr.* **7** (2012) 1315-1325.
12. M. García-Hipólito, C.D. Hernández-Pérez, O.E. Martínez, J. Guzmán-Mendoza and C. Falcony, *Opt. Mat.* **22** (2003) 345-351.
13. R.J. Wiglusz and T. Grzyb, *Opt. Mater.* **33** (2011) 1506-1513.
14. K.K. Satapathy, G.C. Mishra and F. Khan, *Chem Sci Trans.* **2** (2013) 1262-1267.

15. X. Wang, M. Zhang, H. Ding, H. Li and Z. Sun, *J. Alloys Compd.* **509** (2011) 6317-6320.
16. Y. Yang, X. Qu, Y. Luo and A. Yang, *J. Adv. Mater. Res.* **216** (2011) 514-517.
17. A.R. Phani, M. Passacantando and S. Santucci, *Mater. Chem. Phys.* **68** (2001) 66-71.
18. W.A.I. Tabaza, H.C. Swart and R.E. Kroon (2012) submitted to South African Institute of Physics (SAIP), Pretoria.
19. J.S. Bae, B. K. Moon, B.C. Choi, J.H. Jeong, S.S. Yi, W. Kim and J.S. Lee, *Thin Solid Films* **424** (2003) 291-295.
20. C. Aydın, H.M. El-Nasser, F. Yakuphanoglu, I.S. Yahia and M. Aksoy, *J. Alloys Compd.* **509** (2011) 854-858.
21. A. Yousif, H.C. Swart, O.M. Ntwaeaborwa and E. Coetsee, *Appl. Surf. Sci.* **270** (2013) 331- 339.
22. K.D. Childs, B.A. Carlson, L.A. LaVanier, J.F. Moulder, D.F. Paul, W.F. Stickle and D.G. Watson, *Handbook of Auger Electron Spectroscopy*, 3rd Ed., Physical Electronics (Eden Prairie, 1995).
23. C.B. Carter and M.G. Norton, *Ceramic Materials Science and Engineering*, Springer Science and Business Media (New York, 2007).
24. W.J. Tropf, M.E. Thomas and T.J. Harris, *Optical and Physical Properties of Materials in Handbook of Optics, Volume II, Measurements and properties*, 2nd Ed, McGraw-Hill (New York, 1995).
25. H.A.A. Seed Ahmed, O.M. Ntwaeaborwa, M.A. Gusowski, J. R. Botha and R.E. Kroon, *Phys. B* **407** (2012) 1653-1655.

9 PLD grown $\text{Mg}_{0.75}\text{Zn}_{0.25}\text{Al}_2\text{O}_4:\text{Tb}$ phosphor thin films

9.1 Introduction

Luminescent thin films are of great interest from both a scientific and technological point of view. The research interest in luminescent thin films has been reflected by the rapid developments in a variety of thin film luminescent devices, including flat-panel displays, light sources, solar cells and integrated optics systems [1]. Displays based on thin film phosphors are characterized by high contrast and resolution, good thermal conductivity as well as a high degree of uniformity and better adhesion [2-4]. Oxide thin film phosphors have received considerable attention due to their good luminescent characteristics, stability in high vacuum and absence of corrosive gas emission under electron bombardment [5]. There are several techniques that have been developed to prepare thin phosphor materials, namely sputtering [6, 7], spray pyrolysis [8] sol-gel processing [9], chemical vapour deposition [10] and pulsed laser deposition (PLD) [11, 12]. Most phosphor materials consist of multi-components and their luminescence efficiency is largely affected by the right stoichiometry and growth parameters, in particular for PLD the material source, substrate type and temperature, laser wavelength, laser fluency, target-to-substrate distance, laser repetition rate and gas ambient pressure [13]. In addition, one of the most important things in the deposition of a phosphor thin film is the stoichiometric transfer of target material to the substrate [14]. It is well known that the PLD technique can produce a wide variety of complex compounds with controlled composition and properties.

The most promising spinel oxides are magnesium aluminate (MgAl_2O_4) and zinc aluminate (ZnAl_2O_4) which have received special attention as technologically important materials [15, 16]. In the normal oxide spinel (AB_2O_4) structure with space group of $Fd\bar{3}m$, Mg^{2+} and Zn^{2+} ions occupy the tetrahedrally coordinated A-sites, whereas Al^{3+} ions occupy the B-sites which are octahedrally coordinated. Both these materials are used as phosphor hosts for a variety of luminescent ions [17-20] and have been considered for thin film electroluminescence [21, 22]. MgAl_2O_4 and ZnAl_2O_4 thin films prepared by sol-gel technique have already been reported [23, 24]. However, since Mg and Zn ions are similar in size, the lattice constants of these materials are close to one another and it is interesting to consider the intermediate material ($\text{Mg}_x\text{Zn}_{1-x}$) Al_2O_4 as a possible phosphor host.

In this study, we have investigated the properties of $\text{Mg}_{0.75}\text{Zn}_{0.25}\text{Al}_2\text{O}_4:\text{Tb}^{3+}$ thin films deposited on Si(100) substrate by using PLD technique. The main purpose of this work is to examine the effects of deposition substrate temperature and different working atmosphere (base pressure, O_2 , N_2 and Ar) on the morphology and the photoluminescence (PL) of the films.

9.2 Experimental

$\text{Mg}_{0.75}\text{Zn}_{0.25}\text{Al}_2\text{O}_4:\text{Tb}^{3+}$ powder was first prepared by the combustion method using the chemicals $\text{Mg}(\text{NO}_3)_2 \cdot 6\text{H}_2\text{O}$, $\text{Zn}(\text{NO}_3)_2 \cdot 4\text{H}_2\text{O}$, $\text{Al}(\text{NO}_3)_3 \cdot 9\text{H}_2\text{O}$ and urea ($\text{CH}_4\text{N}_2\text{O}$). Doping of samples with 0.5 mol% Tb^{3+} ions was achieved by replacing an appropriate amount of $\text{Al}(\text{NO}_3)_3 \cdot 9\text{H}_2\text{O}$ with the same amount of $\text{Tb}(\text{NO}_3)_3 \cdot 5\text{H}_2\text{O}$. More information of the preparation process and the properties of the powder can be found in ref [25]. This powder was then pressed without binders in a 2.5 cm diameter die using a hydraulic press with an applied pressure of 10 tons to prepare a pellet that was used as an ablation target. This

target was annealed at 250 °C for 24 h in air to remove water vapour and other volatile compounds that might be trapped in it before placing it in the target holder of the PLD system. Cleaved pieces of Si(100) wafers were used as the substrate. They were cleaned with ethanol for 15 min in an ultrasonic water bath and then blown dry with N₂. The distance between the target and the substrate was kept at 45 mm. The deposition chamber was evacuated to a base pressure of 1.4×10^{-5} mbar using a turbo pump and the substrate temperature was increased to the desired temperature. The films were grown by PLD using a Nd:YAG pulsed laser with a wavelength of 266 nm and a frequency of 10 Hz. The beam of the laser with an energy density of 8.1 J/cm² was guided into the high vacuum chamber and focused on the surface of the target. Note that rotational as well as linear motion of the target restricted laser ablation induced degradation of the target surface.

Firstly, thin films were deposited using substrate temperatures of 300, 500 and 700 °C at the base pressure. When using a heater the substrates must be bonded to the heater block with thermally conductive metal paste. For our work silver paste was used up to 300 °C or nickel paste up to 700 °C to achieve good thermal conductivity between the block and substrate. An attached thermocouple was used for temperature measurement. After cooling to room temperature in the vacuum system, the samples were removed. A second set of thin film were deposited using different gas atmospheres of O₂, N₂ and Ar at 30 mTorr (i.e. 4.0×10^{-2} mbar) for a fixed substrate temperature of 300 °C. Before deposition the vacuum chamber was evacuated down to the base pressure and then back-filled with the desired gas.

X-ray diffraction (XRD) data was collected by using a Bruker D8 Advance diffractometer operating at 40 kV and 40 mA with CuK_α radiation of wavelength 1.5406 Å in the 2θ range

from 15° to 40° , with a counting time of 1s for each step size of 0.004° . The surface topography and roughness were examined from images captured in contact mode using Shimadzu SPM-9600 atomic force microscopy (AFM). The root-mean-square (rms) roughnesses were estimated by analyzing the topography scans of the film surface using software (SPM manager 3.04). Auger electron spectroscopy (AES) measurements were performed using a PHI 700 Scanning Auger Nanoprobe. AES surveys were done with a 25 kV 10 nA electron beam. Sputtering for depth profiles was performed with a 2 kV, 2 mA Ar ion beam for a $1 \times 1 \text{ mm}^2$ raster area. Photoluminescence (PL) properties of the films were measured with a Cary Eclipse spectrophotometer and the films were excited at room temperature by using a monochromatized xenon flash lamp.

9.3 Effects of substrate temperature on the properties of the thin films grown in vacuum

9.3.1 Structure

The crystallinity of PLD thin films can be highly dependent on the deposition conditions, in particular substrate temperature, ambient gas pressure and the post-annealing conditions [26]. Figure 9.1 shows the XRD patterns of the powder used for the target and the thin films deposited at different substrate temperatures of 300°C , 500°C and 700°C . All peaks of the XRD patterns of the as-deposited thin films were consistent with the spinel structure of the starting powder. In some cases XRD peaks from the Si substrate were observed (not shown), but these could always be eliminated by repositioning the sample and cleaving the sample to retain only the centre part where the film was thickest. The (311) peak is the main peak of the standard powder as well as the thin films. All the peaks of the powder and thin film are in good agreement. The (311) peaks from the thin films are shifted to slightly higher angles ($\sim 36.95^\circ$) compared to the powder ($\sim 36.85^\circ$). The expected angle for

the (311) peak of ZnAl_2O_4 is 36.823° while that for MgAl_2O_4 is 36.862° . The measured position of the (311) peaks for the thin films are therefore outside the expected range for the $(\text{Mg}_x\text{Zn}_{1-x})\text{Al}_2\text{O}_4$ mixed spinels. Shifting in XRD peaks can occur when the height of the sample is changed. It is difficult to ensure that the height for the powder and the thin film samples are identical, and the shift is attributed to this effect. From the XRD measurements it is not clear if there was correct stoichiometric transfer of the target material to the substrate during PLD. No preferred orientation in the thin film patterns was observed for any of the substrate temperatures because the relative peak heights are similar to the randomly oriented powder. The FWHM of the XRD peaks for the thin films were similar to those of the powder, which has a crystallite size of 25 nm (see chapter 7). Although strain broadening may also contribute to the width of XRD peaks, this indicates that the grain size of the thin films is very small.

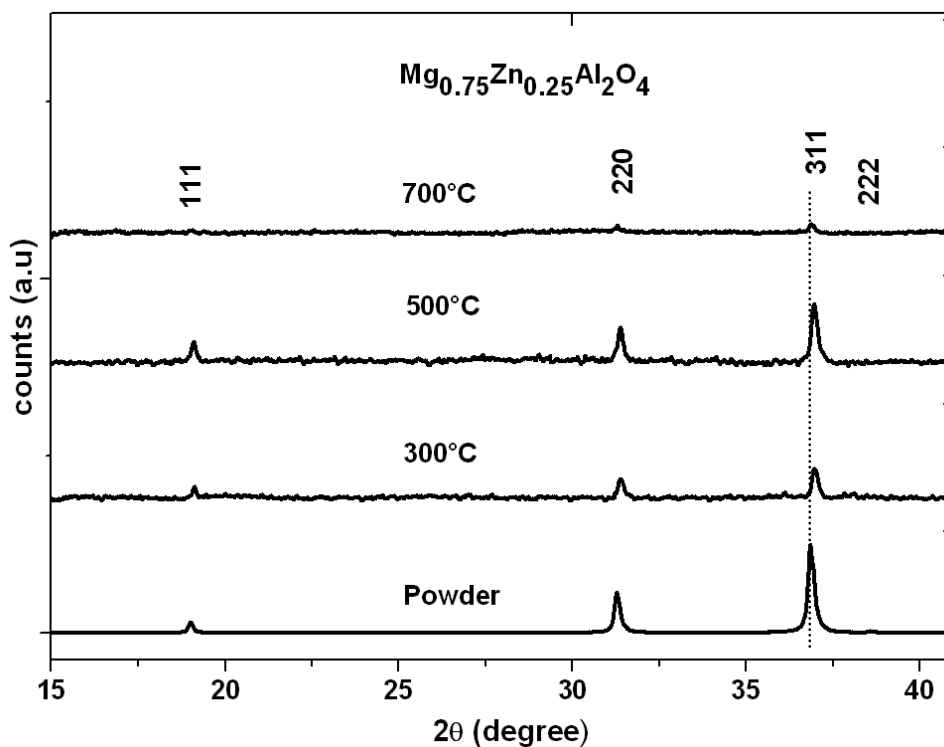


Figure 9.1: XRD spectra of $\text{Mg}_{0.75}\text{Zn}_{0.25}\text{Al}_2\text{O}_4:\text{Tb}^{3+}$ powder and thin films deposited by PLD at base vacuum pressures for different substrate temperatures.

9.3.2 Morphology

It is well known that AFM is a powerful analysis method with high resolution and it has been applied to study the surface structure of various materials successfully [27]. Here the AFM images were recorded in order to study the effect of different substrate temperatures on the surface topography of the as deposited thin films.

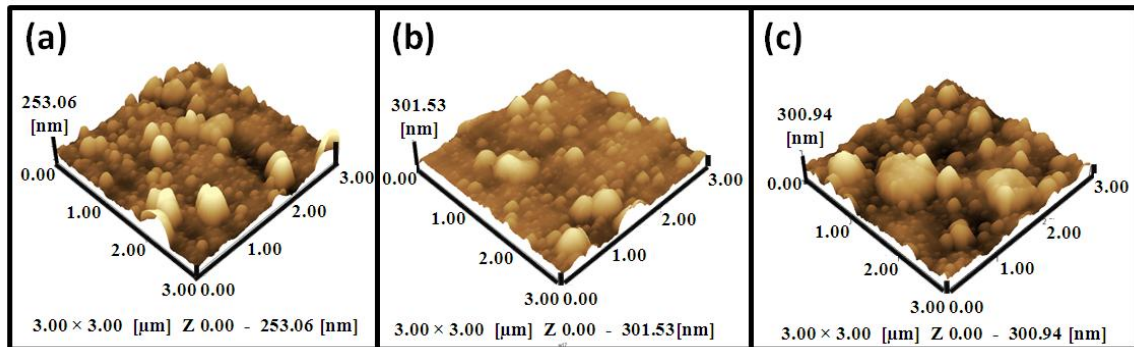


Figure 9.2: AFM images of the surface of thin films deposited by PLD at base vacuum pressure for different substrate temperatures of (a) 300 °C, (b) 500 °C and (c) 700 °C.

The substrate temperature determines the atom mobility on the surface and within the bulk and as the temperature increases, the adatom mobility increases, producing films that change from amorphous to polycrystalline and finally to single-crystal epitaxial growth. The substrate temperature for PLD can typically be chosen to be around 50–75% of the melting temperature of the film. This is because the diffusive motion of atoms is possible in the bulk, on the surface and along grain boundaries at roughly temperature ratios of 0.4, 0.2 and 0.1 respectively [28]. The melting temperature of $\text{Mg}_{0.75}\text{Zn}_{0.25}\text{Al}_2\text{O}_4$ can be estimated from the phase diagram in Petrova et al. [29] to be about 2050 °C, so the ratio of substrate temperature to the film's melting temperature (both in K) are 0.25, 0.33 and 0.42 for the substrate temperatures of 300 °C, 500 °C and 700 °C respectively. The substrate temperature of 300 °C is then close to the limit for mobility of atoms on the surface, while

at the highest substrate temperature of 700 °C the mobility in the bulk is definitely possible.

Figure 9.2 and figure 9.3 show the AFM and SEM images respectively for the films deposited at different substrate temperatures of 300 °C, 500 °C and 700 °C. Although the morphology of the thin films varies to some degree with position (corresponding to the radial distance from the centre of the PLD plume) and is not homogeneous, there is a good correlation between the surface structure seen in the AFM and SEM results.

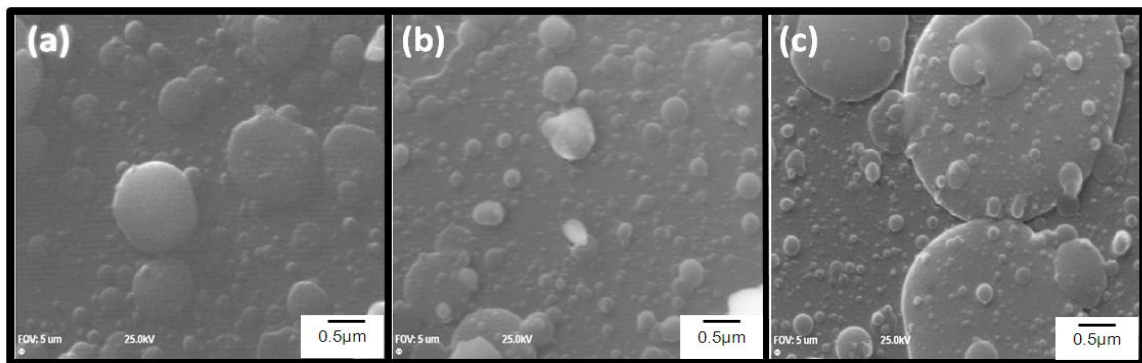


Figure 9.3: SEM images for the thin films deposited by PLD at base vacuum pressure for substrate temperatures of (a) 300 °C, (b) 500 °C and (c) 700 °C.

For all of the images the surface is not smooth, but contains flat rounded particles of different sizes and shapes which could be formed from local melting and ejected from the target to the substrate and which are typically found in laser ablation experiments [30, 31]. These are present because the laser ablation process that produces the atomization of the target material has an explosive-like character and is accompanied by the formation of particulates which are transferred by the ablation plume to the substrate and incorporated in the growing film [28]. From the images it appears that this material is still liquid when it reaches the substrate surface and flattens to form discoidal particulates. Although the

particulates range in size considerably (from 1 μm down to nanometre size for the film that was deposited at a substrate temperature of 300 $^{\circ}\text{C}$), the largest of several micrometres are seen for the sample produced with the highest substrate temperature of 700 $^{\circ}\text{C}$. The higher substrate temperature may allow these larger particulates to adhere to the substrate, whereas for the sample made with the lower substrate temperatures the larger particulates may be lost from the surface. In addition, the greater mobility of the surface atoms for the higher substrate temperature may facilitate bonding of the larger particulates to the film surface.

The rms surface roughness for the films deposited at substrate temperatures of 300 $^{\circ}\text{C}$, 500 $^{\circ}\text{C}$ and 700 $^{\circ}\text{C}$ were 39 nm, 34 nm and 54 nm respectively. The sample annealed at 700 $^{\circ}\text{C}$ and having the largest particulates also had the maximum rms roughness. Similar behaviour was reported for PLD deposited $\text{SrAl}_2\text{O}_4:\text{Eu}^{2+},\text{Dy}^{3+}$ thin films [32] where the films deposited at a higher substrate temperatures of 700 $^{\circ}\text{C}$ were shown to have rougher surfaces and larger particle sizes than those deposited at lower substrate temperatures. However, it is interesting that the sample produced with a substrate temperature of 500 $^{\circ}\text{C}$ is smoother than the sample produced at 300 $^{\circ}\text{C}$. This can be explained by considering the surface mobility which depends on the substrate temperature. For the substrate temperature of 300 $^{\circ}\text{C}$ there is very little mobility of atoms possible over the surface, which would contribute to a rougher surface, while for a substrate temperature of 500 $^{\circ}\text{C}$ the increased surface mobility would lead to a smoother surface with lower rms roughness. However, the surface roughness is highly dependent on the particulates on the surface, which are not homogeneous over the surface. The AFM and SEM results indicate that for a smooth thin film the optimum substrate temperature is 500 $^{\circ}\text{C}$.

9.3.3 NanoSAM analysis

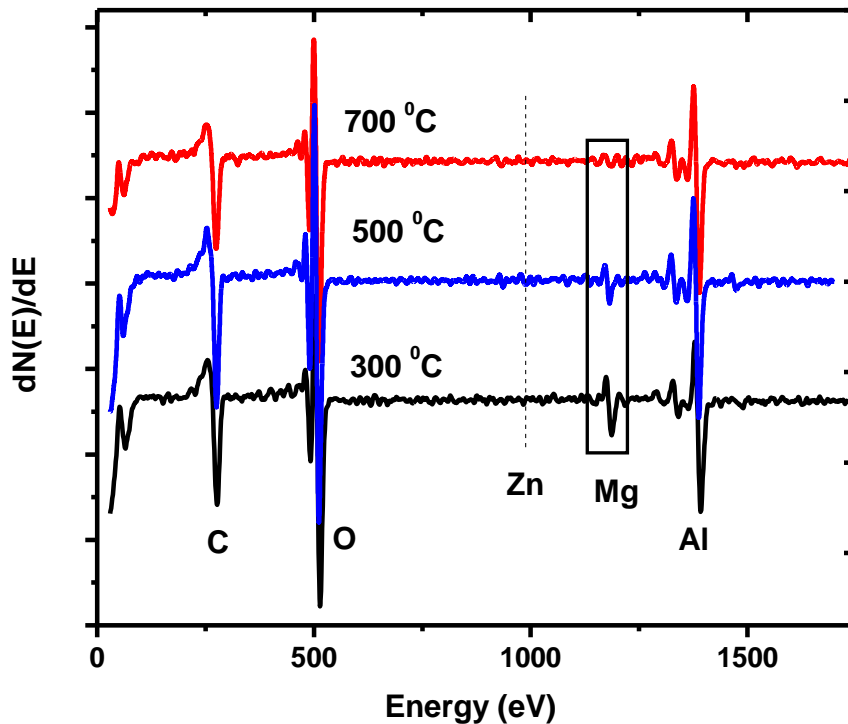


Figure 9.4: Surface AES spectra for the thin films deposited by PLD at base vacuum pressure for substrate temperatures of (a) 300 °C, (b) 500 °C and (c) 700 °C.

Figure 9.4 show the AES spectra obtained on the surface of the samples deposited at 300 °C, 500 °C and 700 °C substrate temperatures. The spectra confirm the presence of a number of elements in the target material namely Mg, Al, and O, but the expected peak from Zn was not observed. Additionally, there was adventitious C on the surface. The doping concentration of Tb (0.5 mol%) was too small for it to be easily detected.

Although the Zn concentration in $\text{Mg}_{0.75}\text{Zn}_{0.25}\text{Al}_2\text{O}_4$ is small, the Zn peak was observed in thin films made with sol-gel spin-coating (see figure 8.7). The absence of the zinc in the thin film made by PLD is due to the low sticking coefficient of Zn, because the melting

point of the Zn (420 °C) is much lower than Mg (650 °C) and Al (660 °C). Stoichiometric transfer of the target composition is known to be problematic at elevated temperatures if any of the cation species has a high vapour pressure, e.g. K, Li, Na, Tl, Mg, Pb, Cd, and Zn and the loss of Zn for ZnGa₂O₄ thin films produced by PLD has also been reported [28]. Auger depth profiles of the samples (figure 9.5) show that the Zn is not only absent from the surface but through the whole film, which therefore does not retain the stoichiometry of the Mg_{0.75}Zn_{0.25}Al₂O₄ target, but is closer to MgAl₂O₄. Both MgAl₂O₄ and ZnAl₂O₄ have the same structure and almost the same lattice parameter (because of the similar sizes of the Mg and Zn ions), so this change in stoichiometry was not apparent from the XRD measurements where the peaks remained in the same position for the thin films and target material.

Also in figure 9.4 one can see a reduction in the Mg peak intensity with increasing substrate temperature. This is also due to the sticking factor of Mg, which becomes less as the substrate temperature increases. Figure 9.5 shows the measured AES depth profiles of the films that were deposited at 300 °C, 500 °C and 700 °C and show that the Mg concentration was not only changed on the surface but lower through the whole film as the substrate temperature increased. Assuming a sputtering rate of 27 nm/min (measured for Si), the thickness of the films was estimated by using the point (depth) where the Si concentration in the AES profiles is 50% of the maximum concentration, the thickness of the film deposited at substrate temperatures of 300 °C, 500 °C and 700 °C were approximately 175 nm, 200 nm and 260 nm respectively. However, the film deposited at 500°C was sputtered for 1 min (which is why the apparent surface concentration of C is low), so a better estimate of its thickness is 227 nm.

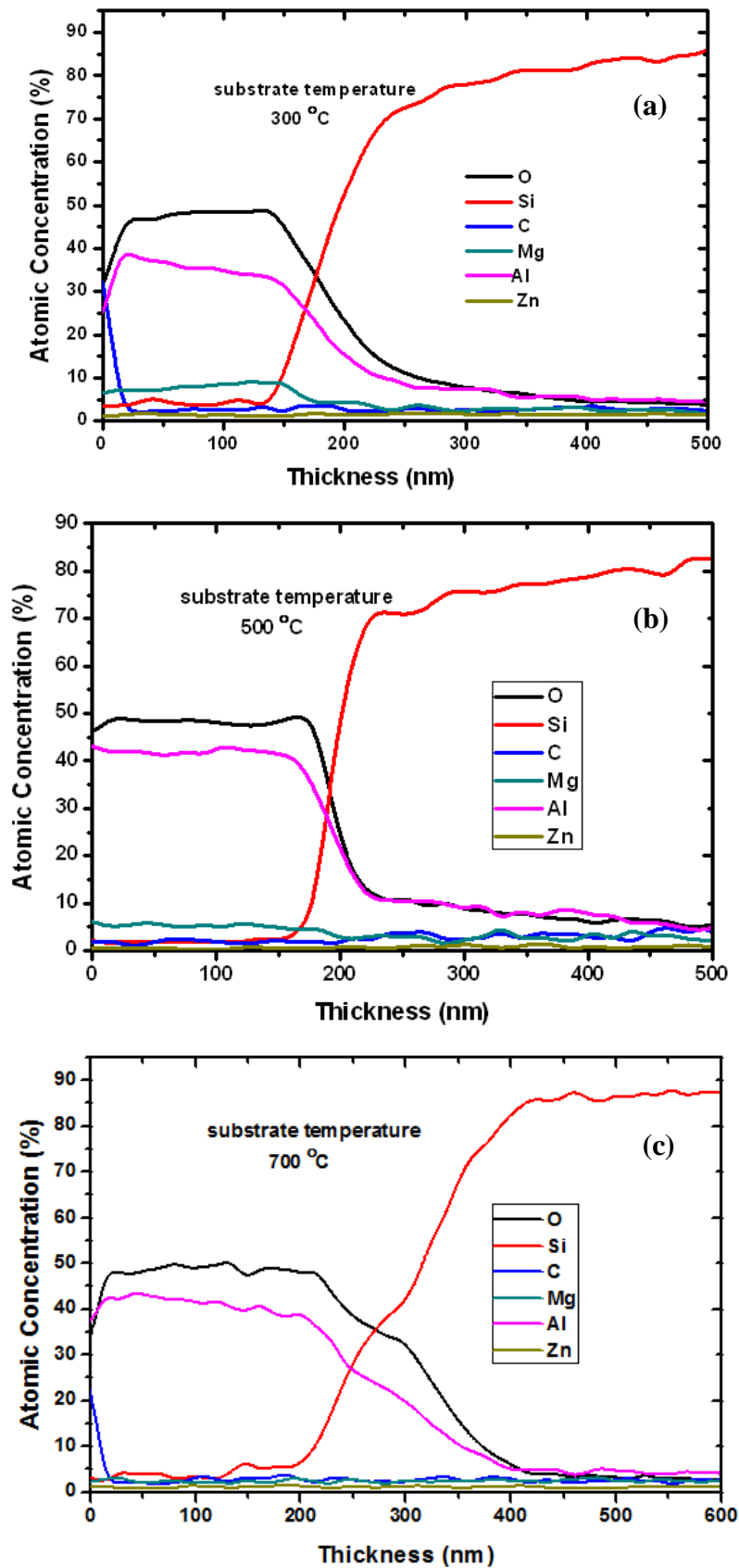


Figure 9.5: AES depth profiles for the thin films deposited by PLD at base vacuum pressure for substrate temperatures of (a) 300 °C, (b) 500 °C and (c) 700 °C.

The interface region for the sample grown with a substrate temperature of 500 °C is narrower than when the substrate temperature was 300 °C. This can be attributed to the better crystallinity of the thin film material formed at the interface region at the higher temperature, which may inhibit the diffusion between the film and substrate. The interface between the substrate and thin film is wide for the sample deposited at 700 °C. For this sample the Zn and Mg have very low sticking coefficients and it is mostly O and Al that are deposited on the surface. The excess O due to the loss of the Zn and Mg cations causes an oxidation of the Si substrate, while the film consists mainly of Al and O, with a small amount of Mg. The film therefore consists of a mixture of aluminium oxide (probably Al_2O_3) and a lesser amount of MgAl_2O_4 . The XRD pattern of this thin film (figure 9.1, top) shows small intensity peaks corresponding to spinel, but no other peaks from the thin film. It has previously been reported that Al_2O_3 grown by PLD forms an amorphous thin film when the substrate temperature is low [33]. Although the substrate temperature of 700 °C is not as low as in the previous report, it appears that the aluminium oxide material produced in this study is in the amorphous state since no corresponding XRD peaks are observed. The increased substrate temperature and the poor quality of the thin film due to the loss Zn and Mg cause an increase in the diffusion between the substrate and thin film resulting in a wide interface region.

9.3.4 Optical properties

Fig. 9.6 shows the PL spectra of the films deposited at substrate temperatures ranging from 300 °C to 700 °C. The excitation spectrum shows a broad band from 200 to 300 nm with a maximum at about 227 nm. The Tb^{3+} ion exhibits narrow line emissions located between 350 and 650 nm. All line emissions are due to the spin-allowed f-f transitions of Tb^{3+} . The blue light below 480 nm can be attributed to $^5\text{D}_3 \rightarrow ^7\text{F}_J$ ($J=4,5,6$) transitions, while the green

emission above 480 nm results from the ${}^5D_4 \rightarrow {}^7F_J$ ($J=3,4,5,6$) transitions. Typically, as for many different hosts doped with Tb, the strongest emission was green light from the ${}^5D_4 \rightarrow {}^7F_5$ line at 545 nm. The intensity of the 545 nm peak increased for the film prepared with a substrate temperature of 500 °C compared to that for a substrate temperature of 300 °C. This can be attributed to an increase in the quality of the thin film. However, the intensity dropped greatly when the substrate temperature was increased to 700 °C. At this high substrate temperature the PLD film contains no Zn and only a small amount of Mg, so the quantity of spinel ($MgAl_2O_4$) is low, resulting in poor emission. A recent publication by Yi et al. [34] reported similar behaviour for $ZnGa_2O_4$. The films were grown at different substrate temperatures (450 °C, 550 °C and 650 °C) and they found that at a higher temperature above 550 °C the intensity of luminescence decreased. They attribute this to the possibility of the Zn atom to diffuse out being increased at higher temperature, but based on results it is suggested it could be due to the loss of Zn.

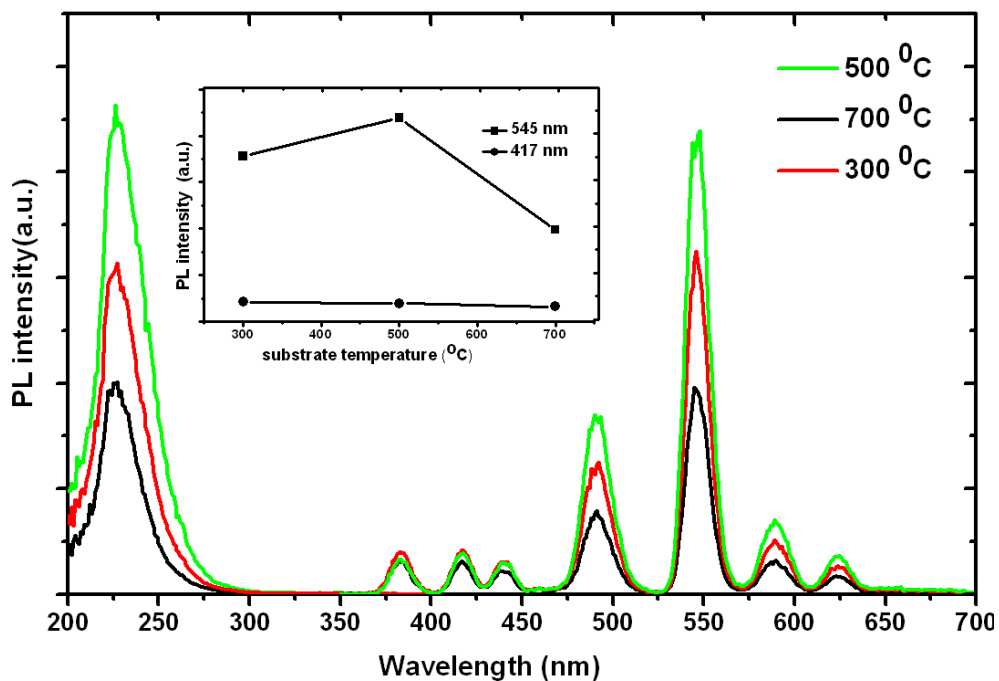


Figure 9.6: Room temperature luminescence spectra of $Mg_{0.75}Zn_{0.25}Al_2O_4:Tb^{3+}$ films at different substrate temperature and (inset) PL intensity as function of substrate temperature.

9.4 Effects of different gas atmospheres on properties of thin films grown with a substrate temperature of 300 °C

9.4.1 Structure

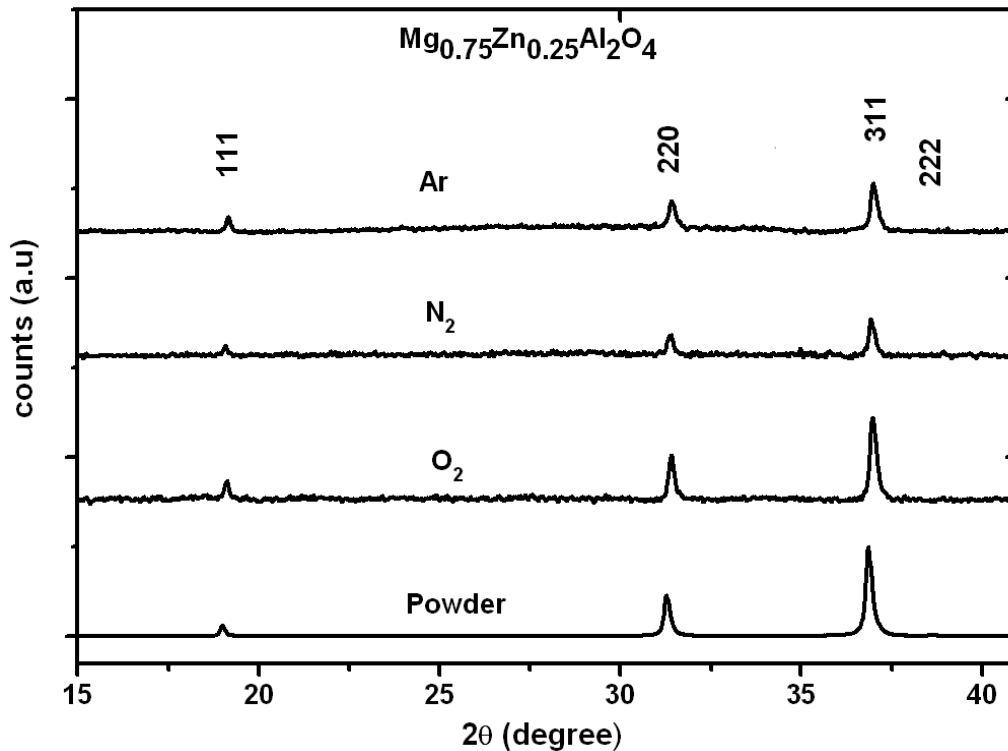


Figure 9.7: XRD spectra of $\text{Mg}_{0.75}\text{Zn}_{0.25}\text{Al}_2\text{O}_4:\text{Tb}^{3+}$ powder and thin films deposited by (PLD) in the different gas atmospheres of O_2 , N_2 and Ar respectively.

Figure 9.7 shows the XRD patterns of the powder and films deposited on Si(100) substrate in the different gas atmospheres of O_2 , N_2 and Ar. The crystallinity of the films in the different gas atmospheres are dependent on the type of gas. Similar XRD patterns were observed for all the films that deposited in the different working atmospheres. The peaks (111), (220) and (311) of the powder and thin film are in good agreement. The orientation of the crystallites in the thin film patterns for any of the gas atmospheres is random with no

texture. The XRD peaks for the film that was deposited in the O₂ atmosphere are more intense compared with the others. This is due to the greater thickness of this film, as will be shown later by the Auger depth profile results.

9.4.2 Morphology

Films with different roughnesses and morphologies are often obtained by changing the gas atmospheres [35]. Figure 9.8 show the AFM images for the films that were deposited using different gas atmospheres of O₂, N₂ and Ar. For all samples, the regions evaluated show that the substrate was well covered with no cracks. It is observed that the size and the distribution density of the particulates were larger and higher for the deposited thin film originating from O₂ compared to the other gases. The high resolution AFM pictures show well packed grains for the films deposited in the O₂ atmospheres with relatively rougher surfaces than the other deposited in vacuum, N₂ and Ar. A similar behaviour was observed by Yousif *et al.* [36] for Y₃(Al;Ga)₅O₁₂:Tb thin films when the films were deposited in O₂ gas atmospheres. The smoothest film is that deposited in the Ar gas atmosphere and consists of small nanoparticles. During deposition in vacuum the plume leaves the target with very high energy and travels through the chamber to the substrate. In the absence of a background gas, the particles making up the plume (atoms, ions and electrons) have a high likelihood of being reflected when they reach the substrate or the already growing film.

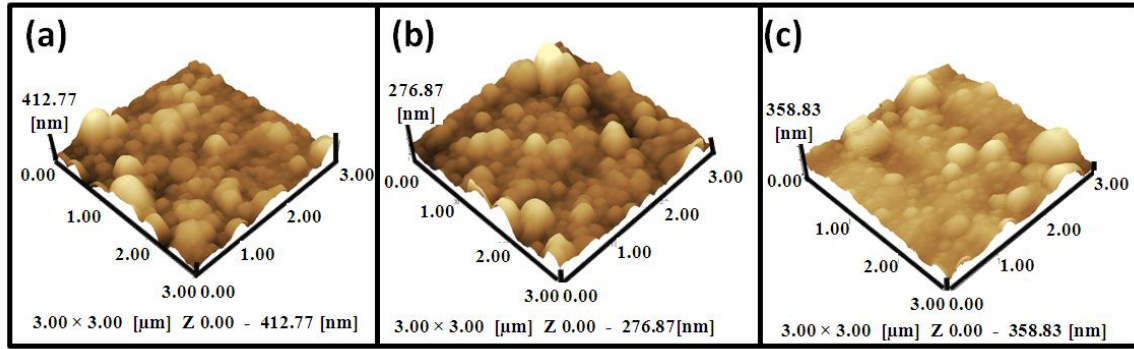


Figure 9.8: AFM images of the surface of (a) $\text{Mg}_{0.75}\text{Zn}_{0.25}\text{Al}_2\text{O}_4:\text{Tb}^{3+}$ thin films on Si substrate, deposited in the different gas atmospheres (a) O_2 , (B) N_2 and (C) Ar respectively.

The rms surface roughness of the thin films were 39 nm, 48 nm, 37 nm and 26 nm for the films deposited in vacuum, O_2 , N_2 and Ar atmospheres, respectively. The films deposited in O_2 are rougher than the rest of the thin films, while films deposited with Ar as a background gas were the smoothest. This is because the plume speed was reduced by the gas molecules to allow a better nucleation process of the film particles on the substrate. The film that was deposited in the Ar atmosphere shows a better surface with less features on the surface due to the fact that the Ar gas has a density higher than that of O_2 and N_2 .

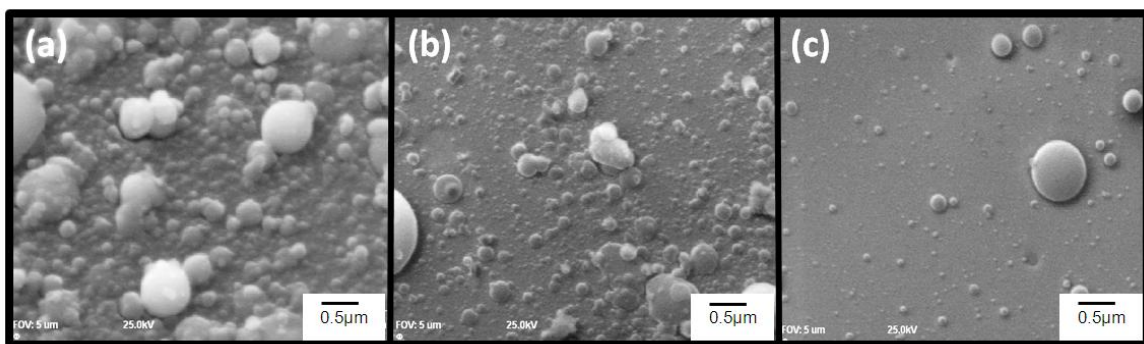


Figure 9.9: SEM images, for the thin film surfaces deposited in the different gas atmospheres (a) O_2 , (b) N_2 and (c) Ar respectively.

Investigations were also carried out to observe the surface morphology of the deposited films. Figure 9.9 shows the SEM micrographs of the surface of the films deposited in the different gas atmospheres (a) O₂, (b) N₂ and (c) Ar. The distribution density of the particulates depends on the type of the gas. The film surfaces are in enriched rounded particles of different sizes and shapes which seem to be formed from local melting and ejected from the target to the substrate which are typically found in laser ablation experiments. Droplets were the main feature that can be observed on the prepared thin films by PLD deposition. It is thought that the droplets consist of material ejected in molten form from the target due to the inhomogeneity of the power density distribution of the laser beam. These droplets formed with a relatively wide range of sizes, shape and concentration density. It is believed that both the ambient gas and gas-pressure was the main contributors to this films behaviour. A recent publication showed the influence of the ambient gas and gas-pressure plays a crucial role in the droplet formation [37]. Since these droplets might have effect on the optical property of thin films, it would be useful if their growth could be controlled. For the film deposited in vacuum the surface was rough and contained particle diameters of around 0.1 to 0.7 μm (figure 9.3). The film deposited in O₂ and N₂ have rougher surface morphologies. The film deposited in the O₂ contained more densely distributed particulates than the other films. The film deposited in the N₂ has droplets of various sizes but the ranging of these droplets was smaller than the film deposited in the O₂ ambient gas. For the film deposited in Ar ambient gas, the film surface was smooth and contained mostly small size droplets (few tens of nanometer) with some particles with different diameters and the particulates were nearly free on the surface of the film. High collisions between the ultrafine particles (vaporized particles close to the target) at ambient pressure in O₂ can lead to nucleation and growth into bigger particles of oxide material before arrival at the substrate.

9.4.3 NanoSAM analysis

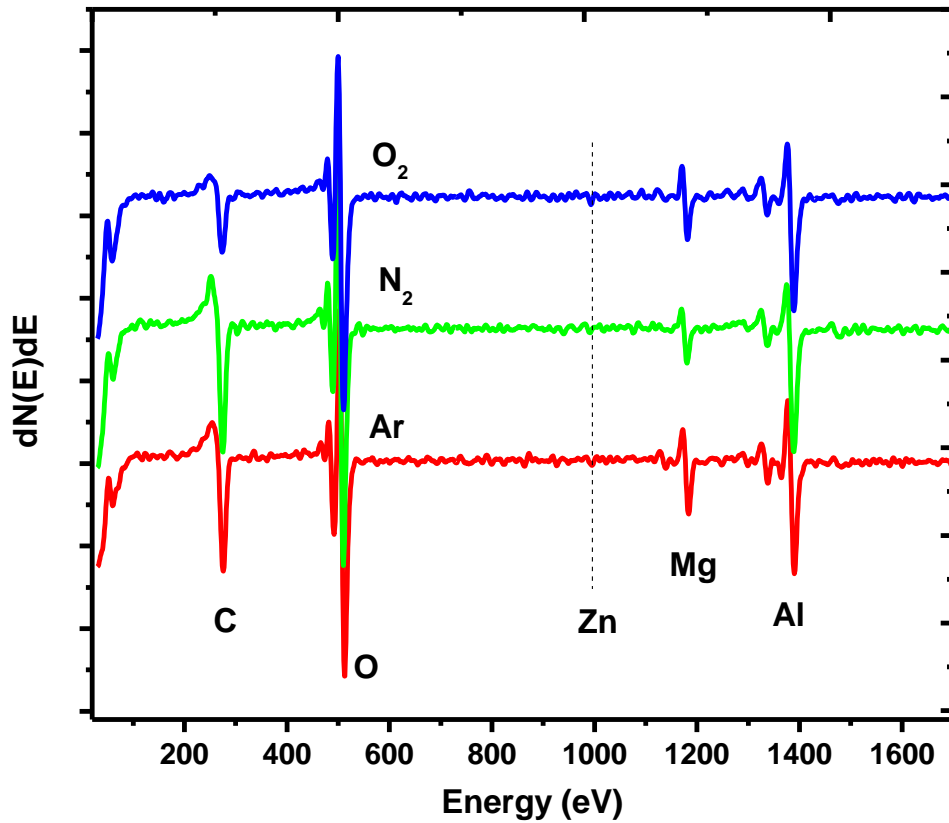


Figure 9.10: Surface AES spectra of $Mg_{0.75}Zn_{0.25}Al_2O_4:Tb$ thin films deposited in the different gas atmospheres of vacuum, O_2 , N_2 and Ar respectively.

Figure 9.10 show the AES spectra of the samples deposited in the different gas atmospheres of vacuum, O_2 , N_2 and Ar. The results confirm the presence of all major elements in the target material ($Mg_{0.75}Zn_{0.25}Al_2O_4:Tb$), namely Mg, Al, and O, but the expected peak from Zn it is not pronounced, which is due to the low sticking coefficient of Zn. Additionally, there was adventitious C on the surface.

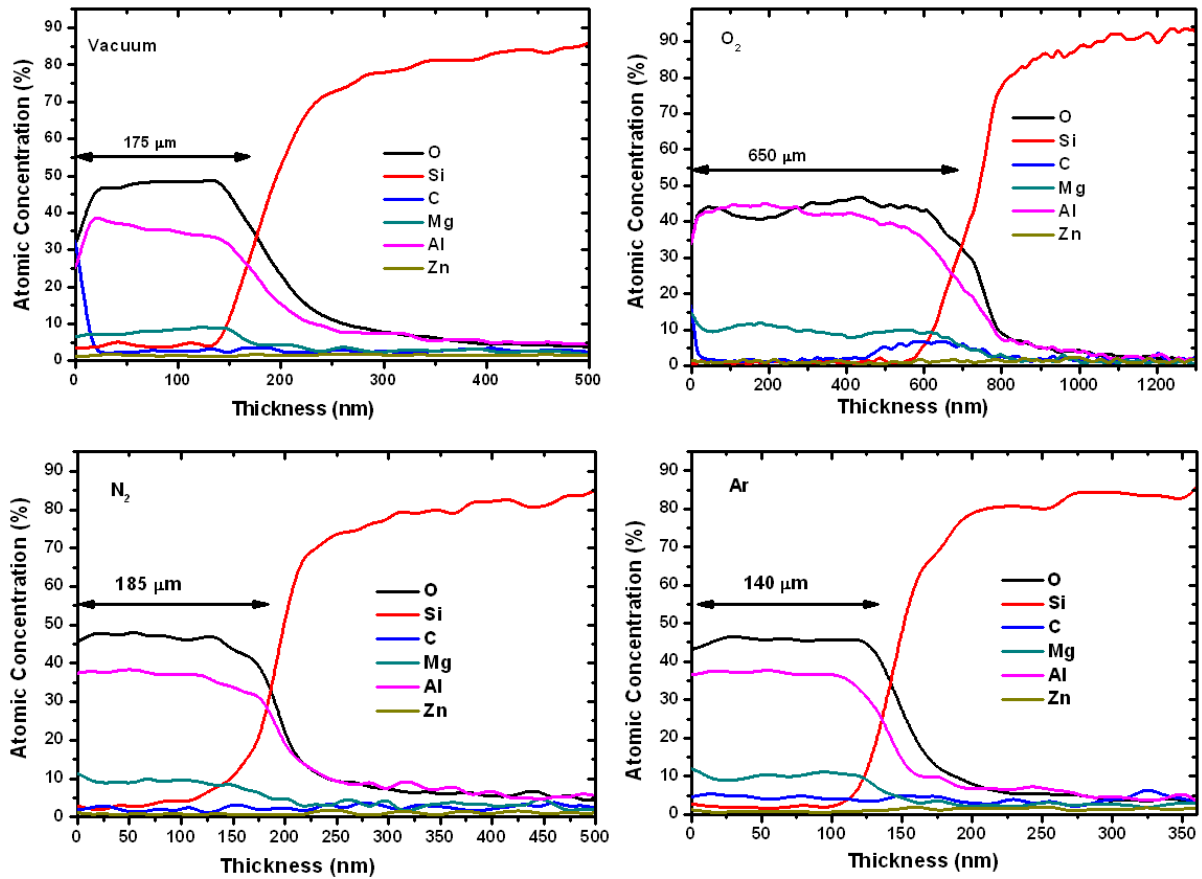


Figure 9.11: The depth profiles for the thin film in the different gas atmospheres (a) vacuum, (b) O_2 , (c) N_2 and (d) Ar.

Figure 9.11 shows the measured AES depth profiles of the films grown with different atmospheres. Assuming a 27 nm/min sputtering rate, we estimate the thickness of the films by using the point (depth) where the Si concentration in the AES profiles is about 50% of the maximum Si concentration. The thicknesses for the film deposited in vacuum, O_2 and Ar background were determined approximately as 175 nm, 650 nm and 140 nm respectively. The films prepared in Ar are clearly thinner than the other films and the region of the interface is thinner because the particles arrived at the substrate with low kinetic energy.

9.4.4 Optical properties

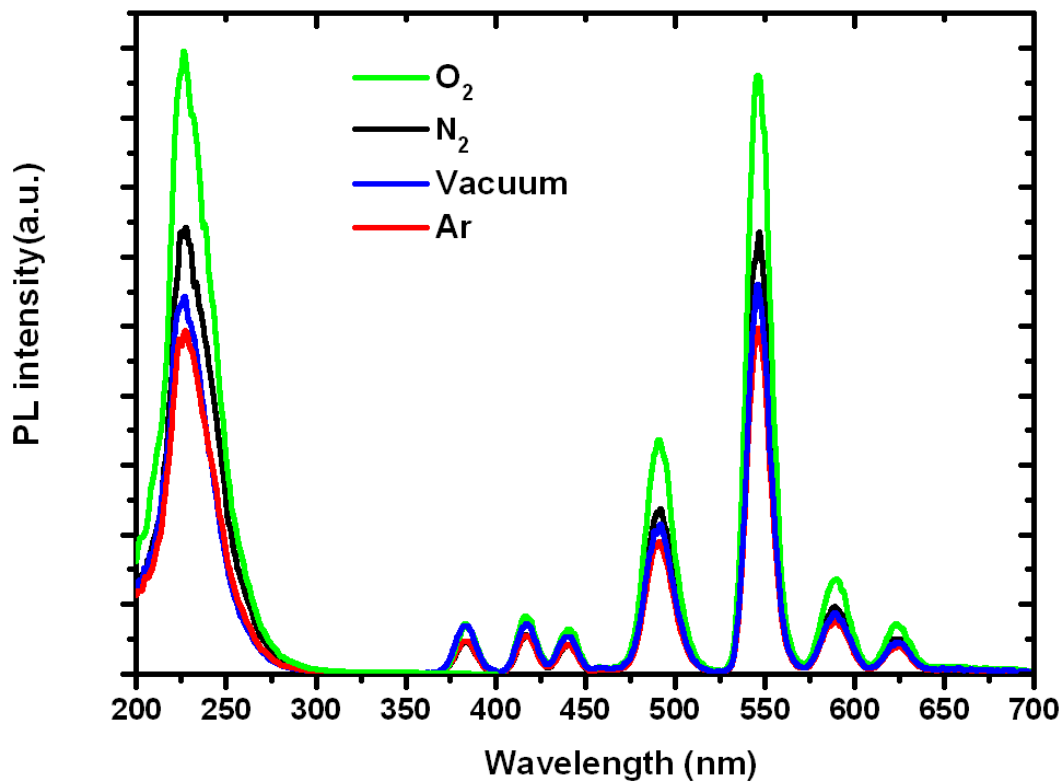


Figure 9.12: Room temperature luminescence spectra of thin films grown in different atmospheres.

The roughness and morphology of the thin films had a strong effect on the PL emission of the films. Figure 9.12 shows the excitation and emission spectra of the films that were deposited in different gases atmospheres. The excitation spectra shows a broad band from 200 to 300 nm with a maximum at about 227 nm. This broad band is the same for all deposition atmospheres. For the emission spectra all the samples were excited at 227 nm. The green emission peak that is located at 545 nm is ascribed to the $^5D_4 \rightarrow ^7F_5$ transition of Tb^{3+} . The unannealed film deposited in the O_2 atmosphere has a higher intensity than those prepared in the other gases atmospheres. This is because the thickness and the roughness are higher than for the other films. The lowest intensity was recorded from the unannealed film prepared in Ar. Published work on thin films have suggested that the increase in the

PL intensity for thin films deposited in an O₂ atmosphere can be associated with rougher surfaces and improved optical properties of larger particle sizes at higher roughness [36].

9.5 Conclusion

Mg_{0.75}Zn_{0.25}Al₂O₄:Tb³⁺ thin films phosphors were prepared on Si(100) substrates by using the PLD technique. The XRD patterns showed that all of the thin films were grown with a spinel structure and none showed any texture since the relative peaks intensities were the same as for the randomly oriented powder. The AFM and SEM results indicate that for a smooth thin film the optimum substrate temperature is 500 °C and Ar gas atmospheres. The intensity of emission was greater for the film prepared with a substrate temperature of 500 °C compared to those for a substrate temperature of 300 °C and 700 °C. The film deposited in O₂ atmosphere showed the best luminescence intensities. The absence of the zinc in the thin film is due to the low sticking coefficient of Zn, also due to the sticking factor of Mg, which becomes less as the substrate temperature increases.

9.6 References

1. Y. Zhang and J. Hao, *J. Mater. Chem. C* **1** (2013) 5607-5618.
2. A.M. Chinie, S. Georgescu, A. Mateescu and A. Stefan, *Romania J. Phys.* **51** (2006) 827-831.
3. D. Kim and W. Kang, *J. Bull. Korean Chem. Soc.* **25** (2004) 1524-1928.
4. J. Choe, D. Ravichandran, S.M. Blomquist, D.C. Morton, K.W. Kirchner, M.H. Ervin and U. Lee, *J. Appl. Phys. Lett.* **78** (2001) 3800-3802.
5. S.S. Yi, J.S. Bae, K.S. Shim, B.K. Moon, H.J. Seo, J.H. Jeong and J.H. Kim, *Appl. Phys. A* **80** (2005) 727-730.

6. T. Miyata, J. Ishino, K. Sahara and T. Minami, *Thin Solid Films* **519** (2011) 8095-8099.
7. C.P. Liu and G.R. Jeng, *J. Alloys Compd.* **468** (2009) 343-349.
8. Z. Lou and J. Hao, *Appl. Phys. A* **80** (2005) 151-154.
9. W. Zhang, J. Zhang, Y. Li, Z. Chen and T. Wang, *Appl. Surf. Sci.* **256** (2010) 4702-4707.
10. J. Yang, T. Liu, C. Hsu, L. Chen, K. Chen and C. Chen, *Nanotechnology* **17** (2006) S321-S326.
11. S.S. Yi, I.W. Kim, H.L. Park, J.S. Bae, B.K. Moon and J.H. Jeong, *J. Cryst. Growth* **247** (2003) 213-218.
12. H.C. Swart, O.M. Ntwaeaborwa, P.D. Nsimama and J.J. Terblans, *Phys. B* **407** (2012) 1660-1663.
13. J.H. Markna, P.S. Vachhani, N.A. Shah, J. John, D.S. Rana, S.K. Malik and D.G. Kuberkar, *Indian J. Eng. Mater. Sci.* **16**, (2009) 123-127.
14. L.P. Peng, L. Fang, X.F. Yang, Y.J. Li, Q.L. Huang, F. Wu and C.Y. Kong, *J. Alloys Compd.* **484** (2009) 575-579.
15. X. Y. Chen, C. Ma and S. P. Bao, *Solid State Sci.* **12** (2010) 857-863.
16. V. Singh, S. Watanabe, T.K. GunduRao, J.F.D. Chubaci, I. Ledoux-Rak and H.Y. Kwak, *Appl Phys B* **98** (2010) 165-172.
17. R.J. Wiglusz and T. Grzyb, *Opt. Mat.* **33** (2011) 1506-1513.
18. K.G. Tshabalala, S-H. Cho, J-K. Park, S.S. Pitale, I.M. Nagpure, R.E. Kroon, H.C. Swart and O.M. Ntwaeaborwa *J. Alloys Compd.* **509** (2011) 10115-10120.
19. P. Gluchowski, R. Pązik, D. Hreniak and W. Stręk, *Chemical Physics* **358** (2009) 52-56.
20. X.Y. Chen and C. Ma, *Opt. Mat.* **32** (2010) 415-421.

21. K.K. Satapathy, G.C. Mishra and F. Khan, *Chem. Sci. Trans.* **2** (2013) 1262-1267.
22. L.H. Ha, P.T. Lanh, N.N. Long and T.T. Loan, *J. Phys.: Conf. Ser.* **187** (2009) 012053.
23. Y. Yang, X. Qu, Y. Luo and A. Yang, *J. Adv. Mater. Res.* **216** (2011) 514-517.
24. A.R. Phani, M. Passacantando, S. Santucci, *Mater. Chem. Phys.* **68** (2001) 66-71.
25. W.A.I. Tabaza, H.C. Swart and R.E. Kroon (2012). Submitted to: South African Institute of Physics (Pretoria).
26. D. P. Norton, *Materials Science and Engineering R* **43** (2004) 139-247.
27. C.F. Zhu, I. Lee, J. W. Li, C. Wang, X.Y. Cao, H. Xu and R.B. Zhang, *J. Mater. Res.* **14** (1999) 1084-1090.
28. R. Eason (Ed.), *Pulsed Laser Deposition of Thin Films: Applications-Led Growth of Functional Materials*, John Wiley & Sons (Hoboken, 2007).
29. M.A. Petrova, G.A. Mikirticheva, A.S. Novikova and V.F. Popova, *J. Mater. Res.* **12** (1997) 2584-2588.
30. E. Gyorgy, I.N. Mihailescu, M. Kompitsas and A. Giannoudakos, *Appl. Surf. Sci.* **195** (2002) 270-276.
31. E. Gyorgy, I.N. Mihailescu, M. Kompitsas and A. Giannoudakos, *Thin Solid Films* **446** (2004) 178-183.
32. O.M. Ntwaeaborwa, P.D. Nsimama, J.T. Abiade, E. Coetsee and H.C Swart, *Phys. B* **404** (2009) 4436-4439.
33. G. Balakrishnan, S. TripuraSundari, R. Ramaseshan, R. Thirumurugesan, E. Mohandas, D. Sastikumar, P. Kuppusami, T.G. Kim and J.I. Song, *Ceram. Int.* **39** (2013) 9017-9023.
34. S.S. Yi, I.W. Kim, H.L. Park, J.S. Bae, B.K. Moon and J.H. Jeong, *J. Cryst. Growth* **247** (2003) 213-218.

35. H.K. Yang, B.K. Moon, B.C. Choi and J.H. Jeong, *J. Korean Phys. Soc.* **49** (2006) 2413-2417.
36. A. Yousif, H.C. Swart and O.M. Ntwaeaborwa (2012). Submitted to: South African Institute of Physics (Pretoria).
37. C. Wang, B.L. Cheng, S.Y. Wang, H.B. Lu, Y.L. Zhou, Z.H. Chen and G.Z. Yang, *Thin Solid Films* **485** (2005) 82-89.

10 Conclusion

10.1 Summary

The MgAl_2O_4 powder was successfully synthesized by the combustion method with different dopants. XRD showed that the dopant was successfully incorporated in the lattice for all dopants. Samples of Ce doped MgAl_2O_4 show luminescence after annealing in a reducing atmosphere of 4% H_2 in Ar. The maximum intensity of green emission was measured as a function of Ce doping concentration, with the maximum occurring for 0.75 mol%. UV-vis diffuse reflectance spectroscopy and XPS results provide evidence that the annealing in reducing atmosphere is required to convert Ce from the non-luminescent Ce^{4+} oxidation state to the luminescent Ce^{3+} oxidation state. There are two XPS doublets associated with the Ce^{3+} ions but the results indicate a correlation of the Ce luminescence intensity with only the $\text{Ce}^{3+}(3d^94f^1)\text{O}(2p^6)$ configuration, suggesting that the $\text{Ce}^{3+}(3d^94f^2)\text{O}(2p^5)$ configuration for which the Ce^{3+} ion's 4f electron orbitals are strongly influenced by the oxygen 2p orbitals may be non-luminescent.

For the samples of Bi doped MgAl_2O_4 , show a broad band blue fluorescence emission centred at 400 nm for excitation at 335 nm, which is attributed to the $^3\text{P}_1 \rightarrow ^1\text{S}_0$ transition of Bi^{3+} ions. The emission intensity was measured as a function of Bi doping concentration, with the maximum occurring at 0.5 mol% of Bi doping. The results indicate that doping MgAl_2O_4 with Bi ions may be an attractive alternative to doping it with Ce ions, which give broad blue-green luminescence in this host but requires reducing at a high

temperature (1400 °C) to convert non-luminescent Ce⁴⁺ ions to the luminescent Ce³⁺ charge state.

The Bi, Tb co-doped MgAl₂O₄ samples, shows that the Bi emission band overlaps Tb³⁺ f-f excitation peaks. This leads to significant enhancement of Tb emissions from the ⁵D₄ level for excitation wavelengths between 300 nm and 380 nm, thereby extending the useable excitation band of Tb to much longer wavelengths compared to Tb single doped samples. The results suggest that Bi offers an attractive alternative to Ce which is often used to sensitize Tb in many other hosts.

The mixed spinel (Mg_xZn_{1-x})Al₂O₄ was successfully synthesized using the combustion method and doped with Tb. The maximum PL intensity of the green emission at 544 nm occurred for Mg_{0.75}Zn_{0.25}Al₂O₄ and the optimum Tb concentration was found to be 0.5 mol%. The blue emission at 416 nm was almost absent for ZnAl₂O₄, but increased with the Mg content and was a maximum for MgAl₂O₄. This is attributed to the increasing bandgap with Mg content.

Mg_{0.75}Zn_{0.25}Al₂O₄:Tb³⁺ thin films phosphors were prepared on Si(100) substrates by using sol-gel spin-coating technique and PLD technique. The XRD patterns showed that all the thin films were grown with spinel structure. For thin film prepared by spin-coating, the crystallinity was improved with strong (111) texture and that the crystallite size increased with increasing annealing temperature. All lines of emission increased after annealing at 800 °C compared to 600 °C. The intensity of the 545 nm peak increased with increasing annealing temperature up to 1000 °C. After annealing the thin film at 1200 °C, the intensity of the blue lines increased and the surface morphologies changed from smooth

and flat to a rough structure similar to hills and valleys. The results show that diffusion of Si from the substrate occurs through the thin film which increases in thickness. The results show that diffusion from the Si substrate at 1000 °C and at 1200 °C cause a new host containing Si to be formed.

For thin film prepared by PLD technique no preferred orientation in the thin film patterns was observed for any of the substrate temperatures because the relative peak heights are similar to the randomly oriented powder. The surface of the 700 °C shows that the sample is completely different from the rest of the films, with relatively bigger and was therefore expected to give the highest PL intensity, but the emission is weak. At a higher temperature above 500 °C, the intensity of luminescence became weaker. The film that was prepared at 500 °C showed smoothness, and the film's surface was much more uniform and smaller particle size was obtained compared to the films prepared at 300 °C and 700 °C. The smoothest film that consisted of small nanoparticles was the film deposited in Ar gas atmospheres. The thin films deposited at a 500 °C substrate temperature and deposited in O₂ atmosphere showed the best luminescent intensities. The absence of the zinc in the thin film made by PLD is due to the low sticking coefficient of Zn, also due to the sticking factor of Mg, which becomes less as the substrate temperature increases.

The PLD is a good technique for synthesizing of the thin films at lower substrate temperatures, but a lot of parameters have to be used in order to get best thin film and the correct stoichiometric transfer of the target material to the substrate during deposition. The spin-coating process is an effective and easy alternative method for growing the thin films which avoids the loss of certain elements of high vapour pressure during the PLD process.

10.2 Suggestions for future work

For future work the following is suggested:

1. Measurement of the lifetime of the Bi emission of the Bi, Tb co-doped MgAl_2O_4 to study the mechanism of the energy transfer.
2. Study of the energy transfer between the Bi and other lanthanides e.g. Eu in MgAl_2O_4 .
3. Prepare other aluminate hosts doped with the Bi (e.g. SrAl_2O_4) and compare the results with MgAl_2O_4 host. This will be interesting because SrAl_2O_4 does not have the spinel structure.
4. Prepare sol-gel spin-coated $\text{MgAl}_2\text{O}_4:\text{Tb}$ and $\text{ZnAl}_2\text{O}_4:\text{Tb}$ thin films for different annealing temperatures and compare the luminescence to that from the mixed spinel $\text{Mg}_{0.75}\text{Zn}_{0.25}\text{Al}_2\text{O}_4:\text{Tb}$ characterized in this work.
5. To try solve the problem of the loss of Zn during preparation of PLD thin films, prepare the thin films with room temperature substrates and then study the effect of annealing temperature on these films. Alternatively, one can add different quantities of ZnO to the target material to try compensate for the loss of Zn.
6. To characterise the phosphors produced during this study using cathodoluminescence.
7. Prepare an electroluminescence device by using the spin-coated sol-gel thin films of $\text{Mg}_{0.75}\text{Zn}_{0.25}\text{Al}_2\text{O}_4:\text{Tb}$ characterized in this work.